CFD SIMULATION OF SOOT FORMATION AND FLAME RADIATION

by

Christopher William Lautenberger

A Thesis

Submitted to the Faculty

of the

WORCESTER POLYTECHNIC INSTITUTE

In partial fulfillment of the requirements for the

Degree of Master of Science

In

Fire Protection Engineering

By

_____

January 2002

APPROVED:

_____

Professor Nicholas A. Dembsey, Major Advisor

_____

Professor Jonathan R. Barnett, Co-Advisor

_____

Dr. John L. de Ris, Co-Advisor
Factory Mutual Research Corporation

_____

David A. Lucht, Head of Department

ABSTRACT

The Fire Dynamics Simulator (FDS) code recently developed by the National Institute of Standards and Technology (NIST) is particularly well-suited for use by fire protection engineers for studying fire behavior. It makes use of Large Eddy Simulation (LES) techniques to directly calculate the large-scale fluid motions characteristic of buoyant turbulent diffusion flames. However, the underlying model needs further development and validation against experiment in the areas of soot formation/oxidation and radiation before it can be used to calculate flame heat transfer and predict the burning of solid or liquid fuels. WPI, Factory Mutual Research, and NIST have undertaken a project to make FDS capable of calculating the flame heat transfer taking place in fires of hazardous scale.

The temperatures predicted by the FDS code were generally too high on the fuel side and too low on the oxidant side when compared to experimental data from small-scale laminar diffusion flames. For this reason, FDS was reformulated to explicitly solve the conservation of energy equation in terms of total (chemical plus sensible) enthalpy. This allowed a temperature correction to be applied by removing enthalpy from the fuel side and adding it to the oxidant side. This reformulation also has advantages when using probability density function (PDF) techniques in larger turbulent flames because the radiatively-induced nonadiabaticity is tracked locally with each fluid parcel. The divergence of the velocity field, required to obtain the flow-induced perturbation pressure, is calculated from an expression derived from the continuity equation.

A new approach to soot modeling in diffusion flames was developed and added to the FDS code. The soot model postulated as part of this work differs from others because it is intended for engineering calculations of soot formation and oxidation in an arbitrary hydrocarbon

fuel. Previous models contain several fuel-specific constants that generally can only be determined by calibration experiments in laminar flames. The laminar smoke point height, an empirical measure of a fuel's sooting propensity, is used in the present model to characterize fuel-specific soot chemistry. Two separate mechanisms of soot growth are considered. The first is attributed to surface growth reactions and is dependent on the available surface area of the soot aerosol. The second is attributed to homogeneous gas-phase reactions and is independent of the available soot surface area. Soot oxidation is treated empirically in a global (fuel-independent) manner. The local soot concentration calculated by the model drives the rate of radiant emission.

Calibration against detailed soot volume fraction and temperature profiles in laminar axisymmetric flames was performed. This calibration showed that the general approach postulated here is viable, yet additional work is required to enhance and simplify the model. The essential mathematics for modeling larger turbulent flames have also been developed and incorporated into the FDS code. An assumed-beta PDF is used to approximate the effect of unresolved subgrid-scale fluctuations on the grid-scale soot formation/oxidation rate. The intensity of subgrid-scale fluctuations is quantified using the principle of scale similarity. The modified FDS code was used to calculate the evolution of soot in buoyant turbulent diffusion flames. This exercise indicated that the subgrid-scale fluctuations are quantitatively important in LES of turbulent buoyant diffusion flames, although no comparison of prediction and experiment was performed for the turbulent case.

ACKNOWLEDGEMENTS

I would like to thank the organizations that directly funded this research. FM Global provided generous financial support in the form of an internship. The SFPE Educational and Scientific Foundation also partially funded this research. Additionally, I would like to thank the other organizations that did not directly fund this research but provided some level of financial support throughout the course of my graduation education. I am grateful to WPI's Center for Firesafety Studies for 12 months of support as a Research Assistant, as well as one semester's support as a Teaching Assistant. I also appreciate the generous financial contributions of both the Massachusetts and St. Louis chapters of the Society of Fire Protection Engineers as well as Marsh Risk Consulting and Code Consultants, Incorporated.

Several individuals have been instrumental in this research. Dr. John de Ris at Factory Mutual has provided daily insight and direction for the last 14 months. I would like to thank him for many useful discussions as well as the numerous contributions that he has made to this project. I would also like to thank my thesis advisor at WPI, Professor Nicholas Dembsey. Even though he is extremely busy advising several theses/dissertations and teaching classes, he was always available to offer guidance and pedagogical advice, read over lengthy interim reports, and spend several hours at the blackboard going over the more subtle points of this work. I would also like to extend thanks to Professor Jonathan Barnett for piquing my interest in fire protection engineering as a sophomore, serving as my academic advisor, and for leading me through my graduate education.

This project would not have been possible without Dr. Kevin McGrattan, Dr. Howard Baum, and their coworkers at NIST for it is through their efforts over the last quarter century that Fire Dynamics Simulator has come to fruition. I would like to thank Dr. McGrattan for his help

in getting a modified version of the FDS code up and running, and answering my many questions.

TABLE OF CONTENTS

LIST OF FIGURES

Appendix A

Appendix B

Appendices C-M

LIST OF TABLES

Appendix A

Appendices C-M

NOMENCLATURE

A_0	Soot inception area [m^2 soot/m^3 mixture]
A_f	Flame surface area [m^2]
A_s	Specific soot surface area [m^2 soot/m^3 mixture]
c_p	Constant-pressure specific heat [kJ/kg · K]
C_{scale}	Scale similarity constant [-]
C_{smag}	Smagorinsky constant [-]
C_{κ_s}	Constant relating f_v and T to κ_s [$(mK)^{-1}$]
D	Diffusivity [m^2/s]
$\boldsymbol{f}$	Body force vector excluding gravity [N/m^3]
f_v	Soot volume fraction [m^3/m^3]
$\boldsymbol{g}$	Gravity vector [m/s^2]
h	Sensible enthalpy [kJ/kg]
h°	Enthalpy of formation [kJ/kg]
h_T	Total enthalpy ($h + h^\circ$)[kJ/kg]
ΔH	Heat of combustion [kJ/kg]
$\mathcal{H}$	Total pressure divided by density [m^2/s^2]
I	Radiant intensity [W/m^2]
k	Turbulent kinetic energy[$kg \cdot m^2/s^3$]
k	Thermal conductivity [W/m · K]
ℓ_s	Laminar smoke point height [m]
L	Path-length, mean bean length [m]
Le	Lewis number [-]
M	Molecular weight of a single species [kg/mole]
$\mathcal{M}$	Molecular weight of a gas mixture [kg/mole]
N	Soot number density [particles/m^3]
p	Total pressure [Pa]
p_0	Background pressure [Pa]
$\tilde{p}$	Flow-induced perturbation pressure [Pa]
P	Partial Pressure [Pa]
Pr	Prandtl number [-]
$\dot{q}$	Heat release rate [W or kW]
$\dot{Q}$	Heat release rate [W or kW]
Q	Volumetric flowrate [cm^3/s]
R	Universal gas constant [kJ/kg · K]
s	Stoichiometric mass of oxidant per unit mass of fuel [-]
Sc	Schmidt number [-]

T Temperature [K]
T_0 Reference temperature (temperature datum) [K]
u Velocity component [m/s]
$\boldsymbol{u}$ Velocity vector [m/s]
V Velocity [m/s]
V Volume [m^3]
X Mole fraction [-]
Y Mass fraction [-]
Z Mixture fraction [-]

Greek Symbols

β Constant for estimating soot surface area from f_v [m^2 soot/m^3 mixture]
β Spectral slope in Kolmogorov cascade[-]
γ Specific heat ratio, c_p/c_v [-]
ε Dissipation rate of turbulent kinetic energy [$kg \cdot m^2/s^2$]
κ Emission/absorption coefficient [m^{-1}]
λ Wavelength [μm]
μ Viscosity [$kg/m \cdot s$]
ν Stoichiometric coefficient [-]
ν Viscosity [m^2/s]
ρ Density, general [kg/m^3]
ρ_2 Density, two-phase [kg/m^3]
ρ_g Density, gas-phase [kg/m^3]
σ Stefan-Boltzmann constant [5.67×10^{-8} W/m^2K^4]
$\boldsymbol{\tau}$ Reynolds Stress / viscous stress tensor (Vector notation) [m^2/s^2]
τ_{ij} Reynolds Stress (Cartesian Tensor notation) [m^2/s^2]
ϕ Equivalence ratio [-]
ϕ Parameter for setting slope of mixture fraction polynomial at Z_L and Z_H [-]
χ Local nonadiabaticity [-]
χ_r Global radiative fraction [-]
χ_{ij} Interaction parameter for calculating the viscosity of a gas mixture [-]
ψ Multiplying factor in mixture fraction soot polynomials, equal to Z/Z_{st} [-]
$\dot{\omega}$ Formation rate [kg/s]
ω Vorticity vector [s^{-1}]

Subscripts

a air, absorption
ad adiabatic
CO carbon monoxide
CO_2 carbon dioxide
e emitted, emission

f	flame
F	fuel
g	gas or gas-phase
H_2O	water vapor
i	species i
i	coordinate direction i in Cartesian tensor notation
j	coordinate direction j in Cartesian tensor notation
L	low
o	oxidant
O_2	oxygen
p	products
P	peak
H	high
r	reactants
s	soot
st	stoichiometric
so	soot oxidation
sp	smokepoint
sf	soot formation
t	turbulent
μ	viscosity
∞	ambient

Superscripts

$''$	per unit area
$'''$	per unit volume

Abbreviations

Exp.	Experimental
HAB	Height above burner
HRR	Heat release rate
Pred.	Predicted
PUA	Per unit area
PUV	Per unit volume

1.0 DOCUMENT ORGANIZATION

The text of this document is divided into two sections. The first (Chapters 1-4) describes the essence of the work that has been completed here and its broader implications for the fields of fire research and fire protection engineering. This section sets the context for the second section, a series of appendices that constitute the core of this thesis. Appendix A explains the development of a new engineering model for soot formation and oxidation in laminar atmospheric hydrocarbon diffusion flames. Appendix B discusses the mathematics that are required to extend this model to the simulation of turbulent diffusion flames. Appendices A and B are intended to serve as drafts of future publications on these topics; therefore, any publications dated later than January 2002 take precedence. Appendices C through M give additional information relevant to this MS Thesis that was not included icn either draft.

1.1 Guide to Appendices

Appendix A An Engineering Approach to Soot Formation and Oxidation in Atmospheric Diffusion Flames of an Arbitrary Hydrocarbon Fuel

This appendix describes in general terms the soot formation and oxidation model that has been postulated here. Modifications made to FDS v2.0[1,2] are discussed, including a reformulation to explicitly solve the energy equation, application of a temperature correction, and insertion of the soot model. A quantitative comparison of the model predictions to experimental data in laminar axisymmetric flames is given and the model constants necessary to apply the model to an arbitrary hydrocarbon fuel are established.

Appendix B Mathematical Framework for Engineering Calculations of Soot Formation and Flame Radiation Using Large Eddy Simulation

This appendix explains how the model described in Appendix A was applied to turbulent flames with the use of a probability distribution function (PDF). The mathematics necessary to model large turbulent flames are developed, and sample calculations of a qualitative nature are presented.

Appendix C Mixture Fraction and State Relations

This appendix presents a derivation of the classical mixture fraction, an important concept in numerical calculations of nonpremixed combustion. Also discussed are several types of state relations that can be used to relate the gas-phase composition to the mixture fraction in diffusion flames.

Appendix D Reformulation of FDS in Terms of Total Enthalpy

As part of this work it was necessary to reformulate the FDS code so that a conservation equation is solved for the total (chemical plus sensible) enthalpy. This appendix describes how this was done and introduces the concept of nonadiabaticity, an important component of turbulent calculations.

Appendix E Derivation of Velocity Divergence Expressions

A key feature of the NIST FDS model is that the flow-induced perturbation pressure is determined from the divergence of the velocity field. This allows the fluid mechanical equations to be solved using efficient Fast Fourier Transforms. In the original code, the equation for conservation of mass is explicitly solved and the energy conservation equation is not explicitly solved, but rather used to form the divergence of the velocity field. However, as part of this work the code was reformulated to explicitly solve the energy equation and use the conservation of mass equation to determine the divergence of the velocity field. This appendix presents a

derivation of expressions for the velocity divergence using the energy conservation and mass conservation equations as the starting points.

Appendix F Adjustment of Temperature Prediction

It was found that flame temperatures were generally overpredicted at fuel-rich conditions and underpredicted at fuel-lean conditions. For this reason, a temperature correction was applied to artificially decrease the fuel-rich temperatures, and increase the fuel-lean temperatures. This appendix describes how this was done by removing enthalpy on the fuel side and adding it to the oxidant side.

Appendix G Setting up the Soot Formation Polynomials

The soot formation and oxidation rates are expressed as the product of explicit polynomial functions of mixture fraction and temperature. This appendix describes how the polynomial coefficients are determined by specifying a series of point-value or point-slope pairs and solving the resultant set of linear equations.

Appendix H Soot Absorption Coefficient

This appendix explains the procedure through which the soot volume fraction calculated by the model is translated into the soot absorption coefficient. The importance of the soot absorption coefficient is that it drives the overall flame radiation.

Appendix I A New Qualitative Theory for Soot Oxidation

This appendix hypothesizes that the rate of soot oxidation in diffusion flames is not controlled by the available surface area, but rather by the diffusion of molecular oxygen toward the flame sheet.

Appendix J Efficient Integration Techniques in Turbulent Flames

Turbulent fluctuations are approximated by integrating over a probability density function. This is a computationally-expensive task when using a "brute-force" technique such as approximation by rectangles. This appendix presents two numerical techniques that can be used to efficiently integrate over a PDF using more efficient methods. The first is a recursive algorithm that is useful for approximating the effect of temperature fluctuations on radiant emission. The second makes use of Fast Fourier Transforms and Chebyshev polynomials to approximate the effect of fluctuations on soot formation and oxidation rates.

Appendix K Thermodynamic Properties and Transport Coefficients

This appendix lists in tabular format the thermodynamic data and transport coefficients that have been incorporated into the code or used in calculations presented throughout the manuscript. The sources where these data were obtained are also cited.

Appendix L User's Guide to New Features

The additions and modifications that were made to the FDS code[1,2] are accessible through the standard FDS input file. Appendix L explains how these features can be used.

Appendix M User's Guide to SLICETOCSV Companion Program

As part of this work, a companion program dubbed SLICETOCSV (Slice file to .CSV file) was written to extract data from a standard FDS slice file and generate a .CSV (comma separated variable) ASCII file which can be easily imported into a spreadsheet package. This program can extract data at a single instant in time, or time-average the data over a user-specified interval. This is explained in Appendix M.

2.0 THESIS OVERVIEW

The research expounded herein falls under the general umbrella of "soot formation and flame radiation in diffusion flames". However, this does not adequately describe the breadth of subject matter. Although the outcome of this research is a model for soot formation and flame radiation, it represents the synergy of many separate components drawing from the fields of chemistry, thermodynamics, turbulence, computational fluid dynamics, statistics, heat transfer, numerical analysis, vector calculus, and others.

At the heart of this research is the numerical modeling of diffusion flames, an extremely challenging endeavor due to the inextricably coupled nature of the underlying phenomena. Reaction rates, including soot formation, generally increase with temperature; yet an increased soot production causes the local temperature to be depressed by continuum radiation from the soot cloud. There are also instances of positive feedback—an increase in soot formation low in the flame augments soot production farther "downstream". It is therefore difficult to modify one aspect of the calculation without altering another, intentionally or otherwise.

In the classical models of soot formation and oxidation in diffusion flames, separate expressions are solved for the rate of particle inception/nucleation, coagulation/agglomeration, surface growth, and oxidation[3]. These models usually contain several fuel-specific constants that must be established by "calibration" against laminar flame data[4]. A conservation equation is solved for the soot mass fraction (or equivalently volume fraction) and the particle number density.

The model postulated as part of this work deviates from this classical approach to modeling soot formation and oxidation. Inception, nucleation, coagulation, and agglomeration are not explicitly considered. A conservation equation is solved *only* for the soot mass fraction.

The model is generalized to multiple fuels by relating the peak rate of soot formation to the fuel's laminar smoke point height, an empirical measurement of a fuel's relative sooting propensity[5]. Differences in stoichiometry among fuels are handled by using simple scaling relationships. This eliminates the need to determine fuel-specific constants that makes most other soot models impractical for most engineering applications.

In the present model, both surface area-dependent and surface area-independent growth mechanisms are considered. The soot formation and oxidation rates are calculated as the product of two polynomial functions, one having temperature as the independent variable and the other having the mixture fraction as the independent variable. The mixture fraction is a commonly used tool in numerical calculations of diffusion flames[6] and is defined in this work as the fraction of gas-phase material that originated as fuel[7]. This particular formulation was inspired by an experimental study[8] in which soot growth rates in laminar ethylene and ethane flames were reported in terms of mixture fraction and temperature. The polynomial coefficients are determined by specifying a series of point-value and point-slope pairs and solving the resulting set of linear equations using Gauss-Jordan elimination[9]. This is transparent to the user. The soot formation and oxidation postulated here was incorporated into Fire Dynamics Simulator (FDS) v2.0[1,2], a Computational Fluid Dynamics (CFD) code developed by the National Institute of Standards and Technology (NIST). This code can simulate both laminar and turbulent flames, with the latter being handled by Large Eddy Simulation (LES)[10] techniques. FDS can be run in two-dimensional or three-dimensional Cartesian coordinates as well as two-dimensional cylindrical (axisymmetric) coordinates.

It was determined that the flame temperatures computed by FDS v2.0[1,2] for small-scale laminar axisymmetric flames did not match experimental data[11]. The temperatures were

generally overpredicted in fuel-rich regions and underpredicted in fuel-lean regions. Since the soot formation and oxidation rates were modeled as strong functions of temperature, some sort of a correction was necessary to improve the temperature predictions. However, this was difficult due to the manner in which the FDS v2.0[1] combustion model is formulated. A major restructuring of the FDS code was performed to allow a temperature correction to be applied. This also has advantages when calculating the soot formation and oxidation rates in turbulent diffusion flames using PDF techniques[12].

The model was reformulated to explicitly solve the energy conservation equation in terms of total (chemical plus sensible) enthalpy. A "radiatively perturbed laminar flamelet"[13] approach was used in which the temperature is known as a function of mixture fraction and total enthalpy. The local value of enthalpy reflects the radiative history of a particular fluid parcel. This is advantageous in turbulent calculations where unresolved subgrid-scale fluctuations in species composition and temperature may exist because the temperature is known explicitly as a function mixture fraction for a given level of nonadiabaticity, *i.e.* radiative loss[13]. This allows the soot formation rate (known as a function of mixture fraction and temperature) to be directly integrated over the mixture fraction PDF for a given level of radiation loss, thereby accounting for the unresolved subgrid-scale fluctuations.

Flame radiation is handled by defining a single local absorption coefficient for each cell that is the sum of a soot contribution and a gas-phase contribution. The soot contribution is determined from the local soot volume fraction as calculated from the soot conservation equation, and the gas-phase contribution is estimated from the local gas-phase composition as determined from the complete combustion state relations. The narrow band radiation model

RADCAL[14] is used to account for the spectral nature of gas radiation. Since RADCAL requires a radiation pathlength to be specified, the mean beam length of the overall flame volume is used.

In turbulent calculations, the mixture fraction PDF was assumed to follow a beta distribution[12]. This presumed form can approximate single-delta and double-delta (unmixed) distributions as well as Gaussian (well-mixed) and asymmetric distributions[15]. It is a two-parameter system requiring as input only the first two moments of the mixture fraction distribution (its mean and variance). The mean value of mixture fraction is determined from the mixture fraction conservation equation and its variance is predicted using scale similarity. This principle presumes that the *unresolved* small scales are isotropic and similar to the smallest *resolved* scales[10]. Therefore, the statistics of the unresolved scales can be inferred from the statistics of the resolved scales.

The soot model was calibrated by comparing the predicted soot volume fraction profiles in small-scale laminar axisymmetric methane, propane, and ethylene flames to those measured experimentally[11]. A set of "global" model constants was established, and the peak soot formation rate was determined to be approximately proportional to the inverse laminar smoke point height raised to the 3/5 power. A correlation between the enthalpy of formation and the inverse square root of the smokepoint was noted for non-aromatic fuels, but aromatic fuels are sootier than the correlation indicates. Since a fuel's enthalpy of formation is a measure of the chemical energy stored in its molecular bonds, this correlation indicates the formation of incipient soot particles in diffusion flames may be controlled by the rate at which fuel fragments are converted to aromatic soot precursors. It was therefore postulated that the incipient soot surface area[8] should be proportional to the fuel's enthalpy of formation and the peak soot surface growth rate.

The model was applied to turbulent flames using the PDF methods described above. A quantitative comparison of prediction and experiment was not performed. Rather, the effect of subgrid-scale fluctuations on the evolution of soot throughout a buoyant turbulent diffusion flame was studied. A 100kW propane flame on a square burner was simulated with the formation/oxidation rates calculated from the mean value of mixture fraction and temperature, and then with the formation/oxidation rates integrated over the mixture fraction PDF. It was determined that for the flame studied, subgrid-scale fluctuations cause less soot to form low in the flame, slightly more soot in an intermediate region, and less soot in the upper regions compared to the simulation with formation/oxidation rates based only on mean properties.

3.0 CONCLUSION

3.1 Significant Contributions

The primary significance of this work is that an entirely new approach to calculating soot formation and oxidation rates in diffusion flames has been formulated, incorporated into a CFD code, and shown to be feasible. Whereas other soot formation models are fuel-specific, this model has the potential to be applied to multiple fuels by using the laminar smoke point height to characterize an arbitrary fuel's sooting propensity. The model is still in an intermediate stage of development and more work is required in this area.

Also significant is the development of an alternate formulation of the FDS code[1,2] wherein the energy equation is explicitly solved in terms of total enthalpy and the conservation of mass equation is used to form an expression for the divergence of the velocity field. This has been called a radiatively perturbed flamelet approach by other authors[13] because the temperature is a function only of mixture fraction at a particular degree of radiant loss. This formulation

allows the flame temperature predictions to be improved by applying an enthalpy correction in mixture fraction space.

Another important component of this work is the development of mathematical techniques that can be used in Large Eddy Simulation of turbulent diffusion flames. The reformulation described above has advantages in turbulent calculations where subgrid-scale fluctuations may significantly impact soot formation and oxidation rates. The mathematics required to account for such fluctuations in Large Eddy Simulation of buoyant turbulent flames have been developed, incorporated, and tested qualitatively. An efficient mathematical algorithm that can be used to account for the effect of subgrid-scale temperature fluctuations on radiant emission has been developed but not yet tested. Another efficient algorithm that can be used to integrate the soot formation and oxidation rates over the mixture fraction PDF using Chebyshev polynomials and Fast Fourier Transforms has been developed but not yet tested.

Finally, the modifications and additions that have been made to the FDS[1,2] code provide a general framework that can be used to test new theories of soot formation and oxidation. All of the new features/additions to the code can be turned on or off via the standard FDS input file. As an example, the user may specify that soot formation is to occur by surface area-dependent, surface area-independent, or both growth mechanisms. A general means was provided to specify a series of up to six point-value or point-slope pairs for each of the soot formation or oxidation polynomials. This allows others workers to use the software developed here to test new theories of soot formation or oxidation by postulating different forms of polynomial functions. Wherever possible, the FORTRAN implementation of this work has been kept general and "hardcoding" has been avoided. Rather, the model parameters are accessible through the standard FDS input file.

In summary, significant progress has been made toward solving the classical problem of engineering calculations of soot formation and flame radiation in laminar and turbulent flames. However, due to the sheer scope of this topic, it was not possible to resolve all of the details in the length of time alotted for an MS thesis. Many issues remain, the most important of which are identified in the following section.

3.2 Recommendations for Future Research

The recommendations for future research fall into three major categories: (1) FDS-related implementation issues; (2) Enhancement and simplification of the soot model itself; (3) Rigorous testing of the model and comparison of prediction and experiment.

3.2.1 FDS-Related Implementation Issues

The new expression for the divergence of the velocity that was derived from the conservation of mass equation has been shown to be problematic near boundaries, particularly near the fuel inlet. In laminar simulations, this causes the velocity to fluctuate nonphysically near the lip of the burner. However, this problem is exacerbated in turbulent calculations and gave nonphysical results due to unrealistic expansion immediately above the burner. For this reason it was necessary to use the original FDS v2.0[1] expression for the divergence of the velocity field in turbulent calculations.

The expressions for the velocity divergence derived from the conservation of mass and conservation of energy equations given in Appendix E should be examined for consistency and analogous terms identified. The manner in which each of these are implemented should be checked. Particular care must be given to the treatment of boundary conditions. Since steep gradients in scalar quantities (mixture fraction and total enthalpy) exist near boundaries, it is

possible that the use of central differences causes numerical oscillations and it may be possible to eliminate this problem by using one-sided (upwinded) differences.

Much can be done to reduce the computational expense of the reformulated code, which tends to be slower than the original code[1]. Much of this difference is attributed to the iterative procedure through which the gas-phase density ρ_g is obtained at each timestep. Since the equations are solved on a per-unit-volume basis, conservation equations are solved for the quantities $\rho_g h_T$ and $\rho_g Z$ (the product of gas-phase density and total enthalpy or mixture fraction). The values of h_T and Z can be found from $\rho_g h_T$ and $\rho_g Z$ by simple division if ρ_g is known. However, ρ_g is not known because the conservation of mass equation is not explicitly solved, but rather used to obtain the divergence of the velocity field. Therefore, a value of ρ_g is guessed and trial values of h_T and Z are obtained by division. A unique temperature T corresponds to a certain value of h_T and Z (see Appendix D). The gas-phase density ρ_g can then be calculated from this T using the ideal gas law. If this density is the same as the guessed density, then the true density of the gas has been found. If not, more iterations are necessary. Convergence is typically achieved in less than five iterations, but this procedure is expensive, particularly considering it must be done in every cell at every timestep. Several weeks were spent trying to develop a more efficient method to obtain ρ_g from the quantities $\rho_g h_T$ and $\rho_g Z$, but this attempt was unsuccessful in the end.

Finally, the two efficient integration techniques for use in turbulent flames given in Appendix J must be implemented and/or tested. Appendix J.1 gives a recursive algorithm to evaluate the integral of a general polynomial and an assumed beta PDF. This can be used to approximate the effect of turbulent fluctuations on radiant emission source term, as described in

Appendix B. The coding for implementation of this integration technique has been performed, but the algorithm has not been tested in turbulent calculations. Appendix J.2 gives an efficient technique that can be used to integrate the soot formation and oxidation polynomials over the PDF by fitting them to Chebyshev polynomials[9] with the coefficients evaluated via Fast Fourier Transforms[9]. This technique has not yet been implemented or tested; however, it has the potential to reduce the computational expense associated with using the PDF technique to approximate subgrid fluctuations.

3.2.2 Simplification and Enhancement of the Soot Model

The soot model as postulated in Appendix A needs further simplification. The soot formation rates have both a surface area-dependent and surface area-independent formation terms. During the model calibration process, it was found that agreement between prediction and experiment in small-scale laminar flames could not be obtained with a single growth mechanism. However, in turbulent flames where the flame sheet is not resolved, the necessity of retaining two separate growth mechanisms is unclear.

Additionally, the soot formation polynomials are fifth-order, thereby requiring that six sets of point-value or point-slope pairs be specified and six model constants. This was also found to be necessary during the model calibration process to obtain agreement between prediction and experiment. However, it is a worthwhile endeavor to recalibrate the global model constants using only third-order polynomials so that two model constants can be eliminated from each polynomial.

3.2.3 Testing and Validation

The model needs to be tested against experimental data for different burners and fuels. This can proceed concurrently with the research suggested above because it provides guidance as to how to improve and simplify the model.

4.0 REFERENCES

1. McGrattan, K.B., Baum, H.R., Rehm, R.G., Hamins, A., Forney, G.P., Floyd, J.E. and Hostikka, S., "Fire Dynamics Simulator (Version 2) – Technical Reference Guide," National Institute of Standards and Technology, NISTIR 6783, 2001.
2. McGrattan, K.B., Forney, G.P, Floyd, J.E., "Fire Dynamics Simulator (Version 2) – User's Guide," National Institute of Standards and Technology, NISTIR 6784, 2001.
3. Lindstedt, P.R., "Simplified Soot Nucleation and Surface Growth Steps for Non-Premixed Flames," in *Soot Formation in Combustion Mechanisms and Models*, Edited by H. Bockhorn, pp 417-441, Springer-Verlag, Berlin, 1994.
4. Moss, J.B. and Stewart, C.D. "Flamelet-based Smoke Properties for the Field Modeling of Fires," *Fire Safety Journal* **30**: 229-250 (1998).
5. de Ris, J. and Cheng, X.F., "The Role of Smoke-Point in Material Flammability Testing," *Fire Safety Science – Proceedings of the Fourth International Symposium*, 301-312 (1994).
6. Peters, N. *Turbulent Combustion*, Cambridge University Press, Cambridge, UK, 2000.
7. Sivathanu, Y.R. and Gore, J.P., "Coupled Radiation and Soot Kinetics Calculations in Laminar Acetylene/Air Diffusion Flames," *Combustion and Flame* **97**: 161-172 (1994).
8. Honnery, D.R., Tappe, M., and Kent, J.H., "Two Parametric Models of Soot Growth Rates in Laminar Ethylene Diffusion Flames," *Combustion Science and Technology* **83**: 305-321.

9. Press, W.H., Teukolksy, S.A., Vetterling, W.T., and Flannery, B.P., *Numerical Recipes in Fortran 77 The Art of Scientific Computing* 2nd Edition, Cambridge University Press, Cambridge, 1992.

10. Ferziger, J.H., and Peric, M., *Computational Methods for Fluid Dynamics*, Second Edition, Springer-Verlag Berlin, 1999.

11. Smyth, K.C. http://www.bfrl.nist.gov (1999).

12. Cook, A.W. and Riley, J.J., "A Subgrid Model for Equilibrium Chemistry in Turbulent Flows," *Physics of Fluids* **6**:2868-2870 (1994).

13. Young, K.J. and Moss, J.B., "Modeling Sooting Turbulent Jet Flames Using an Extended Flamelet Technique," *Combustion Science and Technology* **105**: 33-53 (1995).

14. Grosshandler, W.L., "RADCAL: A Narrow-Band Model for Radiation Calculations in a Combustion Environment," National Institute of Standards and Technology, NIST Technical Note 1402, 1993.

15. Wall, C., Boersma, J., and Moin, P., "An Evaluation of the Assumed Beta Probability Density Function Subgrid-scale Model for Large Eddy Simulation of Nonpremixed Turbulent Combustion with Heat Release," *Physics of Fluids* **12**:2522-2529 (2000).

APPENDIX A AN ENGINEERING APPROACH TO SOOT FORMATION AND OXIDATION IN ATMOSPHERIC DIFFUSION FLAMES OF AN ARBITRARY HYDROCARBON FUEL

1.0 INTRODUCTION

Factory Mutual Research and the National Institute of Standards and Technology (NIST) have undertaken a project to make NIST's Fire Dynamics Simulator (FDS) code[1,2] capable of calculating the flame heat transfer taking place in fires of hazardous scale. The FDS code is particularly well suited for use by fire protection engineers for the study of fire behavior. However, the underlying model needs further development and validation against experiment in areas of soot formation/oxidation and radiation before it can be used to reliably calculate flame heat transfer and predict the burning of solid or liquid fuels. The present paper extends the FDS code to predict the soot formation/oxidation and radiation from small laminar diffusion flames. An accompanying paper[3] develops the mathematics needed to model larger turbulent flames.

This paper emphasizes the calculation of temperature and soot concentrations in diffusion flames due to their importance for flame radiation. The central component of this work is the development of a generalized soot formation and oxidation model for diffusion flames of an arbitrary hydrocarbon fuel. The effort to obtain a realistic description of the evolution of soot throughout the flame is not in itself the desired end, but rather one of the many components necessary to calculate radiation from diffusion flames.

Markstein[4] discovered that the radiation from turbulent buoyant diffusion flames is correlated by the fuel's tabulated smoke point height. Markstein and de Ris[5] and others[6,7] showed that the distributions of soot and radiation throughout axisymmetric laminar diffusion flames at their smoke points are correlated by the value of the smoke point for hydrocarbon fuels

burning in air. That is, the detailed distributions become similar after being scaled by the smoke point flame height.

The present paper exploits these experimental findings in the development of a new approach to modeling soot formation in diffusion flames. Its significance is that a new mathematical framework for soot processes in diffusion flames that could potentially be applied to an arbitrary hydrocarbon fuel has been developed and subjected to an initial calibration. The intent of disseminating this research at an intermediate stage is to stimulate other workers to make use of the ideas contained herein and make progress in an area for which there is currently no entirely tractable solution for engineering calculations.

This paper consists of three major parts: (1) Postulation of a new soot formation and oxidation model; (2) Modification of NIST FDS v2.0[1,2] to provide an acceptable framework within which to calibrate this model; (3) Comparison of theory and experiment for small-scale, optically-thin, laminar flames. Lautenberger[8] gives details not provided here. The companion publication[3] discusses extension of the new soot model to turbulent flames and combines it with a finite volume treatment[9] of the radiative transport equation.

2.0 SOOT MODELING

There is no single universally accepted soot model for use in diffusion flames. One reason for this is that the chemical mechanisms responsible for soot formation and oxidation have not yet been unambiguously identified. It is likely that a fundamental model for calculating soot processes in hydrocarbon flames will eventually emerge as the combustion community's understanding of these underlying mechanisms improves. However, use of such a model in turbulent flame calculations will probably not be feasible for quite some time due to the associated computational expense. Until scientists unravel the many unknown components of

soot processes in diffusion flames and are able to solve the resulting equations with acceptable computational time, simplified soot models with a considerable degree of empiricism will remain the most practical way of calculating soot formation and oxidation for engineering calculations.

Many such models already exist, and Kennedy[10] has provided an excellent review of work before 1997. These models usually rely on empirical data, either directly or indirectly. Some models make direct use of experimentally measured or inferred quantities[12,13,14]. Other models indirectly use experimental measurements for calibration, where adjustable parameters are tweaked until agreement between prediction and experiment is obtained[15]. Unfortunately, there is no set of rules that that explains how to determine these constants for an arbitrary fuel. One shortcoming of this type of approach is that these models are usually appropriate for use only with a specific fuel, oxidant, and combustor. Extension of a model beyond the operating conditions for which it was developed may lead to unreliable predictions.

Most semi-empirical soot models contain expressions to quantify a limited number phenomena usually considered to be important for soot formation and oxidation. As pointed out by Lindstedt[16], it is generally agreed that a simplified model of particulate formation in diffusion flames should account for the processes of nucleation/inception, surface growth, coagulation/agglomeration, and oxidation. For this reason, most models explicitly consider these four processes. This paradigm is based on the classical view of soot formation in diffusion flames where incipient soot particles with diameters on the order of several nanometers form in slightly fuel-rich regions of the flame by inception or nucleation. These particles then undergo surface growth, perhaps by the Hydrogen Abstraction by C_2H_2 Addition (HACA) mechanism[17] wherein H-atoms impacting on the soot surface activate acetylene addition, thereby increasing the mass of existing soot particles. This occurs concurrently with coagulation, where small

particles coalesce to form larger primary particles, and agglomeration where multiple primary particles line up end-to-end to form larger structures resembling a string of pearls. Soot particles may be transported toward the flame front where they pass through an oxidation region in which the mass of soot is decreased by heterogeneous surface reactions between soot particles and oxidizing species. Any soot not completely oxidized is released from the flame envelope as "smoke"[18].

Most models of soot formation and oxidation provide a means to quantify the basic phenomena outlined above. They are embedded within a CFD model that provides the necessary flowfield quantities such as mixture fraction (the local fraction of material that originated in the fuel stream), temperature, and velocity. Typically, conservation equations are solved for the soot volume fraction f_v and the soot number density N. The conservation equations contain separate terms to account for the increase in f_v attributed either to particle inception/nucleation or the surface growth described above. Conversely, a term is included to account for the sink of f_v ascribed to soot particle oxidation. Models that explicitly consider particle inception/nucleation and coagulation/agglomeration must also solve a conservation equation for N that includes a source representing particle inception, and a sink representing particle coagulation/agglomeration. The rates of particle inception, coagulation, agglomeration, surface growth, and oxidation are then quantified through the postulated expressions that constitute the soot model.

Reilly *et. al.*[19,20], citing their experimental findings in acetylene diffusion flames using Real-Time Aerosol Mass Spectrometry (RTAMS), have questioned whether the classical view of soot formation embodied in these models is representative of the actual physical and chemical phenomena that lead to soot formation in diffusion flames. It is fair to ask whether a successful

soot model must include expressions for each of the components identified above. Lindstedt[16] showed that his predictions of soot volume fraction in three counterflow ethylene flames were relatively insensitive to the particular form of the nucleation model used. Kent and Honnery[14] obtained excellent agreement between prediction and experiment in axisymmetric ethane and ethylene diffusion flames using a soot model that relied heavily on experimental data but did not explicitly account for soot nucleation or coagulation.

3.0 A NEW SOOT MODEL

In light of the above discussion, a semi-empirical soot model that deviates slightly from the classical view of soot formation and oxidation is postulated. The processes of nucleation, inception, coagulation, and agglomeration are not explicitly considered. This helps minimize computational expense because there is no need to solve a conservation equation for the number density. The basic form of the soot model was inspired by the work of Kent and Honnery[14]. They correlated soot growth rates with mixture fraction and temperature in laminar ethane and ethylene flames by combining the mixture fraction and velocity fields obtained from numerical flame simulations with experimental soot and temperature measurements. The result was a parametric soot model with which the soot surface growth rate could be estimated from only the local mixture fraction and temperature.

Since Kent and Honnery[14] defined the soot formation rates on a per unit soot surface area basis, it was necessary to estimate the soot surface area per unit volume of gas mixture. They found that the soot surface area deduced from laser extinction and scattering measurements could be adequately represented by a linear function of soot volume fraction offset by an initial "inception area". They obtained excellent agreement between prediction and experiment by combining the parametric soot formation rates with the simple expression for the soot surface

area, although they noted that the predictions were sensitive to the value of the initial inception area specified.

A similar approach has been adopted here, except that the soot formation and oxidation rates are calculated as *analytic* expressions of mixture fraction and temperature. The model is generalized to an arbitrary hydrocarbon fuel by relating peak soot formation rates to the laminar smoke point height, an empirical measure of a fuel's relative sooting propensity in diffusion flames. The laminar smoke point height is the maximum flame height of the fuel burning in air at which soot is not released from the flame tip. An advantage of using the laminar smoke point height to characterize soot generation is that it overcomes the difficulty of establishing fuel-specific model constants. Since the smoke point height has been measured for most fuels (including gases, liquids, and solids), the new model can be applied to other fuels by inferring the soot formation rates from the smoke point and applying simple scaling relationships to account for differences in stoichiometry.

The final product is a model for soot formation and oxidation in atmospheric diffusion flames that can be applied to any hydrocarbon fuel provided its stoichiometry and laminar smoke point height are known. Implicit in this approach is the assumption that the ranges in mixture fraction space over which soot formation and oxidation occur for different fuels can be related to the stoichiometric value of mixture fraction. This bold simplification neglects any details in fuel-specific chemistry not already incorporated in the smoke point. Soot oxidation is treated by a global, fuel-independent mechanism attributed to OH*. Details are provided below.

3.1 Soot Conservation Equation and Source Terms

The CFD model used in this work is a modified version of the Fire Dynamics Simulator[1,2] code developed by NIST primarily for the simulation of compartment fires. We

refrain from a full discussion of the gas-phase conservation equations until Section 4.2, and focus here on the soot conservation equation, expressed in vector notation:

$$\frac{\partial(\rho_2 Y_s)}{\partial t} + \boldsymbol{u}\cdot\nabla\rho_2 Y_s + \rho_2 Y_s \nabla\cdot\boldsymbol{u} = 0.55\nabla\cdot\frac{Y_s\mu}{T}\nabla T + \dot{\omega}_s''' \tag{1}$$

The two-phase (total) density ρ_2 is related to the gas-phase density ρ_g and the soot mass fraction Y_s as:

$$\rho_2 = \frac{\rho_g}{1-Y_s} \tag{2}$$

It has been assumed in writing Equation 1 that the transport of soot particles due to molecular diffusion processes is negligible, but that thermophoresis is quantitatively important. In other words, soot particles do not diffuse due to gradients in soot concentration, yet thermophoretic forces attributed to temperature gradients do in fact cause a movement of soot. The thermophoretic term $0.55\nabla\cdot(Y_s\mu/T)\nabla T$ presumes a free molecular aerosol[21].

Experimental observations in diffusion flames show that species known to participate in soot formation may be simultaneously present with species known to contribute to soot oxidation[22,23], indicating the two processes proceed concurrently. For this reason, the net volumetric source term $\dot{\omega}_s'''$ $\left(\mathrm{kg/m^3\cdot s}\right)$ appearing in Equation 1 is taken to be the sum of the soot formation rate $\dot{\omega}_{sf}'''$ and the soot oxidation rate $\dot{\omega}_{so}'''$:

$$\dot{\omega}_s''' = \dot{\omega}_{sf}''' + \dot{\omega}_{so}''' \tag{3}$$

Throughout this work, a subscript *s* denotes soot, a subscript *sf* implies soot formation, and a subscript *so* denotes soot oxidation.

3.2 Basic Model Formulation

The crux of this and any soot model is to quantify the soot formation and oxidation rates appearing in Equation 3. It is known that in diffusion flames these rates are affected by many factors, including temperature, gas-phase composition, and pressure. Zelepouga *et. al.*[24] reported that for axisymmetric methane flames burning in a mixture of nitrogen and oxygen, preheating the reactants to 170°C increased the peak soot concentrations by a factor of three to four compared to the unheated flame. Axelbaum, Flower and Law[25] and Axelbaum and Law[26] showed that soot formation rates are proportional to the fuel concentration in the fuel supply stream for both opposed-flow and co-flow diffusion flames. When moderate amounts of inerts are added to the fuel stream, the temperature reduction is typically very small so the effects of dilution can be considerably greater than the effects of temperature reduction. de Ris[27] predicted and subsequently de Ris, Wu and Heskestad[28] confirmed experimentally that soot formation rates in hydrocarbon/air diffusion flames are second order in pressure.

Soot formation rates may also depend on the history or age of soot particles through the notion of active sites, as well as the amount of soot surface area (m^2 soot/m^3 mixture) available for growth or oxidation, usually referred to as the specific soot surface area. Soot surface area is probably important in lightly sooting flames such as methane, but several researchers have questioned its importance in other fuels.

Wieschnowsky *et. al.*[29] examined soot formation in low-pressure *premixed* acetylene-oxygen flames seeded with cesium chloride. The ionic action of the salt very quickly charged incipient soot particles, thereby preventing coagulation and dramatically increasing the number densities and specific soot surface area compared to unseeded flames. They found that the properties of the seeded and unseeded flames were virtually identical with regard to flame

temperature, chemical composition, and soot appearance rates. One would expect that if the rate of soot formation were proportional to the available soot surface area, then the seeded flames should contain much more soot. This was clearly not the case. However, Wieschnowsky *et. al.*[29] specifically caution against inferring the independence of soot concentration on surface area in *nonpremixed* flames. In a similar study, Bonczyk[30] investigated the effect of ionic additives on particulate formation in diffusion flames. His results showed an order of magnitude increase in the soot number density with only a slight increase in the soot volume fraction, indicating the available soot surface area may not be the controlling mechanism in the flames studied.

Delichatsios[31], relying heavily on experimental observations, postulated that homogeneous gas-phase reactions and not heterogeneous surface growth reactions are the controlling mechanisms of soot formation in diffusion flames. He used dimensional analysis to show that the results of several experimental studies cannot be readily explained if the rate of soot formation is dependent on the specific surface area.

It is likely that both surface area-dependent and surface area-independent mechanisms contribute to the overall rate of soot formation in diffusion flames. Early in the present work, it was found that the soot volume fraction profiles reported by Smyth[32] for axisymmetric methane, propane, and ethylene flames could not be reproduced with a model that considered either a surface area-dependent or a surface area-independent growth mechanism, but not both. When using only surface growth, the "wings" (soot that forms low in the flames far from its axis) could be reproduced reasonably well, but the soot loading at the "core" (near the flame axis) was underpredicted. Similarly, when using only a volumetric growth mechanism, the soot loading at the core could be reproduced, but far too much soot was predicted in the wings. Furthermore, the volumetric growth model was not capable of reproducing the soot profiles in the lightly

sooting methane flames. This has led to the surmisal that the abundance of H* radicals near the outer wings of the diffusion flame cause the soot to form there by the HACA mechanism[17] subject to surface area control. In the core regions, where negligible H* atoms are present, soot generation takes place primarily by the formation of polycyclic aromatic hydrocarbons (PAHs) subject largely to gas-phase control.

Hwang and Chung[33] reached a similar conclusion through an experimental and computational study of counterflow ethylene diffusion flames that was conducted to examine the relative importance of acetylene and PAHs in soot growth. They reported that satisfactory agreement between predicted and measured soot mass growth rates could be obtained if two separate pathways to soot formation were considered. They concluded that the HACA mechanism is the dominant mode of soot formation in the high temperature regions, but coagulation between PAH and soot particles is quantitatively important in the low temperature regions. The latter may account for up to 40% of the contribution to soot formation[33].

This basic hypothesis is also supported by the experimental study of Zelepouga *et. al.*[24] in which laminar coflow methane flames were doped with acetylene and PAHs. For the flame burning in a 21%-79% mixture of O_2-N_2, the peak soot concentrations were increased by approximately 40-75% when the flames are seeded with 1.0 carbon percent (C%) pyrene (a PAH), but only by 15-50% when seeded with 3.7C% acetylene. The seeding levels are reported in C% to account for the different C:H ratios of the various agents. A larger increase in soot volume fraction was induced by doping the flame with acetylene than with pyrene low in the flame near the high-temperature reaction sheet. However, the pyrene induces a larger increase in soot volume fraction compared to acetylene at greater distances from the reaction zone and near the core. This indicates that different soot formation mechanisms are dominant in different

regions of this flame. Near the flame sheet, the HACA mechanism[17] (dependent on the available surface area) is controlling; yet near the core, a mechanism involving growth by PAHs that is independent of surface area becomes significant.

For the reasons cited above, the soot formation model postulated in this work presumes a linear combination of surface growth and volumetric growth terms. Soot formation is considered to be the sum of a surface area-controlled growth process and a surface area-independent process. Soot oxidation is treated as a surface area-dependent process.

$$\dot{\omega}_s''' = A_s\left(\dot{\omega}_{sf}'' + \dot{\omega}_{so}''\right) + \dot{\omega}_{sf}''' \tag{4}$$

The soot surface area is estimated as a function of soot volume fraction as was done by Kent and Honnery[14]:

$$A_s = A_0 + \beta f_v \tag{5}$$

A superscript triple prime (‴) denotes a quantity defined on a per unit volume basis, *e.g.* $\dot{\omega}_{sf}'''$ has units of $\mathrm{kg\,soot}/\left(\mathrm{m^3\ mixture}\cdot\mathrm{s}\right)$, and a superscript double prime (″) denotes a quantity defined on a per unit surface area basis, *e.g.* $\dot{\omega}_{sf}''$ has units of $\mathrm{kg\,soot}/\left(\mathrm{m^2\ soot}\cdot\mathrm{s}\right)$. A_s is the specific soot surface area and has units of $\mathrm{m^2\ soot}/\mathrm{m^3\ mixture}$. The quantity A_0 is the effective "soot inception area", which is small for lightly-sooting fuels and increases with a fuel's sooting propensity. A method for estimating this quantity is presented in Section 6. The quantity β is also a fuel-dependent parameter, which Kent and Honnery[14] found to be 7.88×10^7 for ethylene and 7.13×10^7 for ethane. It is difficult to determine how this constant should vary among different fuels and is therefore held invariant at 8.0×10^7. Equation 5 presumes spherical soot particles with a constant diameter due to the linear dependence of surface area on f_v. The soot

formation and oxidation rates appearing in Equation 4 are determined from the product of an analytic function of mixture fraction and an analytic function of temperature:

$$\dot{\omega}''_{sf} = f''_{Zsf}(Z) f^{PUA}_{Tsf}(T) \tag{6}$$

$$\dot{\omega}''_{so} = f''_{Zso}(Z) f^{PUA}_{Tso}(T) \tag{7}$$

$$\dot{\omega}'''_{sf} = f'''_{Zsf}(Z) f^{PUV}_{Tsf}(T) \tag{8}$$

Here, $f''_{Zsf}(Z)$ and $f''_{Zso}(Z)$ have units of $\mathrm{kg\,soot}/\left(\mathrm{m^2\ soot \cdot s}\right)$, whereas $f'''_{Zsf}(Z)$ has units of $\mathrm{kg\,soot}/\left(\mathrm{m^3\ mixture \cdot s}\right)$. The three temperature functions, $f^{PUA}_{Tsf}(T)$, $f^{PUA}_{Tso}(T)$, and $f^{PUV}_{Tsf}(T)$ are dimensionless factors that account for the temperature-dependency of surface area-dependent soot formation, surface area-dependent soot oxidation, and surface area-independent soot formation, respectively. The superscript PUA and PUV denote per unit area and per unit volume, although the functions themselves are dimensionless. The subscript *Z* and *T* denote that mixture fraction and temperature, respectively, are the independent variables of the function.

3.3 Analytic Soot Formation Functions

Experimental measurements were consulted for guidance in selecting the general shapes of the soot formation and oxidation functions. Kent and Honnery[12] give a soot formation rate map in which the volumetric rate of soot formation ($\mathrm{kg\,soot}/\left(\mathrm{m^3\ mixture \cdot s}\right)$) is plotted in terms of mixture fraction and temperature. This map is analogous to the surface area-independent growth function $f'''_{Zsf}(Z) f^{PUV}_{Tsf}(T)$ used in the present model. The soot formation rates[12] show an approximately parabolic trend in mixture fraction and a less-discernable trend in temperature, but also approximately parabolic. Peak soot formation rates occur at mixture fraction values between 0.10 and 0.15, and over the temperature range 1500K to 1600K.

Honnery, Tappe, and Kent[13] and Kent and Honnery[14] later presented similar soot formation rate maps for ethylene and ethane in which growth rates were plotted as a function of the soot surface area ($\mathrm{kg\,soot}/\left(\mathrm{m}^2\ \mathrm{soot}\cdot\mathrm{s}\right)$). Their data for ethylene show trends similar to the earlier work of Kent and Honnery[12] in that the soot formation rate is approximately parabolic in Z (at least for $T > 1450\mathrm{K}$). The overall trend in T is less apparent. The peak soot formation rates (for ethylene) occurred in the range $0.12 \le Z \le 0.18$ at temperatures ranging from 1575K to 1675K.

It is worth pointing out that these soot formation maps[12,13,14], although cast either in terms of volumetric or surface growth, actually reflect the net effect of both mechanisms. Since the model being developed here separately considers both means of soot generation, the soot formation functions cannot be determined simply by fitting these maps.

Several analytic forms of the soot formation functions were considered. In the end, general polynomials ($f(x)=\sum_{n=0}^{N} a_n x^n$, where the a_n's are the polynomial coefficients) were selected due to their ability to approximate a wide variety of shapes—near Gaussian, exponential (Arrhenius), and linear. Both $f''_{Zsf}(Z)$ and $f'''_{Zsf}(Z)$ were chosen as polynomials that rise from a formation rate of zero at a mixture fraction of Z_L to a peak formation rate at a mixture fraction of Z_P, and then fall back to zero at a mixture fraction of Z_H. Foreseeing that it may be necessary to make the functions rise faster on one side than the other in order to optimize agreement between prediction and experiment, the polynomials were forced to be 5$^{\text{th}}$ order (6 coefficients) so that the slope could be specified at both Z_L and Z_H. In this way, the coefficients of the polynomial can be determined by solving a set of linear equations after specifying the value and slope of the polynomial at Z_L, Z_P, and Z_H. The polynomial coefficients are determined by solving the

resulting matrix by Gauss-Jordan elimination[34]. Details can be found in Appendix G of Lautenberger[8].

Figures 1a and 1b show sample shapes of the mixture fraction polynomials. The values of Z_L, Z_P, and Z_H for each polynomial are related to the stoichiometric value of mixture fraction Z_{st} by a parameter ψ, *e.g.* $\psi_{sf,Z_P}^{PUA} Z_{st}$ is the mixture fraction value at which the peak soot formation rate occurs for surface area-controlled growth. The ψ constants are discussed in Section 5.

The temperature functions applied to the soot formation rate ($f_{Tsf}^{PUA}(T)$ and $f_{Tsf}^{PUV}(T)$) were selected as fifth order polynomials normalized between zero and unity. These polynomials take on a value of zero at T_L, rise to a peak value of 1 at T_P, and fall back to 0 at T_H. For both soot formation mechanisms, T_L can be interpreted as the minimum temperature at which soot formation occurs by that mechanism. Similarly, T_P is the temperature at which peak soot formation occurs, and T_H is the maximum temperature at which soot forms.

Sample shapes of the temperature functions are given in Figure 2. Consistent with the discussion in Section 3.2, the surface area-independent soot formation temperature function $f_{Tsf}^{PUV}(T)$ in Figure 2 restricts this mechanism of soot formation to low temperatures. The surface area-dependent soot formation temperature function $f_{Tsf}^{PUA}(T)$ allows soot to form at higher temperatures.

A caveat of the model as currently postulated is that the soot formation rates peak at a certain temperature and then fall off at higher temperatures. No soot is formed above a critical temperature. This general trend is not consistent with experimental observations and soot formation theory. The soot loading in diffusion flames increases significantly when the fuel and/or oxidant streams are preheated[24]. The HACA theory[17] also predicts that soot formation

rates should increase with temperature. However, in the pure-fuel, atmospheric diffusion flames against which this model was calibrated[32], it was not possible to obtain agreement between prediction and experiment if the temperature dependency of soot formation increased indefinitely with temperature. Far too much soot formed low in the flames in the high temperature regions. Therefore, the present can only be applied to atmospheric diffusion flames. Future research is planned to make the model consistent with the experimental observations cited above.

3.4 Analytic Soot Oxidation Functions

Several species have been linked to soot oxidation in hydrocarbon diffusion flames, most notably OH*, O_2, and O*. There has been a considerable debate over the relative importance of these oxidizing species. Neoh *et. al.*[35] clearly demonstrated the importance of soot oxidation by OH* radical, particularly on the fuel side of stoichiometric. They concluded that under the conditions studied, OH* was the principal oxidant, with molecular oxygen becoming important only for O_2 concentrations above 5%. The O* radical usually occurs in low concentrations so it is of less concern here.

Soot oxidation should therefore occur at values of mixture fraction where OH* is present. However, as noted by Puri *et. al.*[36,37], OH* concentrations in diffusion flames are quite sensitive to the presence of soot particles. Therefore it is not practical to estimate OH* concentrations in diffusion flames and then attribute an oxidation rate to this concentration. Rather, by using the measurements reported by Smyth[32] that were taken from methane on a Wolfhard-Parker burner, the range of mixture fraction values over which OH* was found was examined. This was used as a baseline for placing the soot oxidation function in mixture fraction space. Similar to the soot formation functions, the soot oxidation mixture fraction function falls from a value of zero at Z_L to its peak negative value at Z_P, and then rises to a value of zero at Z_H. The resulting soot

oxidation rate as a function of mixture fraction was then adjusted to optimize agreement between theory and prediction. No attempt was made to account for the effect of a fuel's H:C ratio on OH* concentrations. Similarly, no attempt was made to account for the change of collision efficiency between OH* and soot particles attributed to age.

The oxidation rate was assumed to be linearly proportional to temperature, with no oxidation occurring below a critical value. Note that the maximum soot oxidation rate calculated by the model may therefore be stronger than the "peak" oxidation rate because the temperature function may take on values greater than unity, whereas the formation temperature functions are normalized between zero and one. Sample shapes of the mixture fraction soot formation and oxidation functions are shown below in Figure 1, and the dimensionless temperature functions are shown in Figure 2.

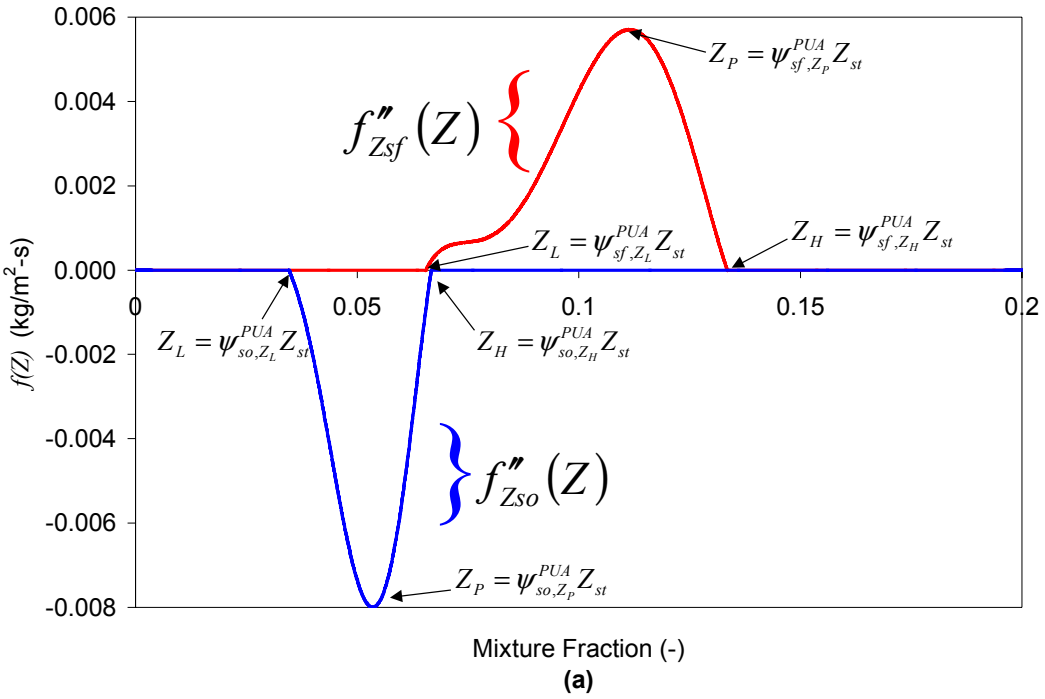

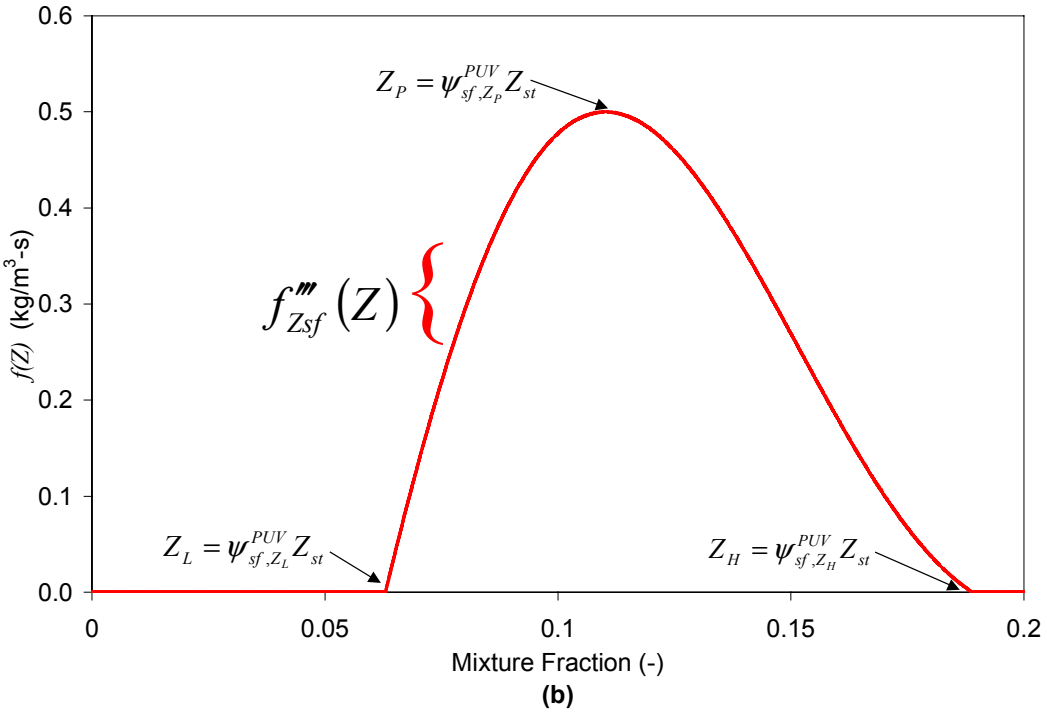

Figure 1. Sample mixture fraction polynomials: (a) per unit area; (b) per unit volume. The arrows point to the Z_L, Z_P, and Z_H values of mixture fraction identified in the text.

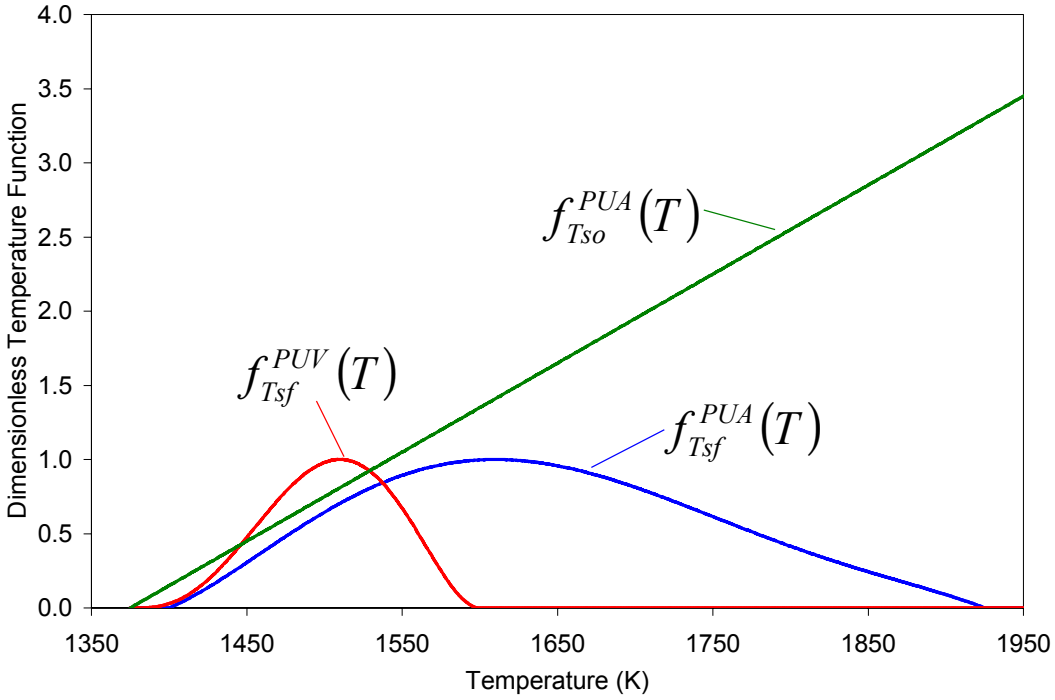

Figure 2. Sample dimensionless temperature polynomials.

4.0 CFD FRAMEWORK: NIST FDS V2.0

The CFD code within which the new soot model has been embedded is v2.0 of NIST's Fire Dynamics Simulator[1,2]. FDS is a large eddy simulation (LES) code with a mixture fraction combustion model that has been developed specifically for use in fire safety engineering. In this discipline, "far-field" phenomena such as buoyant smoke transport and compartment filling during a fire event are usually of greater interest than the local phenomena within the "near-field" combustion region. However, the focus here is soot formation/oxidation and flame radiation in the near-field, both of which are strongly dependent on temperature. For this reason, relatively accurate temperature predictions are required. It does not make sense to calibrate a soot model with temperature-dependent formation/oxidation rates and calculate flame radiation with its fourth power dependency on temperature if the underlying code does not reproduce experimental temperature profiles reasonably well. Therefore, a considerable amount of effort was devoted to improving the near-field flame temperature predictions of the FDS code.

Figure 3 shows the temperature profiles calculated for the 247W axisymmetric methane flame reported by Smyth[32] using the *unmodified* code[1,2]. This flame was selected because methane is lightly sooting and radiative losses should be much less than for sootier fuels. A radiative fraction of 0.15 was specified for the simulation, which implies that 85% of the energy released during combustion increases the temperature of the gas-phase; the other 15% is emitted as radiation and is lost to the simulation.

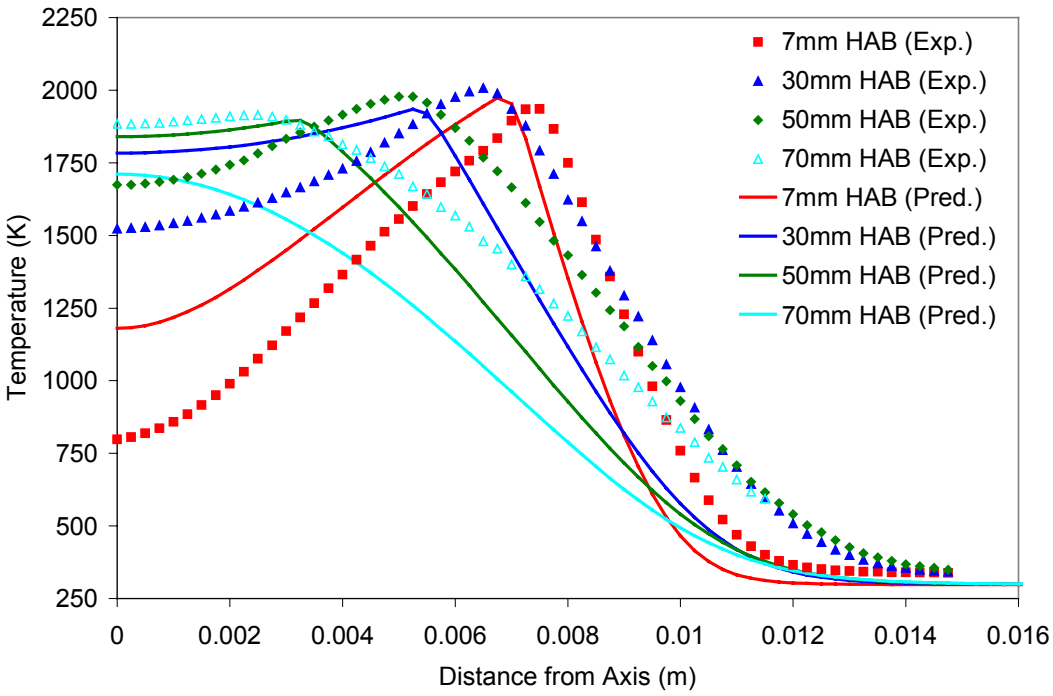

Figure 3. NIST FDS v2.0 temperature predictions in 247W methane flame at several heights above the burner (HAB). "Exp." corresponds to experimental data and "Pred." corresponds to the model predictions.

Figure 3 is representative of the temperature predictions of the unmodified code in the small-scale laminar flames that were examined. The temperature is overpredicted on the fuel side, and underpredicted on the oxidant side. The fuel side occurs to the left of the peak in the temperature profile in Figure 3 (for heights above burner below 70mm), and the oxidant side occurs to the right of this peak. Due to the temperature-dependent nature of soot formation and oxidation, the FDS code could not be used as-is for calibration of the soot model. The

temperature predictions could have been improved by modifying specific heats and transport properties, but this proved to be quite difficult.

The energy conservation equation is not solved explicitly in FDS v2.0[1,2], but rather used to form an expression for the divergence of the velocity field $\nabla \cdot \boldsymbol{u}$. The primary advantage of doing so is that the flow-induced perturbation pressure can be obtained directly from a Poisson equation that can be solved efficiently using Fast Fourier Transforms, eliminating the need for iteration typically associated with the solution of elliptic partial differential equations. The combustion model[1] is formulated so that the local rate of heat release is determined from the rate of oxygen consumption as calculated from the mixture fraction conservation equation and complete combustion fast chemistry oxygen state relation[1]:

$$\frac{\dot{q}'''}{\Delta H_{O_2}} = \rho D \frac{d^2 Y_{O_2}}{dZ^2} |\nabla Z|^2 \tag{9}$$

In this way, all of the heat release occurs at the flame sheet, *i.e.* the stoichiometric value of mixture fraction. Strictly speaking, there is no explicit relation between mixture fraction and temperature because Equation 9 is the mechanism through which heat is released into the computational domain. The combustion model in Equation 9 was replaced with a formulation where the temperature is determined from the local value of gas-phase mixture fraction and total (chemical plus sensible) gas-phase enthalpy. Both the mixture fraction and the total enthalpy are conserved scalars. A Lewis number of unity is implicitly assumed. The mixture fraction fixes the chemical composition of the gas phase, and the total enthalpy includes the effect of radiative losses that a particular fluid parcel has experienced. The present approach has the advantage that the mixture fraction-enthalpy-temperature relationship can be modified by applying an "enthalpy

correction" in mixture fraction space as discussed in Section 4.1. A similar approach has been dubbed a "radiatively perturbed laminar flamelet approach" by Young and Moss[38].

By tracking the total gas-phase enthalpy, the local nonadiabaticity induced by radiative losses is known from the enthalpy deficit, *i.e.* the difference between the adiabatic enthalpy and the actual enthalpy. As shown in a companion publication[3], this formulation is also advantageous when performing calculations in turbulent diffusion flames. However, to retain compatibility with the efficient numerical method used to obtain the perturbation pressure as implemented in FDS v2.0[1,2], an alternate method is required to determine the divergence of the velocity field. An expression for $\nabla \cdot \boldsymbol{u}$ that is compatible with this reformulation was derived from the continuity equation and incorporated into the code:

$$\nabla \cdot \boldsymbol{u} = \frac{1}{T}\left(\frac{DZ}{Dt}\left.\frac{\partial T}{\partial Z}\right|_{h_T} + \frac{Dh_T}{Dt}\left.\frac{\partial T}{\partial h_T}\right|_{Z} \right) - \frac{1}{\mathscr{M}}\frac{DZ}{Dt}\frac{d\mathscr{M}}{dZ} \tag{10}$$

The complete derivation of Equation 10 is given in Appendix E of Lautenberger[8]. In Equation 10, $D\eta/Dt = \partial\eta/\partial t + \boldsymbol{u}\cdot\nabla\eta$ is the material derivative. $\mathscr{M}(Z) = \left(\sum_i Y_i(Z)/M_i \right)^{-1}$ is the mean molecular weight of the mixture. The terms DZ/Dt and Dh_T/Dt are determined from the mixture fraction and total enthalpy conservation equations, given as Equations 24 and 25 below. The terms $\left.\partial T/\partial Z\right|_{h_T}$, $\left.\partial T/\partial h_T\right|_Z$, and $d\mathscr{M}/dZ$ are evaluated at the start of a calculation and stored in lookup tables.

4.1 An Enthalpy Correction To Improve Temperature Predictions

Consider a mixture of i gases each with mass fractions Y_i. The total enthalpy is the sum of the chemical and sensible enthalpy:

$$h_T(T) = \sum_i Y_i \left(h_i^\circ + h_i(T) \right) \tag{11}$$

Here h_i° is the standard enthalpy of formation of species *i at the reference temperature* T_0, and $h_i(T)$ is the additional sensible enthalpy of species i at temperature T, defined by

$$h_i(T) = \int_{T_0}^{T} c_{p,i}(T) dT \tag{12}$$

Now consider an adiabatic nonpremixed combustion system, initially at temperature T_0, in which r reactants with mass fractions Y_r form p products with mass fractions Y_p. Total enthalpy is perfectly conserved under these idealized conditions because no energy is lost to thermal radiation. Conservation of energy dictates that the decrease in chemical enthalpy when going from reactants to products must be balanced by an increase in sensible enthalpy of equal magnitude:

$$\sum_r Y_r h_r^\circ = \sum_p Y_p \left(h_p^\circ + h_p(T_p) \right) \tag{13}$$

Therefore, the temperature of an adiabatic nonpremixed combustion system can be determined if the chemical composition (or more accurately, the chemical enthalpy) of the reactants and the products are known. The chemical enthalpy of the reactants can be expressed as a function of mixture fraction by making the assumption that the fuel and oxidant have equal diffusivities, a simplification inherent in use of the mixture fraction:

$$h_r^\circ(Z) = Z h_f^\circ + h_o^\circ (1 - Z) \tag{14}$$

Here, h_f° is the chemical enthalpy of the fuel, and h_o° is the chemical enthalpy of the oxidant, approximately zero for air. The chemical composition of the products can also be determined as a function of mixture fraction using many approaches, some of which are: (1) idealized complete combustion reactions in the fast chemistry limit[1], (2) empirical correlations[39], (3) equilibrium calculations[40], and (4) detailed experimental measurements[32].

Much can be learned by using such state relations in combination with Equations 11 through 14 to calculate theoretical temperatures and compare them with experimental measurements. One of the most complete data sets against which to compare such calculations is that compiled by Smyth[32] for a methane flame on a Wolfhard-Parker slot burner. Thermocouple temperatures (corrected and uncorrected for radiation), gas velocities, and the concentrations of 17 chemical species are given. Measurements were made at a number of discrete heights, but only the measurements at a height of 9mm contain data for all 17 species. At this height, the system is almost adiabatic due to the short flow time and lack of soot particles.

Although these Wolfhard-Parker measurements were made in physical space, it is desirable to examine the data in a geometry-independent coordinate such as the mixture fraction. The mixture fraction can be determined from the species composition measurements at each location using Bilger's mixture fraction expression[41]. This not only allows for direct comparison of measurements made on different experimental burners, but also enables one to compare the experimental data with theoretical calculations performed in mixture fraction space.

Figure 4 shows a comparison of the measured temperatures and those calculated with the composition of the products determined by: (1) "Schvab-Zeldovich" complete combustion to H_2O and CO_2, (2) correlation of measurements given by Sivathanu and Faeth[39], (3) equilibrium chemistry[40], and (4) calculated from experimental measurements of Smyth[32]. In performing

these calculations, the chemical enthalpy of the reactants was determined from Equation 14. The temperature dependency of each species' specific heat (Equation 12) was taken from the polynomial fits given in the Chemical Equilibrium Code thermodynamic database[40].

In Figure 4, the temperature "Calculated from Experiment" uses the measured species composition[32]. It represents the best accuracy of a temperature prediction in diffusion flames based on "frozen" species compositions and simple thermodynamic theory. This calculation includes the effect of dissociation because the computed temperatures were obtained from an enthalpy balance based on detailed experimental measurements of 17 species, many of which are dissociated with positive standard enthalpies of formation.

It is therefore expected that less-desirable results would be obtained when using either the "Schvab-Zeldovich" complete combustion reactions where the only products are carbon dioxide and water vapor or the empirical correlation of "Sivathanu and Faeth"[39], which also includes carbon monoxide and molecular hydrogen. Each of these calculations are based on their assumed composition together with the simple mixing and thermodynamics given by Equations 11 through 14. This is confirmed by Figure 4, where it can be seen that these predictions are much worse. The equilibrium temperatures are acceptable only on the oxidant side ($Z < 0.055$).

The same general trend shown above in Figure 3 for the axisymmetric methane flame examined in physical space is also apparent in Figure 4 for the Wolfhard-Parker methane flame examined in mixture fraction space. As expected, the best agreement is obtained using the experimental composition measurements. But in all cases, the temperatures are overpredicted on the fuel side and underpredicted on the oxidant side. The Schvab-Zeldovich and Sivathanu and Faeth[39] state relations are considerably worse, overpredicting temperatures by between 100K and 400K on the fuel side ($Z > 0.055$), but underpredicting them on the oxidant side. In all cases, the

peak calculated temperatures are located closer to the fuel side than the experimentally measured peak. The entire calculated temperature profiles are shifted toward fuel-rich when compared to experiment.

There are several potential explanations for this systematic discrepancy. Conduction heat loss to the burner may be important. Experimental uncertainties in species composition and temperature measurements may also contribute to these inconsistencies. (The data compiled by Smyth was originally published by Norton *et. al.*[42], where it was reported that the sum of the experimentally measured mole fractions was close to 1.2 at some locations, and therefore normalized to unity.) Radiant losses have not been accounted for in this temperature calculation. Radiant losses via continuum radiation from soot particles are negligible because the measurements are taken at a height of 9mm where no soot has formed. Slight losses may be attributed to gas radiation, but this is at most a few percent and cannot explain the magnitude of the temperature overprediction on the fuel side. Furthermore, if failure to account for radiant losses causes the calculated temperatures to be high in the fuel-rich regions, then the calculated temperature should also have been high in the fuel-lean regions.

One of the most likely causes of the low temperatures seen experimentally on the fuel side is the finite-rate chemistry. Additionally, in using Equation 13 to calculate the chemical enthalpy of the reactants as a function of mixture fraction, it has been implicitly assumed that all species have equal diffusivities. If this is not the case, the relationship between adiabatic sensible enthalpy and mixture fraction would be altered, potentially contributing to the lack of agreement between theory and experiment. Finally, Lautenberger[8] in his Appendix F.1 shows preferential diffusion of heat over species, *i.e.* nonunity Lewis number effects, may result in a net transfer of enthalpy away from the fuel side and toward the oxidant side. There is a sizeable flux

of CO, H_2, and other intermediate species diffusing across the flame from the fuel side to the oxidant side.

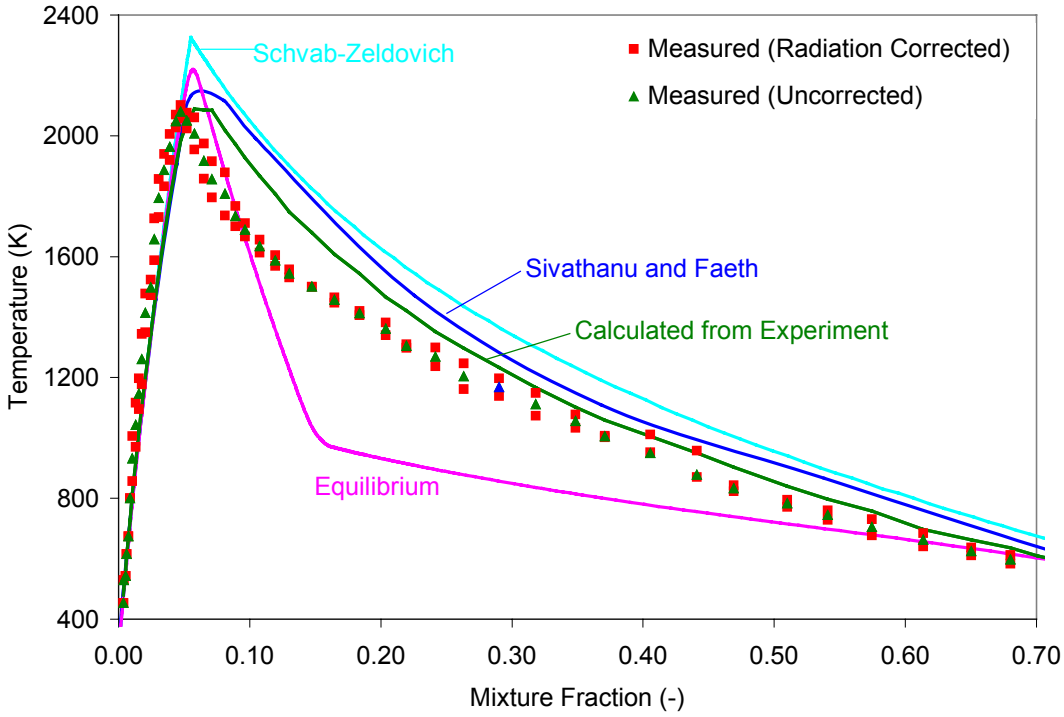

Figure 4. Comparison of calculated and measured temperatures in mixture fraction space. Experimental data are for methane on a Wolfhard-Parker slot burner. The solid lines are calculated profiles which presume an adiabatic system, equal diffusivities, unit Lewis number, and "frozen" chemical reactions.

Regardless of the cause, it is apparent that the temperature must be decreased on the fuel side and increased on the oxidant side in order to obtain agreement between theory and experiment. Although Figure 4 shows that the temperature calculated with the Sivathanu and Faeth correlation[39] is slightly better than that calculated with the Schvab-Zeldovich state relations, the latter were chosen as the starting point to apply an enthalpy correction owing to their simplicity.

After numerically smoothing the Schvab-Zeldovich state relations near the stoichiometric value of mixture fraction to eliminate the sharp peak (see Appendix C.2 of Lautenberger[8]), an enthalpy correction was applied by removing enthalpy from the fuel side and adding it to the

oxidant side. Details regarding how this correction was constructed are given by Lautenberger[8] in his Appendix F.2. The enthalpy correction is shown in Figure 5. A positive value of this function corresponds to an addition of enthalpy relative to adiabatic, and a negative value corresponds to the removal of enthalpy relative to adiabatic. Figure 6 shows the comparison between calculated and measured temperatures for the Wolfhard-Parker methane flame in mixture fraction space, using complete combustion state relations before and after the enthalpy correction was applied. Note that this shows the *adiabatic Z-T* relationship. In numerical calculations, the actual temperature is reduced below its adiabatic value due to radiative losses throughout most of the flame.

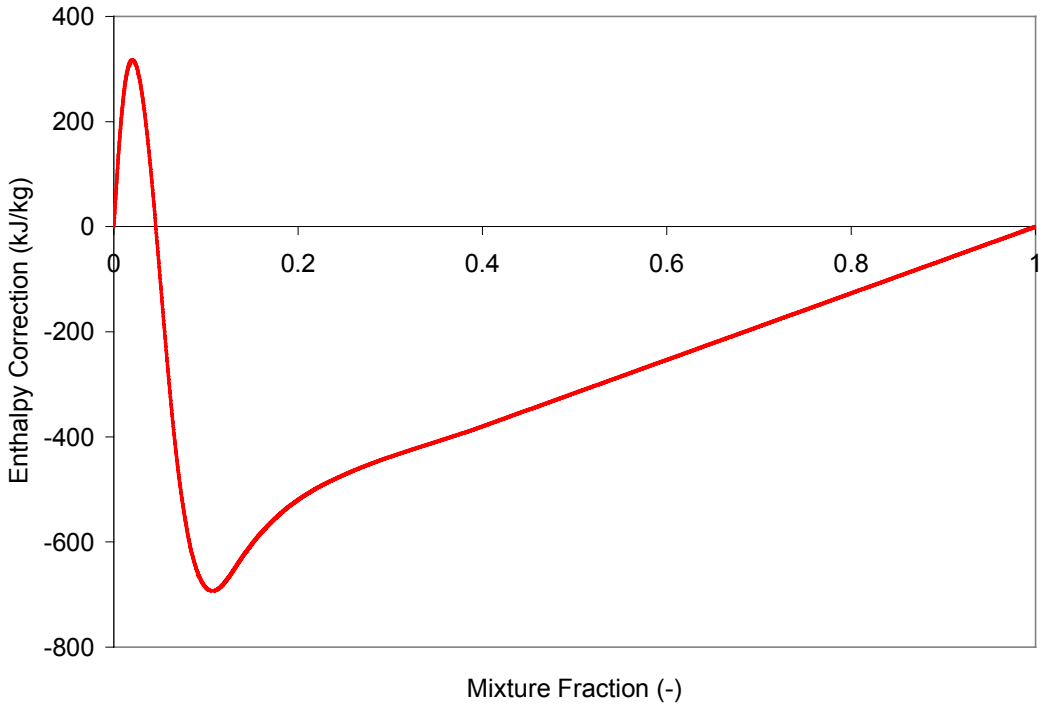

Figure 5. Enthalpy correction used to set adiabatic mixture fraction-temperature relationship. Positive values correspond to the addition of enthalpy relative to adiabatic. Negative values correspond to the removal of enthalpy relative to adiabatic.

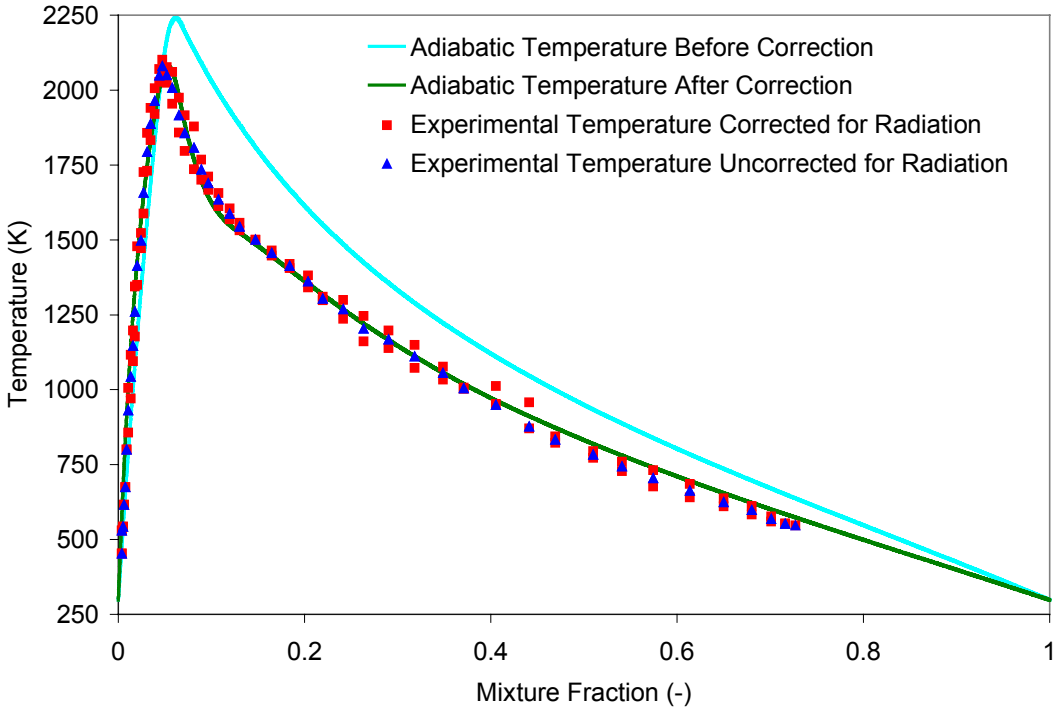

Figure 6. Relationship between mixture fraction and temperature for methane before/after correction. Experimental data are for methane on a Wolfhard-Parker slot burner. The complete combustion state relations have been numerically smoothed to eliminate the sharp peak at stoichiometric.

4.2 Governing Equations

The gas-phase conservation equations solved by the modified version of FDS v2.0[1,2] that was used in this work are given as Equations 15 through 25. The reader should refer to the FDS v2.0 Technical Reference Guide[1] for details. Although the simulations reported in this paper were conducted in 2D cylindrical coordinates, the code can be also be used for 2D and 3D Cartesian simulations. For this reason, conservation equations are given in general vector notation:

$$\frac{\partial \rho_g}{\partial t} + \nabla \cdot \rho_g \boldsymbol{u} = 0 \tag{15}$$

$$\frac{\partial \boldsymbol{u}}{\partial t} + \boldsymbol{u} \times \omega + \nabla \mathcal{H} = \frac{1}{\rho_g}\left(\left(\rho_g - \rho_\infty\right)\boldsymbol{g} + \boldsymbol{f} + \nabla \cdot \boldsymbol{\tau}\right) \tag{16}$$

$$\frac{\partial(\rho_g Z)}{\partial t} + \boldsymbol{u} \cdot \nabla \rho_g Z + \rho_g Z \nabla \cdot \boldsymbol{u} = \nabla \cdot \rho_g D \nabla Z - \dot{\omega}_s''' \tag{17}$$

$$\frac{\partial(\rho_g h_T)}{\partial t} + \boldsymbol{u} \cdot \nabla \rho_g h_T + \rho_g h_T \nabla \cdot \boldsymbol{u} = \nabla \cdot \rho_g D \nabla h_T + \dot{\omega}_{sf}''' h_f^\circ + \dot{\omega}_{so}''' h_{CO}^\circ + \dot{q}_e''' \tag{18}$$

Equation 15 is the continuity equation (used to form the divergence of the velocity field, Equation 10) and Equation 16 is the conservation of momentum equation. In Equation 16, $\mathcal{H}$ is the total pressure divided by the gas-phase density, ω is the vorticity vector, $\boldsymbol{f}$ is the external body force vector (neglecting gravitational forces), and $\boldsymbol{\tau}$ is the viscous stress tensor. Equation 17 is the conservation equation for *gas-phase* mixture fraction.

Following Sivathanu and Gore[43], the gas-phase mixture fraction is defined as the local fraction of material in the gas phase that originated in the fuel stream. Soot formation occurs when gaseous fuel constituents are converted into particulate soot. It therefore represents a redistribution of mass from the gas-phase to the solid-phase. During the soot oxidation process, solid-phase soot is liberated to the gas phase. The gas-phase mixture fraction is not a perfectly conserved scalar. Its conservation equation includes a source term of equal magnitude but opposite sign to the soot formation or oxidation rate. This source-sink relationship between the mixture fraction and soot mass fraction is usually ignored because it is small in lightly sooting flames. However, in some heavily sooting fuels, 30% or more of the local fuel mass can be converted to soot.

Similarly, Equation 18 is the conservation equation for the gas-phase total enthalpy. It contains two source terms to account for the change in gas-phase enthalpy caused by soot formation/oxidation. Again following Sivathanu and Gore[43], the change in enthalpy caused by soot formation is equal to the net rate of soot formation multiplied by the fuel's enthalpy of

formation on a mass basis, $\dot{\omega}_{sf}''' h_f^\circ$. Soot oxidation represents a source of gas-phase enthalpy, and is estimated from the soot oxidation rate (negative in sign) multiplied by the enthalpy of formation of CO, $\dot{\omega}_{so}''' h_{CO}^\circ$. This is a rough approximation, and the effect of soot formation and oxidation on the gas-phase energetics requires more research.

The final source term in the conservation of total enthalpy equation is the radiation loss:

$$\dot{q}_e''' = -4\kappa\sigma T^4 \tag{19}$$

The total absorption coefficient κ in Equation 19 is the sum of a gas component κ_g and a soot component κ_s:

$$\kappa = \kappa_g + \kappa_s \tag{20}$$

The gas-phase absorption coefficient κ_g is determined as a function of mixture fraction and temperature using the radiation model RADCAL[44] as implemented in FDS v2.0 by McGrattan *et. al.*[1]. RADCAL can be used to calculate the absorption coefficient for a particular radiation pathlength through a nonisothermal and nonhomogeneous medium containing CO_2, H_2O, CH_4, CO, N_2, O_2, and soot. It is a narrow-band model meaning that the entire radiation spectrum is divided into hundreds of discrete bands. The absorption coefficient (or radiant intensity) at a given wavelength is calculated by the program using the spectral characteristics of each gas as tabulated within the program or approximated theoretically.

However, in this work a mean absorption coefficient averaged over all wavelengths is desired. At the start of a calculation, the band-mean absorption coefficient is stored as a function of mixture fraction and temperature by evaluating the integral in Equation 21 with RADCAL[44]:

$$\kappa_g(Z,T) = \int_{\lambda_1}^{\lambda_2} \kappa\left(T, L, P_{H_2O}, P_{CO_2}, P_F, \lambda\right) d\lambda \tag{21}$$

This represents only the *gas-phase* contribution to the absorption coefficient. The limits of integration in Equation 21 are $\lambda_1 = 1.0\mu$m and $\lambda_2 = 200.0\mu$m. The fuel is assumed to have identical radiative characteristics to those of methane. The partial pressures of water vapor, carbon dioxide, and fuel (P_{H_2O}, P_{CO_2}, and P_F) are calculated from the background pressure p_0 and the mole fractions of each species as determined from the Schvab-Zeldovich complete combustion state relations.

The path-length L in Equation 21 is the mean beam length for the overall problem given by

$$L = 3.6\frac{V_f}{A_f} \tag{22}$$

where V_f and A_f are respectively the characteristic flame volume and surface area. The value of κ_g was found to be quite insensitive to the parameter L for the present small axisymetric diffusion flames because the gas-phase absorption coefficient approaches its Planck limit at these short pathlengths.

For most fuels, the gas contribution to the absorption coefficient is significantly less than the soot contribution, which is calculated here as:

$$\kappa_s = C_{\kappa_s} f_v T \tag{23}$$

In Equation 23, C_{κ_s} is given a conventional value of 1186 (mK)$^{-1}$ consistent with the Dalzell and Sarofim[45] dispersion relationship commonly used for measuring soot volume fractions. See Appendix H of Lautenberger[8] for details.

4.3 Thermodynamic and Transport Properties

At the start of a calculation, a lookup table is generated for $T(Z, h_T)$. The enthalpies of formation and temperature-dependency of each species' specific heat are taken from the NASA Chemical Equilibrium Code[40]. The molecular viscosity of a gas mixture μ_{mix} is calculated as a function of mixture fraction and temperature using the complete combustion state relations in combination with Equations 24 and 25[40]:

$$\mu_{mix} = \sum_{i=1}^{s} \frac{\mu_i}{1 + \frac{1}{X_i} \sum_{\substack{j=1 \\ j \neq i}}^{s} X_j \chi_{ij}} \tag{24}$$

$$\chi_{ij} = \frac{1}{\sqrt{8}} \left(1 + \frac{M_i}{M_j}\right)^{-1/2} \left[1 + \left(\frac{\mu_i}{\mu_j}\right)^{1/2} \left(\frac{M_i}{M_j}\right)^{1/4}\right]^2 \tag{25}$$

The mole fractions in Equation 24 are determined from complete combustion state relations. Note that soot formation does not affect the molecular viscosity. The temperature dependency of the μ_i's are also taken from the NASA Chemical Equilibrium Code[40]. Chapman-Enskog theory and the Lennard-Jones Parameters[46,51] are used to estimate the viscosity of fuels not included in the NASA code[40]. In those cases where no viscosity data are available, the fuel is arbitrarily assumed to have the viscosity of methane.

The value of $\rho_g D$ is related to the molecular viscosity through a constant Schmidt number:

$$\rho_g D = \frac{\mu_{mix}}{\mathrm{Sc}} \tag{26}$$

5.0 MODEL CALIBRATION

The soot model developed as part of this work has been incorporated FDS v2.0[1,2] modified as described above. A calibration exercise was performed to determine the optimal model parameters for three fuels. Based on these values, a set of "global" parameters that could potentially be used for an arbitrary hydrocarbon fuel are suggested. The model was calibrated against experimental data for small-scale axisymmetric laminar flames[32] burning on a 1.1cm diameter fuel tube with a coflowing air stream. Experimental data from three prototype flames (a 247W methane flame, a 213W propane flame, and a 212W ethylene flame) were used in this exercise. The velocity of the coflow stream was 79mm/s for the methane flame and 87mm/s for the propane and ethylene flames. A grid spacing of 0.25mm in the radial direction and 0.5mm in the axial direction was used for the numerical simulation of these flames.

The calibration exercise involved determining the ψ values that yielded the Z_L, Z_P, and Z_H values for each of the three mixture fraction polynomials (see Figure 1) that provided the optimal agreement between prediction and experiment for each flame. The optimal Z values are reported normalized by the stoichiometric mixture fraction of each fuel, *e.g.* $Z_L = \psi_{Z_L} Z_{st}$, in the first three rows of Table 1. The peak soot formation and oxidation rates that provided the best agreement were also determined for each flame. These are denoted as $f(Z_P)$ in Table 1. Note that in the two columns labeled "PUA" $f(Z_P)$ has units of $\mathrm{kg\,soot}/(\mathrm{m^2\ soot}\cdot\mathrm{s})$, but in the column labeled "PUV" $f(Z_P)$ has units of $\mathrm{kg\,soot}/(\mathrm{m^3\ mixture}\cdot\mathrm{s})$. Finally, the slopes of each of the polynomials at Z_L and Z_H that gave the optimal agreement were determined. Since the peak soot formation or oxidation rate affects the slope of the polynomial at Z_L and Z_H, the slopes of the functions at these points are defined in terms of the parameter ϕ given as Equations 27 through 32:

$$\frac{df''_{Zsf}(Z_L)}{dZ} = \phi^{PUA}_{sf,Z_L} \frac{f''_{Zsf}(Z_P)}{Z_P - Z_L} \tag{27}$$

$$\frac{df''_{Zsf}(Z_H)}{dZ} = \phi^{PUA}_{sf,Z_H} \frac{f''_{Zsf}(Z_P)}{Z_P - Z_H} \tag{28}$$

$$\frac{df'''_{Zsf}(Z_L)}{dZ} = \phi^{PUV}_{sf,Z_L} \frac{f'''_{Zsf}(Z_P)}{Z_P - Z_L} \tag{29}$$

$$\frac{df'''_{Zsf}(Z_H)}{dZ} = \phi^{PUV}_{sf,Z_H} \frac{f'''_{Zsf}(Z_P)}{Z_P - Z_H} \tag{30}$$

$$\frac{df''_{Zso}(Z_L)}{dZ} = \phi^{PUA}_{so,Z_L} \frac{f''_{Zso}(Z_P)}{Z_P - Z_L} \tag{31}$$

$$\frac{df''_{Zso}(Z_H)}{dZ} = \phi^{PUA}_{so,Z_H} \frac{f''_{Zso}(Z_P)}{Z_P - Z_H} \tag{32}$$

The parameter ϕ is defined such that its value is always positive. It can be thought of as the slope of the polynomial function at Z_L or Z_H normalized by the slope of a straight line connecting the peak value of the function at Z_P to its zero value at either Z_L or Z_H.

An analogous exercise was performed to determine the optimal values of the temperature polynomial parameters. The first three rows of Table 2 give the optimal values of T_L, T_P, and T_H for each function. T_L corresponds to the minimum temperature at which soot formation or oxidation occurs, T_P is the temperature at which peak soot formation occurs, and T_H is the temperature above which soot does not form. Note that the maximum value of the formation temperature polynomials is unity, but the oxidation polynomial increases indefinitely with temperature. Consequently: (1) it is not necessary to specify a peak value of the function; (2) $df(T_L)/dT$ and $df(T_H)/dT$ can be specified directly without using a normalizing procedure as was necessary for the mixture fraction polynomials.

Finally, the optimal values of A_0, β, and Sc for each flame are given in Table 3. The optimal values of the parameters given in Tables 1 through 3 were determined by a manual calibration exercise and should be considered first approximations. Admittedly, all possible combinations were not investigated and it is therefore likely that better agreement can be obtained using different combinations of parameters. A more rigorous way to establish these constants is to systematically vary each parameter and quantify the correlation between prediction and experiment for each variation. Future work is planned in this area.

The resulting soot volume fraction predictions are presented in Figures 7 through 11. Temperature and velocity comparisons are also given where experimental data were available.

Table 1. Optimal mixture fraction polynomial constants for prototype flames.

	Soot Formation PUA			Soot Formation PUV			Soot Oxidation PUA		
	CH_4	C_3H_8	C_2H_4	CH_4	C_3H_8	C_2H_4	CH_4	C_3H_8	C_2H_4
ψ_{Z_L}	1.02	1.03	1.04	1.02	1.03	1.00	0.55	0.55	0.55
ψ_{Z_P}	1.70	1.67	1.77	1.60	1.57	1.75	0.85	0.85	0.85
ψ_{Z_H}	2.30	2.00	2.12	2.00	1.9	3.00	1.08	1.08	1.06
$f(Z_P)$	0.003	0.0046	0.0057	0.10	0.65	0.50	-0.007	-0.008	-0.007
ϕ_{Z_L}	1.7	1.7	1.7	0.60	1.9	1.9	0.6	1.7	0.6
ϕ_{Z_H}	1.2	1.2	1.2	1.10	0.5	0.5	1.1	1.2	1.1

Table 2. Optimal temperature polynomial constants for prototype flames.

	Soot Formation PUA			Soot Formation PUV			Soot Oxidation PUA		
	CH_4	C_3H_8	C_2H_4	CH_4	C_3H_8	C_2H_4	CH_4	C_3H_8	C_2H_4
T_L	1375	1375	1400	1400	1350	1380	1400	1400	1400
T_P	1600	1590	1610	1450	1425	1510	-	-	-
T_H	1925	1925	1925	1500	1500	1600	-	-	-
$df(T_L)/dT$	0.0045	0.0045	0.0045	0.0002	0.0002	0.0002	0.006	0.006	0.006
$df(T_H)/dT$	-0.004	-0.004	-0.004	-0.0005	-0.0005	-0.0005	-	-	-

Table 3. Optimal values of A_0, β, and Sc.

	Methane	Propane	Ethylene
A_0 (m^2/m^3)	1.1	10.0	60.0
β (m^{-1})	8×10^7	8×10^7	8×10^7
Sc (-)	0.85	0.76	0.80

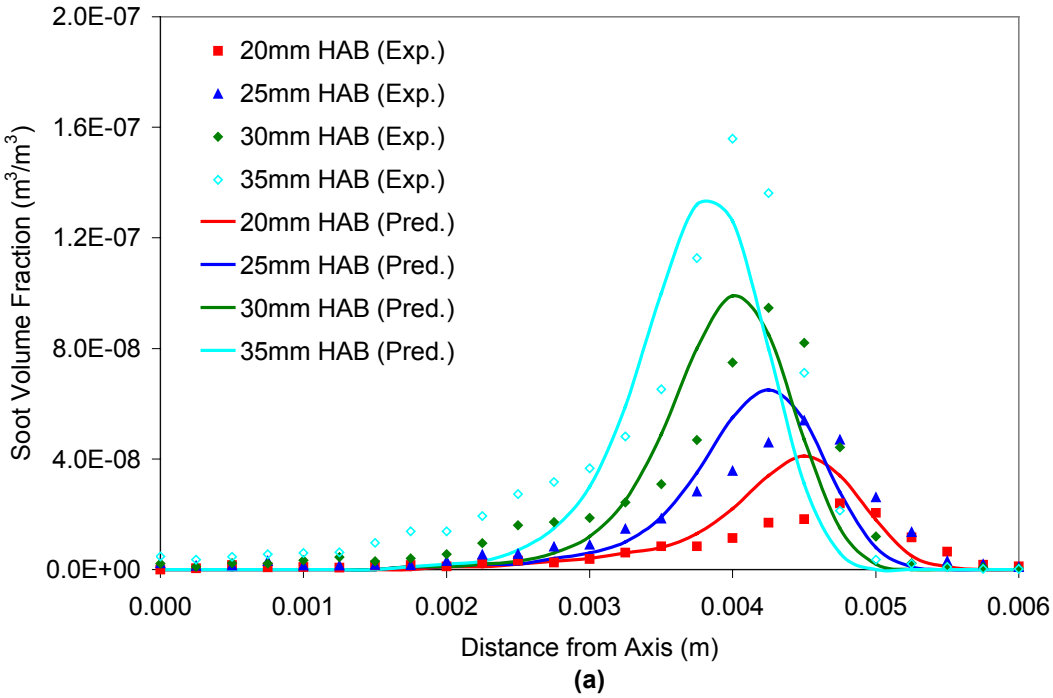

(a)

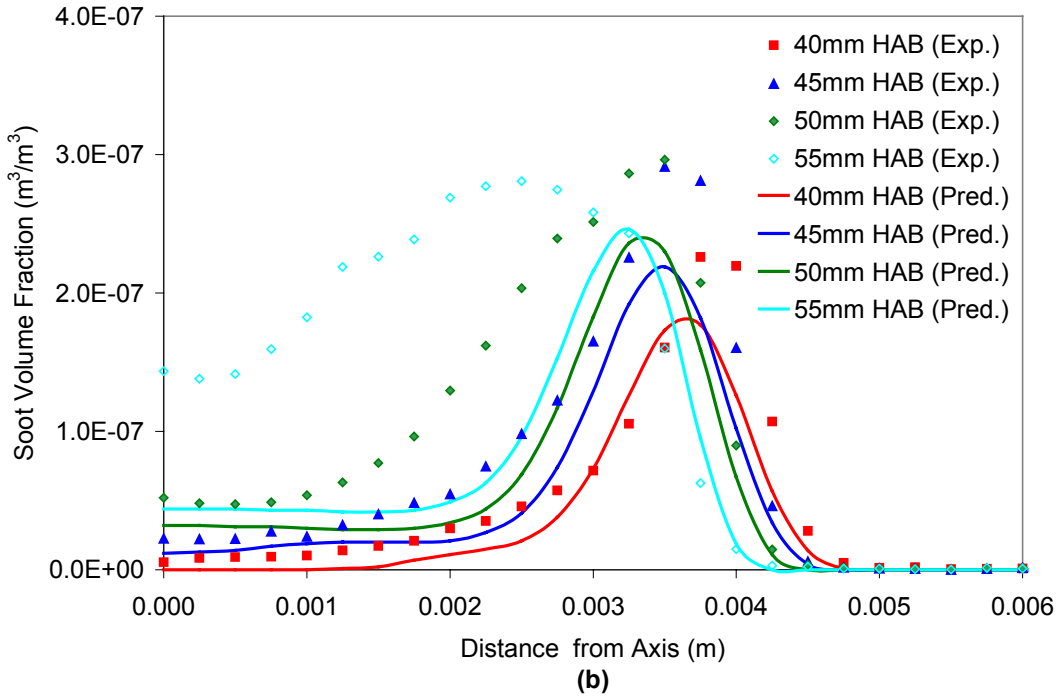

(b)

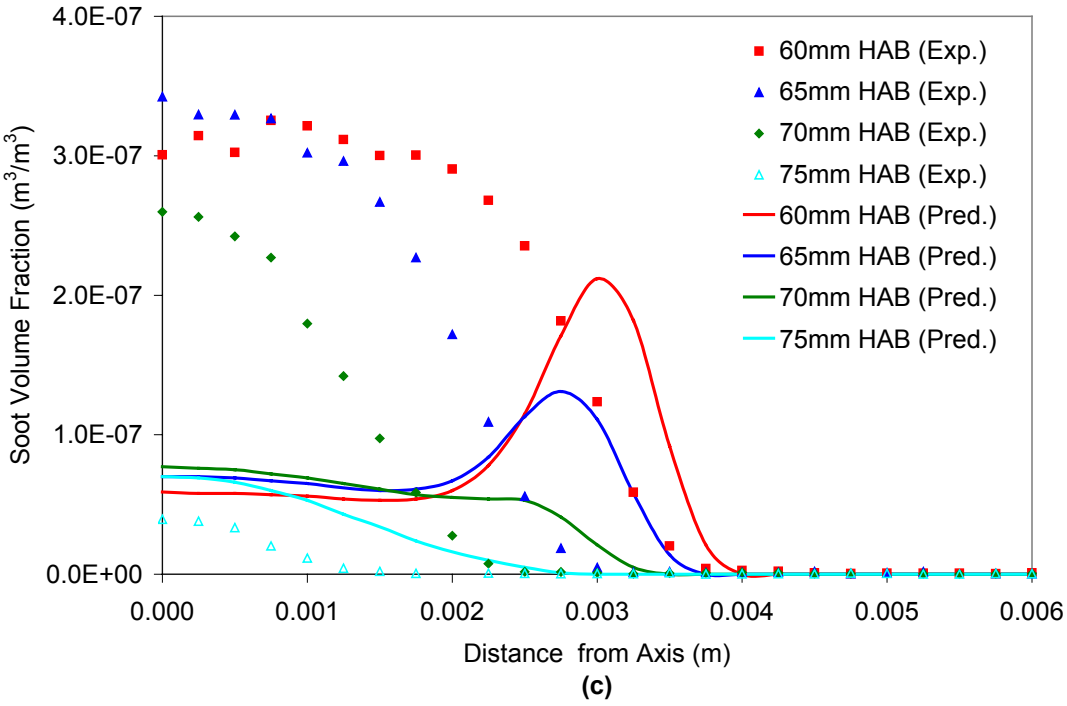

(c)

Figure 7. Optimal f_v predictions in 247W methane flame at several heights above burner (HAB): (a) 20-35 mm; (b) 40-55 mm; (c) 60-75 mm. "Exp." corresponds to experimental data and "Pred." corresponds to the model predictions.

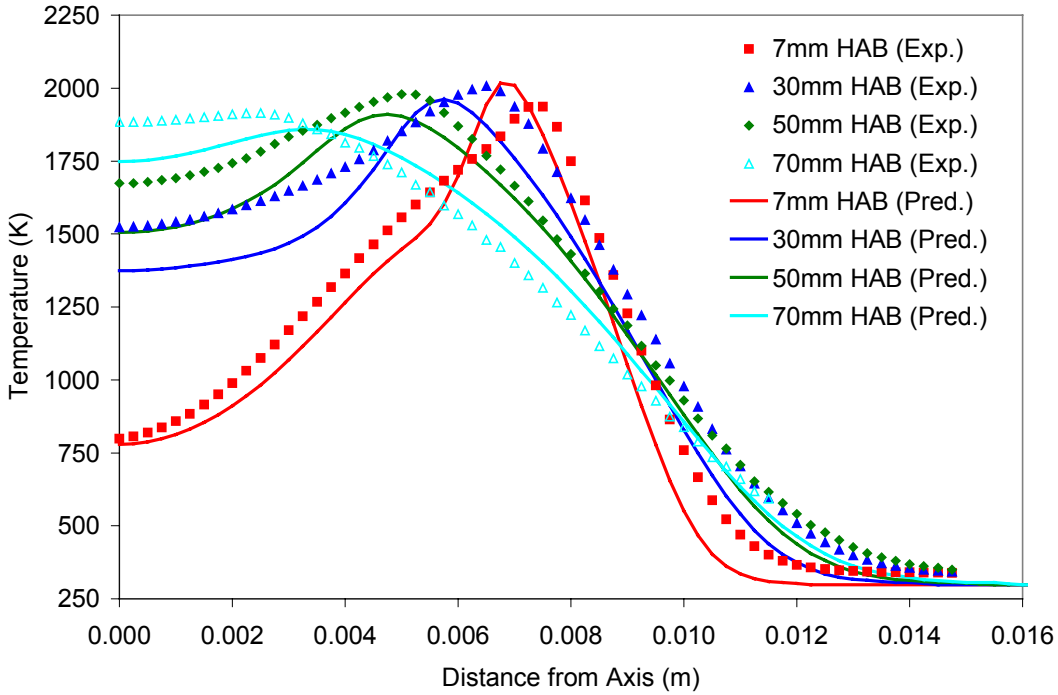

Figure 8. Optimal *T* predictions in 247W methane flame at several heights above burner (HAB). "Exp." corresponds to experimental data and "Pred." corresponds to the model predictions.

In the 247W methane flame, the soot volume fraction profiles are not well produced, particularly near the axis and with increasing height in the flame. Low in the flame, soot forms too far to the fuel side. The soot loading in the "wings" was found to be highly sensitive to the value of A_0 due to the surface area-dependent nature of soot formation in this region. The temperatures in the methane flame are generally underpredicted except at 70mm HAB (see Figure 8). This indicates that the magnitude of the enthalpy correction shown in Figure 5 may be too great on the fuel side. However, the temperature predictions are improved compared to those of the unmodified FDS v2.0[1,2] for the same flame shown above as Figure 3. A comparison of the measured and predicted soot volume fractions in the 213W propane flame is given below in Figures 9a through 9c.

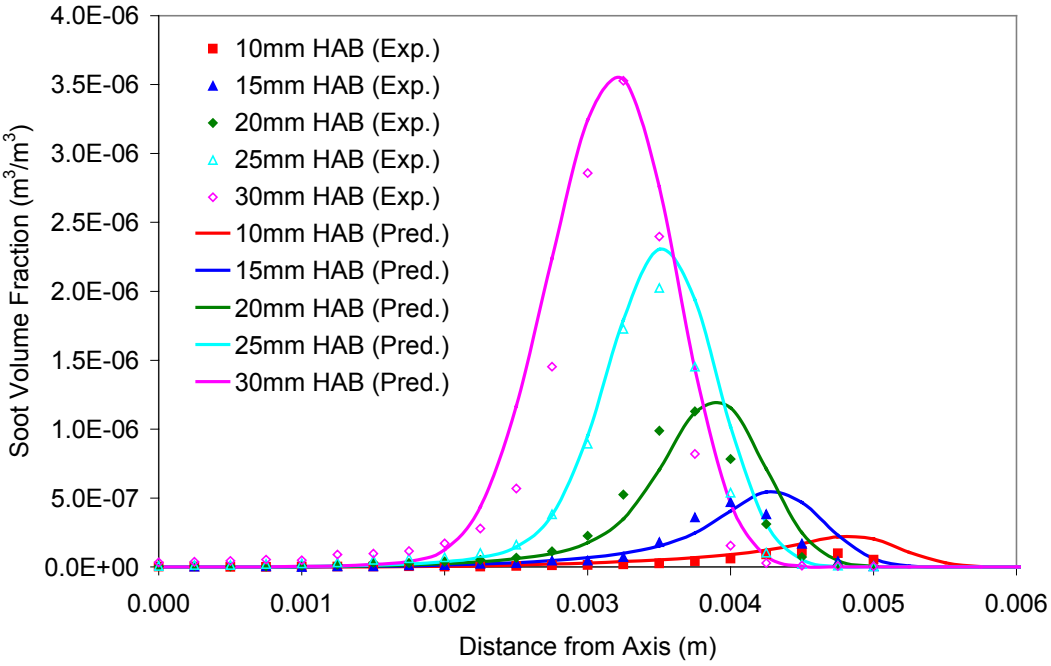
4.0E-06
3.5E-06
3.0E-06
2.5E-06
2.0E-06
1.5E-06
1.0E-06
5.0E-07
0.0E+00
Soot Volume Fraction (m3/m3)
0.000
0.001
0.002
0.003
0.004
0.005
0.006
Distance from Axis (m)
10mm HAB (Exp.)
15mm HAB (Exp.)
20mm HAB (Exp.)
25mm HAB (Exp.)
30mm HAB (Exp.)
10mm HAB (Pred.)
15mm HAB (Pred.)
20mm HAB (Pred.)
25mm HAB (Pred.)
30mm HAB (Pred.)

(a)

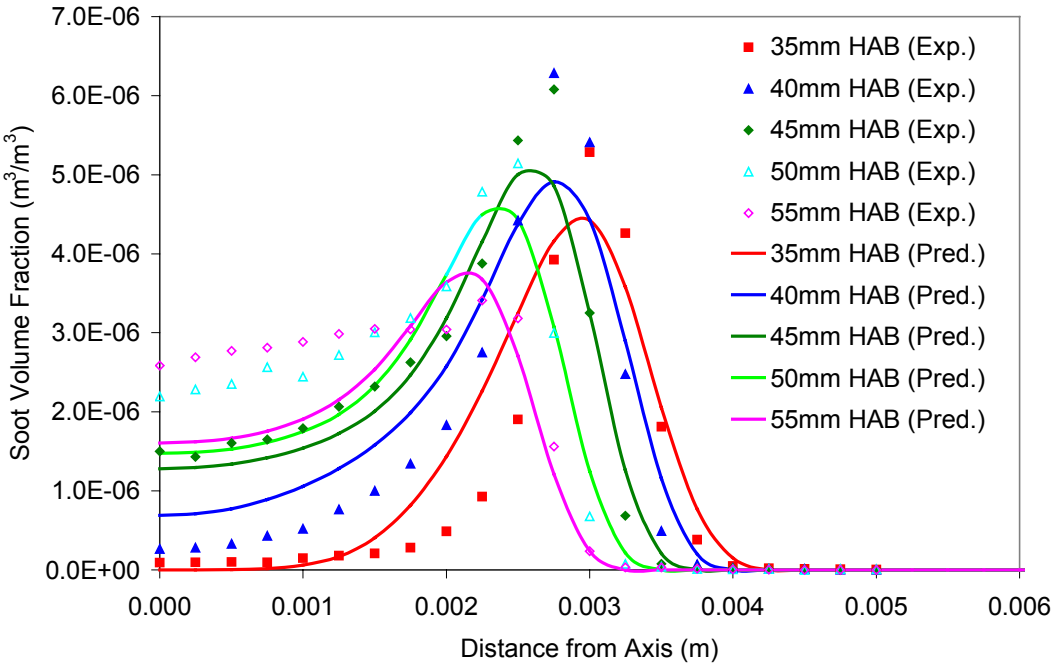
7.0E-06
6.0E-06
5.0E-06
4.0E-06
3.0E-06
2.0E-06
1.0E-06
0.0E+00
Soot Volume Fraction (m3/m3)
0.000
0.001
0.002
0.003
0.004
0.005
0.006
Distance from Axis (m)
35mm HAB (Exp.)
40mm HAB (Exp.)
45mm HAB (Exp.)
50mm HAB (Exp.)
55mm HAB (Exp.)
35mm HAB (Pred.)
40mm HAB (Pred.)
45mm HAB (Pred.)
50mm HAB (Pred.)
55mm HAB (Pred.)

(b)

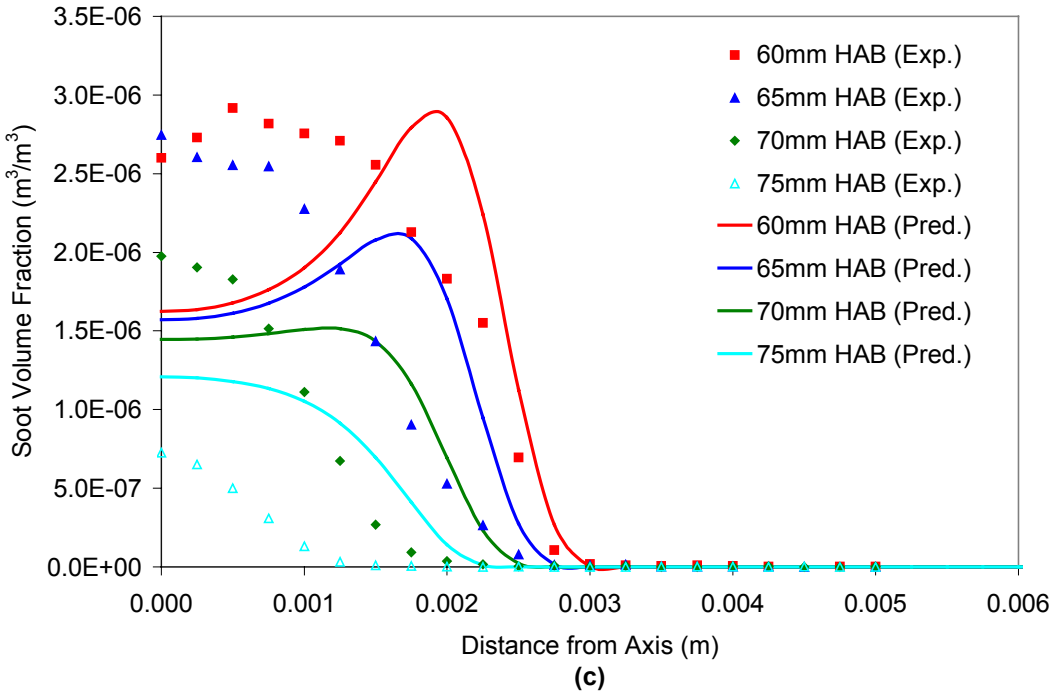

Figure 9. Optimal f_v predictions in 213W propane flame at several heights above burner (HAB): (a) 10-30 mm; (b) 35-55 mm; (c) 60-75mm. "Exp." corresponds to experimental data and "Pred." corresponds to the model predictions.

In the propane flame, the soot volume fraction profiles are reproduced reasonably well low in the flame (see Figure 9), although soot tends to form too far from the axis. By 25mm HAB, the soot has been pushed closer to the axis by thermophoresis and the predicted and experimental profiles match more closely. At greater HAB's, the quality of the predictions decreases, particularly near the core. Soot burnout in the upper flame regions was not strong enough. No temperature data were available for this propane flame.

A comparison of the measured and predicted soot volume fractions in the 212W ethylene flame is given below in Figures 10a and 10b. The temperature predictions are given as Figure 11, the vertical velocity profiles are given as Figures 12a and 12b, and the horizontal velocity profiles are given as Figures 13a and 13b.

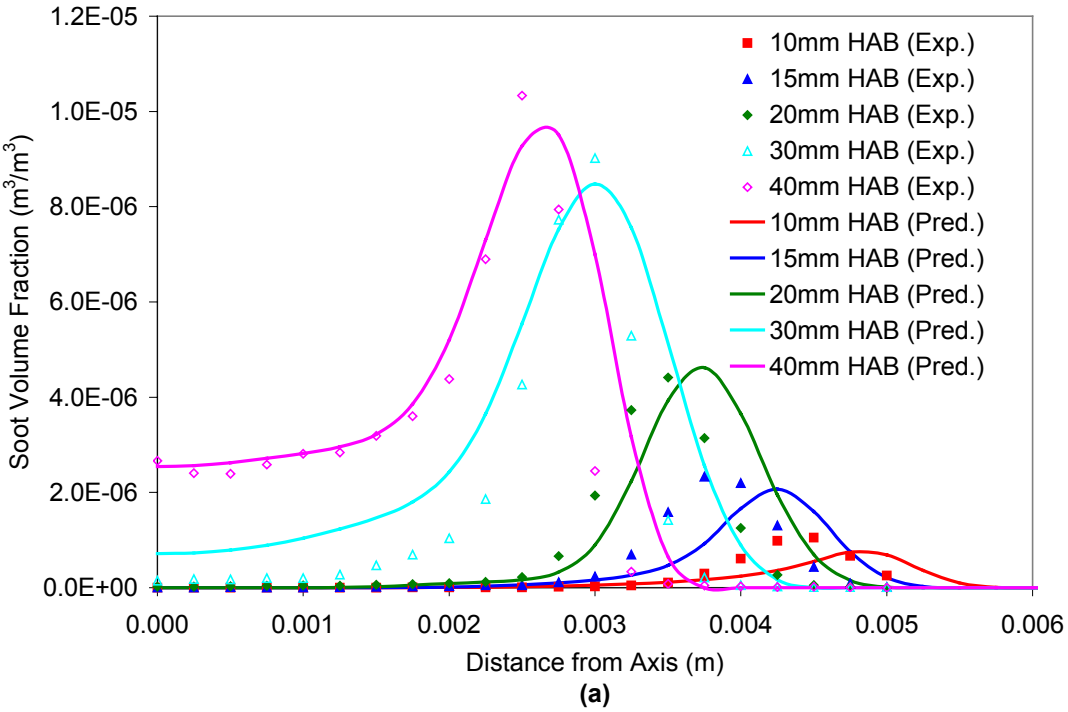

(a)

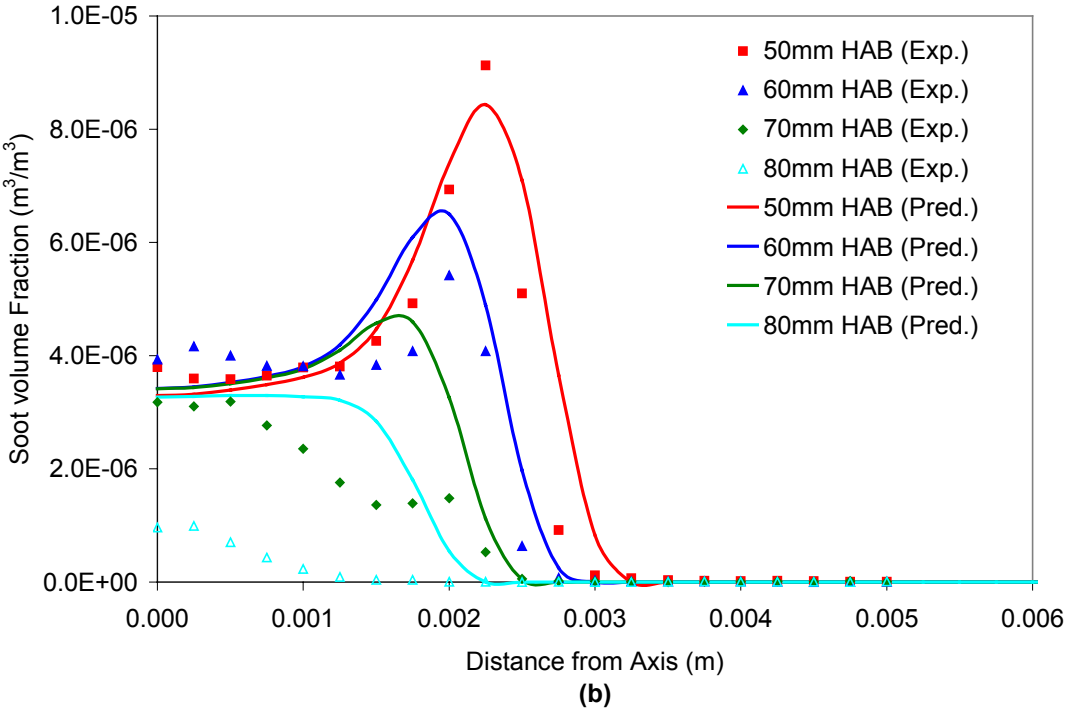

(b)

Figure 10. Optimal f_v predictions in 212W ethylene flame at several heights above burner (HAB): (a) 10-40 mm; (b) 50-80 mm. "Exp." corresponds to experimental data and "Pred." corresponds to the model predictions.

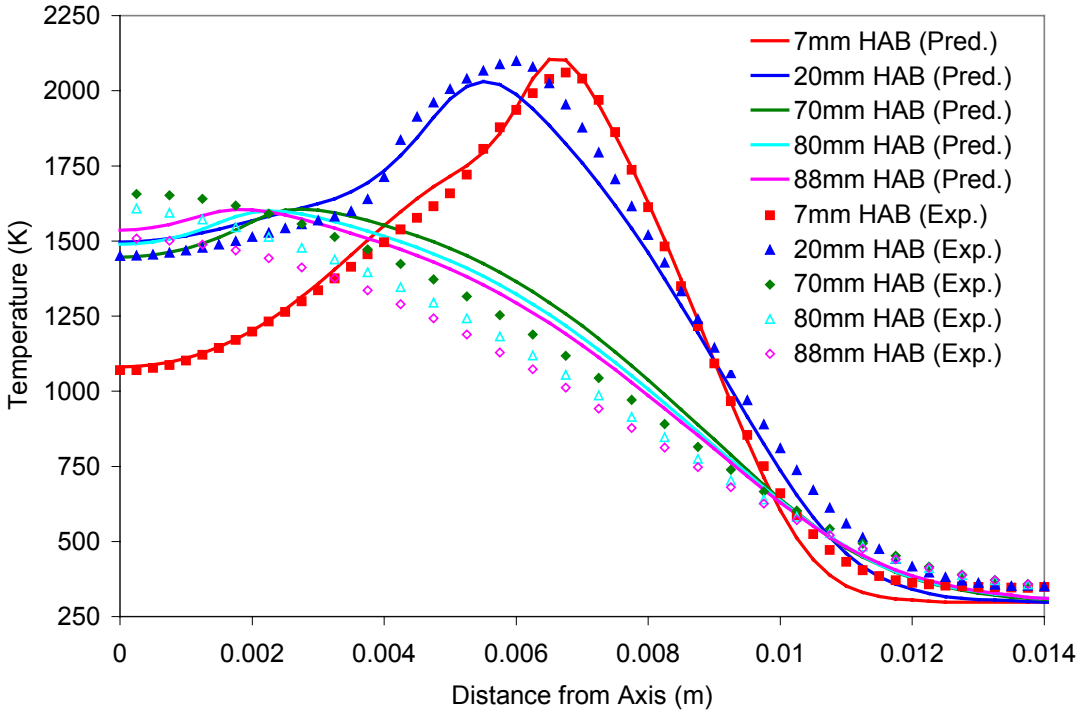

Figure 11. Optimal temperature predictions in 212W ethylene flame at several heights above burner (HAB). "Exp." corresponds to experimental data and "Pred." corresponds to the model predictions.

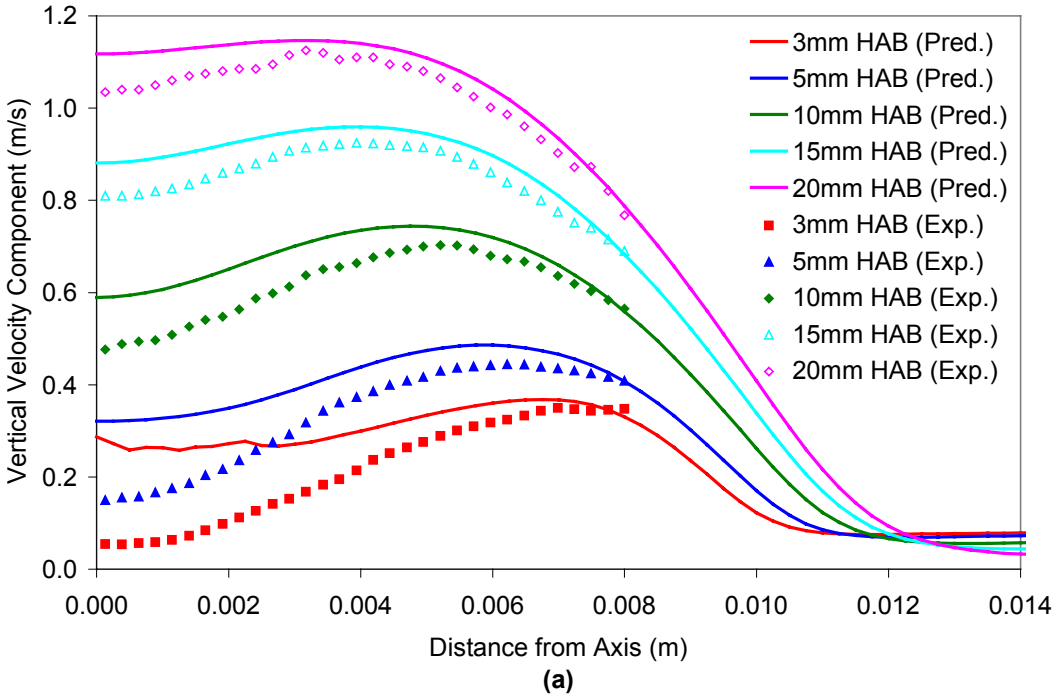

(a)

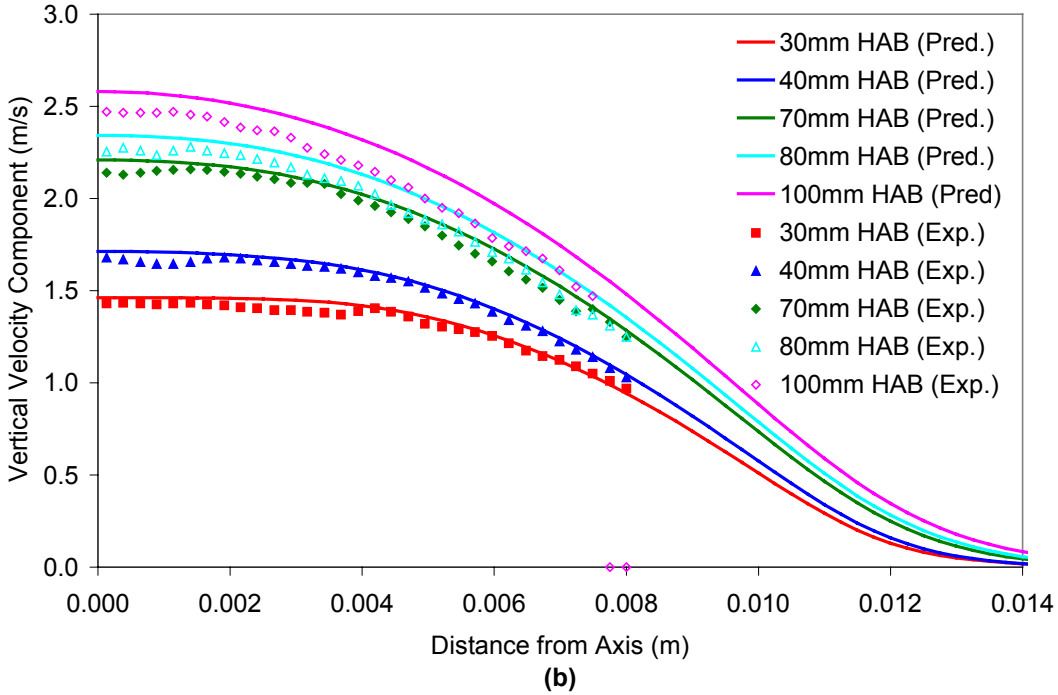

(b)

Figure 12. Optimal vertical velocity predictions in 212W ethylene flame at several heights above burner (HAB): (a) 3-20 mm; (b) 30-100 mm. "Exp." corresponds to experimental data and "Pred." corresponds to the model predictions.

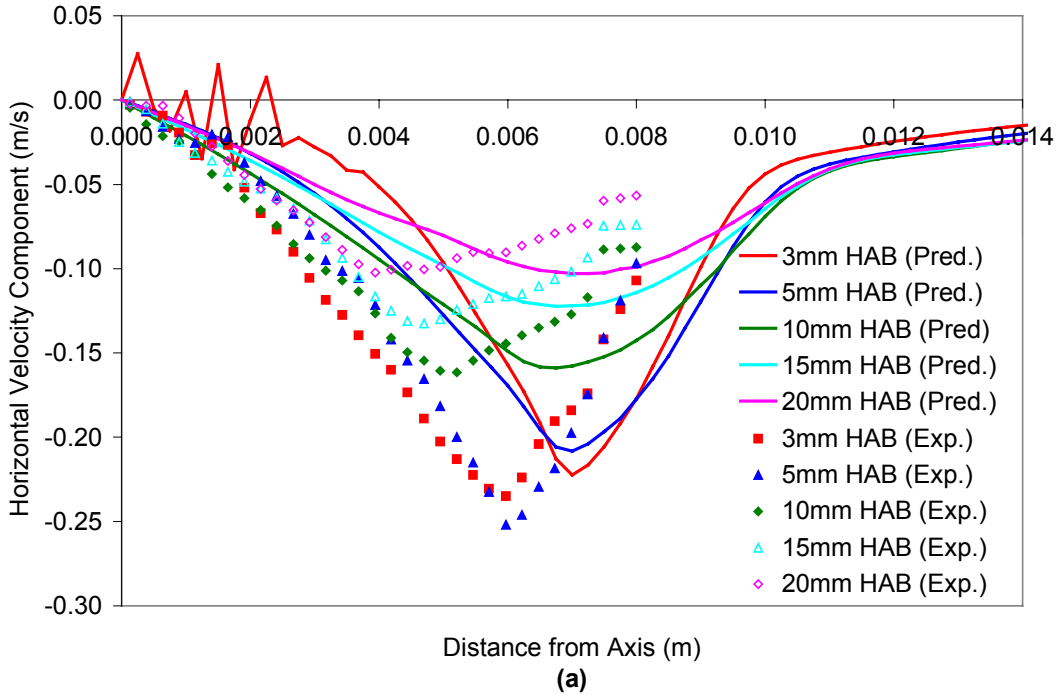

(a)

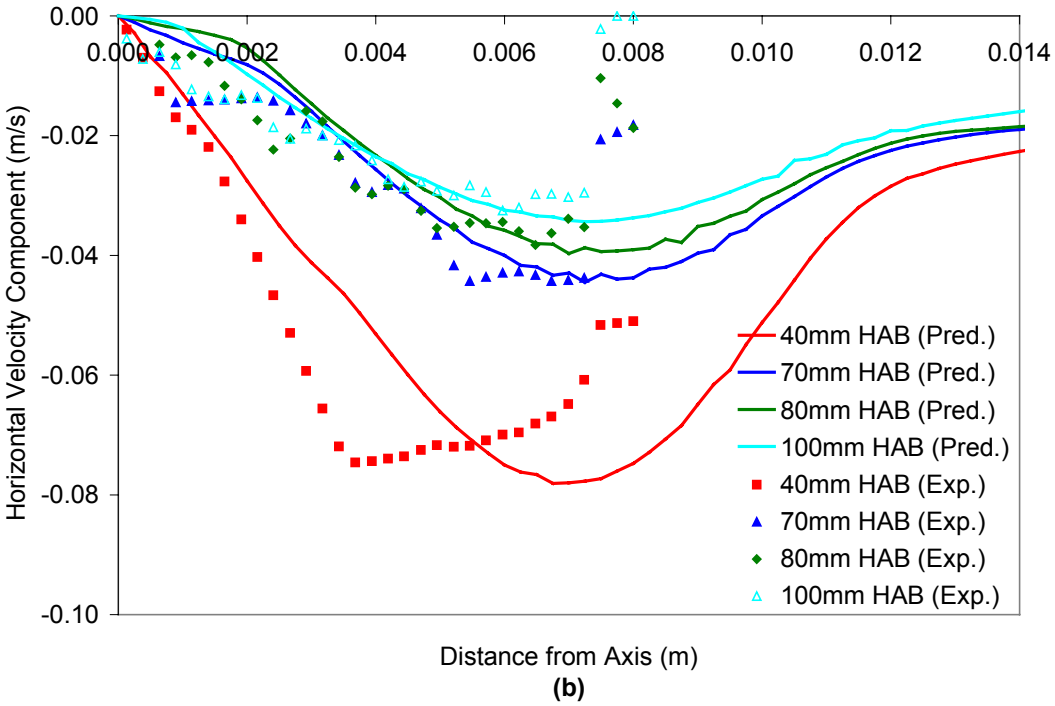

(b)

Figure 13. Optimal horizontal velocity predictions in 212W ethylene flame at several heights above burner (HAB): (a) 3-20 mm; (b) 40-100 mm. "Exp." corresponds to experimental data and "Pred." corresponds to the model predictions.

In the ethylene flame, the predicted soot volume fraction profile peaks slightly farther from the axis than the measured soot volume fraction profile at low HAB's. As with the propane flame, thermophoresis pushes the soot toward the axis and by 30mm HAB the peak of the predicted and measured profiles match quite well. The soot loading on the axis is well predicted at 40mm, but not at greater HAB's. Oxidation is generally underpredicted in the upper flame regions. The predicted temperature profile matches the experimental data very well at 7mm HAB. The quality of the prediction deteriorates higher up in the flame, and the off-axis temperatures are significantly overpredicted from 70 to 88mm HAB.

The vertical velocity profiles are overpredicted low in the flame, but improve with increasing height. The shape and magnitude of the vertical velocity profiles match reasonably well above 10mm HAB, although the velocities tend to be overpredicted. The horizontal velocity profiles do not match well. The nonphysical oscillations in the predicted horizontal

velocity profile at 3mm in the ethylene flame are caused by a problem with the new expression for the velocity divergence (Equation 10) that occurs near boundaries where the fuel is introduced to the computational domain. This also negatively impacts the vertical velocity profiles, although this is attenuated with increasing height in the flame.

6.0 MODEL GENERALIZATION

Section 5 showed graphically the best-case soot volume fraction profiles that were obtained with this model by approximating the soot formation and oxidation rates as explicit polynomial functions of mixture fraction and temperature. The model has been postulated with a sufficient number of constants that reasonable agreement can usually be achieved by adjusting different combinations of parameters. In general, the usefulness of a model decreases as the number of adjustable constants is increased[48]. However, a model retains its practicality if the constants are global, or if nonglobal constants can be estimated from simple rules or empirical material properties.

This is the approach taken with the present model. Based on the calibration exercise reported in Section 5, a set of global model constants listed in Tables 4 and 5 is recommended for application of this model to fuels other than methane, propane, and ethylene. Inherent in this is a compromise. Since the constants are general, the predictions for any given fuel will generally be of lesser quality than the predictions shown in Section 5 where the optimal constants for each fuel were used. The global constants suggested in Tables 4 and 5 were determined more by "art" than "science" by using engineering judgement. Generally, the optimal constants for the ethylene and propane flames were weighed more heavily than the optimal constants for the methane flames because the agreement between prediction and experiment was better for the former two fuels.

It is important not to lose sight of the fact that this model is intended for use in engineering calculations of radiation from turbulent flames, rather than for predicting detailed soot volume fraction profiles in laminar flames. In turbulent flames, there is considerably more uncertainty and a soot model that can capture global trends may be adequate.

Table 4. Suggested universal mixture fraction function constants for generalization of soot model to arbitrary hydrocarbon fuels.

Constant	Description	Value
ψ_{sf,Z_L}^{PUA}	Sets Z_L for $f''_{Zsf}(Z)$	1.03
ψ_{sf,Z_P}^{PUA}	Sets Z_P for $f''_{Zsf}(Z)$	1.7
ψ_{sf,Z_H}^{PUA}	Sets Z_H for $f''_{Zsf}(Z)$	2.1
ϕ_{sf,Z_L}^{PUA}	Sets $df''_{Zsf}(Z)/dZ$ at Z_L	1.7
ϕ_{sf,Z_H}^{PUA}	Sets $df''_{Zsf}(Z)/dZ$ at Z_H	1.2
ψ_{sf,Z_L}^{PUV}	Sets Z_L for $f'''_{Zsf}(Z)$	1.02
ψ_{sf,Z_P}^{PUV}	Sets Z_P for $f'''_{Zsf}(Z)$	1.65
ψ_{sf,Z_H}^{PUV}	Sets Z_H for $f'''_{Zsf}(Z)$	2.2
ϕ_{sf,Z_L}^{PUV}	Sets $df'''_{Zsf}(Z)/dZ$ at Z_L	1.9
ϕ_{sf,Z_H}^{PUV}	Sets $df'''_{Zsf}(Z)/dZ$ at Z_H	0.5
ψ_{so,Z_L}^{PUA}	Sets Z_L for $f''_{Zso}(Z)$	0.55
ψ_{so,Z_P}^{PUA}	Sets Z_P for $f''_{Zso}(Z)$	0.85
ψ_{so,Z_H}^{PUA}	Sets Z_H for $f''_{Zso}(Z)$	1.07
ϕ_{so,Z_L}^{PUA}	Sets $df''_{Zso}(Z)/dZ$ at Z_L	1.0
ϕ_{so,Z_H}^{PUA}	Sets $df''_{Zso}(Z)/dZ$ at Z_H	1.1
$\dot{\omega}''_{sf,P}$	Peak PUA soot formation rate $\left(\mathrm{kg/m^2 \cdot s}\right)$	$0.0015/\ell_s^{0.6}$
$\dot{\omega}'''_{sf,P}$	Peak PUV soot formation rate $\left(\mathrm{kg/m^3 \cdot s}\right)$	$0.15/\ell_s^{0.6}$
$\dot{\omega}''_{so,P}$	Peak soot oxidation rate $\left(\mathrm{kg/m^2 \cdot s}\right)$	-0.007

Table 5. Suggested universal temperature function constants for generalization of soot model to arbitrary hydrocarbon fuels.

Constant	Description	Value
$T_{L,sf}^{PUA}$	Minimum temperature for PUA soot formation	1400K
$T_{P,sf}^{PUA}$	Temperature for peak PUA soot formation	1600K
$T_{H,sf}^{PUA}$	Maximum temperature for PUA soot formation	1925K
$df_{Tsf}^{PUA}(T_L)/dT$	$df_{Tsf}^{PUA}(T)/dT$ at $T_{L,sf}^{PUA}$	0.0045
$df_{Tsf}^{PUA}(T_H)/dT$	$df_{Tsf}^{PUA}(T)/dT$ at $T_{H,sf}^{PUA}$	-0.004
$T_{L,sf}^{PUV}$	Minimum temperature for PUV soot formation	1375K
$T_{P,sf}^{PUV}$	Temperature for peak PUV soot formation	1475K
$T_{H,sf}^{PUV}$	Maximum temperature for PUV soot formation	1575K
$df_{Tsf}^{PUV}(T_L)/dT$	$df_{Tsf}^{PUV}(T)/dT$ at $T_{L,sf}^{PUV}$	0.0002
$df_{Tsf}^{PUV}(T_H)/dT$	$df_{Tsf}^{PUV}(T)/dT$ at $T_{H,sf}^{PUV}$	-0.0005
$T_{L,so}^{PUA}$	Minimum temperature for soot oxidation	1400K
$df_{Tso}^{PUA}(T_L)/dT$	Slope of $f_{Tso}^{PUA}(T)$ at $T_{L,so}^{PUA}$	0.006

The peak soot formation rates and the value of the soot inception area vary from fuel to fuel and cannot be specified in a global manner. Note that in Table 4 the peak soot formation rates are given as a function of the laminar smoke point height ℓ_s:

$$\dot{\omega}''_{sf,P} = \frac{0.0015}{\ell_s^{0.6}} \quad \left(\mathrm{kg/m^2 \cdot s}\right) \tag{33}$$

$$\dot{\omega}'''_{sf,P} = \frac{0.15}{\ell_s^{0.6}} \quad \left(\mathrm{kg/m^3 \cdot s}\right) \tag{34}$$

The expressions in Equations 33 and 34 were determined by attempting to match the optimal peak soot formation rates given in Table 1 for each fuel to a general expression containing the

laminar smoke point height. The fact that the numerators in Equations 33 and 34 have the same mantissa is fortuitous.

The model predictions were found to be highly sensitive to the value of the initial soot inception area A_0, as was also noted by Kent and Honnery[14]. It proved to be quite difficult to postulate an expression similar to Equations 33 and 34 that could be used to relate A_0 to the laminar smoke point height. However, while conducting this research, the relationship shown in Figure 14 between the inverse square root of the laminar smoke point height and the enthalpy of formation on a mass basis was noticed:

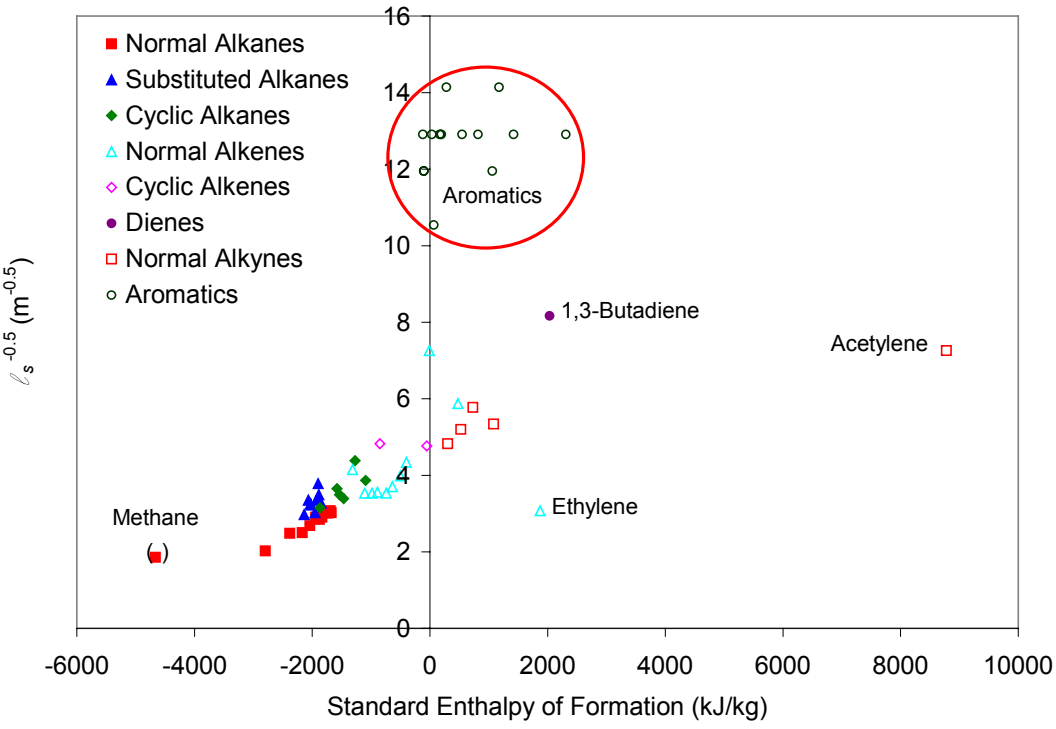

Figure 14. Correlation between enthalpy of formation and inverse square root of smoke point height.

Methane is placed in parentheses in Figure 14 because it is generally thought to not have a smoke point since the flame becomes turbulent before it emits smoke. However, here it is assigned a smoke point of 29cm. Figure 14 shows a reasonable correlation for non-aromatic fuels; however, aromatic fuels have much shorter smoke point heights (*i.e.* they are sootier) than

other fuels having similar enthalpies of formation. One possible explanation for this is that the formation of incipient soot particles in diffusion flames is controlled by the chemical energy available to transform fuel fragments into aromatic soot precursors. If this is the case, the appearance of incipient soot particles in the flame should be proportional to (1) the fuel's enthalpy of formation, which drives the formation of aromatic precursors, and (2) the peak rate of surface growth which controls the rate at which mass is added to these precursors, transforming them into "soot". Based on this hypothesis, the following expression is suggested for non-aromatic fuels to relate A_0 to the enthalpy of formation and its peak surface growth rate (given as Equation 33):

$$A_0 \approx 1.0 + 1.6\dot{\omega}''_{sf,P}\left(h^\circ - h^\circ_{CH_4}\right) \quad \left(\mathrm{m^2\ soot/m^3\ mixture}\right) \tag{35}$$

Finally, it is recommended that a molecular Schmidt number of 0.80 be used.

7.0 PREDICTIONS USING THE GENERALIZED MODEL

The procedure used to generalize the model to other fuels described in Section 6 was given a cursory test by comparing the model predictions to the soot absorption cross section per unit height α_s (m) in laminar ethylene and propylene flames as measured by Markstein and de Ris[5]. The soot absorption cross section per unit height is a measure of the total integrated amount of soot present at a given height and is a more global test of the soot model than the detailed comparisons shown in Section 5. The constants in Tables 4 and 5 were used in conjunction with Equations 33 through 35 to determine the model parameters. It is worth noting that although an ethylene flame was simulated in Section 5 using the optimal ethylene model parameters, the global (fuel-independent) parameters were used for the ethylene flames simulated in this section.

Markstein and de Ris[5] measured the soot absorption cross section per unit height via laser light extinction with wavelength $\lambda = 0.94\mu\text{m}$[5]. It was determined as a function of height above the burner for eight axisymmetric ethylene and propylene flames burning on a 6mm ID fuel tube with a coflowing air stream. Note that the flames simulated in Section 5 were burning on an 11mm ID fuel tube. Table 6 gives the relevant thermochemical properties of ethylene and propylene, and Table 7 gives the experimental configurations of the eight flames included in the Markstein and de Ris data set[5]. In this table, V_a is the air coflow velocity in mm/s, V_F is the fuel velocity in mm/s, and Q_F is the fuel flowrate in cm^3/s. The corresponding heat release rate is listed in the rightmost column.

Table 6. Smoke point and enthalpy of formation for ethylene and propylene.

Fuel Name	Formula	h°	ℓ_s	$\dot{Q}_{sp}$
		kJ/kg	m	W
Ethylene	C_2H_4	1875.0	0.106	212
Propylene	C_3H_6	476.2	0.029	69

Table 7. Axisymmetric ethylene and propylene flames from Markstein and de Ris[5].

Fuel	V_a	V_F	Q_F	HRR
	mm/s	mm/s	cm^3/s	W
Ethylene	50	21.5	2.43	134
Ethylene	50	32.3	3.65	201
Ethylene	50	43.0	4.86	268
Ethylene	50	53.8	6.08	335
Propylene	50	5.1	0.58	46
Propylene	50	7.7	0.87	69
Propylene	50	10.3	1.17	93
Propylene	50	12.9	1.46	117

The significance of the Markstein and de Ris measurements[5], and the reason that they were chosen as a test of the present soot model, is that the experimental soot absorption cross section per unit height profiles exhibit similarity when normalized by $\dot{Q}/\dot{Q}_{sp}$ and plotted as a function of the flame height normalized by the smoke point height. In other words, the measured soot absorption cross section profiles fall on the same curve when plotted after being normalized

in this manner. This is true below values of $H/\ell_f \approx 0.6$ where H is the height above the burner and ℓ_f is the flame height ($\ell_f = \ell_s \dot{Q}/\dot{Q}_{sp}$). Differences at greater values of H/ℓ_f are attributed to the transition from a smoking to a nonsmoking flame.

The value of α_s at a particular height is related to the radial integral of κ_λ, the effective absorption coefficient at wavelength λ:

$$\alpha_s = \int_0^\infty 2\pi r \kappa_\lambda dr \tag{36}$$

$$\kappa_\lambda = \frac{k_e f_v}{\lambda} \tag{37}$$

In Equation 37, k_e is a dimensionless constant between 4 and 10 that depends on the chemical composition of the soot[49], and is presumed to be 4.9 in the present study to be consistent with the Dalzell and Sarofim dispersion relationship[45]. See Appendix H of Lautenberger for details. Equations 36 and 37 were used to express the soot volume fraction predictions of the model in terms of the radially integrated soot absorption cross section to allow for direct comparison with the experimental data[5]. The predicted and measured soot absorption cross section per unit height is shown in Figure 15 for ethylene and Figure 16 for propylene.

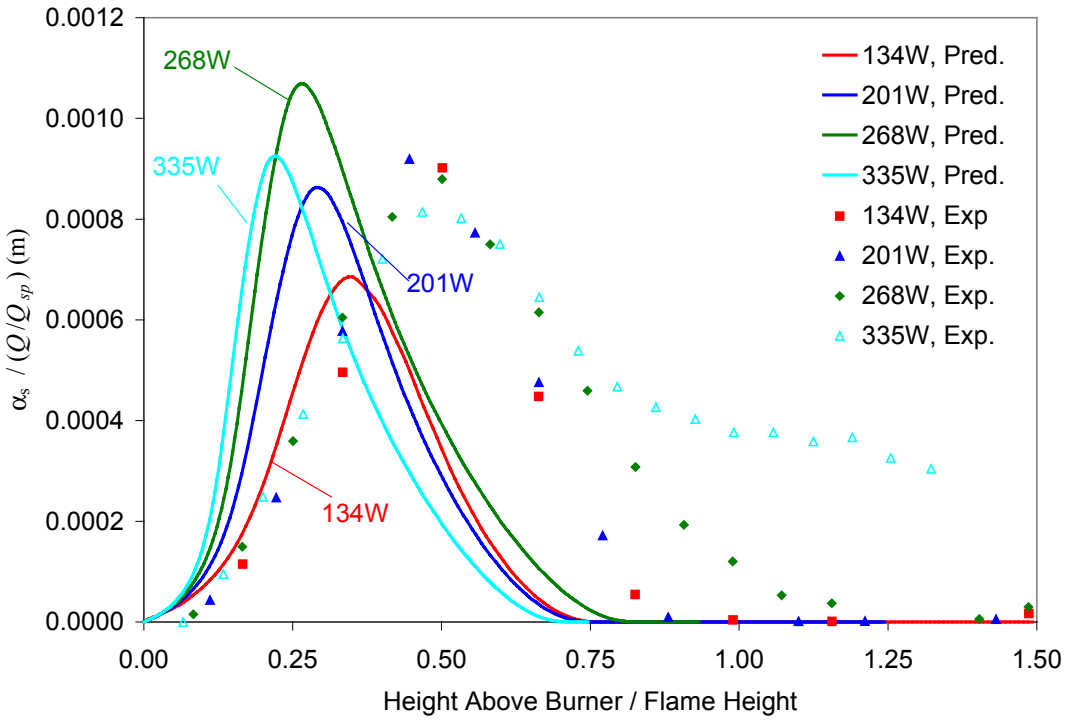

Figure 15. Ethylene absorption cross section per unit height. "Exp." corresponds to experimental data and "Pred." corresponds to the model predictions.

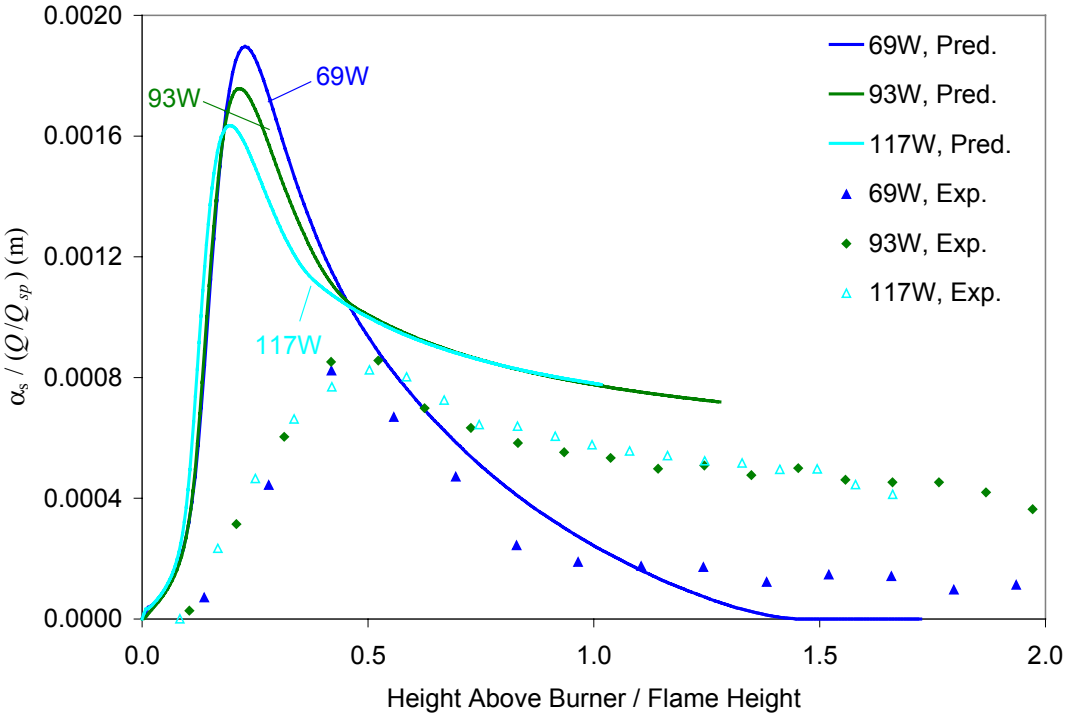

Figure 16. Propylene absorption cross section per unit height. "Exp." corresponds to experimental data and "Pred." corresponds to the model predictions.

It can be seen from the ethylene data shown in Figure 15 that the peak magnitude of the soot absorption cross section is predicted relatively well. However, the predicted profiles peak at much lower values of H/ℓ_f than the experimental profiles. The model predicts all of the soot is burned up in each of the four flames, whereas experimentally only the two smallest flames do not emit smoke. The predicted profiles do not exhibit the same similarity that is observed experimentally[5].

Interestingly, the predicted propylene profiles exhibit a higher degree of similarity than the ethylene profiles. The 93W and 117W flames are predicted to emit smoke, consistent with the experimental data. As was seen with the ethylene profiles, the predicted profiles in the propylene flames peak at much lower values of H/ℓ_f than the experimental profiles. Data for the 46W propylene flame are not shown in Figure 16 because the prediction of this flame was anomalous. A large amount of soot formed immediately at the burner lip presumably due to a boundary condition problem, causing far too much soot to form downstream. This caused the model to predict a strongly smoking flame at 46W, whereas at 69W (which should be sootier than the 46W flame) the model predicted a nonsmoking flame.

The magnitude of the absorption cross section in the propylene flames is overpredicted. This is attributed to a positive feedback mechanism characteristic of the present model wherein the soot inception area A_0 drives the amount of soot formed near the burner due to the surface area-dependent nature of soot formation. The soot formed low in the flame in turn drives the soot formation farther downstream. Recall from Section 6 that the peak soot formation rate in the global model is presumed to be inversely proportional to the fuel's laminar smoke point height ℓ_s raised to a certain power, chosen as 0.6 based on the initial calibration. This exponent was selected to most closely match the peak soot formation rates in laminar methane, propane,

and ethylene diffusion flames[32] that were found to give the best agreement between prediction and experiment. The soot inception area is then estimated from the fuel's enthalpy of formation and its peak surface growth rate (see Section 6).

The overprediction of the soot absorption cross section magnitude in the propylene flames (Figure 16) indicates the peak soot formation rate and soot inception area in the global model may be inversely proportional to ℓ_s raised to an exponent smaller than 0.6. If the peak soot formation rate is proportional to $\ell_s^{-0.5}$ instead of $\ell_s^{-0.6}$, then the peak soot formation rate *and* the initial soot inception area are reduced by approximately 30% since $\left(0.029^{-0.6} - 0.029^{-0.5}\right)/0.029^{-0.6} \approx 0.3$. Due to the positive feedback associated with surface area-dependent soot growth, the peak soot volume fraction would be reduced by considerably more than 30%.

It is apparent from Figures 15 and 16 that the predicted soot cross section profiles peak at much lower values of H/ℓ_f than the experimental profiles. The peak of the soot cross section profiles corresponds to the transition from soot formation to oxidation, which occurs at mixture fraction values close to stoichiometric. Recall from Section 4.2 that the mixture fraction conservation equation contains a source term of equal magnitude but opposite sign to the soot formation/oxidation source term. Therefore, soot formation corresponds to a sink of mixture fraction and "pushes" the mixture fraction closer to its stoichiometric value. In flames where soot formation is overpredicted, the mixture fraction will approach its stoichiometric value more quickly than it should. This causes the transition from soot growth to soot oxidation to occur lower in the flame, explaining why the peak of the soot profile occurs at a lower value of H/ℓ_f than seen experimentally. This highlights the highly coupled nature of the processes being modeled here.

8.0 CONCLUSIONS

This paper details a new mathematical framework intended for engineering calculations of soot formation / oxidation and flame radiation in an arbitrary hydrocarbon fuel. The basic approach, though promising, is still at an intermediate stage of development. The purpose of disseminating this research in its current state is to encourage others to enhance and simplify the model. Although the basic methodology is general and could potentially be integrated within any CFD code, it has already been incorporated within FDS[1,2]. This is a salient point because FDS is a powerful CFD model with publicly available source code and an excellent visualization package[50]. It is therefore possible for future workers to move forward and make progress in this area without starting from scratch.

The draw of the present model is that a set of global (fuel-independent) parameters can be determined, thereby allowing the model to be generalized to multiple fuels. An initial calibration exercise was performed by comparing prediction and experiment in small-scale laminar flames[32] to establish suggested values for these global parameters. Fuel-specific chemistry is handled in a simple way by normalizing the location of the soot growth and oxidation regions in mixture fraction space by the fuel's stoichiometric mixture fraction value. The fuel's peak soot growth rate is related to its laminar smoke point height, an empirical measure of relative sooting propensity. Soot oxidation is treated empirically as a fuel-independent process.

8.1 Explicit Solution of Energy Equation

The FDS code[1,2] was reformulated to explicitly solve an equation for energy conservation in terms of total enthalpy (See Appendix D of Lautenberger[8]) so that the radiatively-induced loss can be tracked locally with each fluid parcel. This allows a control volume's radiative history (*i.e.* nonadiabaticity) to be quantified, which has advantages in turbulent calculations[3,8]. An

alternate expression for the divergence of the velocity field was derived from the continuity equation (see Appendix E of Lautenberger[8]) to retain compatibility with the efficient Poisson pressure solver[1].

Several different state relations were examined for determining the major species concentrations as a function of mixture fraction, including complete combustion ("Schvab-Zeldovich"), the empirical correlation of Sivathanu and Faeth[39], and full chemical equilibrium[40]. The importance of the state relations is that they fix the chemical enthalpy of the combustion products and therefore the adiabatic sensible enthalpy (see Appendix D.1 of Lautenberger[8]). The sensible enthalpy in turn drives the adiabatic flame temperature. Due to their simplicity, the complete combustion state relations (after being numerically smoothed near stoichiometric) were chosen. This was used as a starting point to apply an "enthalpy correction" to modify the adiabatic mixture fraction-temperature relationship based on experimental guidance.

8.2 Enthalpy Correction to Improve Temperature Predictions

An advantage of reformulating the code to explicitly solve the energy equation in terms of total enthalpy is that the adiabatic mixture fraction-temperature relationship can be altered by applying an enthalpy correction in mixture fraction space (see Appendix F of Lautenberger[8]). This was found to be necessary because the adiabatic temperatures calculated using the complete combustion state relations were overpredicted by ~400K on the fuel side, and underpredicted on the oxidant side compared to experimental data in a methane diffusion flame[32]. Since soot formation and oxidation are temperature-dependent processes, a temperature correction was required before the new soot model could be calibrated.

It was possible to match the experimental and predicted temperatures by removing enthalpy from the fuel-rich regions, and adding it to fuel-lean regions. Even when using detailed

experimental measurements of 17 species[32] and fully temperature-dependent specific heats[40], the experimental temperatures could not be satisfactorily matched without applying a correction factor. This is attributed to a number of causes, including finite-rate chemistry, nonequal diffusivities, nonunity Lewis number effects, and the net transport of enthalpy from the fuel side to the oxidant side by intermediate species such as CO, H_2, and radicals. The enthalpy correction developed herein is employed to compensate for these phenomena.

8.3 Treatment of Flame Radiation

Although the focus of this paper is the modeling of soot formation and oxidation in small-scale laminar flames, the desired end result is a practical model for engineering calculations of flame radiation. The soot model is tied to the radiation source term by calculating the local total absorption coefficient as the sum of a soot contribution and a gas-phase contribution. For most fuels, the soot contribution is dominant.

The spectral nature of gas radiation is approximated with the radiation model RADCAL[44]. This code uses the local gas-phase composition and temperature to calculate the gas-phase contribution to the total absorption coefficient, averaged over all radiating wavelengths. This requires the specification of a radiation pathlength to characterize the scale of the problem, which is presumed here to be the mean beam length of the gas volume rather than the actual radiation pathlength. The gas-phase absorption coefficient was found to be relatively insensitive to the specified pathlength for the small flames studied here because it approaches the Planck limit at these small length scales. Although only radiant emission is considered in the present study, a companion publication[3] extends the model to turbulent flames and couples it with Finite Volume Method[9] treatment of the radiative transport equation as implemented in

FDS by McGrattan *et. al.*[1]. This allows for the prediction of radiant emission *and* absorption within the flame envelope as well as the calculation of radiation to external targets.

8.4 New Soot Formation and Oxidation Model

The soot formation or oxidation rate is calculated as the product of an analytic function of mixture fraction and an analytic function of temperature. Standard polynomials were chosen as the functional form of these expressions because polynomials can approximate a wide variety of shapes—Gaussian, exponential (Arrhenius), and linear. The model includes both surface area-dependent and surface area-independent growth mechanisms because there is experimental evidence indicating that different growth mechanisms are dominant in different regions of diffusion flames[24,33]. Furthermore, it was found early in the model development process that agreement between prediction and experiment in axisymmetric candle flames[32] could not be obtained using a single growth mechanism. It was possible to reproduce either the soot wings or the core, but not both. This led to the surmisal that the abundance of H* radicals near the outer wings of the diffusion flame cause the soot to form there by the HACA mechanism[17], subject to surface area control. In the core regions where negligible H* atoms are present, soot generation by the formation PAHs subject largely to gas-phase control becomes significant. Soot oxidation is treated as a surface area-dependent process, although there is evidence that it may in fact be independent of the available soot surface area. See Appendix I of Lautenberger[8] for details.

The computational cost of the present soot model is reduced by solving a conservation equation *only* for the soot mass fraction (which fixes f_v). A separate conservation equation is *not* solved for the soot number density N. Since the mean soot particle diameter (and thus the specific soot surface area) is usually calculated from f_v and N, the soot aerosol cannot be fully

characterized. Therefore, the specific soot surface area A_s (m^2 soot/m^3 mixture) is assumed to be linearly proportional to the soot volume fraction, offset by the initial soot inception area A_0 [14]. The soot inception area is a measure of the smallest soot surface area present in a diffusion flame. It can be determined experimentally from the y-intercept of a plot of A_s vs. f_v. The model predictions were found to be highly sensitive to the value of A_0 because it controls the amount of soot formed near the burner rim, which in turn controls the soot formation farther downstream due to the surface area-dependent nature of the growth process.

An expression for estimating A_0 for an arbitrary hydrocarbon fuel was postulated by noting that a correlation exists between the standard enthalpy of formation h° (on a mass basis) and $\ell_s^{-0.5}$ for nonaromatic fuels, but not for aromatic fuels (see Figure 14). Given h° for a nonaromatic fuel, one can predict ℓ_s. However, aromatic fuels have shorter smoke point heights (*i.e.* they are sootier) than their h° values indicate. One possible explanation for this is that the formation of incipient soot particles in diffusion flames is controlled by the chemical energy available to transform fuel fragments into aromatic soot precursors. The appearance of incipient soot particles should be proportional to the fuel's enthalpy of formation (which drives the formation of aromatic precursors), and its peak rate of surface growth (which controls the rate at which these precursors are transformed into soot). Although interesting from a scientific standpoint, this hypothesis was put to practical use to relate a fuel's soot inception area to its enthalpy of formation and peak surface growth rate.

An initial calibration exercise in small-scale methane, propane, and ethylene laminar flames was used to establish global values for the model constants. A cursory test of the model's applicability to multiple fuels was performed by using the global model parameters to examine

the radially-integrated amount of soot as a function of height above the burner in ethylene and propylene candle flames at several fuel flow rates[5]. This exercise showed that too much soot forms low in the flames, particularly for propylene. This indicates that the peak soot formation rate may not be proportional to $\ell_s^{-0.6}$ as determined in the initial calibration exercise, but rather $1/\ell_s$ raised to a smaller power. As an example, if the peak soot formation rate proportional to $\ell_s^{-0.5}$ instead of $\ell_s^{-0.6}$, then the initial soot inception area *and* the peak soot formation rate are reduced by approximately 30% for propylene. Due to the positive feedback associated with surface area-dependent soot growth, the peak soot loading would be reduced by significantly more than 30%. When using the global model in the ethylene and propylene flames, the radially integrated amount of soot peaks too low in the flame. This may be related to the overprediction of the amount of soot low in the flame since soot formation corresponds to a sink of mixture fraction, causing the transition from soot formation to oxidation to occur too low in the flame. Clearly, more research is required in this area.

8.5 General Mathematical Framework

The software developed as part of this work has been implemented in such a way that the end product is quite flexible and can be adapted to test new theories relatively easily. The model may be as-is, or the user can specify a series of point-value or point-slope pairs to select a different form of the soot formation and oxidation functions. This software is accessible through the standard FDS input file. A polynomial with anywhere between two and six coefficients may be specified. Other options are available, *e.g.* either surface area-dependent or surface area-independent soot formation may be used instead of both. Details are given in Appendix **L** of Lautenberger[8].

8.6 Challenges of Modeling Soot Formation and Oxidation

Modeling soot formation and oxidation in small-scale laminar diffusion flames is an extraordinarily challenging task, particularly due to the interrelated nature of the underlying phenomena. The transport properties (ρD and μ) increase with at least the 2/3 power of temperature. Therefore, diffusion of species and momentum is augmented significantly in regions where the temperature is overpredicted, and diminished where temperatures are underpredicted. If an excessive amount of soot forms low in the flame, more soot will form farther downstream due to the positive feedback mechanism associated with surface area-dependent soot formation. Radiative losses will also be increased, and the rate of oxidation will be decreased in the upper parts of the flame. Due to the fourth power dependency of radiant emission on temperature, small errors in temperature prediction can translate into large errors in radiation. The mixture fraction is coupled to the rate of soot formation to enforce mass conservation. Therefore, an overprediction of the soot loading pushes the mixture fraction towards stoichiometric too quickly, speeding the transition from formation to oxidation and causing the peak amount of soot to occur too low in the flame. These highly coupled (and nonlinear) phenomena exemplify the challenges associated with modeling soot processes and radiation in diffusion flames.

9.0 REFERENCES

1. McGrattan, K.B., Baum, H.R., Rehm, R.G., Hamins, A., Forney, G.P., Floyd, J.E. and Hostikka, S., "Fire Dynamics Simulator (Version 2) – Technical Reference Guide," National Institute of Standards and Technology, NISTIR 6783, 2001.
2. McGrattan, K.B., Forney, G.P, Floyd, J.E., "Fire Dynamics Simulator (Version 2) – User's Guide," National Institute of Standards and Technology, NISTIR 6784, 2001.

3. Lautenberger, C.W. *et. al.*, "Mathematical Framework for Engineering Calculations of Soot Formation and Flame Radiation Using Large Eddy Simulation," (to be submitted for publication, presently Appendix B), 2002.

4. Markstein, G.H., "Relationship Between Smoke Point and Radiant Emission from Buoyant Turbulent and Laminar Diffusion Flames," *Proceedings of the Combustion Institute* **20**: 1055-1061 (1984).

5. Markstein, G.H. and de Ris, J., "Radiant Emission and Absorption by Laminar Ethylene and Propylene Diffusion Flames," *Proceedings of the Combustion Institute* **20**:1637-1646 (1984).

6. Kent, J.H., "Turbulent Diffusion Flame Sooting---Relationship to Smoke-Point Test," *Combustion and Flame* **67**: 223 (1987).

7. Gülder, Ö.L., "Influence of Hydrocarbon Fuel Structural Constitution and Flame Temperature on Soot Formation in Laminar Diffusion Flames," *Combustion and Flame*, **78**: 179-194 (1989).

8. Lautenberger, C.W., "CFD Simulation of Soot Formation and Flame Radiation," MS Thesis, Worcester Polytechnic Institute Department of Fire Protection Engineering, Worcester, MA, 2002.

9. Raithby, G.D. and Chui, E.H., "A Finite-Volume Method for Predicting Radiant Heat Transfer in Enclosures with Participating Media," *Journal of Heat Transfer* **112**:414-423 (1990).

10. Kennedy, I.M., "Models of Soot Formation and Oxidation," *Progress in Energy and Combustion Science* **23**: 95-132 (1997).

11. Cook, A.W. and Riley, J.J., "A Subgrid Model for Equilibrium Chemistry in Turbulent Flows," *Physics of Fluids* **6**:2868-2870 (1994).

12. Kent, J.H., and Honnery, D.R., "A Soot Formation Rate Map for a Laminar Ethylene Diffusion Flame," *Combustion and Flame* **79**: 287-298 (1990).

13. Honnery, D.R., Tappe, M., and Kent, J.H., "Two Parametric Models of Soot Growth Rates in Laminar Ethylene Diffusion Flames," *Combustion Science and Technology* **83**: 305-321 (1992).

14. Kent, J.H. and Honnery, D.R., "Soot Mass Growth in Laminar Diffusion Flames – Parametric Modeling," in *Soot Formation in Combustion Mechanisms and Models*, Edited by H. Bockhorn, pp. 199-220, Springer Verlag, Berlin, 1994.

15. Moss, J.B. and Stewart, C.D., "Flamelet-based Smoke Properties for the Field Modeling of Fires," *Fire Safety Journal* **30**: 229-250 (1998).

16. Lindstedt, P.R., "Simplified Soot Nucleation and Surface Growth Steps for Non-Premixed Flames," in *Soot Formation in Combustion Mechanisms and Models*, Edited by H. Bockhorn, pp. 417-441, Springer-Verlag, Berlin, 1994.

17. Frenklach, M. and Wang, H., "Detailed Modeling of Soot Particle Nucleation and Growth," *Proceedings of the Combustion Institute* **23**: 1559-1566 (1990).

18. Kent, J.H., and Wagner, H. Gg., "Why Do Diffusion Flames Emit Smoke?," *Combustion Science and Technology* **41**: 245-269 (1984).

19. Reilly, P.T.A., Gieray, R.A., Whitten, W.B., and Ramsey, J.M., "Direct Observation of the Evolution of the Soot Carbonization Process in an Acetylene Diffusion Flame via Real-Time Aerosol Mass Spectrometry," *Combustion and Flame* **122**:90-104 (2000).

20. Reilly, P.T.A., Gieray, R.A., Whitten, W.B., and Ramsey, J.M., "Fullerene Evolution in Flame-Generated Soot," *Journal of the American Chemical Society* **122**:11596-11601 (2000).

21. Talbot, L., Cheng, R.K., Schefer, R.W., and Willis, D.R., "Thermophoresis of Particles in a Heated Boundary Layer," *Journal of Fluid Mechanics*, **101**: 737-758 (1980).

22. Sunderland, P.B. and Faeth, G.M., "Soot Formation in Hydrocarbon / Air Laminar Jet Diffusion Flames," *Combustion and Flame* **105**:132-146 (1996).

23. Xu, F. and Faeth, G.M., "Soot Formation in Laminar Acetylene-Air Diffusion Flames at Atmospheric Pressure," *Combustion and Flame* **125**: 804-819 (2001).

24. Zelepouga, S.A., Saveliev, A.V., Kennedy, L.A., and Fridman, A.A., "Relative Effect of Acetylene and PAHs Addition on Soot Formation in Laminar Diffusion Flames of Methane with Oxygen and Oxygen-Enriched Air," *Combustion and Flame* **122**: 76-89 (2000).

25. Axelbaum, R.L., Flower, W.L., and Law, C.K., "Dilution and Temperature Effects of Inert Addition on Soot Formation in Counterflow Diffusion Flames," *Combustion Science and Technology* **61**: 51-73 (1988).

26. Axelbaum, R.L., and Law C.K., "Soot Formation and Inert Addition in Diffusion Flames," *Proceedings of the Combustion Institute* **23**: 1517-1523 (1990).

27. de Ris, J., "A Scientific Approach to Flame Radiation and Material Flammability," *Fire Safety Science –Proceedings of the Second International Symposium,* 29-46 (1989).

28. de Ris, J., Wu, P.K., and Heskestad, G., "Radiation Fire Modeling," *Proceedings of the Combustion Institute* **28:**2751-2759 (2000).

29. Wieschnowsky, U., Bockhorn, H., and Fetting, F., "Some New Observations Concerning the Mass Growth of Soot in Premixed Hydrocarbon-Oxygen Flames," *Proceedings of the Combustion Institute* **22**: 343-352 (1988).

30. Bonczyk, P.A., "In-Situ Optical Measurement of Additive Effects on Particulates in a Sooting Diffusion Flame," *Combustion and Flame* **51**:219-229 (1983).

31. Delichatsios, M.A., "A Phenomenological Model for Smoke-Point and Soot Formation in Laminar Flames," *Combustion Science and Technology* **100**: 283-298 (1994).

32. Smyth, K.C. http://www.bfrl.nist.gov (1999).

33. Hwang, J.Y. and Chung, S.H., "Growth of Soot Particles in Counterflow Diffusion Flames," *Combustion and Flame* **125**: 752-762 (2001).

34. Press, W.H., Teukolksy, S.A., Vetterling, W.T., and Flannery, B.P., *Numerical Recipes in Fortran 77 The Art of Scientific Computing* 2nd Edition, Cambridge University Press, Cambridge, 1992.

35. Neoh, K.G., Howard, J.B., and Sarofim, A.F., "Soot Oxidation in Flames," in *Particulate Carbon Formation During Combustion*, Edited by D.C. Siegla and G.W. Smith, pp 261-277 (1981).

36. Puri, R., Santoro, R.J., and Smyth, K.C., "The Oxidation of Soot and Carbon Monoxide in Hydrocarbon Diffusion Flames," *Combustion and Flame* **97**: 125-144 (1994).

37. Puri, R., Santoro, R.J., and Smyth, K.C., "Erratum - The Oxidation of Soot and Carbon Monoxide in Hydrocarbon Diffusion Flames," *Combustion and Flame* **102**: 226-228 (1995).

38. Young, K.J. and Moss, J.B., "Modeling Sooting Turbulent Jet Flames Using an Extended Flamelet Technique," *Combustion Science and Technology* **105**: 33-53 (1995).

39. Sivathanu, Y.R. and Faeth, G.M., "Generalized State Relationships for Scalar Properties in Nonpremixed Hydrocarbon/Air Flames," *Combustion and Flame* **82**: 211-230 (1990).

40. Gordon, S. and McBride, B.J., "Computer Program for Calculation of Complex Chemical Equilibrium Compositions and Applications," NASA Reference Publication 1311, 1994.

41. Bilger, R.W., "The Structure of Turbulent Nonpremixed Flames," *Proceedings of the Combustion Institute* **22**: 475-488 (1988).

42. Norton, T.S., Smyth, K.C., Miller, J.H., and Smooke, M.D., "Comparison of Experimental and Computed Species Concentration and Temperature Profiles in Laminar Two-Dimensional Methane/Air Diffusion Flames," *Combustion Science and Technology*, **90**: 1-34 (1993).

43. Sivathanu, Y.R. and Gore, J.P., "Coupled Radiation and Soot Kinetics Calculations in Laminar Acetylene/Air Diffusion Flames," *Combustion and Flame* **97**: 161-172 (1994).

44. Grosshandler, W.L., "RADCAL: A Narrow-Band Model for Radiation Calculations in a Combustion Environment," National Institute of Standards and Technology, NIST Technical Note 1402, 1993.

45. Dalzell, W.H. and Sarofim, A.L., *Journal of Heat Transfer* **91**:100 (1969).

46. Strehlow, R.A., *Combustion Fundamentals*, McGraw-Hill Book Company, New York, 1984.

47. Bird, R.B., Stewart, W.E., and Lightfoot, E.N., *Transport Phenomena*, John Wiley & Sons, New York, 1960.

48. Lantz, R.V., "Model Validation in Fire Protection Engineering," Ph.D. Thesis, Worcester Polytechnic Institute Department of Fire Protection Engineering, Worcester, MA 2001.

49. de Ris, J., "Fire Radiation – A Review," *Proceedings of the Combustion Institute* **17***:* 1003-1016 (1979).

50. Forney, G.P and McGrattan, K.B., "User's Guide for Smokeview Version 2.0 – A Tool for Visualizing Fire Dynamics Simulation Data," National Institute of Standards and Technology, NISTIR 6761, 2001.

APPENDIX B MATHEMATICAL FRAMEWORK FOR ENGINEERING CALCULATIONS OF SOOT FORMATION AND FLAME RADIATION USING LARGE EDDY SIMULATION

1.0 INTRODUCTION

In recent years, there has been a worldwide movement away from prescriptive building codes and toward performance-based codes. In a performance regulatory structure, the fire protection package is designed to deliver a known level of safety rather than simply fulfilling a series of prescriptive code requirements. The promise of performance-based design is that fire safety can be achieved more efficiently by establishing a desired level of safety and then performing an engineering analysis to predict whether or not certain candidate designs would deliver the necessary level of safety.

The crux of performance-based design involves the use of probabilistic and deterministic computational tools to predict whether building occupants not intimately involved with ignition would be able to safely evacuate before space through which they must egress becomes untenable due to hostile fire. The engineer may choose any computational tools he deems appropriate, ranging from simple hand calculations and empirical correlations to sophisticated computer fire models. Until recently, "fire modeling" in industry has usually been restricted to the use of two-layer zone models because Computational Fluid Dynamics (CFD) analyses ("field modeling") were too expensive and had a much longer turnaround time than zone modeling.

CFD became a more viable tool for fire safety engineering with the release of Fire Dynamics Simulator (FDS) v1.0 in February 2000[1,2] by the National Institute of Standards and Technology (NIST). The FDS code directly calculates the large-scale motion of buoyant turbulent fire flows using Large Eddy Simulation (LES) techniques. FDS is freely distributed by NIST and can be run on an ordinary PC. Calculations can be performed in a reasonable amount

of time, partly due to the ever-increasing speed of computers, but also because the governing equations have been formulated in such a way that efficient Fast Fourier Transforms are used to solve the velocity-pressure coupling *directly*. This eliminates the need for expensive iteration that usually plagues numerical solution of fully elliptic flows such as fire phenomena.

Simulations can be easily set up through a single input file, and the results are visualized with the companion package Smokeview,[3] also freely distributed by NIST. Smokeview extracts data from FDS simulations and generates realistic-looking 3D animations and still-shots that can be easily understood by an Authority Having Jurisdiction. The convenient user interface and excellent flow visualization tools[3] have much to do with the popularity of FDS among fire protection engineers. In fact, FDS has gained widespread acceptance in the United States and has become the most widely used CFD tool in fire protection engineering in this country.

NIST has made several enhancements to FDS v1.0, and v2.0 was released in December 2001[4,5,6]. New features include a better treatment of combustion and radiative transfer. Due to the inherently complicated nature of "fire", FDS will undoubtedly continue to grow and evolve as existing components are improved and new phenomena are added to the model. The present paper reports progress that has been made toward enhancing the ability of the FDS code to calculate flame radiation from fires at hazardous scales. Specifically, the essential mathematics required to extend a model of soot formation and oxidation in laminar flames[7] to turbulent flames are developed.

As will be discussed below, the processes of soot formation and oxidation are crucial for the calculation of radiation from diffusion flames, which is dominated by emission from incandescent soot particles. Although this is the primary motivation for this research, soot formation and oxidation in diffusion flames also have other practical relevance to fire safety

engineering and fire research. The emission of particulate "smoke" from a diffusion flame is controlled by the balance between soot formation in the lower parts of the flame and oxidation of this soot the upper parts of the flame. Smoke that escapes from the flame envelope can obscure an occupant's visibility and cause irritation.

1.1 Challenges of Calculating Radiation from Diffusion Flames

The modern understanding of diffusion flames began with Burke-Schumann[8] who showed how the flame shapes are determined by diffusion of fuel and oxidant toward the common flame sheet lying between the sources of fuel and oxidant. Zeldovich[9] extended this understanding to include the heat release and local temperature in the flow field. Spalding[10] and Emmons[11] applied the understanding to the vaporization and combustion of liquid fuels in the absence of significant radiant heat transfer.

During the 1960's and 1970's, Spalding[12,13], Magnussen[14], and many others developed semi-empirical $k \sim \varepsilon$ models for turbulent flow and combustion. These models have been successfully applied to furnace combustion, where flows are generally driven by forced convection. They have been less successfully applied to fires, which are usually driven by buoyant convection.

Particularly challenging is the numerical computation of radiation from diffusion flames, which is of central importance to fire research and engineering. Radiation is the dominant mode of heat transfer in fires having characteristic fuel lengths greater than 0.2m[15]. Radiant heat feedback to a burning solid or liquid fuel controls the overall heat release rate[15,16,17]. Under most circumstances, forward heating by radiation governs the rate of flame spread and fire growth. Radiant heat transfer can trigger the ignition fuel packages remote from the initial fire.

Engineering calculations of flame radiation have traditionally been performed by assuming that a constant fraction of the energy released during combustion is radiated away as the global "radiant fraction" or "radiative fraction". In turbulent flames, the radiative fraction of a particular fuel is roughly constant for fire diameters D between 0.4m and 4.0m. However, the global radiative fraction tends to decrease with increasing scale due to a reabsorption of radiation inside the flame envelope and by the "soot mantle". Experimental data indicate the radiative fraction decreases proportional to $D^{-0.5}$ for heptane and $D^{-0.6}$ for kerosene[17] for fire diameters greater than several meters.

It is an extremely challenging task to calculate radiation from diffusion flames by modeling the actual phenomena that produce the radiation rather than invoking a simplifying assumption such as the constant radiant fraction. Sophisticated models are available to calculate flame radiation[4,18]. However, the canonical problem is that the "correct" amount of soot and its distribution within the flame envelope, which are generally unknown, must be specified. The reason for this is that continuum (spectrally gray) radiation from incandescent soot particles is the dominant source of radiation for most fuels[15].

In addition to this gray contribution from soot, flame radiation also has a non-gray component attributed to gaseous combustion products. A comprehensive numerical computation of flame radiation must therefore include components for the calculation of (1) the composition of the gas-phase, and (2) the evolution of soot particles throughout the flame. Gas-phase chemical reactions in buoyant flames are much faster than the characteristic fluid mechanical time-scales and can be approximated in a straightforward manner from the local stoichiometry, *i.e.* from complete combustion reactions in the fast chemistry limit. Unfortunately, soot concentrations in diffusion flames cannot be directly related to stoichiometry because soot

formation and oxidation reactions occur on timescales of similar magnitude to the fluid mechanics. Rather, an expression must be used to account for the kinetically limited nature of soot generation and destruction[19].

Further complicating the problem is the highly coupled nature of soot formation, flame radiation, and the underlying fluid mechanics. Small errors in the temperature prediction can translate to large errors in radiant emission due to their fourth power relation. Local temperatures are lowered as radiation extracts sensible enthalpy from the gas-phase, thereby altering the soot formation / oxidation rates and increasing the gas density. Therefore, a fully coupled solution where the radiation heat loss is tracked locally with the fluid is necessary[20].

For these reasons, it is a considerable undertaking simply to quantify the magnitude of radiant emission from hydrocarbon diffusion flames. The optically thin limit is a commonly used approximation where radiant emission is explicitly considered but radiant absorption is considered to be negligible[21]. This is a reasonable simplification for very small flames having short characteristic pathlengths, but as mentioned above the net reabsorption of radiation increases with increasing scale[17]. It becomes important for flame heat transfer to objects inside the flame envelope as well as the shielding of external objects by the cold soot mantle characteristic of large-scale fires. In fires where this re-absorption phenomenon is important, it is necessary to calculate not only the quantity of radiation that is *emitted*, but also its directional distribution and potential re-absorption by combustion gases and soot.

This requires the solution of a Radiative Transport Equation (RTE) in addition to the underlying fluid mechanical equations, considerably increasing the complexity and computational cost over optically thin simulations. In principle, absorption depends on the spectral distribution of the incoming radiation as determined for a particular pathlength[15]. For

engineering purposes, a *single* characteristic pathlength (*e.g.* mean beam length) is chosen for the whole problem when evaluating the absorption coefficient. However, the characteristic mean beam length must be chosen for each problem of interest. This simplification significantly reduces the computational expense and allows one to treat the effects of absorption with only a modest increase in computational time. Furthermore, this provides a means to calculate the radiant flux to both internal and external targets.

The result is a powerful computational tool with many practical applications. The work reported in this paper has been motivated by the desire to develop such a tool for use in fire research and engineering. The focus of the present paper is the development of the mathematics required to model soot formation and oxidation in turbulent flames.

1.2 Soot Modeling in Turbulent Flames

As described previously, an acceptable representation of the evolution of soot throughout the flame is necessary to calculate radiation from diffusion flames without resorting to the use of a constant radiative fraction. Due to the "slow" nature of soot formation and oxidation, an accurate description of the evolution of soot in diffusion flames can be obtained only with a model that explicitly accounts for the finite rate of soot formation and oxidation.

Soot modeling is an active research area in the combustion community and Kennedy has provided an excellent review of the pre-1997 literature[19]. Much of this research involves small-scale laminar flames where it is possible to use a very fine computational mesh. Soot formation and oxidation reactions occur at length scales smaller than 1mm. A mesh spacing of this size is easily attainable on today's computers when simulating small flames. However, the finest grid spacing possible for typical calculations of larger turbulent flames is at least an order of magnitude greater. Therefore, the processes of soot formation and oxidation cannot be directly

resolved, and a statistical technique such as a probability density function (PDF) must be implemented for closure of the chemical source term.

Several detailed models for soot formation and oxidation already exist and have been applied to turbulent *jet* diffusion flames, generally with good results[22,23]. These models usually implemented within Reynolds Averaged Navier-Stokes (RANS) codes that decompose the governing equations into time-averaged and fluctuating components. RANS codes typically use a turbulence model (*e.g.* $k \sim \varepsilon$ or one of its variations) for closure of the time-averaged equations. They embody a significantly different treatment of turbulence than LES codes such as FDS[4,5] where the temporal (transient) nature of the flow is directly calculated. RANS codes generally give "smoother" results than LES codes. PDF techniques required for closure of the chemical source term have been used in RANS codes since the 1980's[24]. However, analogous PDF techniques have been developed for LES codes only recently[25].

For these reasons, most studies of soot modeling in turbulent diffusion flames have used a RANS code with $k \sim \varepsilon$ turbulence. Liu and Wen[26] very recently pointed out ". . . LES codes are not as far advanced as RANS- or FANS-based codes in terms of the coupling with state-of-art combustion, radiation and soot sub-models . . .". One of the few LES studies of soot formation is that of Desjardin and Frankel[27] who simulated a strongly radiating acetylene-air flame using the soot model of Leung *et. al.*[28]. However, they performed two-dimensional calculations of a momentum driven turbulent jet-flame, quite dissimilar from the hazards of interest in fire research and fire safety engineering.

This is a salient point. Few researchers have applied detailed soot models to the simulation of *buoyant* flames, and there is a corresponding dearth of experimental data for model validation in this area. Instead, most computational studies of soot formation and oxidation in

turbulent diffusion flames involve momentum dominated fuel jets having significantly different physics than turbulent *buoyant* diffusion flames typical of unwanted fire.

Little research has explored the use of soot models in field modeling of compartment fires where the characteristic fire size and grid resolution may be of similar magnitudes. Luo and Beck[29] applied the soot model of Tesner *et. al.*[30,31] to the simulation of polyurethane mattresses burning in a multi-room building using a CFD code with $k \sim \varepsilon$ turbulence. As one would expect, they found that the soot formation model strongly affects the calculated radiant heat fluxes. The model was relatively successful at predicting the radiant heat flux history from the hot layer to the floor. However, their focus was temperature and species predictions, making it difficult to draw any conclusions regarding the soot model. Novozhilov[32] accurately summarized the present status soot modeling in compartment fires in a recent review paper: "The detailed models . . . are still at the stage of intensive development and validation. They have not yet been widely applied in practical fire simulations, but may be expected to substitute simplified soot conversion treatment in the near future".

Fortunately, some workers are conducting research to advance the state of the art. Moss and Stewart[33] present a methodology to apply their previously developed soot model[34,35] to the field modeling of fires via the laminar flamelet approach. The model[33] is typical of others in that several fuel-dependent constants must be specified. They are established by a calibration exercise in which the predictions are compared to data from laminar flame experiments and the model's adjustable constants are tweaked until agreement is achieved. To date, there are no general rules for specifying the soot constants for an arbitrary fuel.

The above discussion illustrates some of the hindrances associated with incorporating a model for soot formation and oxidation into the FDS code that would result in a practical tool for

engineering calculations of flame radiation from buoyant turbulent flames. In summary: (1) The fuel-specific model constants appearing in most existing soot models cannot be determined by a set of general rules or equations. Such a model may only be reliably applied to a fuel for which it has been calibrated. (2) Most simulations of soot formation and oxidation in turbulent flames have been performed with RANS codes using a PDF for closure of the chemical source term. The analogous mathematics required for LES (*i.e.* FDS) are relatively new and have not yet been broadly applied to soot formation and oxidation. (3) Most of the previous work in this area has involved momentum-dominated fuel jets with different physics than buoyant flames. There are therefore few "lessons learned" in the literature and little experimental data for comparison of prediction and experiment.

A companion publication[7] addresses item (1). A new framework for modeling soot formation and oxidation in diffusion flames was postulated wherein the peak soot formation rate of an arbitrary hydrocarbon fuel is related to its laminar smoke point height, an empirical measure of relative sooting propensity. The need to specify fuel-dependent constants is eliminated, and the model can be generalized to any fuel. The laminar smoke point height can be thought of as a "material property" or a "flammability property"[36] that characterizes a particular fuel's radiative characteristics and sooting tendency. The smoke point height is analogous to other bench-scale material properties that are used to predict large-scale fire behavior. It has been measured for gaseous, liquid, and solid fuels[36].

The present paper addresses item (2) above. It provides a clear presentation of the mathematics required for implementation of a soot formation model within a LES code such as FDS[4]. It is intended to disseminate some of the mathematical techniques that can be used for modeling soot processes and radiation in turbulent diffusion flames. It is important for the reader

to understand that research reported here is a work in progress. The soot formation and oxidation model that has been developed[7] is still a research tool under development. Although it has been embedded within FDS[4], this coding was done outside of NIST and the model will not necessarily be included in a future version of FDS, nor is it endorsed by NIST.

Future work is planned to enhance and simplify the model and its integration into the FDS code. Nonetheless, the new soot formation and oxidation model has been postulated in general terms[7], and we encourage other researchers to make simplifications, modifications and enhancements. Lautenberger[37] gives recommendations for the possible direction of such future research.

2.0 TURBULENCE, LARGE EDDY SIMULATION, AND FDS

Most buoyant flames of practical interest to the engineer are turbulent in nature. Combustion reactions occur at length scales on the order of a millimeter or less, but turbulent mixing may occur at length scales larger by three orders of magnitude[4]. Simulations in which this range of length scales is directly resolved cannot be performed even on today's most powerful computers. Large Eddy Simulation is a computational technique where the large-scale motion of a buoyant turbulent flow is directly calculated on the grid-scale, and processes occurring below the grid scale, such as chemical reactions, are modeled[25]. NIST Fire Dynamics Simulator[4,5] is a Large Eddy Simulation code because large-scale fluid motions are calculated directly and the effects of small-scale motions are relegated to modeling.

2.1 Filtering the Governing Equations

In LES, the small-scale fluid motions are removed from the governing equations by applying a filter[38]. The resolved component of a filtered variable is usually denoted with an

overbar, *e.g.* $\bar{f}$. It is the local average or mean value of f in a control volume centered at location $\boldsymbol{x}$. For this reason the terminology "mean", "filtered", and "resolved" are often used interchangeably. A resolved quantity at a spatial location $\boldsymbol{x}$ is defined by:

$$\bar{f}(\boldsymbol{x}) = \int_{-\infty}^{+\infty} \overline{G}(\boldsymbol{x}, \boldsymbol{x}') f(\boldsymbol{x}') d\boldsymbol{x}' \tag{1}$$

In Equation 1, $\overline{G}$ is a grid filter function that must satisfy the relation:

$$\int_{-\infty}^{+\infty} \overline{G}(\boldsymbol{x}, \boldsymbol{x}') d\boldsymbol{x}' = 1 \tag{2}$$

Several types of grid filter functions can be used in LES. In some instances, the filter function has been explicitly selected to achieve a certain result. A Fourier cutoff filter is applied in wave space to remove scales above a certain wavenumber, but retain scales below this wavenumber[38]. In other instances, the grid filter function is implicitly coupled to the discretization scheme through which the governing continuous differential equations are reduced to a system of algebraic equations[39]. A "top hat" filter function is implicitly applied when the governing equations are discretized using finite differences[39]. The top-hat filter function is given using Cartesian tensor notation (i is each of the three spatial coordinates) as Equation 3:

$$\overline{G}\left(x_i - x_i^{'}\right) = \begin{cases} 1/\overline{\Delta}_i & \left|x_i - x_i^{'}\right| \le \overline{\Delta}_i/2 \\ 0 & \left|x_i - x_i^{'}\right| > \overline{\Delta}_i/2 \end{cases} \tag{3}$$

FDS is a finite difference code; thus Equation 3 is the form of the grid filter implicitly used in FDS. Here, $\overline{\Delta}_i$ is the filter width in the i direction, equal to the width of a grid cell in that direction. The grid filter width should be greater than the Kolmogorov microscale but smaller than the integral scale of the turbulence. In this way the large-scale irregular motions are

directly calculated on the grid-scale, but the small-scale isotropic motions occurring below the grid scale are modeled.

2.2 Subgrid-Scale Modeling in LES: Hydrodynamics

The unresolved hydrodynamic scales that are removed from the governing equations by filtering affect the resolved hydrodynamic scales by inducing a grid-scale momentum flux. The isotropic small-scale motions appear in the filtered Navier-Stokes equations as subgrid-scale Reynolds stresses τ_{ij}, which (in Cartesian tensor notation) are defined as:

$$\tau_{ij} = \overline{u_i u_j} - \overline{u}_i \overline{u}_j \tag{4}$$

$$\overline{u_i u_j} \neq \overline{u}_i \overline{u}_j \tag{5}$$

The correlation for τ_{ij} given as Equation 4 is unknown and must be modeled to close the filtered system of equations. This is known as subgrid-scale (SGS) modeling in the literature, and has received considerable attention in recent years. Eddy viscosity models are the simplest class of subgrid-scale models. Noting that increased transport and dissipation are the primary effects of the SGS Reynolds Stresses, the influence of unresolved small scales is approximated by introducing an artificial "turbulent eddy viscosity":

$$\tau_{ij} = \frac{1}{3}\tau_{kk}\delta_{ij} - 2\nu_T \overline{S}_{ij} \tag{6}$$

In Equation 6, δ_{ij} is the Kronecker delta (equal to unity when $i = j$, and zero otherwise), ν_T is the turbulent eddy viscosity (an artificial property of the flow, independent of the fluid's intrinsic kinematic viscosity ν), and $\overline{S}_{ij}$ is the grid-scale strain rate tensor:

$$\overline{S}_{ij} = \frac{1}{2}\left(\frac{\partial \overline{u}_i}{\partial x_j} + \frac{\partial \overline{u}_j}{\partial x_i} \right) \tag{7}$$

FDS uses the Smagorinsky eddy viscosity model[40], which is the simplest and most widely used eddy viscosity model. By presuming that the small-scale turbulence is more isotropic than the large-scale structures, Smagorinsky postulated a model to estimate the turbulent eddy viscosity from the straining rate of the resolved field $\overline{S}$:

$$\nu_T = C_{smag}^2 \overline{\Delta}^2 \left|\overline{S}\right| \tag{8}$$

where C_{smag} is the model parameter known as the Smagorinsky constant, reported by Germano[41] to vary between 0.10 to 0.23 depending on the flow conditions. $\overline{\Delta}$ is a length scale defined in Equation 10, and $\left|\overline{S}\right|$ is the magnitude of the grid-scale strain rate tensor $\overline{S}_{ij}$:

$$\left|\overline{S}\right| = \left(2\overline{S}_{ij}\overline{S}_{ij}\right)^{1/2} \tag{9}$$

In a finite difference large eddy simulation such as FDS, the length scale $\overline{\Delta}$ is directly related to the mesh size:

$$\overline{\Delta} = \left(\Delta_1 \Delta_2 \Delta_3\right)^{1/3} \tag{10}$$

2.3 Subgrid-Scale Modeling in LES: Chemistry and Scalar Fluctuations

The Smagorinsky eddy viscosity discussed in Section 2.2 is used to estimate the effect of unresolved subgrid-scale motions on the grid-scale hydrodynamics in FDS. It affects the fluid mechanics. Analogously, in reacting flows such as nonpremixed combustion, unresolved subgrid-scale fluctuations in species concentrations may also affect chemical reactions such as

soot formation and oxidation. These reactions occur at length scales of less than 10^{-3} meters, but typical grid spacing used in fire safety engineering applications is in on the order of 10^{-2} to 10^{0} meters. The chemical reactions cannot be directly resolved in these simulations, but a subgrid model of a slightly different nature than those discussed above can be used approximate the effect of unresolved fluctuations.

The simplest approach to subgrid-scale chemistry in large eddy simulations of turbulent combustion is the use of a probability density function (PDF) to estimate subgrid-scale fluctuations[24]. A probability density function is a statistical tool similar to a histogram that gives the probability that a variable has a value lying in a certain range. The probability that a variable has a value between x and $x + \Delta x$ is equal to the area under its PDF from x to $x + \Delta x$, and the area under the entire PDF must sum to unity. Probability density functions are commonly used in nonpremixed combustion to determine the mean value of a function f that depends only on a conserved scalar such as the mixture fraction[25]. If the probability density function of the mixture fraction is known, the mean value of f can be determined by integration over the PDF:

$$\overline{f}(Z) = \int_0^1 f(Z)P(Z)dZ \tag{11}$$

In general, the value of $\overline{f}$ determined by explicitly considering fluctuations (Equation 11) is not equal to the value of the function f evaluated at mean value of mixture fraction $\overline{Z}$:

$$\overline{f}(Z) \neq f\left(\overline{Z}\right) \tag{12}$$

The above statement has particular relevance to the modeling soot formation and oxidation in diffusion flames because the rates of soot formation and oxidation are strong functions of both mixture fraction and temperature in the soot model developed as part of this work[7,37]. Therefore,

subgrid-scale fluctuations in turbulent flames should significantly impact the grid-scale soot formation and oxidation rates when calculated by integrating over a PDF. In a numerical simulation of a turbulent ethylene diffusion flame, Said *et. al.*[23] reported a 200% difference in the computed soot volume fraction when turbulent fluctuations were not taken into account.

FDS v2.0[4,5] has no subgrid-scale model for scalar fluctuations. However, it was deemed a worthwhile endeavor to investigate the impact of fluctuations on soot formation and oxidation rates in turbulent flames. For this reason, a simple subgrid-scale model to account for the effect of unresolved scalar fluctuations on the soot formation rate has been incorporated. The goal of doing so is to determine the impact of subgrid fluctuations on the soot formation rates calculated in turbulent flames using the present model and examine global trends. Future work is planned to perform an in-depth quantitative comparison of prediction and experiment.

3.0 MODELING SOOT FORMATION AND OXIDATION IN BUOYANT TURBULENT DIFFUSION FLAMES

The processes of soot formation and oxidation are not explicitly modeled in FDS v2.0[4,5] Rather, the soot formation rate in a cell is proportional to the heat release rate in the cell, that is, a constant fraction of fuel is converted to soot during the combustion reactions. The code as presently constituted does not include soot oxidation. This is clearly an oversimplification. It is known from laminar flame studies that soot formation in diffusion flames is proportional to the micro-scale flow times[42]. Also, a significant fraction of the soot generated in a turbulent flame is oxidized within that flame.

It is worth nothing that in typical building fire simulations for which FDS is most often used, the “flames” only occupy a small fraction of the cells in the computational domain. Buoyant smoke transport and bulk fluid flow far from the fire source are generally of greater

interest to the fire safety engineer than "near-field" phenomena associated with the combustion region. As mentioned earlier, grid resolutions in the range of 0.1m to 1.0 m are commonly used in these simulations. Except in the case of very large fires where many mesh cells span the fire, this grid resolution does not provide sufficient fidelity to explicitly calculate soot formation and oxidation rates with the model postulated in this work. The use of a constant "soot yield" is a necessary and reasonable approximation in this type of simulation.

However, if the goal of a simulation is to resolve the evolution of soot throughout the flame envelope and calculate the resulting radiation distribution, a finer mesh is required and the use of a constant soot yield does not capture the essential phenomena. A separate soot conservation equation that includes a source term to account for the finite rate of soot formation and oxidation must be solved.

3.1 Adding a Soot Model to FDS

The FDS code has been modified to explicitly solve the following form of the conservation equation for the soot mass fraction in turbulent calculations:

$$\frac{\partial\left(\overline{\rho_2 Y_s}\right)}{\partial t} + \bar{\boldsymbol{u}}\cdot\nabla\overline{\rho_2 Y_s} + \overline{\rho_2 Y_s}\nabla\cdot\bar{\boldsymbol{u}} = \nabla\cdot\overline{(\rho D)_t}\nabla\overline{Y_s} + \overline{\dot{\omega}_s'''} \tag{13}$$

$$\overline{(\rho D)_t} = \frac{\mu_t}{\mathrm{Sc}_t} \tag{14}$$

In Equation 14, μ_t is the turbulent eddy viscosity calculated from the Smagorinsky[40] model as implemented in FDS v2.0[4,5], and Sc_t is the turbulent Schmidt number. Although the molecular diffusivity of soot particles is negligible, Equation 13 contains the diffusive term $\nabla\cdot\overline{(\rho D)_t}\nabla\overline{Y_s}$ because "diffusion" in turbulent flows is primarily due to turbulent mixing rather than molecular interactions. While thermophoresis (the movement of soot caused by

temperature gradients) is quantitatively important in laminar flames, its importance in turbulent flames is unclear and thermophoresis has therefore been omitted from Equation 13. The source term $\overline{\dot{\omega}_s'''}$ in Equation 13 is the filtered rate of soot formation or oxidation. It is computed using the soot model postulated by Lautenberger *et. al.*[7] by assuming that the same growth mechanisms in laminar flames also apply to turbulent flames:

$$\dot{\omega}_s''' = A_s\left(\dot{\omega}_{sf}'' + \dot{\omega}_{so}''\right) + \dot{\omega}_{sf}''' \tag{15}$$

In Equation 15, $\dot{\omega}_{sf}''$ and $\dot{\omega}_{so}''$ are soot surface growth and oxidation rates. They describe the rate at which soot mass is added to or removed from the existing soot aerosol surface and have units $\mathrm{kg\,soot}/\left(\mathrm{m^2\ soot}\cdot\mathrm{s}\right)$. $\dot{\omega}_{sf}'''$ is a soot formation rate that is independent of the available aerosol surface area and has units $\mathrm{kg\,soot}/\left(\mathrm{m^3\ mixture}\cdot\mathrm{s}\right)$. It represents soot mass growth by gas-phase reactions that are independent of the available soot aerosol surface area. The soot surface area per unit volume of mixture A_s $(\mathrm{m^2\,soot}/\mathrm{m^3\,mixture})$ is presumed to be linearly proportional to the soot volume fraction f_v offset by an initial "inception area" A_0 as observed experimentally by Honnery *et. al.*[48]. This linear relationship between soot volume fraction and surface area presumes that the soot aerosol consists of spherical constant-diameter particles:

$$A_s = A_0 + \beta f_v \tag{16}$$

In Equation 16, A_0 is a fuel-dependent constant. A method for approximating A_0 is given elsewhere[7]. Based on the measurements of Honnery *et. al.*[48] and preliminary simulations in laminar flames, β is held invariant at $8.0\times10^7\ \mathrm{m^2\,soot}/\mathrm{m^3\,mixture}$. The soot formation and oxidation rates in Equation 15 are calculated as the product of an explicit polynomial function of mixture fraction and an explicit polynomial function of temperature[7]. In this way only the local

values of mixture fraction and temperature are needed to determine the local soot formation or oxidation rate:

$$\dot{\omega}''_{sf} = f''_{Zsf}(Z) f^{PUA}_{Tsf}(T) \tag{17}$$

$$\dot{\omega}''_{so} = f''_{Zso}(Z) f^{PUA}_{Tso}(T) \tag{18}$$

$$\dot{\omega}'''_{sf} = f'''_{Zsf}(Z) f^{PUV}_{Tsf}(T) \tag{19}$$

In Equations 17 through 19, a subscript Z denotes a function of mixture fraction, and a subscript T denotes a function of temperature. A subscript *sf* denotes soot formation, and a subscript *so* denotes soot oxidation. Note that a function with a superscript double prime ($''$) has units of $\mathrm{kg\,soot}/\left(\mathrm{m^2\,soot}\cdot\mathrm{s}\right)$, but a function with a superscript PUA (per unit area) is the dimensionless multiplier associated with that function. Similarly, a function with a superscript triple prime ($'''$) has units of $\mathrm{kg\,soot}/\left(\mathrm{m^3\,mixture}\cdot\mathrm{s}\right)$, but a function with a superscript PUV (per unit volume) is the dimensionless multiplier associated with that function. Sample shapes of these functions are shown in Figure 1, and details describing how the functions are determined for an arbitrary fuel are given in a companion publication[7]. Note the units on the ordinate of each panel in Figure 1.

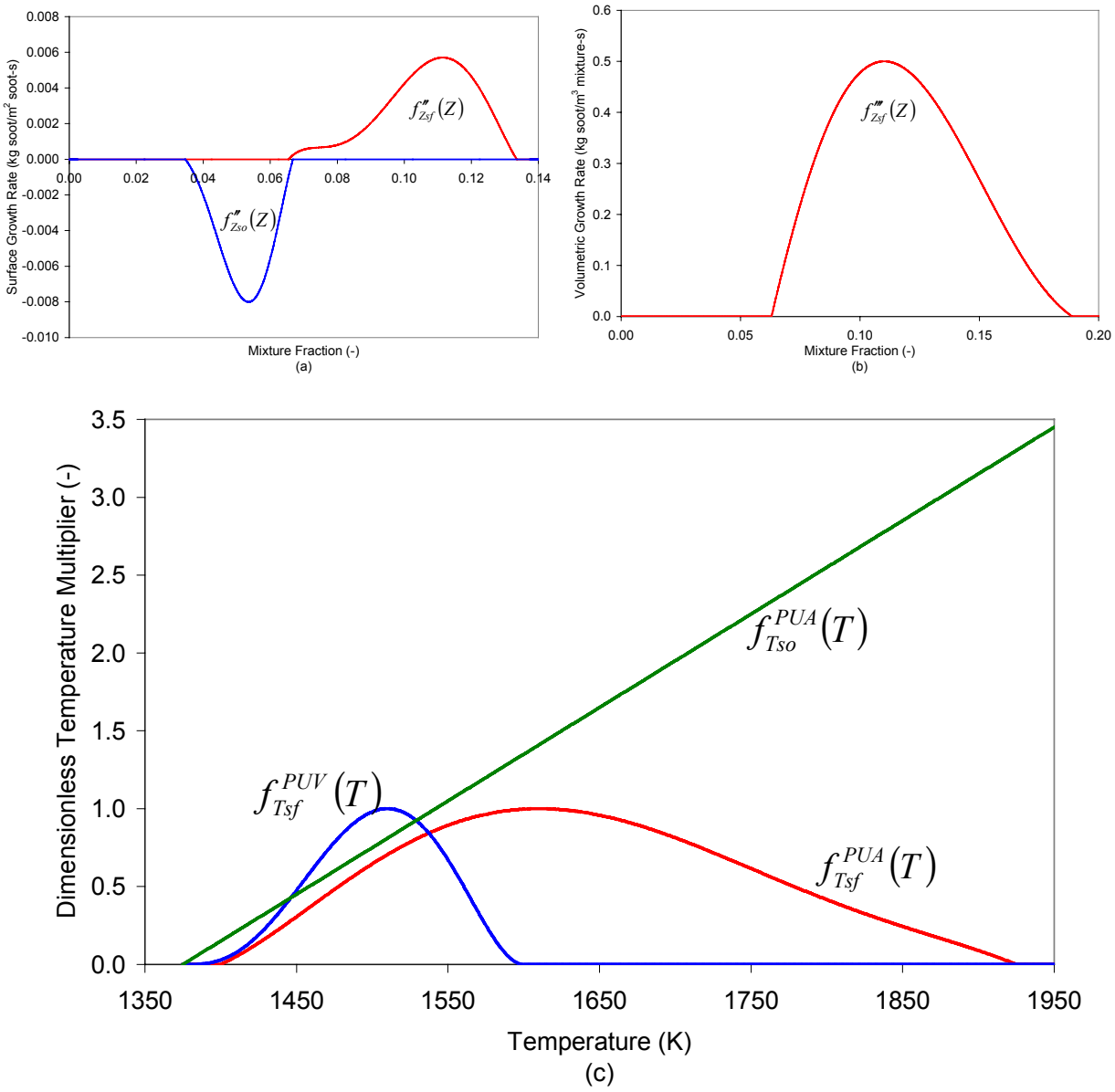

Figure 1. Sample shapes of soot formation and oxidation polynomials in Equations 17 through 19: (a) Surface growth rate mixture fraction function; (b) Volumetric growth rate mixture fraction function; (c) Dimensionless temperature multipliers.

The soot model summarized in Equations 15 through 19 was calibrated against calculations of small-scale laminar flames where a grid resolution close to 0.25mm was employed[7]. This provided sufficient spatial fidelity to resolve the soot formation and oxidation zones for the purposes of model calibration. However, the best numerical resolution that can be afforded in turbulent calculations is at least one order of magnitude coarser. All relevant length

scales cannot be directly resolved. Unresolved subgrid-scale fluctuations in both mixture fraction and temperature exist. Analogous to the discussion of Section 2.3, the filtered rate of soot formation/oxidation calculated if fluctuations are explicitly considered is not necessarily equal to that calculated from mean properties:

$$\overline{\dot{\omega}_s'''}(Z,T) \neq \dot{\omega}_s'''\left(\overline{Z},\overline{T}\right) \tag{20}$$

Unfortunately, integration over the mixture fraction PDF (Equation 11) cannot be directly used to evaluate the filtered soot formation rate because significant subgrid-scale fluctuations in temperature also exist:

$$\overline{\dot{\omega}_s'''} \neq \int_0^1 \dot{\omega}_s'''(Z,\overline{T})P(Z)dZ \tag{21}$$

However, this difficulty was overcome by reformulating the FDS model[4,5] to explicitly solve a conservation equation for total (chemical plus sensible) enthalpy h_T. Details can be found elsewhere[7,37]. The local nonadiabaticity χ in a particular cell can be determined from the local value of total enthalpy. The advantage of this formulation is that *the temperature is a unique function of mixture fraction at a constant value of* χ:

$$\chi = 1 - \frac{\overline{h_T}}{h_{T,ad}\left(\overline{Z}\right)} \tag{22}$$

$$T = T(Z)\big|_{\chi} \tag{23}$$

In Equation 22, $\overline{h_T}$ is the mean value of total enthalpy as calculated from its conservation equation, and $h_{T,ad}\left(\overline{Z}\right)$ is the adiabatic sensible enthalpy, which is known as a function of the mean mixture fraction. The nonadiabaticity varies from zero in cells where no enthalpy has been lost as radiation to unity in cells where all sensible enthalpy has been lost as radiation, although

the latter can only be reached as $t \to \infty$. The relationship between Z and T for ethylene is shown in Figure 2 at several values of χ. This plot was generated after applying the "enthalpy correction" discussed in a companion publication[7] and Appendix F of Lautenberger[37].

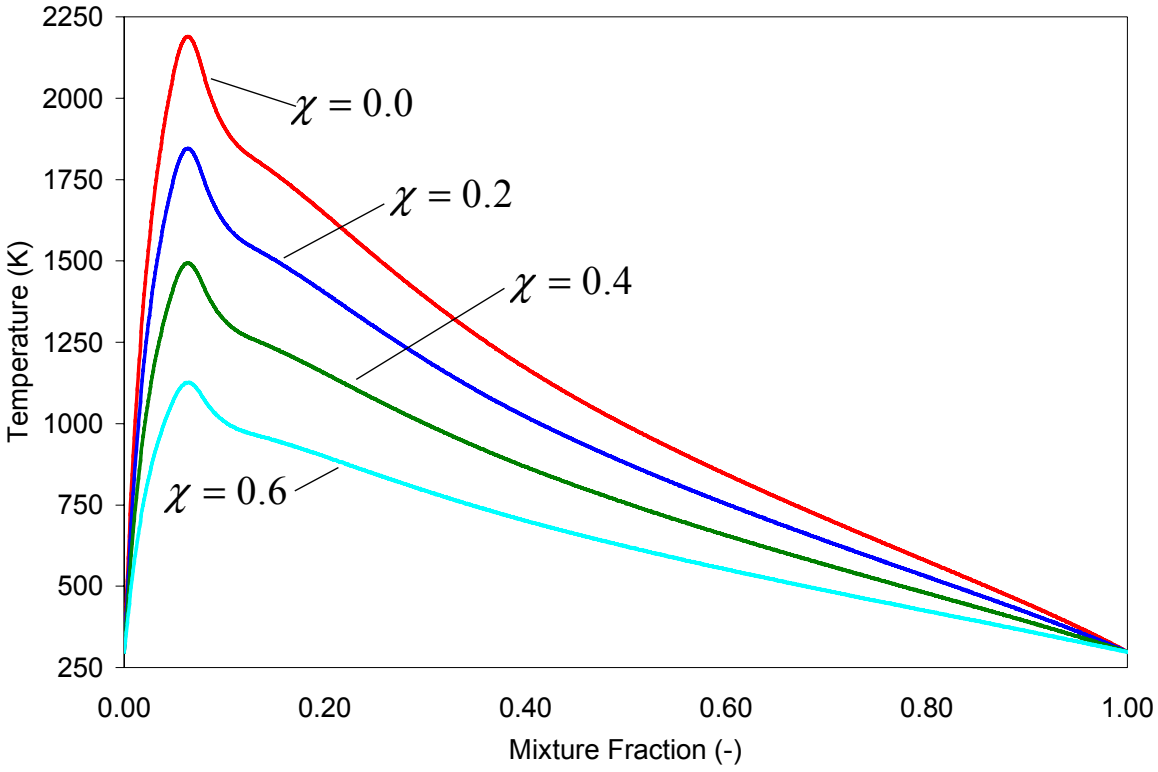

Figure 2. Relation between mixture fraction and temperature at several values of χ.

By making the assumption that the entire gas mixture in a particular cell control volume has the same degree of nonadiabaticity χ, the temperature fluctuation in that control volume is known in terms of mixture fraction. A similar formulation has been dubbed a "radiatively perturbed laminar flamelet" approach by Young and Moss[21]. Once the local nonadiabaticity and the probability density function $P(Z)$ have been determined, the filtered soot formation rate can be calculated by evaluating three integrals of the form:

$$\overline{f}(Z) = \int_0^1 f_1(Z) f_2\left(T(Z)\big|_\chi\right) P(Z) dZ \tag{24}$$

where $f_1(Z)$ and $f_2(T)$ are the soot formation and oxidation polynomials in Equations 17 through 19. The method used to determine $P(Z)$ is given in the next section.

3.2 Approximating Subgrid-Scale Fluctuations of a Passive Scalar using an Assumed Beta Distribution

In numerical computations of turbulent reacting flows, the subgrid-scale PDF of a scalar quantity is usually assigned a predetermined form, such as the clipped Gaussian or beta distribution. Cook and Riley[25] proposed the use of an assumed beta distribution to represent the PDF of a passive scalar:

$$P(Z) = \frac{Z^{a-1}(1-Z)^{b-1}}{B(a,b)} \tag{25}$$

The constants *a* and *b* are uniquely determined from the mean value of the mixture fraction $\overline{Z}$ and its first moment, the subgrid-scale variance $\overline{Z''^2}$ [25] which can be construed as a measure of the level of subgrid-scale fluctuations:

$$a = \overline{Z}\left(\frac{\overline{Z}(1-\overline{Z})}{\overline{Z''^2}} - 1\right) \tag{26}$$

$$b = (a/\overline{Z}) - a \tag{27}$$

In Equation 25, $B(a,b)$ is the beta function, defined as:

$$B(a,b) = \int_0^1 f^{a-1}(1-f)^{b-1} df \tag{28}$$

The beta function can be expressed in terms of several gamma functions:

$$B(a,b) = \frac{\Gamma(a)\Gamma(b)}{\Gamma(a+b)} \tag{29}$$

The gamma function is related to the factorial as:

$$\Gamma(a) = (a-1)! \tag{30}$$

Sample shapes of an assumed beta distribution for three different combinations of $\overline{Z}$ and $\overline{Z''^2}$ are shown in Figure 3. As mentioned above, the probability that Z has a value between Z and $Z + \Delta Z$ is equal to the area under the curve from Z and $Z + \Delta Z$. Therefore the total area under each curve is unity.

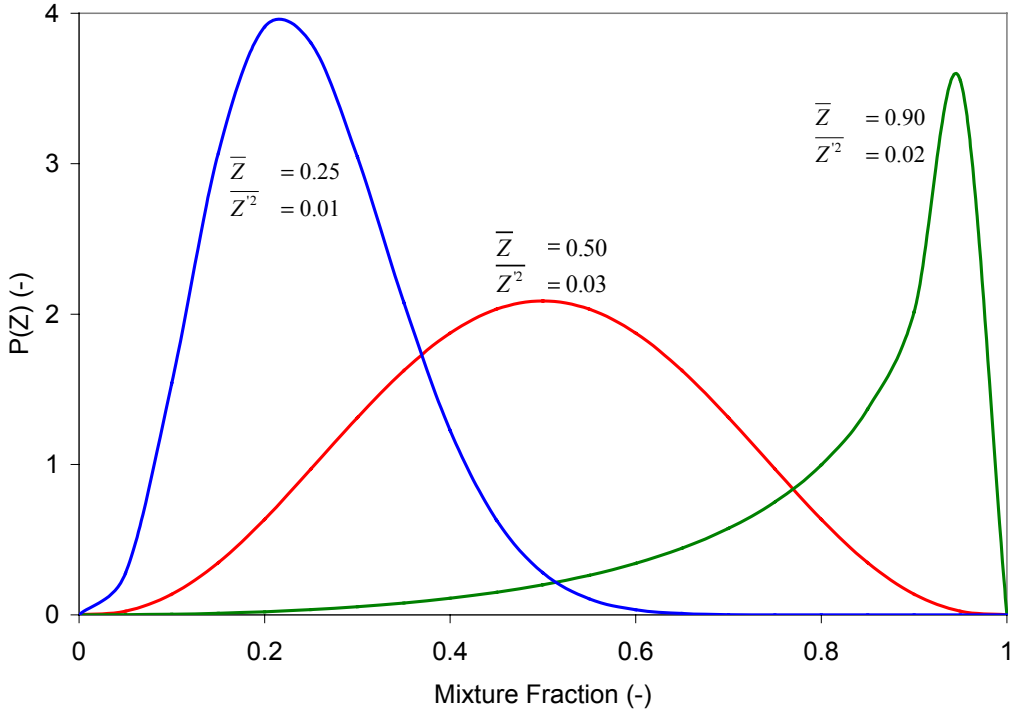

Figure 3. Sample shapes of the beta distribution.

Surprisingly, this simple two-parameter system is capable of giving an excellent approximation to the subgrid-scale PDF if the variance can be accurately determined[44]. Whereas the mean mixture fraction $\overline{Z}$ is directly calculated in a large eddy simulation, its variance $\overline{Z''^2}$ is not explicitly known, but can be predicted using one of the methods that have been proposed in the literature in recent years.

Wall *et. al.*[44] evaluated two such methods for predicting the mixture fraction variance: a scale similarity model[25] and a dynamic model[41,45,46]. They examined Direct Numerical Simulation (DNS) data from simulation of a nonpremixed reacting jet in spherical coordinates. They found that the dynamic model gave a better prediction of the subgrid-scale mixture fraction variance than the scale similarity model for that particular case. However, the dynamic model is much more difficult to implement and is more computationally expensive than the scale similarity model. For this reason, the scale similarity model has been chosen for this work.

3.3 Using Scale Similarity to Determine the Mixture Fraction Variance

The principle of scale similarity is based on the notion that the small-scale statistics of a scalar quantity in a turbulent flow can be inferred from the statistics of the smallest resolved structures. Noting the fractal nature of turbulence, subgrid-scale turbulent structures are approximated by assuming that the unresolved scales are similar to the smallest resolved scales[38], hence *scale similarity*. This method involves filtering the resolved mixture fraction field with a second "test" filter $\overline{\overline{\Delta}}$ that is used to gather information about the fluctuation in mixture fraction on the smallest *resolved* scales.

The test filter length $\overline{\overline{\Delta}}$ is greater than the grid-scale filter length $\overline{\Delta}$, *i.e.* $\overline{\overline{\Delta}} > \overline{\Delta}$. Although the ratio $\overline{\overline{\Delta}}/\overline{\Delta}$ could be treated as a user-specified model parameter, most workers have used $\overline{\overline{\Delta}} = 2\overline{\Delta}$ without investigating the sensitivity of the predictions to this choice. One exception is Cook and Riley[25] who used $\overline{\overline{\Delta}} = 1.8\overline{\Delta}$ and state ". . . this filter width has been optimized only for this particular case and may not hold, in general". In this work, a test filter of width of $\overline{\overline{\Delta}} = 2\overline{\Delta}$ is used, although there is no rigorous justification for this choice.

Denoting a scalar quantity filtered on the test level with two overbars, the scale similarity hypothesis can be used to estimate the subgrid-scale variance in mixture fraction as[25]:

$$\overline{Z'^2} \equiv \overline{\left(Z - \overline{Z}\right)^2} = \overline{Z^2} - \overline{Z}^2 \approx C_{scale}\left[\overline{\overline{Z}^2} - \overline{\overline{Z}}^2\right] \tag{31}$$

The notation $\overline{\overline{Z}^2}$ implies the mean value of mixture fraction is squared and then the resulting field is test filtered, whereas $\overline{\overline{Z}}^2$, implies the mean value of mixture fraction is first test filtered, and then the resulting field is squared. In Equation 31, C_{scale} is a dimensionless constant of order unity. It is different from a similar parameter C that used in the scale similarity turbulence models to relate the subgrid-scale Reynolds stresses to the resolved scales. It is also different from the Smagorinsky constant C_{smag}. Jiménez *et. al.*[47] use spectral reasoning to arrive at the following expression for C_{scale}:

$$C_{scale} = \left(2^{\beta-1} - 1\right)^{-1/2} \tag{32}$$

where β is the spectral slope, equal to 5/3 in the Kolmogorov cascade. Equation 32 can be used to argue that $C_{scale} \approx 1.3$, and this value has been selected for this work in lieu of additional information.

Assuming the test filter length is twice that of the grid filter, the test-filtered value of mixture fraction can be calculated by evaluating the integral[39]:

$$\overline{\overline{Z}} = \frac{1}{2\overline{\Delta}}\int_{-\overline{\Delta}}^{\overline{\Delta}} \overline{Z}\left(x'\right)dx' \tag{33}$$

On a Cartesian finite difference grid with scalar quantities defined at cell centers, the trapezoid rule can be used to numerically approximate Equation 33 from a three-point computational molecule:

$$\overline{\overline{Z}}_i \approx \frac{1}{4}\left(\overline{Z}_{i-1} + 2\overline{Z}_i + \overline{Z}_{i+1}\right) = \frac{1}{2}\overline{Z}_i + \frac{1}{4}\left(\overline{Z}_{i-1} + \overline{Z}_{i+1}\right) \tag{34}$$

In Equation 34 the subscript i refers to cell i, not to be confused with Cartesian tensor notation. Extension of Equation 34 to more than one dimension is discussed in Section 5.

4.0 MODELING RADIATION FROM BUOYANT TURBULENT DIFFUSION FLAMES

Up to this point, the focus of this paper has been the modeling of soot formation and oxidation in diffusion flames. However the primary motivation for doing so is the calculation of flame radiation. In this work, the FDS v2.0[4,5] Radiant Transport Equation (RTE) solver was used, with modifications being made only to the procedure through which the source terms are determined. The generalized RTE for a non-scattering gas is given as Equation 35:

$$\boldsymbol{s}\cdot\nabla I_\lambda(\boldsymbol{x},\boldsymbol{s}) = \kappa(\boldsymbol{x},\lambda)\left[I_b(\boldsymbol{x}) - I(\boldsymbol{x},\boldsymbol{s})\right] \tag{35}$$

In Equation 35 $\boldsymbol{s}$ is the unit normal direction vector, $\boldsymbol{x}$ is a spatial position, I_λ is the radiation intensity at wavelength λ, κ is the emission/absorption coefficient, and I_b is the blackbody intensity, $I_b = \sigma T^4/\pi$. Equation 35 is solved using the Finite Volume Method (FVM)[18] which is so-named because it treats radiation with techniques similar to those used for the convective terms in finite volume calculations of fluid flow. The reader is referred to Sections 4 and 7.6 of the FDS v2.0 Technical Reference Guide[4] for details. The modifications that have been made to the treatment of the source terms are discussed here in Section 4.

4.1 Calculation of Mean Absorption Coefficient

Of crucial importance in numerical calculations of flame radiation is the emission/absorption coefficient κ (1/m). This is a measure of how efficiently a cloud of gaseous combustion products and particulate soot emits and absorbs thermal radiation. It serves as a way to assign a single numerical value to the complex phenomena that govern emission and absorption in participating media. The absorption coefficient is a spatially and temporally varying quantity.

Due to the spectral nature of gas radiation, κ varies with radiation wavelength. It also varies with pathlength due to saturation of spectral bands within these gases[15]. The value of κ is dependent on the partial pressures of fuel, CO_2, H_2O, and other gaseous combustion products; however, gases with symmetric molecules such as N_2 and O_2 do not absorb or emit thermal radiation under normal circumstances because they do not have an electrical dipole moment[15].

Since soot is almost a perfect blackbody, κ also varies strongly with the quantity of soot present and for most fuels the absorption coefficient is dominated by the soot volume fraction. Although gas radiation is distinctly non-gray, a band mean (wavelength-independent) absorption coefficient is used in this work. A single absorption coefficient that includes the effect of soot and gas radiation is used. This is a reasonable approximation for engineering calculations where radiation from soot is the dominant source of radiation because soot has a continuous radiation spectrum. This simplification is less-desirable in cleaner burning fuels such as methane where the spectral nature of gas radiation becomes more important. The wavelength-independent radiative transport equation is simply Equation 35 with the spectral dependence removed:

$$\boldsymbol{s}\cdot\nabla I(\boldsymbol{x},\boldsymbol{s}) = \kappa(\boldsymbol{x})\left[I_b(\boldsymbol{x}) - I(\boldsymbol{x},\boldsymbol{s})\right] \tag{36}$$

The mean emission/absorption coefficient κ influences the gas-phase energetics through a radiative loss term appearing in the energy equation. This term is equal to the divergence of the radiant heat flux vector $-\nabla \cdot \boldsymbol{q}_r(\boldsymbol{x})$:

$$\boldsymbol{q}_r(\boldsymbol{x}) = \int \boldsymbol{s} I(\boldsymbol{x}, \boldsymbol{s}) d\Omega \tag{37}$$

$$-\nabla \cdot \boldsymbol{q}_r(\boldsymbol{x}) = \kappa(\boldsymbol{x}) \left[\int_{4\pi} I(\boldsymbol{x}, \boldsymbol{s}) d\Omega - 4\sigma T(\boldsymbol{x})^4 \right] \tag{38}$$

The first term in the brackets on the RHS of Equation 38 is the radiant absorption term calculated by the RTE solver. The second term in brackets is the radiant emission term. The importance of the numerical value of the absorption/emission coefficient κ is evident from Equations 36 and 38 because radiant emission and absorption are linearly proportional to κ. As discussed above, the magnitude of κ depends on the soot volume fraction, gas-phase composition, and radiation pathlength. In the modified version of FDS used in this work, the spatially and temporally varying soot concentration is known from a conservation equation that accounts for the finite rate of soot formation and destruction. The gas-phase composition can be approximated from the local value of the gas-phase mixture fraction using complete combustion state relations. Therefore, the total absorption coefficient κ is calculated as the sum of a gas-phase contribution κ_g and a soot contribution κ_s:

$$\kappa = \kappa_g + \kappa_s \tag{39}$$

4.1.1 Gas Contribution

The gas-phase absorption coefficient κ_g is determined as a function of mixture fraction and temperature using RADCAL[49] as implemented in FDS v2.0 by McGrattan *et. al.*[4]. RADCAL can be used to calculate the absorption coefficient for a particular radiation pathlength

through a nonisothermal and nonhomogeneous medium containing CO_2, H_2O, CH_4, CO, N_2, O_2, and soot. It is a narrow-band model meaning that the entire radiation spectrum is divided into hundreds of discrete bands. The absorption coefficient (or radiant intensity) at a given wavelength is calculated by the program using the spectral characteristics of each gas as tabulated within the program or approximated theoretically.

However, in this work a mean absorption coefficient averaged over all wavelengths is desired. At the start of a calculation the band-mean absorption coefficient is stored as a function of mixture fraction and temperature by evaluating the integral in Equation 40 with RADCAL[49]:

$$\kappa_g(Z,T) = \int_{\lambda_1}^{\lambda_2} \kappa\left(T, L, P_{H_2O}, P_{CO_2}, P_F, \lambda\right) d\lambda \tag{40}$$

This represents only the *gas-phase* contribution to the absorption coefficient (Equation 39). The limits of integration in Equation 40 are $\lambda_1 = 1.0\mu\text{m}$ and $\lambda_2 = 200.0\mu\text{m}$. The fuel is assumed to have identical radiative characteristics to those of methane. The partial pressures of water vapor, carbon dioxide, and fuel (P_{H_2O}, P_{CO_2}, and P_F) are calculated from the background pressure p_0 and the mole fractions of each species as determined from complete combustion state relations. It is computationally prohibitive to calculate the absorption coefficient as a function of the actual pathlength for each separate ray used by the radiation solver. For this reason the pathlength is specified as the mean beam length of the overall flame volume. The classical expression for the mean beam length of an arbitrarily shaped flame volume is[50]:

$$L = 3.6\frac{V_f}{A_f} \tag{41}$$

where V_f is the volume of the gas body and A_f is its surface area. In turbulent flames, the flame volume-to-area ratio (and therefore the mean beam length) scales approximately with the 1/3 power of heat release rate. Considering the turbulent flame to be a sphere with a constant heat release rate per unit flame volume of 2MW/m^3, Equation 41 can be used to approximate the mean beam length:

$$L \approx 0.06\dot{Q}^{1/3} \tag{42}$$

Obviously, turbulent diffusion flames are not spherical and Equation 42 should be considered only a first approximation. Different values of its coefficient can be derived from simple geometric relations depending on the presumed flame shape.

4.1.2 Soot Contribution

The soot contribution to the absorption coefficient is:

$$\kappa_s = C_{\kappa_s} f_v T \tag{43}$$

The value of C_{κ_s} is somewhere between 800 and 2000. All calculations performed here used a value of 1186, consistent with the Dalzell and Sarofim[51] dispersion relationship commonly used for measuring soot volume fractions. See Appendix H of Lautenberger[37] for details.

4.2 Estimating the Effect of Turbulent Fluctuations on Radiant Emission

The general form of the radiant emission source term is given as Equation 44:

$$\overline{\dot{q}_e'''} = 4\sigma\kappa(Z, T, f_v)T^4 \tag{44}$$

However, significant subgrid-scale temperature fluctuations are expected in turbulent flames. Recall from Section 3.1 that T is a function of Z at a constant nonadiabaticity. Therefore an integral similar to Equation 24 could be used to account for fluctuations:

$$\overline{\dot{q}_e'''} = \int_0^1 4\sigma\kappa(Z, T(Z), f_v) T^4(Z) P(Z) dZ \tag{45}$$

Evaluation of Equation 45 in every cell at every call is prohibitive when using "brute force" integration, *i.e.* approximation by rectangles. However, the numerical result of Equation 45 is dominated by the fourth power dependency of T. It can therefore be simplified by evaluating the absorption coefficient from mean properties and removing it from the integral:

$$\overline{\dot{q}_e'''} \approx 4\sigma\kappa\left(\overline{Z}, \overline{T}, \overline{f_v}\right) \int_0^1 T^4(Z) P(Z) dZ \tag{46}$$

This has computational advantages because the integral in Equation 46 can be evaluated with a highly efficient recursive algorithm by approximating $T^4(Z)$ as a standard polynomial. This algorithm is derived by Lautenberger[37] in his Appendix J.1. It can be used to analytically evaluate an integral of the form $\int_0^1 f(Z) P(Z) dZ$ where $f(Z)$ is a standard polynomial defined on the interval 0 to 1 and $P(Z)$ is an assumed beta probability density function.

When approximating $T^4(Z)$ as a 20th order polynomial, Equation 46 can be evaluated in approximately 150 floating point operations. This is approximately two orders of magnitude less operations than would be required with a brute force technique. Unfortunately, this algorithm can only be used to evaluate a polynomial defined on the interval 0 to 1. For this reason, it cannot be directly used to evaluate an integral involving the soot formation and oxidation polynomials since they are not defined over the entire interval.

This algorithm has been implemented into the FDS code but not yet rigorously tested. Details describing how the algorithm is actually implemented are given in Section 5.3. Future

work is planned to use this algorithm to investigate the effect of subgrid-scale temperature fluctuations on radiant emission. However, the algorithm is universal and has several potential applications in turbulent flames. It is mentioned in the present paper in the interest of disseminating the mathematics required to model radiation from turbulent diffusion flames.

5.0 IMPLEMENTATION

The purpose of this section is to explain how the equations discussed above have been implemented.

5.1 Test Filtering the Mixture Fraction Field to Determine the Subgrid-Scale Variance

Equation 31, with $C_{scale} = 1.3$, is used to approximate the mixture fraction subgrid-scale variance by test filtering the resolved mixture fraction field to estimate $\overline{\overline{Z^2}}$ and $\overline{\overline{Z}}^2$. The finite difference equations used to determine these values are as follows:

$$\begin{aligned}\overline{\overline{Z_{i,j,k}}} &\approx \frac{1}{12}\left(\overline{Z}_{i-1,j,k} + 2\overline{Z}_{i,j,k} + \overline{Z}_{i+1,j,k}\right) + \frac{1}{12}\left(\overline{Z}_{i,j-1,k} + 2\overline{Z}_{i,j,k} + \overline{Z}_{i,j+1,k}\right) + \frac{1}{12}\left(\overline{Z}_{i,j,k-1} + 2\overline{Z}_{i,j,k} + \overline{Z}_{i,j,k+1}\right) \\ &= \frac{1}{2}\overline{Z}_{i,j,k} + \frac{1}{12}\left(\overline{Z}_{i-1,j,k} + \overline{Z}_{i+1,j,k} + \overline{Z}_{i,j-1,k} + \overline{Z}_{i,j+1,k} + \overline{Z}_{i,j,k-1} + \overline{Z}_{i,j,k+1}\right)\end{aligned} \quad (47)$$

The value of $\overline{\overline{Z}}^2$ is simply the square of the numerical result of Equation 47. Similarly, $\overline{\overline{Z^2}}$ is evaluated as

$$\begin{aligned}\overline{\overline{Z^2_{i,j,k}}} &\approx \frac{1}{12}\left(\overline{Z}^2_{i-1,j,k} + 2\overline{Z}^2_{i,j,k} + \overline{Z}^2_{i+1,j,k}\right) + \frac{1}{12}\left(\overline{Z}^2_{i,j-1,k} + 2\overline{Z}^2_{i,j,k} + \overline{Z}^2_{i,j+1,k}\right) + \frac{1}{12}\left(\overline{Z}^2_{i,j,k-1} + 2\overline{Z}^2_{i,j,k} + \overline{Z}^2_{i,j,k+1}\right) \\ &= \frac{1}{2}\overline{Z}^2_{i,j,k} + \frac{1}{12}\left(\overline{Z}^2_{i-1,j,k} + \overline{Z}^2_{i+1,j,k} + \overline{Z}^2_{i,j-1,k} + \overline{Z}^2_{i,j+1,k} + \overline{Z}^2_{i,j,k-1} + \overline{Z}^2_{i,j,k+1}\right)\end{aligned} \quad (48)$$

In Equations 47 and 48, the *i*,*j*,*k* values are indices corresponding to the location of a particular cell, not to be confused with Cartesian tensor notation. The resolved mixture fraction

field is test-filtered at the start of a timestep, and the mixture fraction variance is estimated from scale similarity. The constants *a* and *b* appearing in the beta function can then be calculated from Equation 26 and 27, respectively.

5.2 Integrating Soot Formation Functions Over a PDF

Recall from Equation 29 that the numerical value of $B(a,b)$ can be determined from three gamma functions. However, it can be seen from Equation 30 that $\Gamma(x)$ becomes very large even at moderate *x*. This would normally cause floating point overflows on most computers, but this problem can be avoided by determining $B(a,b)$ from the exponential of the sum of three $\ln\Gamma(x)$'s:

$$B(a,b) = \exp\left(\ln\Gamma(a) + \ln\Gamma(b) - \ln\Gamma(a+b)\right) \tag{49}$$

Press *et. al.*[52] give a routine for calculating $\ln\Gamma(x)$, but evaluation of Equation 49 would normally be quite expensive because each call to $\ln\Gamma(x)$ requires 25 arithmetic operations and two calls to a logarithm. However, it is possible to create a lookup table holding $\ln\Gamma(x)$ because the ranges of *a* and *b* can be determined beforehand from the expected range of $\overline{Z}$ and $\overline{Z''^2}$. Assuming no soot oxidation occurs below Z_1 and no soot formation occurs above Z_2, the integral in Equation 24 can be evaluated by "brute force" over the range Z_1 to Z_2:

$$\begin{aligned} \overline{\dot{\omega}_s'''} &= \int_0^1 \dot{\omega}_s'''\left(Z, T(Z)\big|_\chi\right) P(Z)\,dZ \\ &= \int_{Z_1}^{Z_2} \left[A_s \left(\dot{\omega}_{sf}''(Z)\big|_\chi + \dot{\omega}_{so}''(Z)\big|_\chi \right) + \omega_{sf}'''(Z)\big|_\chi \right] P(Z)\,dZ \end{aligned} \tag{50}$$

In Equation 50, Z_1 is the minimum mixture value at which soot oxidation occurs, and Z_2 is the maximum mixture fraction value at which soot formation occurs. The integral is evaluated numerically using approximation by rectangles with using $\Delta Z = 0.0001$ by default, although the

user may specify the value of ΔZ [37]. This technique is very expensive, but serves as a benchmark for more efficient numerical techniques that can be used to evaluate the integral. One such technique involving the use of Fast Fourier Transforms (FFT's) is given in Appendix J.2 of Lautenberger[37], although this technique has not yet been implemented or tested. Again, this is mentioned here in the interest of disseminating mathematical techniques that could potentially be applied to simulations of soot formation in turbulent diffusion flames.

5.3 Accounting for the Effect of Fluctuations on Radiant Emission Source Term

Equation 46 provides a means to approximate the influence of subgrid-scale temperature fluctuations on the radiant emission source term. This is implemented numerically by first using the lookup table containing the values of $T(Z,h_T)$ that is generated at the start of a calculation to store $T^4(Z)$ in a second lookup table for a discrete number of χ's (*e.g.* 1000). Each $T^4(Z)\big|_\chi$ is then fit with a 50$^{\text{th}}$ order Chebyshev polynomial at each value of χ using the procedure given by Press *et. al.*[52].

A Chebyshev polynomial used to approximate a particular function is almost identical to the minimax polynomial which has the smallest deviation from the true function[52]. Whereas the minimax polynomial cannot be easily determined, the Chebyshev polynomial can be found quite easily. The Chebyshev polynomials are then converted to standard polynomials and truncated at order 20 using another routine given by Press *et. al.*[52]. Higher order standard polynomials were found to be unstable, fluctuating randomly near $Z = 1$.

Once the twenty coefficients have been determined for each $T^4(Z)\big|_\chi$, the lookup table holding $T^4(Z)$ can be deallocated to conserve storage overhead since it is no longer needed. The

integral described in Equation 46 can now be efficiently evaluated using the algorithm described briefly in Section 4.2 and derived in Appendix J.1 of Lautenberger[37].

6.0 CALCULATIONS USING THE MODEL

Ultimately, the soot formation and oxidation model that has been postulated here and incorporated into FDS should be put through a rigorous validation process. At a bare minimum, this must include comparison of prediction and experiment for quantities such as soot volume fraction, temperature, and radiant heat flux to external targets. Only then do the model's predictions take on a high enough level of credence to be used in engineering calculations.

Few measurements of soot volume fraction in buoyant diffusion flames with a gaseous fuel have been reported in the literature. Rather, measurements are usually given for liquid pool fires. Though pool fires represent a practical fire hazard, they are less desirable for model calibration due to the uncertainty associated with the boundary condition at the pool surface. Radiative blocking near the fuel surface causes the burning rate to vary over the pool surface, whereas the burning rate from a gas burner is relatively constant over the burner surface. The same caveat applies to predicting the radiant heat flux from pool fires to external targets.

For these reasons, the model has not been thoroughly tested at this point. Future work is planned in this area. Nonetheless, some calculations performed using the model are examined qualitatively in Section 6.1. The focus here is a comparison between the model predictions using the mean value of mixture fraction and temperature to calculate the soot formation/oxidation rates and the predictions when turbulent fluctuations are explicitly accounted for with the PDF technique described above.

As discussed in an earlier publication[7], an expression was derived for the divergence of the velocity field using the conservation of mass equation as the starting point. This new

divergence expression is compatible with the present reformulation of the FDS code where a conservation equation for total enthalpy is explicitly solved. However, that expression was found to be problematic near the burner inlet in laminar calculations. This is evident from Figure 13a in the earlier publication[37] where the velocity at 3mm above the burner oscillates nonphysically due to this divergence problem. Unfortunately, the problem is exacerbated in turbulent calculations. For this reason, the original velocity divergence expression[4] was used in the turbulent calculations discussed below. Though not rigorous, this should not significantly impact the qualitative observations made here. Future work is intended to identify the cause of this divergence problem.

The flame calculated here is a 100kW propane flame on a square sand burner 17cm on edge. The model was run using the optimal propane parameters listed in Table 1 through Table 3 of the companion publication[7]. The computational domain has physical dimensions of 0.4m by 0.4m by 1.8m and is discretized into a 32 by 32 by 128 cell computational mesh (131,072 cells). A uniform grid was used so that each cell is 1.25cm by 1.25cm by 1.41cm. The flame was run with and without the PDF, and the results are discussed below.

6.1 Qualitative Observations from a Propane Sand Burner Flame

6.1.1 Visualization of Flame Sheet Location

Flame heights calculated with FDS are commonly visualized using Smokeview[6] to plot an "isosurface" of the stoichiometric mixture fraction contour[5]. In a "real life" diffusion flame, the location of the visible flame sheet actually corresponds to the soot burn limit rather than the stoichiometric contour because incandescent soot particles may not be fully oxidized until higher up in the flame where local conditions are fuel-lean. Therefore, one would suspect that flame

heights visualized using the disappearance of soot particles as the flame sheet criterion would tend to be taller than those visualized using the stoichiometric mixture fraction as the criterion.

Figure 4 shows a comparison of the instantaneous flame heights visualized using $Z=Z_{st}$ and $f_v=10^{-7}$ as the criterion for the flame sheet location. The results are as expected: the flame heights visualized using the disappearance of the soot particles tend to be higher than those visualized using the stoichiometric contour as the criterion. This has important implications for numerical prediction of mean flame heights and may eventually provide insight as to how to introduce fuel-specific effects into flame height correlations.

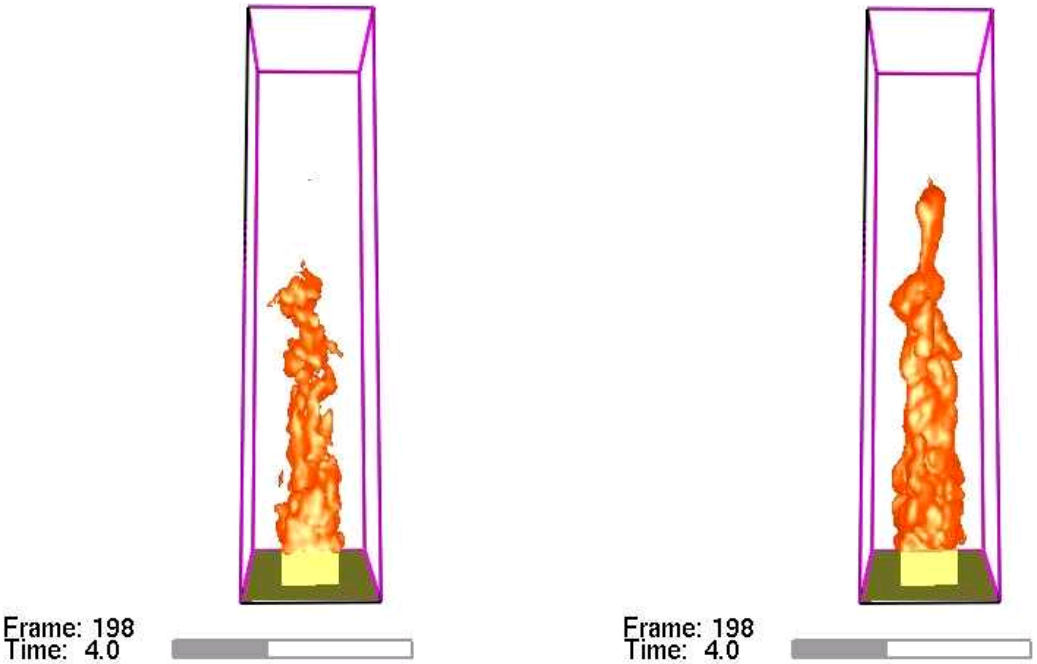

(a) **(b)**

Figure 4. Instantaneous flame sheet visualization using: (a) stoichiometric mixture fraction contour; (b) f_v = 10^{-7} contour.

6.1.2 Centerline Soot Volume Fraction and Temperature

The soot volume fraction and temperature predictions along the centerline were examined with and without the PDF. The predictions are shown below in Figures 5 and 6.

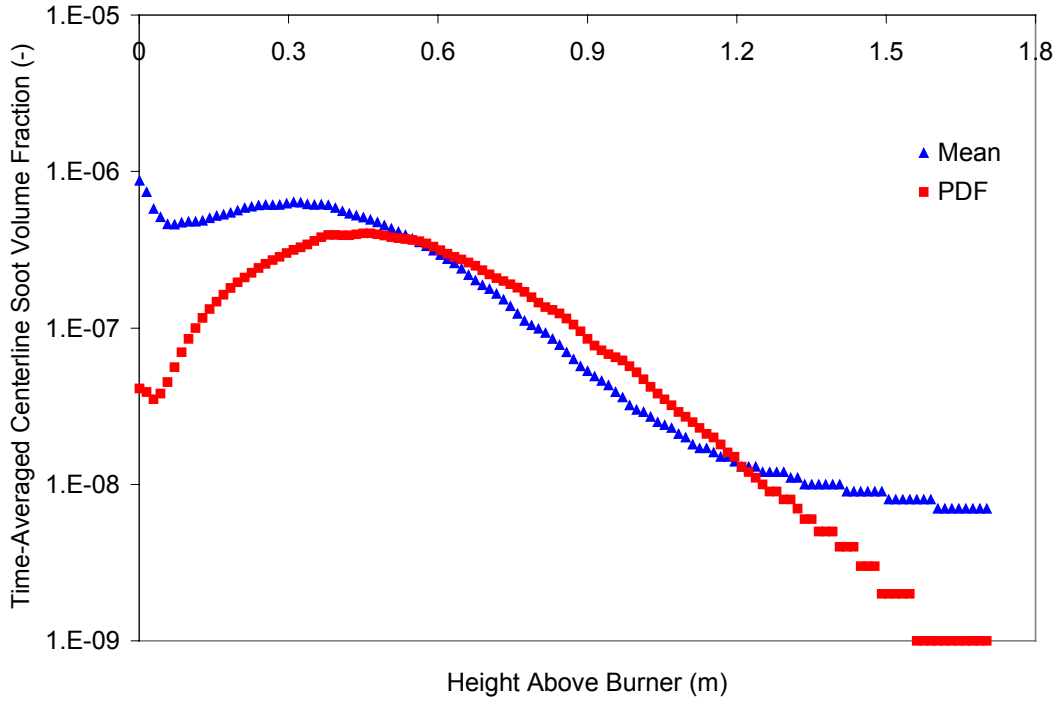

Figure 5. Comparison of predicted time-averaged centerline soot volume fraction in 100kW propane flame with (PDF) and without (Mean) subgrid-scale fluctuations.

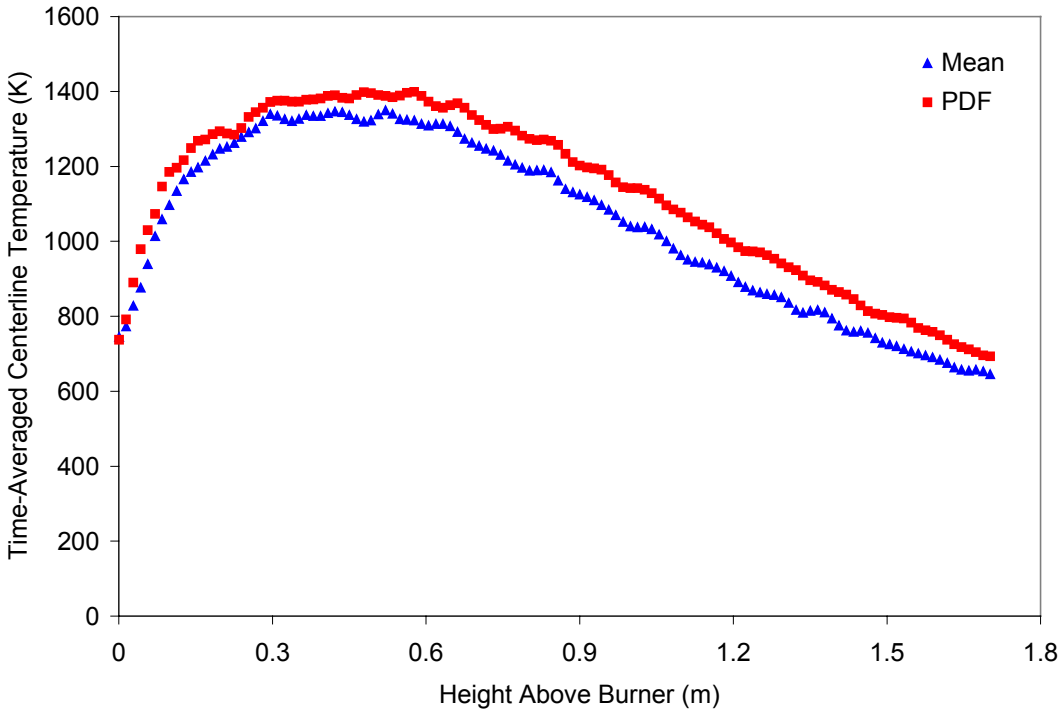

Figure 6. Comparison of predicted time-averaged centerline temperature in 100kW propane flame with (PDF) and without (Mean) subgrid-scale fluctuations.

These computations show that significantly less soot forms low in the flames when turbulent fluctuations are explicitly considered. This causes less radiative losses low in the flame, explaining why the time-averaged temperatures are higher in the PDF flame. This effect is typically less than 100K for the present flame. An interesting trend is apparent from the centerline soot volume fraction profile shown in Figure 5: when using the PDF there is less soot along the centerline for $0\text{m} \le H < 0.6\text{m}$, more soot for $0.6\text{m} \le H < 1.2\text{m}$, and less soot for $H \ge 1.2\text{m}$. This indicates that subgrid-scale turbulent fluctuations affect the soot distribution in a more complicated way than simply increasing or decreasing the total amount of soot.

6.1.3 Soot Volume Fraction and Temperature Profiles at Several Heights Above Burner

In order to provide an idea as to how turbulent fluctuations affect the soot distribution and temperature at locations off the centerline, soot volume fraction and temperature profiles were examined at several heights above the burner (HAB). Representative plots are shown below in Figures 7 and 8.

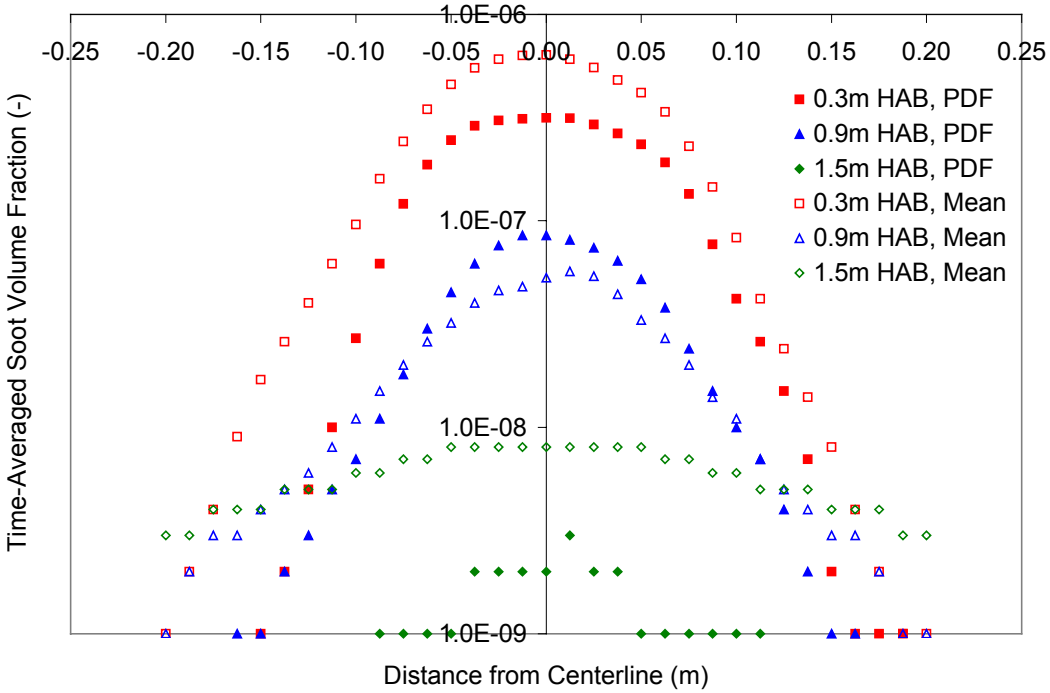

Figure 7. Comparison of predicted time-averaged soot volume fraction profiles at several heights above burner (HAB) in 100kW Propane Flame with (PDF) and without (Mean) subgrid-scale fluctuations.

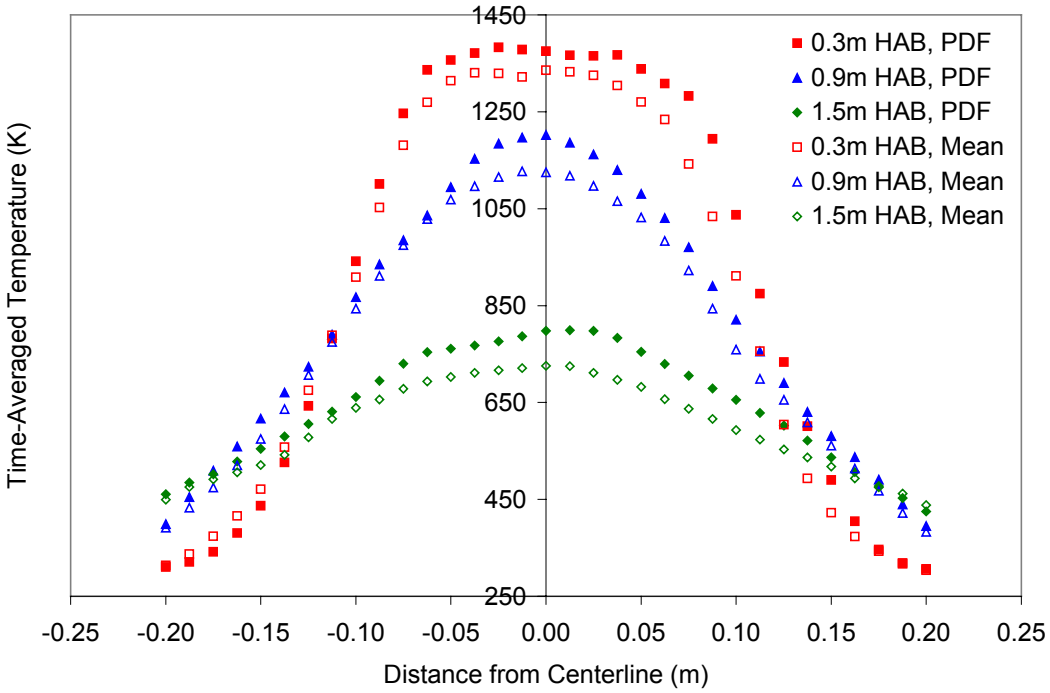

Figure 8. Comparison of predicted time-averaged temperature profiles at several heights above burner (HAB) in 100kW propane flame with (PDF) and without (Mean) subgrid-scale fluctuations.

From Figure 7 it is obvious that the same general trends seen in Figures 5 and 6 also apply at the off-axis locations. The temperatures are higher when using the PDF because less soot forms low in the flames, decreasing the radiative losses. The soot volume fraction profiles in Figure 8 show there is more soot in the vicinity of the centerline at 0.9m HAB when using the PDF. However by 1.5m there is significantly less soot when using the PDF.

7.0 CONCLUSIONS

This paper reviews the mathematics necessary to extend a new soot formation and oxidation model[7] for laminar flames to Large Eddy Simulation (LES) of turbulent buoyant diffusion flames. Whereas Reynolds averaged Navier-Stokes (RANS) codes are relatively mature in terms of being coupled with soot formation / oxidation submodels, LES codes are not as far advanced[26], primarily because the required mathematics have been developed only recently[25]. For this reason, few studies have explored LES of soot formation in buoyant diffusion flames. The present paper (as well as appendix J of Lautenberger[37]) aims to disseminate several mathematical techniques and algorithms with potential application to LES of soot formation and flame radiation in turbulent buoyant diffusion flames.

A new model wherein the soot formation / oxidation rate is an analytic function of mixture fraction and temperature has previously been applied to small-scale laminar flames[7]. It has been incorporated into NIST Fire Dynamics Simulator (FDS) v2.0[4,5], which is modified in the present paper to use the principle of scale similarity[25] to predict the subgrid-scale variance of the mixture fraction distribution. The variance is in turn used to determine the local mixture fraction probability density function (PDF), which is assumed to follow a beta distribution. This accounts for unresolved subgrid-scale fluctuations that are removed during the LES filtering process. The use of a PDF is necessary because soot formation and oxidation occur at length

scales less than 1mm, but the grid resolution employed in typical LES of diffusion flames is at least an order of magnitude greater and all relevant length scales are not directly resolved.

The underlying CFD code[4,5] has been reformulated to explicitly solve a conservation equation for total enthalpy[7]. It is therefore possible to calculate the local radiatively-induced nonadiabaticity. This in turn allows the temperature PDF to be determined from the mixture fraction PDF. Since the rate of soot formation and oxidation is a function of only mixture fraction and temperature[37], the effect of unresolved subgrid-scale fluctuations on the grid-scale soot formation / oxidation rate can be approximated via integration over the mixture fraction and temperature PDFs.

Two efficient algorithms intended for use in numerical simulation of soot formation and flame radiation in turbulent diffusion flames have been developed. They are discussed thoroughly in Appendix J of Lautenberger[37]. The first is a recursive algorithm for evaluating the integral of a general polynomial multiplied by an assumed beta distribution. It has several potential applications to numerical simulation nonpremixed combustion, such as approximating the effect of subgrid-scale temperature fluctuations on the radiant emission source term. The second algorithm gives an efficient means to evaluate the integral of the soot formation / oxidation polynomials and beta distribution product. It makes use of Chebyshev approximations[52], with the Chebyshev coefficients evaluated by Fast Fourier Transforms. It is intended to supplant the present integration technique where the integral of the soot formation / oxidation polynomials and the beta distribution product is evaluated by an inefficient brute force method.

Preliminary results indicate that subgrid-scale fluctuations have a quantitatively significant impact on the amount of soot formed in Large Eddy Simulation of turbulent buoyant

diffusion flames. The effect of these fluctuations was investigated by simulating a diffusion flame with the soot formation / oxidation rate determined from the *mean* values of mixture fraction and temperature, and then by using a PDF to account for subgrid-scale fluctuations. These results showed that less soot is present low in the flames when using the PDF. Moving up in the flame, a region is encountered where more soot is present. However, the soot burns up more quickly in the upper parts of the flame, and this region has less soot when the PDF is used.

A quantitative comparison of model prediction and experiment was not performed as part of this study. This is partly due to the fact that there are few measurements of soot volume fraction and temperature in the near field of gaseous turbulent *buoyant* diffusion flames. Most measurements have been made either in liquid pool fires or momentum-dominated jet flames. Pool fires are less desirable for model calibration than gaseous sand burner fires due to the uncertainty associated with the boundary condition at the pool surface. Momentum dominated jet flames have different physics due to the finite-rate chemistry introduced by the high scalar dissipation rates. It is our hope that this will serve as an impetus for others to make soot volume fraction and temperature measurements on buoyant diffusion flames of gaseous fuels. Such measurements would be quite useful from a model validation standpoint.

This work has shown that the soot formation / oxidation model developed here[7] is feasible for Large Eddy Simulation of soot processes in the near field of buoyant turbulent diffusion flames. However, due to the spatial resolution required to provide a reasonable description of the mixture fraction and temperature fields, the model is not practical for use in most building fires at this time. Furthermore, the underlying model[7] needs additional validation against small-scale laminar flames of various hydrocarbon fuels.

8.0 REFERENCES

1. McGrattan, K.B., Baum, H.R., Rehm, R.G., Hamins, A., Forney, G.P., "Fire Dynamics Simulator – Technical Reference Guide," National Institute of Standards and Technology, NISTIR 6467, 2000.
2. McGrattan, K.B., and Forney, G.P., "Fire Dynamics Simulator – User's Manual," National Institute of Standards and Technology, NISTIR 6469, 2000.
3. Forney, G.P and McGrattan, K.B., "User's Guide for Smokeview Version 2.0 – A Tool for Visualizing Fire Dynamics Simulation Data," National Institute of Standards and Technology, NISTIR 6761, 2001.
4. McGrattan, K.B., Baum, H.R., Rehm, R.G., Hamins, A., Forney, G.P., Floyd, J.E. and Hostikka, S., "Fire Dynamics Simulator (Version 2) – Technical Reference Guide," National Institute of Standards and Technology, NISTIR 6783, 2001.
5. McGrattan, K.B., Forney, G.P, Floyd, J.E., "Fire Dynamics Simulator (Version 2) – User's Guide," National Institute of Standards and Technology, NISTIR 6784, 2001.
6. Forney, G.P and McGrattan, K.B., "User's Guide for Smokeview Version 2.0 – A Tool for Visualizing Fire Dynamics Simulation Data," National Institute of Standards and Technology, NISTIR 6761, 2001.
7. Lautenberger, C.W. *et. al.*, "An Engineering Approach to Soot Formation and Oxidation in Atmospheric Diffusion Flames of an Arbitrary Hydrocarbon Fuel," (to be submitted for publication, presently Appendix A), 2002.
8. Burke, S.P. and Schumann, T.E.W., *Ind. Eng. Chem.* **20**, 998 (1928).
9. Zel'dovich, Y.B., *Zhur. Tekhn. Fiz.* **19** *1199 (1949),* English Translation*,* NACA Tech. Memo, No. 1296 (1950).

10. Spalding, D.B., *Proceedings of the Combustion Institute* **4**: 847-864 (1953).

11. Emmons, H.W., *Z. angew. Math. Mech.,* **36** 60 (1956).

12. Patankar, S.V., and Spalding, D.B., *Heat and Mass Transfer in Boundary Layers,* 2nd Ed, Intertext Books, London (1970).

13. Launder, B.E., and Spalding, D.B., *Mathematical Models of Turbulence,* Academic Press, London, (1972).

14. Magnussen, B.F., and Hjertager, B. F., *Proceedings of the Combustion Institute* **16**: 719 (1969).

15. de Ris, J., "Fire Radiation-A Review," *Proceedings of the Combustion Institute* **19**: 1003-1016 (1979).

16. Orloff, L., Modak, A.T., and Alpert, R.L., "Burning of Large-Scale Vertical Plastic Surfaces," *Proceedings of the Combustion Institute* **16**: 1345-1354 (1976).

17. Yang, J.C., Hamins, A., and Kashiwagi, T., "Estimate of the Effect of Scale on Radiative Heat Loss Fraction and Combustion Efficiency," *Combustion Science and Technology* **96**: 183-188 (1994).

18. Raithby, G.D. and Chui, E.H., "A Finite-Volume Method for Predicting Radiant Heat Transfer in Enclosures with Participating Media," *Journal of Heat Transfer* **112**: 414-423 (1990).

19. Kennedy, I.M., "Models of Soot Formation and Oxidation," *Progress in Energy and Combustion Science* **23**: 95-132 (1997).

20. Gore, J.P., Ip, U.S., and Sivathanu, Y.R., "Coupled Structure and Radiation Analysis of Acetylene/Air Flames," *Journal of Heat Transfer* **114**:487-493 (1992).

21. Kennedy, I.M., Yam, C., Rapp, D.C., and Santoro, R.J., "Modeling and Measurements of Soot and Species in a Laminar Diffusion Flame," *Combustion and Flame* **107**: 368-382 (1996).

22. Young, K.J. and Moss, J.B., "Modeling Sooting Turbulent Jet Flames Using an Extended Flamelet Technique," *Combustion Science and Technology*, **105**: 33-53 (1995).

23. Said, R., Garo, A., and Borghi, R., "Soot Formation Modeling for Turbulent Flames," *Combustion and Flame* **108**: 71-86 (1997).

24. Pope, S.B., "Computations of Turbulent Combustion: Progress and Challenges," *Proceedings of the Combustion Institute* **23**: 591-612 (1990).

25. Cook, A.W. and Riley, J.J., "A Subgrid Model for Equilibrium Chemistry in Turbulent Flows," *Physics of Fluids* **6**:2868-2870 (1994).

26. Liu, F. and Wen, J.X., "The effect of turbulence modeling on the CFD simulation of buoyant diffusion flames," *Fire Safety Journal* **37** 125-150 (2002).

27. Desjardin, P.E. and Frankel, S.H., "Two-Dimensional Large Eddy Simulation of Soot Formation in the Near-Field of a Strongly Radiating Nonpremixed Acetylene-Air Turbulent Jet Flame," *Combustion and Flame* **119**: 121-132 (1999).

28. Leung, K.M., Linstedt, R.P., and Jones, W.P., "A Simplified Reaction Mechanism for Soot Formation in Nonpremixed Flames," *Combustion and Flame* **87**: 289-305 (1991).

29. Luo, M. and Beck, V., "A Study of Non-flashover and Flashover Fires in a Full-scale Multi-room Building," *Fire Safety Journal* **26**: 191-219 (1996).

30. Tesner, P.A., Snegiriova, T.D., and Knorre, V.G., "Kinetics of Dispersed Carbon Formation," *Combustion and Flame* **17**: 253-260 (1971).

31. Tesner, P.A., Tsygankova, E.I., Guilazetdinov, L.P., Zuyev, V.P., and Loshakova, G.V., "The Formation of Soot from Aromatic Hydrocarbons in Diffusion Flames of Hydrocarbon-hydrogen Mixtures," *Combustion and Flame* **17**: 279-285 (1971).

32. Novozhilov, V., "Computational Fluid Dynamics Modeling of Compartment Fires," *Progress in Energy and Combustion Science* **27**: 611-666 (2001).

33. Moss, J.B. and Stewart, C.D., "Flamelet-based Smoke Properties for the Field Modeling of Fires," *Fire Safety Journal* **30**: 229-250 (1998).

34. Moss, J.B., Stewart, C.D., and Syed, K.J., "Flowfield Modeling of Soot Formation at Elevated Pressure," *Proceedings of the Combustion Institute* **22**: 413-423 (1988).

35. Syed, K.J., Stewart, C.D., and Moss, J.B., "Modeling soot formation and thermal radiation in buoyant turbulent diffusion flames," *Proceedings of the Combustion Institute* **23**: 1533-1541 (1990).

36. de Ris, J. and Cheng, X.F., "The Role of Smoke-Point in Material Flammability Testing," *Fire Safety Science – Proceedings of the Fourth International Symposium*, 301-312 (1994).

37. Lautenberger, C.W., "CFD Simulation of Soot Formation and Flame Radiation," MS Thesis, Worcester Polytechnic Institute Department of Fire Protection Engineering, Worcester, MA, 2002.

38. Ferziger, J.H., and Peric, M., *Computational Methods for Fluid Dynamics*, Second Edition, Springer-Verlag Berlin, 1999.

39. Najjar, F.M. and Tafti, D.K., "Study of discrete test filters and finite difference approximations for the dynamic subgrid-scale stress model," *Physics of Fluids* **8**:1076-1088 (1996).

40. Smagorinsky, J., "General Circulation Experiments with the Primitive Equations. I. The Basic Experiment," *Monthly Weather Review* **91**:99 (1963).

41. Germano, M., Piomelli, U., Moin, P., and Cabot, W., "A Dynamic Subgrid-Scale Eddy Viscosity Model," *Physics of Fluids A* **3**:1760-1765 (1991).

42. Markstein, G.H. and de Ris, J., "Radiant Emission and Absorption by Laminar Ethylene and Propylene Diffusion Flames," *Proceedings of the Combustion Institute* **20**, 1637-1646 (1984).

43. Kent, J.H. and Honnery, D., "Soot and Mixture Fraction in Turbulent Diffusion Flames," *Combustion Science and Technology*, **54**:383-397 (1987).

44. Wall, C., Boersma, J., and Moin, P., "An Evaluation of the Assumed Beta Probability Density Function Subgrid-Scale Model for Large Eddy Simulation of Nonpremixed Turbulent Combustion with Heat Release," *Physics of Fluids* **12**:2522-2529 (2000).

45. Moin, P., Squires, K., Cabot, W., and Lee, S., "A Dynamic Subgrid-Scale Model for Compressive Turbulence and Scalar Transport," *Physics of Fluids A* **3**:2746-2757 (1991).

46. Pierce, C. and Moin, P., ''A Dynamic Model for Subgrid-Scale Variance and Dissipation Rate of a Conserved Scalar," *Physics of Fluids* **10**:3041-3044 (1998).

47. Jiménez, J., Liñán, A., Rogers, M., and Higuera, F., "*A priori* testing of subgrid models for chemically reacting non-premixed turbulent shear flows," *Journal of Fluid Mechanics* **349**:149-171 (1997).

48. Honnery, D.R., Tappe, M., and Kent, J.H., "Two Parametric Models of Soot Growth Rates in Laminar Ethylene Diffusion Flames," *Combustion Science and Technology* **83**: 305-321 (1992).

49. Grosshandler, W.L., "RADCAL: A Narrow-Band Model for Radiation Calculations in a Combustion Environment," National Institute of Standards and Technology, NIST Technical Note 1402, 1993.

50. Tien, C.L., Lee, K.Y., and Stretton, A.J., "Radiation Heat Transfer," in *The SFPE Handbook of Fire Protection Engineering*, Second Edition, pp 1-65 to 1-79, National Fire Protection Association, Qunicy, MA, 1995.

51. Dalzell, W.H. and Sarofim, A.L., *Journal of Heat Transfer* **91**:100 (1969).

52. Press, W.H., Teukolksy, S.A., Vetterling, W.T., and Flannery, B.P., *Numerical Recipes in Fortran 77 The Art of Scientific Computing* 2nd Edition, Cambridge University Press, Cambridge, 1992.

APPENDIX C THE MIXTURE FRACTION AND STATE RELATIONS

This Appendix gives the background information for the reader who is not familiar with the concept of the mixture fraction or state relations as they pertain to nonpremixed combustion.

C.1 Classical Derivation of the Mixture Fraction

Following the analysis of Peters[1], consider the "frozen" mixing of fuel and oxidant where no chemical reaction occurs. This could be envisioned as a natural-gas leak in which no ignition source is present. At any spatial location, the composition of the gas-phase is either pure oxidant (air), pure fuel (natural gas), or a mixture of the two. For reasons that will become apparent later in this Appendix, it is convenient to introduce a quantity known as the *mixture fraction* (*Z*). It is a numerical construct used in analysis of nonpremixed combustion systems to describe the degree of scalar mixing between fuel and oxidant. It is a local quantity within the flowfield that varies both spatially and temporally.

The mixture fraction is best understood by visualizing a homogeneous control volume containing a finite quantity of mass in a gaseous state. In a two-feed system consisting of a fuel stream and an oxidant stream, the mass in this control volume originated either as fuel or as oxidant. The mixture fraction in this control volume is classically defined as "the fraction of mass present that originated in the fuel stream".

Let m_1 be a certain quantity of mass that came from the fuel stream. Likewise, m_2 is a certain quantity of mass that originated in the oxidant stream. This nomenclature is typical: a subscript 1 denotes a quantity originating in the fuel stream, and a subscript 2 denotes a quantity that began in the oxidant stream. The total amount of mass present is $m_1 + m_2$. By introducing

this nomenclature, the verbal definition of the mixture fraction given above can be expressed mathematically as:

$$Z = \frac{m_1}{m_1 + m_2} \tag{C.1}$$

In a nonreacting mixture of pure fuel and pure oxygen, the mass fraction of fuel is equal to the value of Z, and the mass fraction of oxygen is equal to the value of 1-Z. However, both the fuel and oxidant stream may contain inert substances such as nitrogen. Let $Y_{\mathrm{F},1}$ be the mass fraction of fuel in the fuel stream (unity for pure fuel) and let $Y_{\mathrm{O}_2,2}$ be the mass fraction of oxygen in the oxidant stream. In this generalized case, the mass fraction of fuel in a completely *unburnt* mixture of fuel and oxidant (designated Y_{F}^u) is

$$Y_F^u = Y_{F,1} Z \tag{C.2}$$

Similarly, the mass fraction of oxygen, designated $Y_{\mathrm{O}_2}^u$ is:

$$Y_{O_2}^u = Y_{O_2,2}(1 - Z) \tag{C.3}$$

Equations C.2 and C.3 give the relationship between the mixture fraction and the mass fraction of fuel and oxygen during mixing of fuel and oxidant in absence of combustion. These are important building blocks for the analysis of reacting systems. Now introduce a reaction describing the complete combustion of a hydrocarbon fuel to form carbon dioxide and water vapor:

$$\nu'_F \mathrm{C}_m\mathrm{H}_n + \nu'_{O_2}\mathrm{O}_2 \rightarrow \nu''_{CO_2}\mathrm{CO}_2 + \nu''_{H_2O}\mathrm{H}_2\mathrm{O} \tag{C.4}$$

The stoichiometric coefficients in Equation C.4 can be defined in terms of ν_F', m, and n as follows:

$$\nu_{O_2}' = \nu_F' \left(m + n/4 \right) \tag{C.5}$$

$$\nu_{CO_2}'' = \nu_F' m \tag{C.6}$$

$$\nu_{H_2O}'' = \nu_F' \, n/2 \tag{C.7}$$

Consider the system described by Equation C.4 in the absence of any reaction, *i.e.* with frozen reactants. This is a stoichiometric mixture consisting of ν_F' moles of fuel, ν_O' moles of oxygen, and zero moles of carbon dioxide and water vapor. The mole fractions of oxygen and fuel are:

$$X_{O_2} = \frac{\nu_{O_2}'}{\nu_{O_2}' + \nu_F'} \tag{C.8}$$

$$X_F = \frac{\nu_F'}{\nu_{O_2}' + \nu_F'} \tag{C.9}$$

In combustion problems it is more convenient to work in terms of mass fractions rather than mole fractions. The reason for this is that mass is perfectly conserved during the combustion process, but moles are *not necessarily* conserved. As an example, the complete combustion of one mole of methane transforms three moles of reactants (1 CH_4 and $2O_2$) to three moles of products (1 CO_2 and 2 H_2O). However, the complete combustion of one mole of propane transforms six moles of reactants (1 C_3H_8 and 5 O_2) to seven moles of products (3 CO_2 and 4 H_2O). For this reason the mole fractions in Equations C.8 and C.9 are rewritten as mass fractions:

$$Y_{O_2} = \frac{\nu_{O_2}' M_{O_2}}{\nu_{O_2}' M_{O_2} + \nu_F' M_F} \tag{C.10}$$

$$Y_{\mathrm{F}} = \frac{v'_F M_F}{v'_{O_2} M_{O_2} + v'_F M_F} \tag{C.11}$$

Dividing Equation C.10 by C.11 and multiplying by Y_F gives an expression that relates the oxygen mass fraction to the fuel mass fraction:

$$Y_{O_2} = Y_F \frac{v'_{O_2} M_{O_2}}{v'_F M_F} \tag{C.12}$$

Define *s* as the stoichiometric oxygen-to-fuel mass ratio:

$$s = \frac{v'_{O_2} M_{O_2}}{v'_F M_F} \tag{C.13}$$

Combining Equations C.12 and C.13 gives:

$$Y_{\mathrm{O}_2} = s Y_{\mathrm{F}} \tag{C.14}$$

Up to this point, we have been considering a nonreacting mixture of fuel and oxygen. As the reaction in Equation C.4 proceeds from left to right, the reactants are consumed and products are generated. From Equation C.14, the change in the oxygen mass fraction dY_{O_2} is linearly proportional to the change in fuel mass fraction dY_{F} by the factor *s*:

$$dY_{\mathrm{O}_2} = s dY_{\mathrm{F}} \tag{C.15}$$

Now allow the reaction to proceed from a completely unburnt state, designated as *u*, to any state of combustion between completely unburnt and completely burnt, designated as *b*. This is equivalent to integrating Equation C.15 from state *u* to state *b*:

$$\int_u^b dY_{\mathrm{O}_2} = s \int_u^b dY_{\mathrm{F}}$$

$$Y_{O_2}^b - Y_{O_2}^u = sY_F^b - sY_F^u$$
$$sY_F^b - Y_{O_2}^b = sY_F^u - Y_{O_2}^u \tag{C.16}$$

As a point of rigor, it is worth noting that Equation C.16 is valid for homogeneous systems in the absence of diffusion. It is valid for spatially for spatially inhomogeneous systems, such as diffusion flames, only if the diffusivities of the fuel and oxygen are equal. The traditional definition of the mixture fraction can be derived by substituting Equations C.2 and C.3 into Equation C.16:

$$sY_F^b - Y_{O_2}^b = sY_{F,1}Z - Y_{O_2,2}(1-Z)$$
$$sY_F^b - Y_{O_2}^b = sY_{F,1}Z - Y_{O_2,2} + Y_{O_2,2}Z$$
$$sY_{F,1}Z + Y_{O_2,2}Z = sY_F^b - Y_{O_2}^b + Y_{O_2,2}$$
$$Z(sY_{F,1} + Y_{O_2,2}) = sY_F^b - Y_{O_2}^b + Y_{O_2,2}$$
$$Z = \frac{sY_F^b - Y_{O_2}^b + Y_{O_2,2}}{sY_{F,1} + Y_{O_2,2}} \tag{C.17}$$

At stoichiometric conditions, both Y_F^b and $Y_{O_2}^b$ are zero because all fuel and oxygen are consumed. Therefore, from Equation C.17 the stoichiometric value of the mixture fraction is:

$$Z_{st} = \frac{Y_{O_2,2}}{sY_{F,1} + Y_{O_2,2}} \tag{C.18}$$

C.2 State Relations: Complete Combustion

First, consider the stoichiometric combustion of one mole of fuel in an oxidant stream consisting only of nitrogen and oxygen:

$$F + \nu_{O_2}\left(O_2 + \frac{X_{N_2}^\infty}{X_{O_2}^\infty}N_2\right) \rightarrow \nu_{H_2O}H_2O + \nu_{CO_2}CO_2 + \nu_{O_2}\frac{X_{N_2}^\infty}{X_{O_2}^\infty}N_2 \tag{C.20}$$

Now consider the generalized reaction in which excess fuel and oxygen are allowed to exist:

$$F+\frac{1}{\phi}\nu_{O_2}\left(O_2+\frac{X^{\infty}_{N_2}}{X^{\infty}_{O_2}}N_2\right)\rightarrow\left(1-\frac{1}{\phi}\right)F+\frac{1}{\phi}\left[\nu_{O_2}-\left(\nu_{CO_2}+\frac{\nu_{H_2O}}{2}\right)\right]\left(O_2+\frac{X^{\infty}_{N_2}}{X^{\infty}_{O_2}}N_2\right)+\frac{1}{\phi}\nu_{CO_2}CO_2+\frac{1}{\phi}\nu_{H_2O}H_2O \quad \text{(C.21)}$$

The equivalence ratio can be related to the mixture fraction as:

$$\phi=\frac{Z}{1-Z}\frac{1-Z_{st}}{Z_{st}} \quad \text{(C.22)}$$

The system is fuel-lean for $0<\phi<1$, stoichiometric at $\phi=1$, and fuel-rich for $1<\phi<\infty$.

Equations C.21 and C.22 can be used to relate the species composition of a nonpremixed combustion system in the complete combustion, fast chemistry limit to the mixture fraction. The mass fractions of the five species included in this analysis are shown below in Figure C-1.

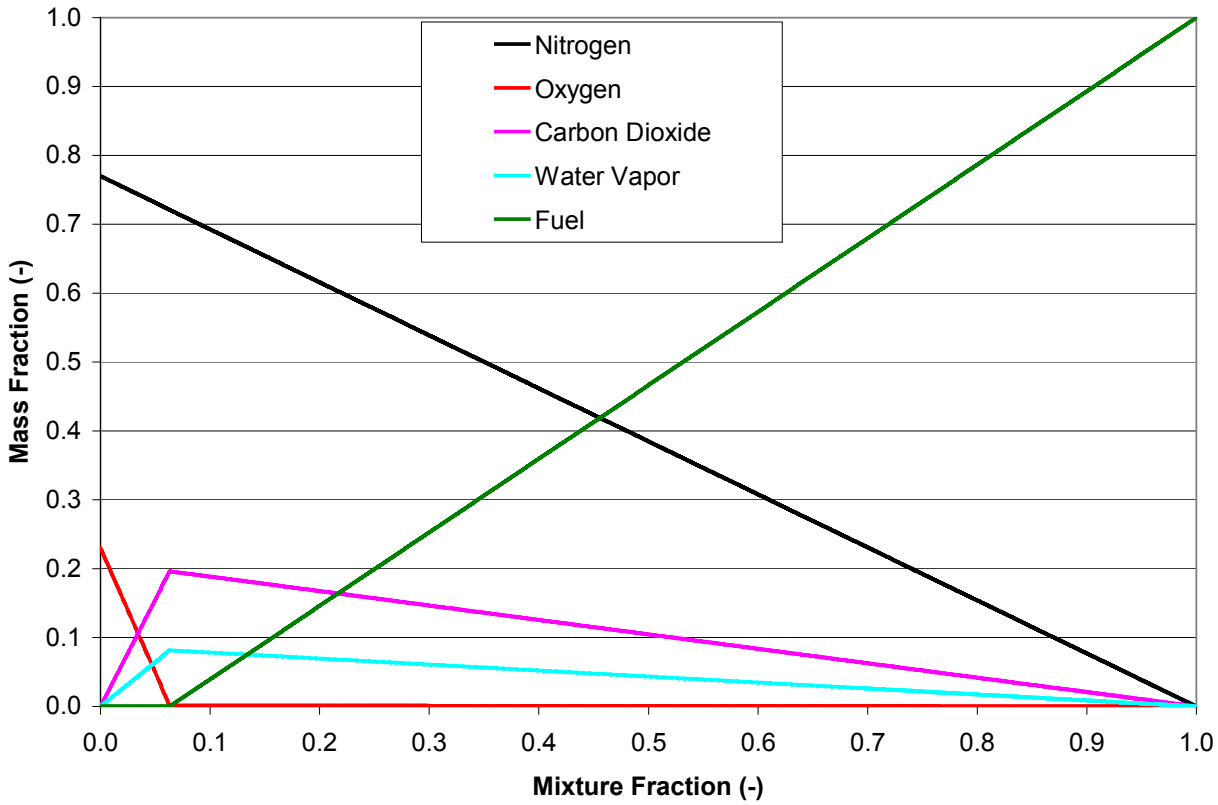

Figure C-1. Complete combustion state relation for ethylene.

Note the mild singularity at the stoichiometric point. In Section C.5, actual experimental species composition measurements show a more smoothed profile near this discontinuity. For this reason, it may be desirable to mathematically "smooth" the state relations near the stoichiometric point. Consider combustion reaction similar to that in Equation C.21, except with the introduction of a parameter ζ that is used to "smooth" the state relations:

$$F + \frac{1}{\phi}\nu_{O_2}\left(O_2 + \frac{X^{\infty}_{N_2}}{X^{\infty}_{O_2}}N_2\right) \rightarrow (1-\zeta)F + \left[\frac{1}{\phi}\nu_{O_2} - \zeta\left(\nu_{CO_2} + \frac{\nu_{H_2O}}{2}\right)\right]\left(O_2 + \frac{X^{\infty}_{N_2}}{X^{\infty}_{O_2}}N_2\right) + \zeta\nu_{CO_2}CO_2 + \zeta\nu_{H_2O}H_2O \quad \text{(C.23)}$$

The parameter ζ is determined as follows:

$$\zeta = \begin{cases} 1/\phi & 1/\phi \le \alpha \\ 1 - B\,\mathrm{erfc}(C + A) & 1/\phi > \alpha \end{cases} \quad \text{(C.24)}$$

$$A = \sqrt{-\ln\left(\sqrt{\pi}/2\right)} \quad \text{(C.25)}$$

$$B = \frac{1-\alpha}{\mathrm{erfc}(A)} \quad \text{(C.26)}$$

$$C = \frac{(x-\alpha)\mathrm{erfc}(A)}{1-\alpha} \quad \text{(C.27)}$$

The parameter α is the degree to which the state relations are smoothed. As $\alpha \rightarrow 1$ the piecewise-linear state relations are retained, and as α decreases the state relations become more smoothed. Similarly, Figure C-2 shows the complete combustion state relation for ethylene with the smoothing parameter α set to 0.25.

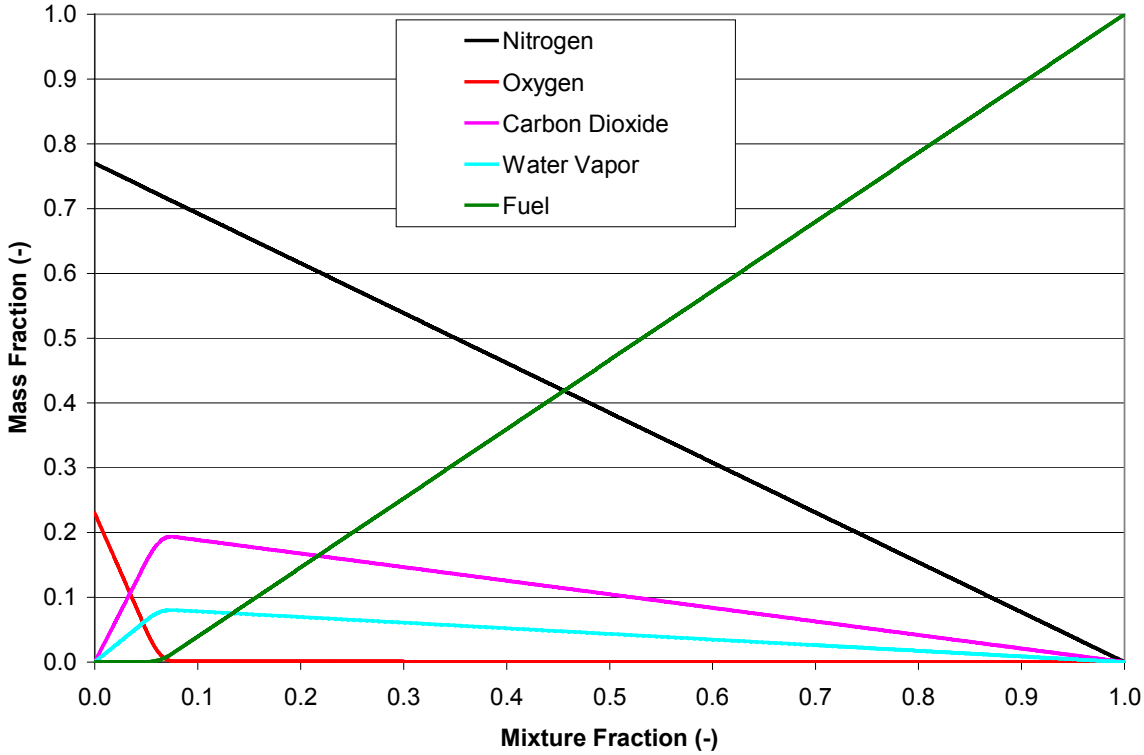

Figure C-2. Complete combustion state relation for ethylene, α=0.80.

C.3 State Relations: Empirical Correlation

Sivathanu and Faeth[2] developed a universal state relation that can be used to estimate the mass fractions of N_2, O_2, fuel, CO_2, H_2O, CO, and H_2 for a range of fuels as a function of the equivalence ratio (or mixture fraction). Its only required inputs are the stoichiometric mass fractions of nitrogen, carbon dioxide, and water vapor—all of which have been measured experimentally or can be estimated from theory.

Consider a C_nH_m-air diffusion flame. Sivathanu and Faeth[2] have provided species-specific values of a parameter ψ for each species that can be used to determine individual species' mass fractions as a function of ϕ. The form of $Y_i(\psi)$ is given below for the seven species.

Table C-1. Summary of generalized state relation functions.

Species	$\psi(Y_i)$	$Y_i(\psi)$
N_2	$\left(\frac{Y_{N_2}^{\infty}-Y_{N_2}^{st}}{Y_{N_2}^{\infty}-Y_{N_2}}\right)\left(\frac{Y_{N_2}}{Y_{N_2}^{st}}\right)$	$\frac{\psi Y_{N_2}^{\infty} Y_{N_2}^{st}}{Y_{N_2}^{\infty}-Y_{N_2}^{st}+\psi Y_{N_2}^{st}}$
O_2	$\left(\frac{32n+8m+M_f Y_{O_2}^{\infty}}{32n+8m+M_f Y_{O_2}}\right)\left(\frac{Y_{O_2}}{Y_{O_2}^{\infty}}\right)$	$\frac{\psi Y_{O_2}^{\infty}(32n+8m)}{32n+8m-\psi Y_{O_2}^{\infty} M_f}$
CO_2	$\left(\frac{44n-M_f Y_{CO_2}^{st}}{44n-M_f Y_{CO_2}}\right)\left(\frac{Y_{CO_2}}{Y_{CO_2}^{st}}\right)$	$\frac{\psi Y_{CO_2}^{st} 44n}{44n-M_f Y_{CO_2}^{st}+\psi Y_{CO_2}^{st} M_f}$
H_2O	$\left(\frac{9m-M_f Y_{H_2O}^{st}}{9m-M_f Y_{H_2O}}\right)\left(\frac{Y_{H_2O}}{Y_{H_2O}^{st}}\right)$	$\frac{\psi Y_{H_2O}^{st} 9m}{9m-M_f Y_{H_2O}^{st}+\psi Y_{H_2O}^{st} M_f}$
CO	$\left(\frac{44n-M_f Y_{CO_2}^{st}}{44n-M_f Y_{CO}}\right)\left(\frac{Y_{CO}}{Y_{CO_2}^{st}}\right)$	$\frac{\psi Y_{CO_2}^{st} 44n}{44n-M_f Y_{CO_2}^{st}+\psi Y_{CO_2}^{st} M_f}$
H_2	$\left(\frac{9m-M_f Y_{H_2O}^{st}}{9m-M_f Y_{H_2}}\right)\left(\frac{Y_{H_2}}{Y_{H_2O}^{st}}\right)$	$\frac{\psi Y_{H_2O}^{st} 9m}{9m-M_f Y_{H_2O}^{st}+\psi Y_{H_2O}^{st} M_f}$
Fuel	Y_f	ψ

The values of $Y_{N_2}^{st}$ $Y_{CO_2}^{st}$ and $Y_{H_2O}^{st}$ can be determined experimentally or theoretically. Sivathanu and Faeth[2] suggest the following values of these parameters for several fuels:

Table C-2. Stoichiometric properties for generalized state relations.

Fuel	C_nH_m	$Y_{N_2}^{st}$	$Y_{CO_2}^{st}$	$Y_{H_2O}^{st}$
Methane	CH_4	0.725	0.151	0.124
Propane	C_3H_8	0.721	0.181	0.098
Heptane	C_7H_{16}	0.719	0.191	0.090
Acetylene	C_2H_2	0.713	0.238	0.049
Ethylene	C_2H_4	0.718	0.200	0.082

The species-specific values of ψ are provided below for each value of ϕ.

Table C-3. Value of generalized state relations.

	$\psi(Y_i, \phi)$						
ϕ	(1) N_2	(2) O_2	(3) CO_2	(4) H_2O	(5) CO	(6) H_2	(7) Fuel
0.00	100.0	1.00	0.0	0.0	0.0	0.0	0.0
0.01	100.0	0.99	0.010	0.010	0.0	0.0	0.0
0.02	50.0	0.98	0.020	0.020	0.0	0.0	0.0
0.05	20.0	0.95	0.050	0.050	0.0	0.0	0.0
0.10	10.0	0.90	0.10	0.10	0.0	0.0	0.0
0.20	5.00	0.80	0.20	0.20	0.0	0.0	0.0
0.50	2.00	0.51	0.48	0.50	0.015	0.0	0.0
0.80	1.25	0.25	0.70	0.78	0.030	0.004	0.0
1.00	1.00	0.11	0.80	0.96	0.115	0.008	0.0
1.50	0.667	0.065	0.82	0.98	0.250	0.018	0.0
2.00	0.500	0.051	0.80	0.97	0.300	0.022	0.028
5.00	0.200	0.041	0.58	0.86	0.260	0.022	0.185
10.0	0.100	0.035	0.40	0.70	0.180	0.020	0.330
20.0	0.050	0.025	0.27	0.49	0.125	0.017	0.550
50.0	0.020	0.018	0.14	0.23	0.070	0.012	0.750
100.0	0.010	0.008	0.06	0.13	0.040	0.0094	0.870
∞	0.0	0.0	0.0	0.0	0.0	0.0	1.0

Note that Table C-3 gives the parameter ψ in terms of the equivalence ratio ϕ. From Equation C.22, the mixture fraction is related to the equivalence ratio as:

$$Z = \frac{\phi}{\frac{1 - Z_{st}}{Z_{st}} + \phi} \tag{C.28}$$

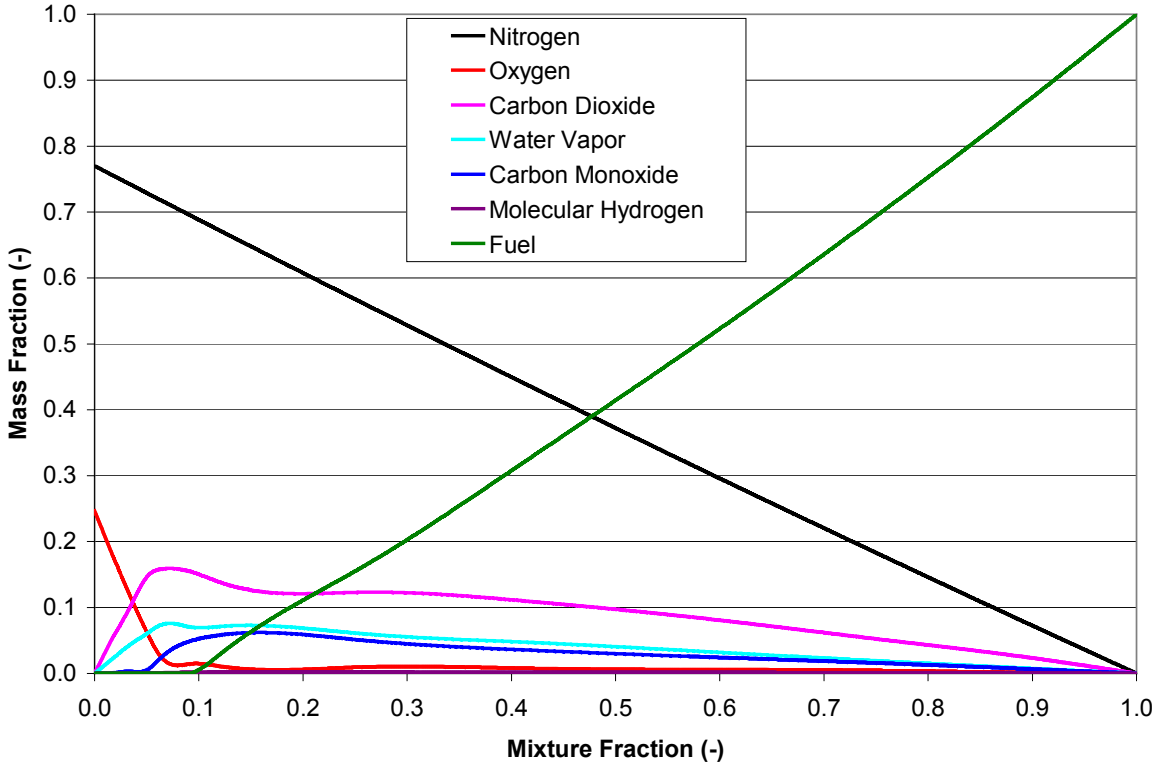

Figure C-3. Sivathanu and Faeth state relation for ethylene.

C.4 State Relations: Equilibrium Chemistry

Another possibility is to use a code that calculates species composition assuming full chemical equilibrium. The NASA CEA (Chemical Equilibrium with Applications) program[3] was used to investigate this possibility. However, the major problem with using this code for flame chemistry state relations is that the CO concentration is greatly overpredicted. Additionally, under full chemical equilibrium, some fuels decompose into graphitic carbon and methane to the fuel-rich side of stoichiometric. A work-around is possible by "freezing" the chemical reaction at a certain equivalence ratio ($\phi \approx 2$) and determining the species mass fractions to fuel rich of this point by assuming frozen scalar mixing. The state relation for ethylene generated with the NASA chemical equilibrium code is shown in Figure C-4. Note the high levels of CO, and the presence of graphitic carbon and methane to the fuel-rich side or stoichiometric.

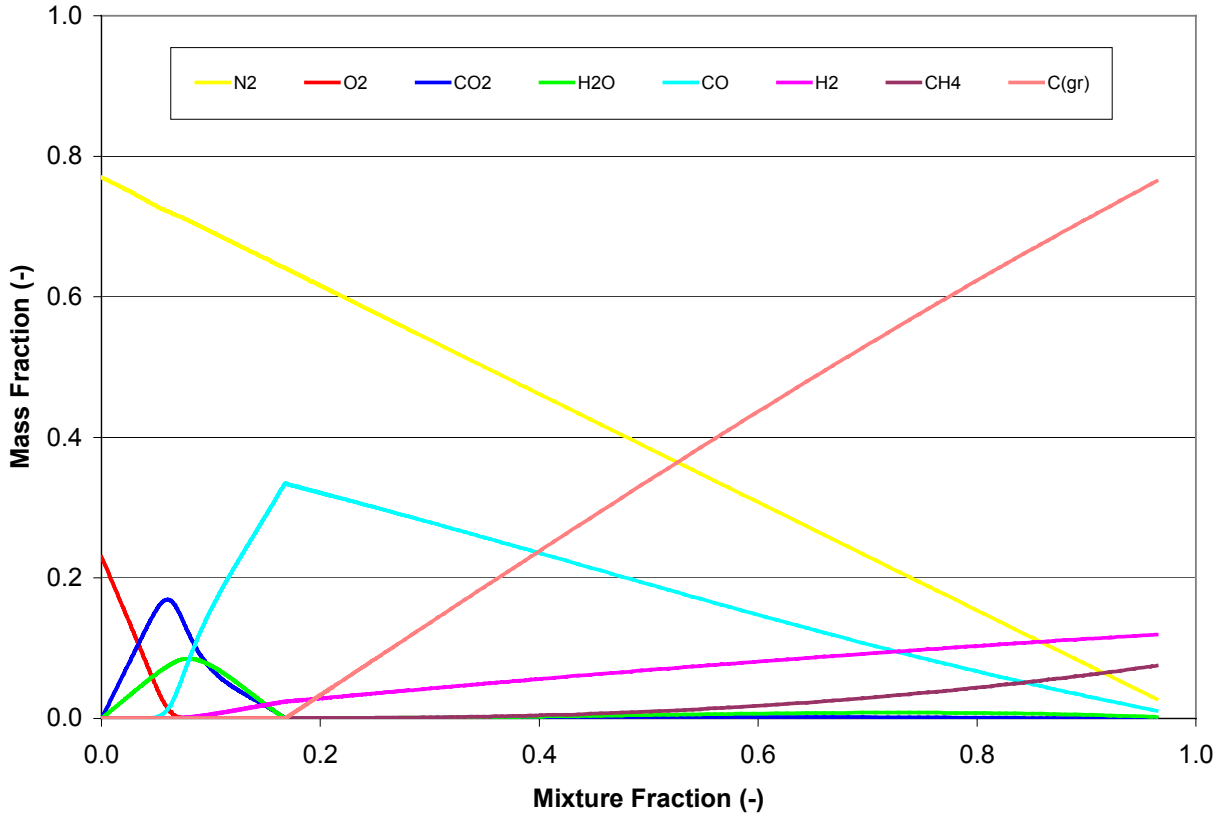

Figure C-4. Equilibrium state relation for ethylene.

C.5 State Relations: Experimental Measurements

Mass fractions of major species have been measured experimentally for a handful of fuels. Measurements of this type present a considerable experimental challenge and are quite tedious. An example of experimentally measured state relations[4] is shown in Figure C-5:

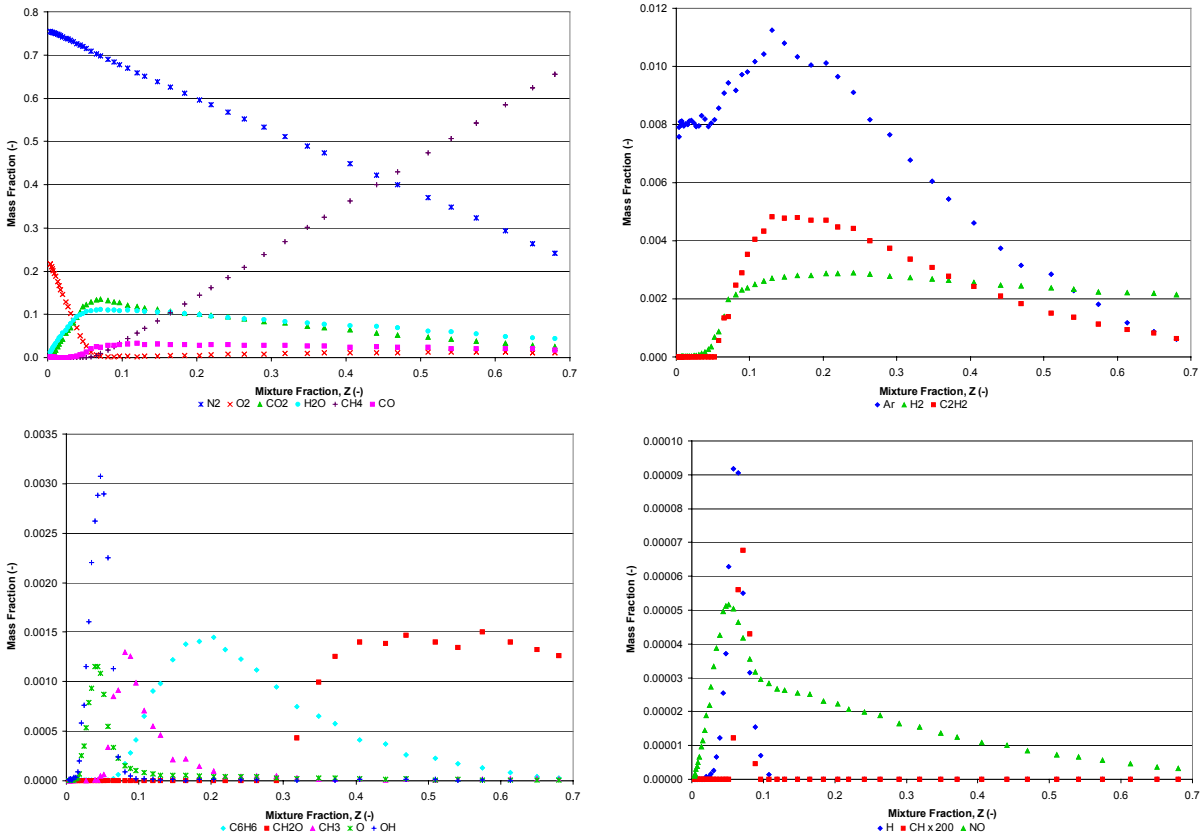

Figure C-5. Experimentally determined state relation for methane.

Note the large number of minor species experimentally observed in the methane flame.

C.6 Appendix C References

1. Peters, N. *Turbulent Combustion*, Cambridge University Press, Cambridge, UK, 2000.

2. Sivathanu, Y.R. and Faeth, G.M., "Generalized State Relationships for Scalar Properties in Nonpremixed Hydrocarbon/Air Flames," *Combustion and Flame* **82**: 211-230 (1990).

3. Gordon, S. and McBride, B.J., "Computer Program for Calculation of Complex Chemical Equilibrium Compositions and Applications," NASA Reference Publication 1311, 1994.

4. Smyth, K.C. http://www.bfrl.nist.gov (1999).

APPENDIX D EXPLICIT SOLUTION OF ENERGY EQUATION

A major part of this work involved reformulating the FDS code to explicitly solve an energy conservation equation. This modification was necessary to apply a correction to bring the temperature predictions of the code in closer agreement with experimental measurements (See Section A.4). This made the modified code more appropriate for calibration of the soot formation and oxidation model developed as part of this work because the soot formation rates are strong functions of temperature. This is also consistent with the desire to calculate radiation from diffusion flames due to the fourth power dependency of radiant emission on temperature.

In FDS v2.0, energy conservation equation is not solved explicitly, but rather used to form an expression for the divergence of the velocity field. The energy conservation equation and the resulting expression for the divergence of the velocity field are given in Equations D.1 and D.2:

$$\frac{\partial(\rho h)}{\partial t} + \nabla \cdot \rho h \boldsymbol{u} = \dot{q}''' - \nabla \cdot \boldsymbol{q}_r + \nabla \cdot k \nabla T \tag{D.1}$$

$$\nabla \cdot \boldsymbol{u} = \frac{\gamma - 1}{\gamma p_0}\left(\dot{q}''' - \nabla \cdot \boldsymbol{q}_r + \nabla \cdot k \nabla T - \frac{1}{\gamma - 1}\frac{dp_0}{dt} \right) \tag{D.2}$$

However, in the modified version of the code, the following form of the energy conservation equation is explicitly solved:

$$\frac{\partial(\rho h_T)}{\partial t} + \nabla \cdot \rho h_T \boldsymbol{u} = \nabla \cdot \rho D \nabla h_T - \nabla \cdot \boldsymbol{q}_r \tag{D.3}$$

and the conservation of mass equation

$$\frac{\partial \rho}{\partial t} + \nabla \cdot \rho \boldsymbol{u} = 0 \tag{D.4}$$

is not explicitly solved, but rather used to form an expression for the divergence of the velocity field:

$$\nabla \cdot \boldsymbol{u} = \frac{1}{T}\left(\frac{DZ}{Dt}\frac{\partial T}{\partial Z}\bigg|_{h_T} + \frac{Dh_T}{Dt}\frac{\partial T}{\partial h_T}\bigg|_{Z} \right) - \frac{1}{\mathscr{M}}\frac{DZ}{Dt}\frac{\partial \mathscr{M}}{\partial Z} \tag{D.5}$$

Appendix D explains how the conservation of energy equation was reformulated in terms of total enthalpy and explicitly solved. Appendix E gives a derivation of Equations D.2 and D.5.

D.2 Sensible Enthalpy, Enthalpy of Formation, and Total Enthalpy

In this work, the *total enthalpy* h_T of a molecule is the sum of its chemical and sensible enthalpies. It is defined on specific (per unit mass basis) and has units of kJ/kg. In classical thermodynamics, the term *total enthalpy* is commonly given the symbol H and is used to refer to the quantity of enthalpy contained in a finite mass of material and therefore has units of kJ. However, in this work the term *total enthalpy* is represented by the symbol h_T and is defined below in Equation D.6.

The *chemical enthalpy* of a molecule is essentially the quantity of energy absorbed (or given off) when it is formed from its atomic constituents at a reference temperature T_0, usually 298.15K. Chemical enthalpy, also referred to as enthalpy of formation h°, is independent of the molecule's temperature. In order to form a molecule with a positive enthalpy of formation, heat must be added to its elemental constituents. Conversely, a substance with a negative enthalpy of formation will liberate energy when it is formed from its elemental constituents. As an example, heat is released when elemental carbon and oxygen combine to yield carbon dioxide, yet heat is

absorbed when elemental carbon and hydrogen react to form ethylene. Table K-2 lists the enthalpy of formation of several substances relevant to diffusion flame thermodynamics.

Unlike chemical enthalpy, *sensible enthalpy* h is a function of temperature. It is a measure of the quantity of heat energy stored in a molecule at a certain temperature. Sensible enthalpy is defined relative to a temperature datum T_0, also usually 298.15K. This is the value of T_0 used in this work.

Consider a mixture of i gases each with mass fractions Y_i. By definition, the total enthalpy is:

$$h_T(T) = \sum_i Y_i \left(h_i^\circ + h_i(T) \right) \tag{D.6}$$

As discussed above, h_i° is the enthalpy of formation of species i and $h_i(T)$ is the sensible enthalpy of species i at temperature T. The sensible enthalpy of a gas is related to the integral of its specific heat from the datum T_0 to T:

$$h_i(T) = \int_{T_0}^{T} c_{p,i}(T) dT \tag{D.7}$$

The temperature-dependency of specific heat is often approximated by a polynomial where the coefficients are determined by a least-squares fit to experimental data. In this country, one of the most commonly used polynomial approximations to specific heat is from the NASA Chemical Equilibrium algorithm of Gordon and McBride [1]. The specific heat (in units of kJ/kg-K) for a large number of gases is given in the following form:

$$c_p(T) = \frac{R}{M} \left(a_1 T^{-2} + a_2 T^{-1} + a_3 + a_4 T + a_5 T^2 + a_6 T^3 + a_7 T^4 \right) \tag{D.8}$$

In Equation D.8, R is 8.31451 kJ/kg-K and the units of M are g/mol, or equivalently kg/kmol. The coefficients a_0 through a_7 appearing Equation D.8 are listed in Appendix K, Tables K-3 and K.4 for several species. The values of M are given in Table K-2. Plots of $c_p(T)$ for several species are shown in Figure D-1 below:

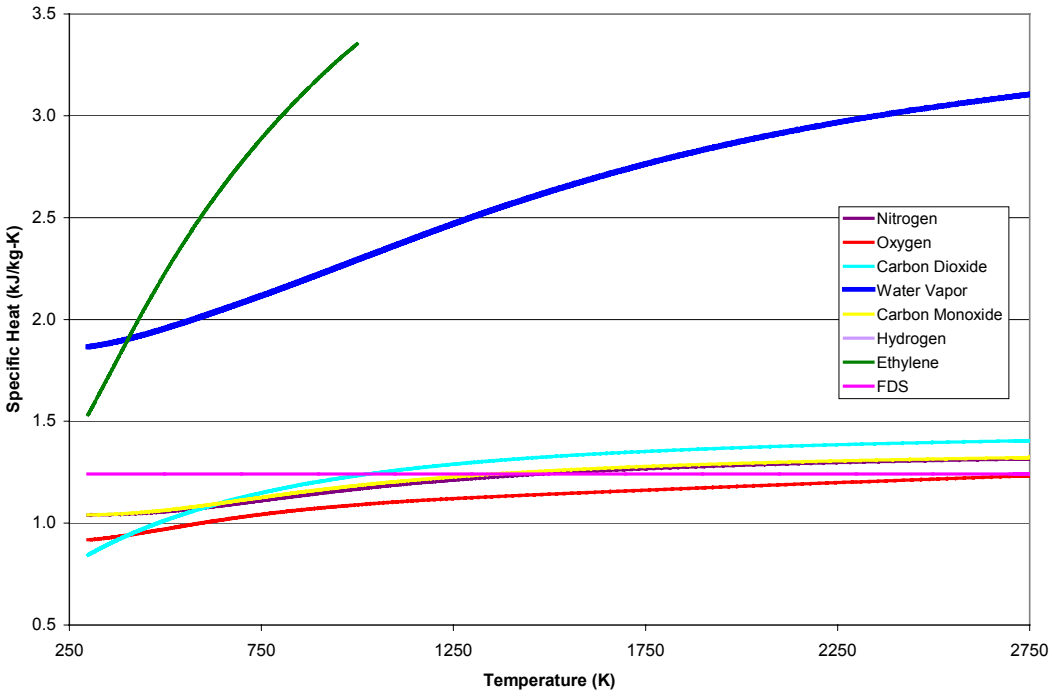

Figure D-1. Temperature dependency of specific heats.

The *total* enthalpy (kJ/kg) is found by integrating Equation D.8 with an appropriate constant of integration, a_8:

$$h_T(T) = \frac{R}{M}\left(-a_1 T^{-1} + a_2 \ln T + a_3 T + \tfrac{1}{2} a_4 T^2 + \tfrac{1}{3} a_5 T^3 + \tfrac{1}{4} a_6 T^4 + \tfrac{1}{5} a_7 T^5 + a_8\right) \qquad \text{(D.9)}$$

The sensible enthalpy (kJ/kg) can be found simply found by subtracting the enthalpy of formation h° given in Table K-2 (in units of kJ/kg) from Equation D.9:

$$h(T) = \frac{R}{M}\left(-a_1 T^{-1} + a_2 \ln T + a_3 T + \tfrac{1}{2} a_4 T^2 + \tfrac{1}{3} a_5 T^3 + \tfrac{1}{4} a_6 T^4 + \tfrac{1}{5} a_7 T^5 + a_8\right) - h^\circ \qquad \text{(D.10)}$$

The values of a_1 through a_8 for 200K < T < 1000K are given in Table K-3. Similarly, the values of a_1 through a_8 for 1000K < T < 6000K are given in Table K-4. The sensible enthalpies of several species are plotted as a function of temperature in Figure D-2:

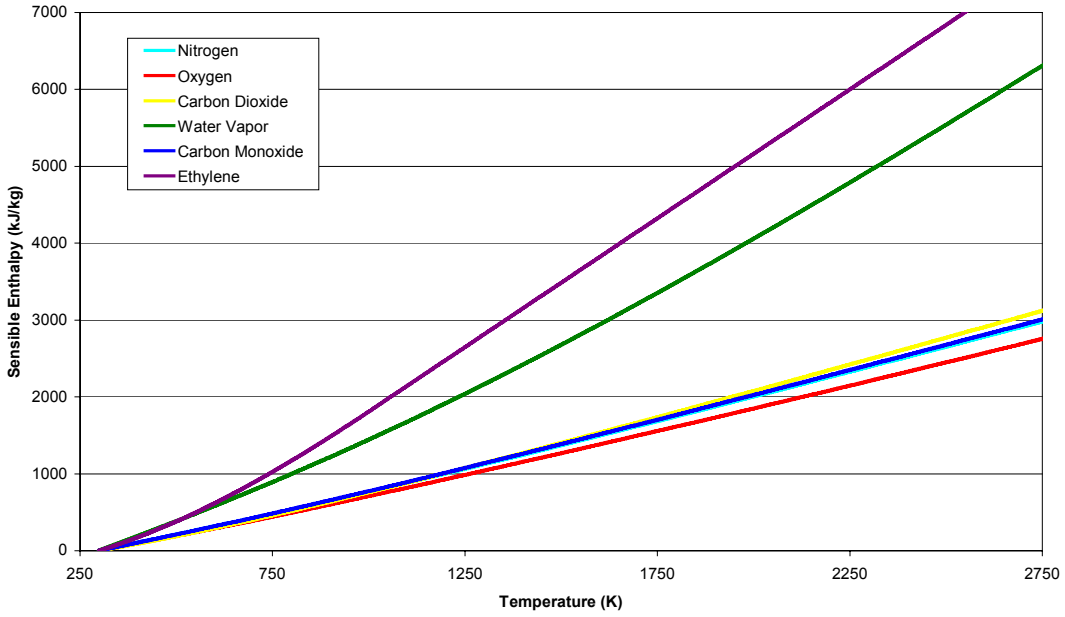

Figure D-2. Sensible enthalpy as a function of temperature.

The total enthalpy is plotted in Figure D-3. Note that this is simply Figure D-2 offset by the enthalpy of formation.

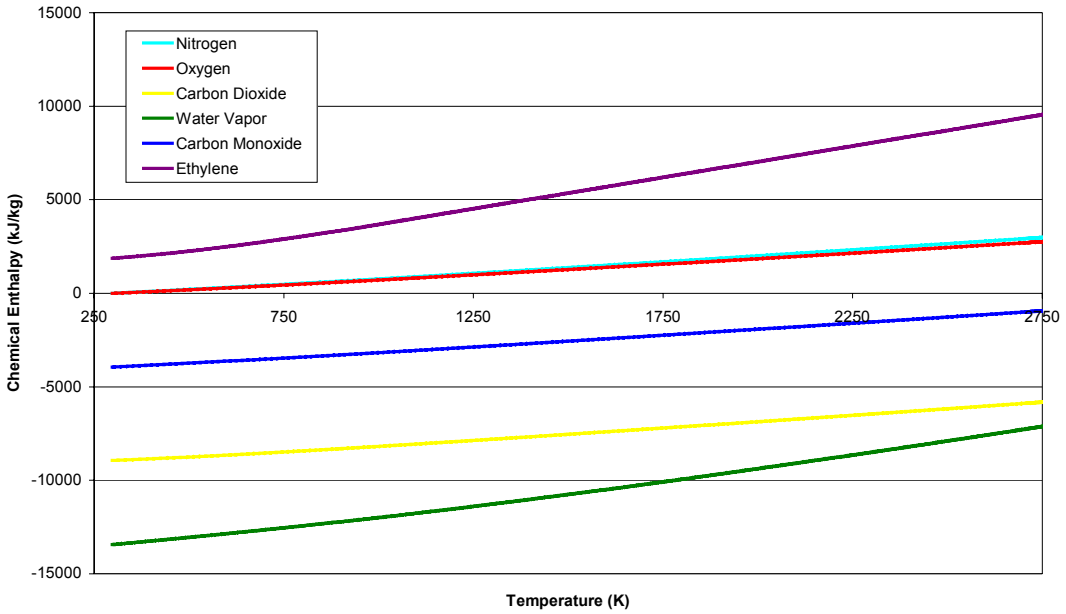

Figure D-3. Total enthalpy as a function of temperature.

D.3 Application to Combustion Systems

Now that total, chemical, and sensible enthalpy have been clearly defined, their relevance to nonpremixed combustion and this work is explained. Consider a diffusion flame in which the fuel and oxidant have equal diffusivities. Furthermore, assume the composition of the products is a unique function of the mixture fraction through a particular set of state relations. This represents a combustion system in which the chemical composition of both the reactants and products are known explicitly in terms of the mixture fraction. Using a subscript r to denote the reactants, and a subscript p to denote the products, the chemical enthalpy of the reactants can be calculated as a function of mixture fraction:

$$h_r^\circ(Z) = Zh_f^\circ + h_o^\circ(1-Z) \tag{D.11}$$

Where h_o° is the chemical enthalpy of the oxidant, equal to zero for an oxidant consisting only of nitrogen and oxygen. The chemical enthalpy of the products is determined as

$$h_p^\circ(Z) = \sum_p Y_p(Z) h_p^\circ \tag{D.12}$$

where the Y_p's are known from a set of state relations, *e.g.* the fast chemistry complete reactions discussed in Appendix C.

In the absence of thermal radiation, total enthalpy is perfectly conserved during the combustion process and the decrease in chemical enthalpy when going from reactants to products is balanced by an increase in sensible enthalpy.

$$\Delta h = \sum_r Y_r h_r^\circ - \sum_p Y_p h_p^\circ \tag{D.13}$$

This is shown graphically in Figure D-4, for methane with complete combustion state relations and the smoothing parameter α set to 0.80.

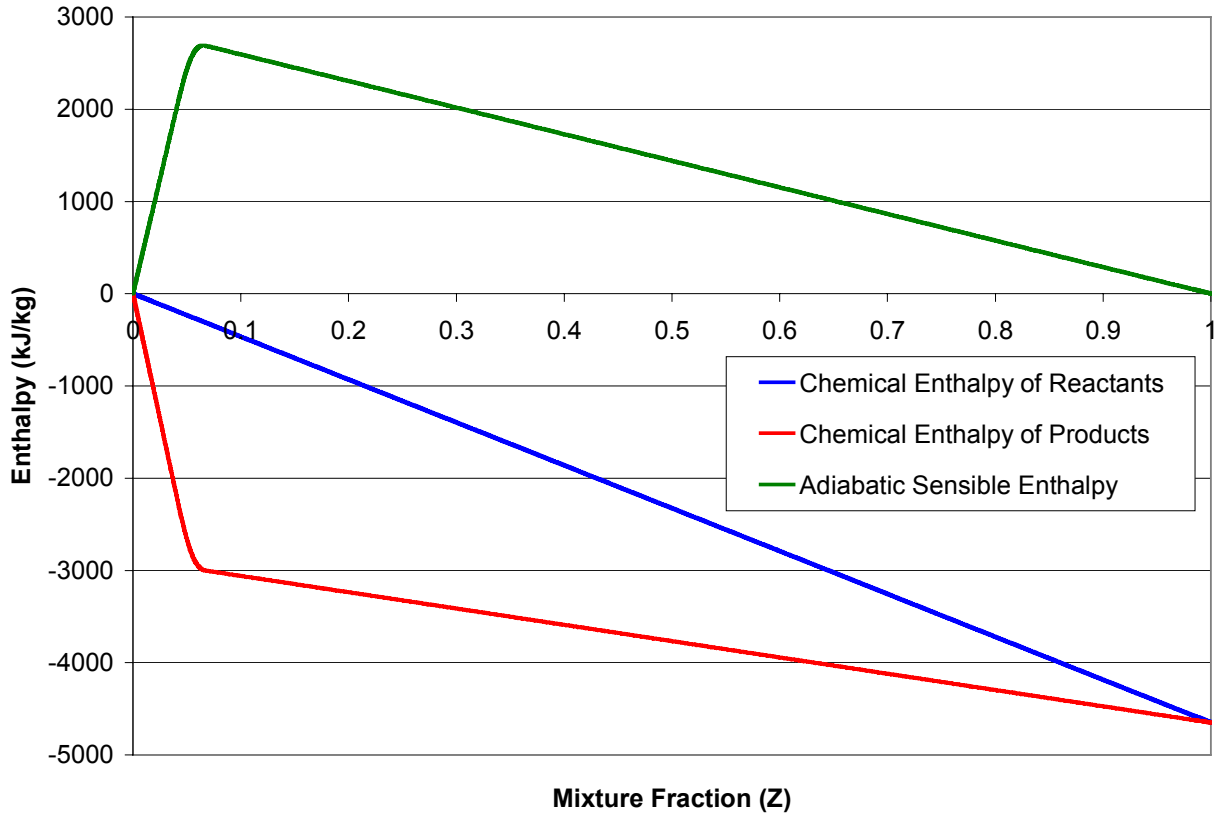

Figure D-4. Adiabatic sensible enthalpy in mixture fraction space.

Per Equation D.7, an increase in temperature must occur as a result of this increase in sensible enthalpy. The most important consequence of this is that the temperature can be determined as a function of chemical composition (mixture fraction) and total enthalpy:

$$T = T\left(Z, h_T\right) \tag{D.14}$$

Although this discussion to this point has presumed an adiabatic combustion system, in actuality thermal radiation will extract sensible enthalpy from the gas phase, causing the sensible enthalpy curve to "sag" and the temperature to drop below its adiabatic value. The nonadiabaticity can be thought of as the fraction of the adiabatic sensible enthalpy that has been lost to radiation. Figure D-5 shows the relationship between mixture fraction and total enthalpy at several nonadiabaticities. Similarly, Figure D-6 shows the relationship between mixture

fraction and sensible enthalpy at several nonadiabaticities. Finally, Figure D-7 shows the resulting mixture fraction-temperature relationship at each of these nonadiabaticities. These plots were generated for complete combustion of methane with $\alpha = 0.80$. This point is important for calculations in turbulent flames, as discussed in Section B.3.1.

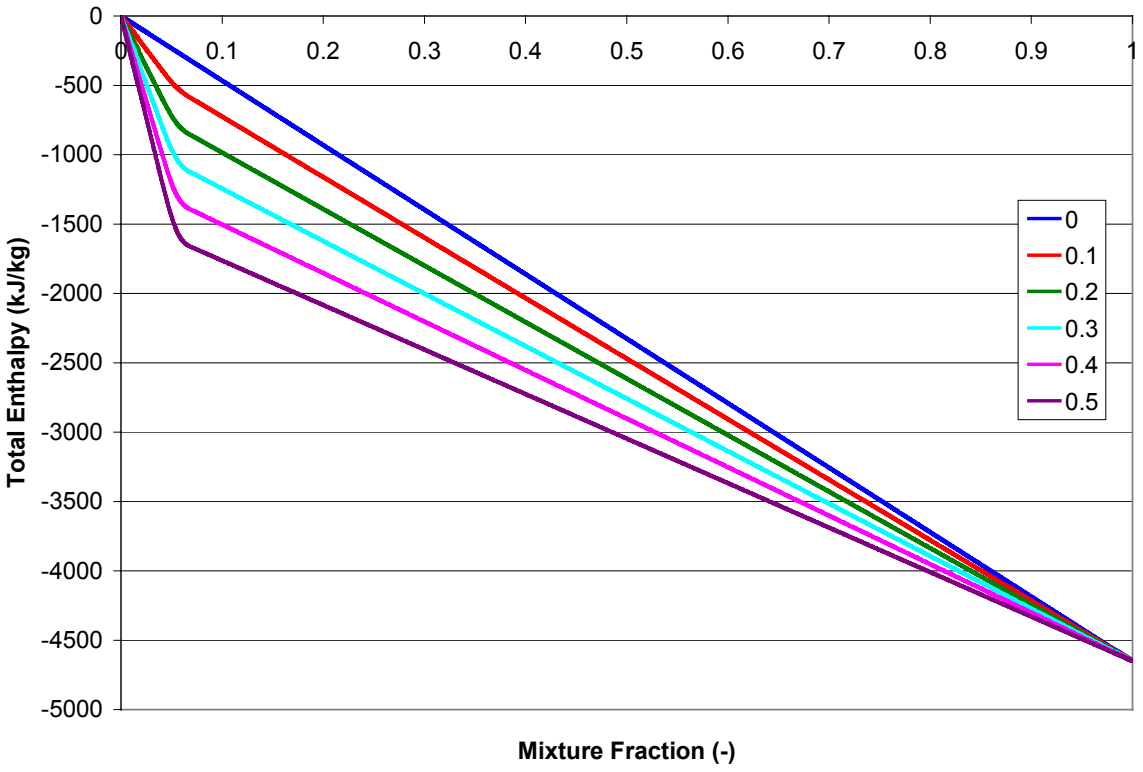

Figure D-5. Relationship between mixture fraction and total enthalpy at several nonadiabaticities.

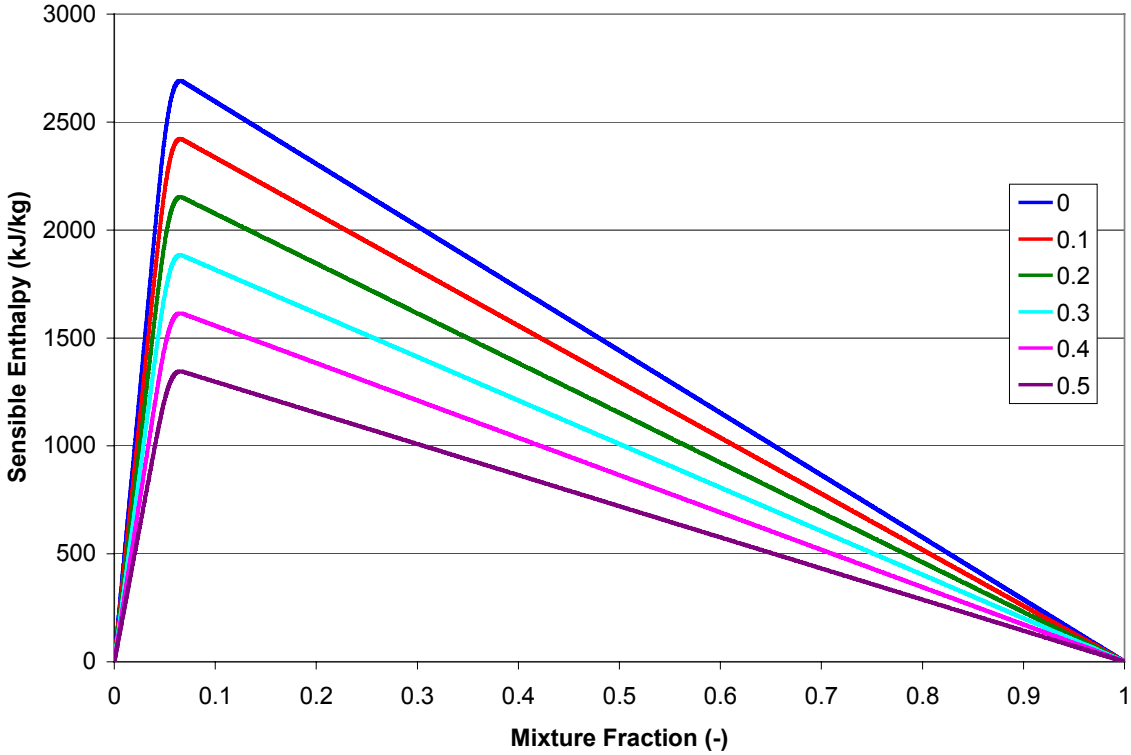

Figure D-6. Relationship between mixture fraction and sensible enthalpy at several nonadiabaticities.

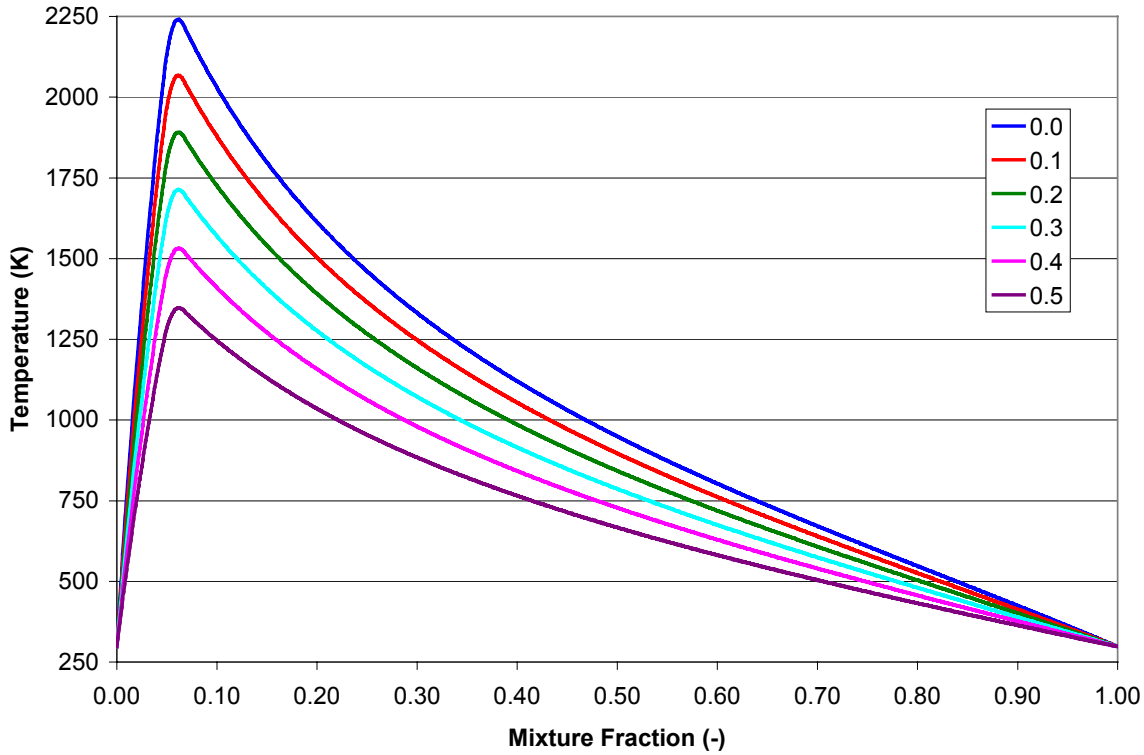

Figure D-7. Relationship between mixture fraction and temperature at several nonadiabaticities.

Figures D-5 through D-7 embody the reason why the decision was made to explicitly solve a conservation of energy equation formulated in terms of total enthalpy. The radiative "history" of a fluid parcel is reflected in its enthalpy. By explicitly solving a conservation equation for mixture fraction and total enthalpy (Equation D.3), the temperature is known at any point in the flowfield. In the modified version of the code, a lookup table is generated that gives the gas-phase temperature for a particular value of mixture fraction and total enthalpy.

The lookup table is generated first by determining the chemical enthalpy of the reactants and the products, for the particular set of state relations being used, from Equations D.11 and D.12. Then, the state relations are used in combination with Equation D.9 to determine the total enthalpy as a function of mixture fraction and temperature, *i.e.* a table for $h_T(Z,T)$ is generated.

This table can then be used to produce a table for $T(Z,h_T)$ through an inverse problem. It was shown in Section A.4 that the temperature predictions in FDS v2.0 were too high on the fuel side, and too low on the oxidant side. An advantage of reformulating the energy equation and generating a lookup table for $T(Z,h_T)$ is that the temperature predictions can be improved simply by subtracting enthalpy on the fuel side, and adding it on the oxidant side.

This was not possible in FDS v2.0 because the combustion model is formulated in a way such that a temperature correction could only be applied by adjusting thermodynamic constants (Pr, Sc) or modifying thermodynamic properties (c_p, μ). Although the temperature predictions could have been improved in this way, it was felt that explicitly solving an equation for the conservation of enthalpy and applying an "enthalpy correction" had more merit.

Although the conservation equation could have been solved in terms of sensible enthalpy, total enthalpy was purposely chosen over sensible enthalpy. The reason for this is the variation of

total enthalpy in mixture fraction space is much smoother than sensible enthalpy (see Figure D-4) and therefore its conservation equation is more amenable to numerical solution.

D.4 Appendix D References

1. Gordon, S. and McBride, B.J., "Computer Program for Calculation of Complex Chemical Equilibrium Compositions and Applications," NASA Reference Publication 1311, 1994.

APPENDIX E DERIVATION OF EXPRESSIONS FOR VELOCITY DIVERGENCE

An essential feature of the NIST FDS model that must be preserved and cannot be modified is the procedure through which the flow-induced perturbation pressure is obtained. More specifically, a Poisson equation for the pressure is solved with a direct (non-iterative) solver that makes use of Fast Fourier Transforms (FFTs). The Poisson equation solved in Fourier space is:

$$\nabla^2 \mathcal{H}^n = -\frac{(\nabla\cdot\boldsymbol{u})^{(n+1)_e} - (\nabla\cdot\boldsymbol{u})^n}{\delta t} - \nabla\cdot\boldsymbol{F}^n \tag{E.1}$$

Here, $\nabla\cdot\boldsymbol{u}$ is the divergence of the velocity field, $\boldsymbol{F}$ is the vector containing the convective, diffusive, and force terms from the momentum equation, and $\nabla\mathcal{H} = \frac{1}{2}\nabla|\boldsymbol{u}|^2 + \frac{1}{\rho}\nabla\tilde{p}$ where $\tilde{p}$ is the flow-induced perturbation pressure. The importance of the $\nabla^2\mathcal{H}$ term is that it is used to obtain the velocity field:

$$\boldsymbol{u}^{n+1} = \frac{1}{2}\left[\boldsymbol{u}^n + \boldsymbol{u}^{(n+1)_e} - \delta t\left(\boldsymbol{F}^{(n+1)_e} + \nabla\mathcal{H}^{(n+1)_e}\right)\right] \tag{E.2}$$

For this reason, any additions or modifications to the thermodynamics of the FDS code, such as solution of a conservation equation for total enthalpy, must preserve the ability to generate an expression for the divergence of the velocity field from thermodynamic quantities.

E.1 NIST FDS v2.0

The first step in developing a new expression for $\nabla\cdot\boldsymbol{u}$ is to derive the expression used in FDS v2.0. Recall that the divergence is formed from the source terms in the conservation of sensible enthalpy equation:

$$\nabla \cdot \boldsymbol{u} = \frac{\gamma - 1}{p_0 \gamma}\left(\dot{q}''' + \nabla \cdot k \nabla T + \nabla \cdot \sum_l h_l (\rho D)_l \nabla Y_l - \frac{1}{\gamma - 1}\frac{dp_0}{dt} \right) \tag{E.3}$$

The derivation begins by defining the total pressure p as a the sum of background pressure p_0, a hydrodsatic pressure $-\rho_\infty gz$, and a flow-induced perturbation pressure $\tilde{p}$:

$$p = p_0 - \rho_\infty gz + \tilde{p} \tag{E.4}$$

The equation of state for an ideal gas is:

$$p = \rho RT \tag{E.5}$$

The low Mach-number assumption involves replacing the pressure total pressure p with the background pressure p_0 in the equation of state. The assumption is that the energy contained in the pressure field is negligible when compared to storage of energy by thermal mechanisms.

$$p \approx p_0 \tag{E.6}$$

Define h as the *sensible enthalpy relative to 0K*, i.e. $T_0 = 0K$ in the integral $h = \int_{T_0}^{T} c_p(T)dT$. For a gas with *constant specific heat* from 0K to *T*:

$$h = c_p T \Rightarrow T = \frac{h}{c_p} \tag{E.7}$$

Substituting Equation E.7 into E.5 and isolating the quantity ρh:

$$p_0 = \frac{\rho R h}{c_p} \Rightarrow \rho h = \frac{p_0 c_p}{R} \tag{E.8}$$

Now introduce the equation for conservation of *sensible* enthalpy:

$$\frac{\partial}{\partial t}(\rho h) + \nabla \cdot \rho h \boldsymbol{u} - \frac{Dp_0}{Dt} = \dot{q}''' + \nabla \cdot k \nabla T + \nabla \cdot \sum_l h_l (\rho D)_l \nabla Y_l \tag{E.9}$$

Note that the $\nabla \cdot \rho h \boldsymbol{u}$ term in Equation E.9 can be expanded as:

$$\nabla \cdot \rho h \boldsymbol{u} = \boldsymbol{u} \cdot \nabla \rho h + \rho h \nabla \cdot \boldsymbol{u} \tag{E.10}$$

Substituting Equation E.10 into E.9 gives:

$$\frac{\partial}{\partial t}(\rho h) + \boldsymbol{u} \cdot \nabla \rho h + \rho h \nabla \cdot \boldsymbol{u} - \frac{Dp_0}{Dt} = \dot{q}''' + \nabla \cdot k \nabla T + \nabla \cdot \sum_l h_l (\rho D)_l \nabla Y_l$$

$$\frac{D\rho h}{Dt} + \rho h \nabla \cdot \boldsymbol{u} - \frac{Dp_0}{Dt} = \dot{q}''' + \nabla \cdot k \nabla T + \nabla \cdot \sum_l h_l (\rho D)_l \nabla Y_l \tag{E.11}$$

Substitute Equation E.8 into Equation E.11, *i.e.* introduce the equation of state.

$$\frac{D}{Dt}\left(\frac{p_0 c_p}{R}\right) + \frac{p_0 c_p}{R} \nabla \cdot \boldsymbol{u} - \frac{Dp_0}{Dt} = \dot{q}''' + \nabla \cdot k \nabla T + \nabla \cdot \sum_l h_l (\rho D)_l \nabla Y_l \tag{E.12}$$

The background pressure does not vary spatially but can vary with time if the enclosure is tightly sealed. Therefore the material derivative can be replaced with the total derivative with respect to time. Making this substitution, considering c_p and R as constants, and performing some algebra gives an expression for the divergence of the velocity field.

$$\frac{c_p}{R}\frac{dp_0}{dt} + \frac{p_0 c_p}{R} \nabla \cdot \boldsymbol{u} - \frac{dp_0}{dt} = \dot{q}''' + \nabla \cdot k \nabla T + \nabla \cdot \sum_l h_l (\rho D)_l \nabla Y_l$$

$$\frac{dp_0}{dt}\left(\frac{c_p}{R} - 1\right) + \frac{p_0 c_p}{R} \nabla \cdot \boldsymbol{u} = \dot{q}''' + \nabla \cdot k \nabla T + \nabla \cdot \sum_l h_l (\rho D)_l \nabla Y_l$$

$$\frac{p_0 c_p}{R} \nabla \cdot \boldsymbol{u} = \dot{q}''' + \nabla \cdot k \nabla T + \nabla \cdot \sum_l h_l (\rho D)_l \nabla Y_l - \frac{dp_0}{dt}\left(\frac{c_p}{R} - 1\right)$$

$$\nabla \cdot \boldsymbol{u} = \frac{R}{p_0 c_p}\left(\dot{q}''' + \nabla \cdot k \nabla T + \nabla \cdot \sum_l h_l (\rho D)_l \nabla Y_l - \frac{dp_0}{dt}\left(\frac{c_p}{R} - 1\right)\right) \tag{E.13}$$

Making the substitution $\frac{R}{c_p} = \frac{\gamma - 1}{\gamma}$ where $\gamma = c_p / c_v$ produces the same expression given in the NIST FDS technical reference that was presented above as Equation E.3:

$$\nabla \cdot \boldsymbol{u} = \frac{\gamma - 1}{p_0 \gamma}\left(\dot{q}''' + \nabla \cdot k \nabla T + \nabla \cdot \sum_l h_l (\rho D)_l \nabla Y_l - \frac{dp_0}{dt}\left(\frac{\gamma}{\gamma - 1} - \frac{\gamma - 1}{\gamma - 1} \right) \right)$$

$$\nabla \cdot \boldsymbol{u} = \frac{\gamma - 1}{p_0 \gamma}\left(\dot{q}''' + \nabla \cdot k \nabla T + \nabla \cdot \sum_l h_l (\rho D)_l \nabla Y_l - \frac{1}{\gamma - 1}\frac{dp_0}{dt} \right) \qquad \text{(E.3)}$$

E.2 Compatible Expression for Explicit Solution Total Enthalpy Conservation

Now that the FDS v2.0 expression has been derived, a new expression that is compatible with an explicit solution of the conservation of total enthalpy equation will be derived. The approach that has been taken here is to begin with conservation of mass and isolate the term $\nabla \cdot \boldsymbol{u}$. Recall that conservation of mass can be written as:

$$\frac{\partial \rho}{\partial t} + \nabla \cdot \rho \boldsymbol{u} = 0 \qquad \text{(E.14)}$$

Make the substitution $\nabla \cdot \rho \boldsymbol{u} = \rho \nabla \cdot \boldsymbol{u} + \boldsymbol{u} \nabla \cdot \rho$:

$$\frac{\partial \rho}{\partial t} + \rho \nabla \cdot \boldsymbol{u} + \boldsymbol{u} \nabla \cdot \rho = 0$$

Substitute $\frac{\partial \rho}{\partial t} + \boldsymbol{u} \nabla \cdot \rho = \frac{D\rho}{Dt}$ and isolate $\nabla \cdot \boldsymbol{u}$:

$$\frac{D\rho}{Dt} + \rho \nabla \cdot \boldsymbol{u} = 0$$

$$\nabla \cdot \boldsymbol{u} = -\frac{1}{\rho}\frac{D\rho}{Dt} \qquad \text{(E.15)}$$

Equation E.15 is the starting point for the new divergence expression. The next step is to make a substitution for ρ from the equation of state, which (making use of the low Mach number assumption and defining a mean molecular weight $\mathscr{M}$) can be written as:

$$p_0 = \rho RT/\mathscr{M} \Rightarrow \rho = \frac{p_0 \mathscr{M}}{RT} \tag{E.16}$$

Substituting Equation E.16 into Equation E.15 and canceling like terms:

$$\nabla \cdot \boldsymbol{u} = -\frac{RT}{p_0 \mathscr{M}} \frac{D}{Dt}\left(\frac{p_0 \mathscr{M}}{RT}\right)$$

$$\nabla \cdot \boldsymbol{u} = -\frac{T}{\mathscr{M}} \frac{D}{Dt}\left(\frac{\mathscr{M}}{T}\right)$$

Apply the quotient rule for differentiation and simplify:

$$\nabla \cdot \boldsymbol{u} = -\frac{T}{\mathscr{M}} \frac{1}{T^2}\left[T \frac{D\mathscr{M}}{Dt} - \mathscr{M} \frac{DT}{Dt}\right]$$

$$\nabla \cdot \boldsymbol{u} = -\frac{1}{\mathscr{M}T} T \frac{D\mathscr{M}}{Dt} + \frac{1}{\mathscr{M}T} \mathscr{M} \frac{DT}{Dt}$$

$$\nabla \cdot \boldsymbol{u} = \frac{1}{T}\frac{DT}{Dt} - \frac{1}{\mathscr{M}} \frac{D\mathscr{M}}{Dt} \tag{E.17}$$

Equation E.17, though and important result, cannot be applied as-is in the FDS code. Note the following:

$$Y_i = Y_i(Z) \Rightarrow \mathscr{M} = \mathscr{M}(\mathrm{Z}) \tag{E.18}$$

$$T = T(Z, h_T) \tag{E.19}$$

Here h_T is the total enthalpy, $h_T = \sum_i Y_i\left(h_i^\circ + h_i(T)\right)$ where h_i° is the enthalpy of formation of species *i* and $h_i(T)$ is the sensible enthalpy of species i at temperature T. The assumptions in Equations E.18 and E.19 allow the following substitutions to be made:

$$\frac{DT}{Dt} = \frac{DZ}{Dt}\frac{\partial T}{\partial Z}\bigg|_{h_T} + \frac{Dh_T}{Dt}\frac{\partial T}{\partial h_T}\bigg|_{Z} \tag{E.20}$$

$$\frac{D\mathscr{M}}{Dt} = \frac{DZ}{Dt}\frac{\partial \mathscr{M}}{\partial Z} \tag{E.21}$$

In Equations E.20 and E.21, the value of $\partial T/\partial Z$ at constant h_T can be evaluated *a priori* and stored in a lookup table using only simple numerical differentiations of the $T(Z,h_T)$ table. Furthermore, the term $\partial T/\partial h_T$ is the inverse of a temperature-dependent specific heat and is a smooth function that is also known beforehand. The term $\partial \mathscr{M}/\partial Z$ is also evaluated quite easily from $Y_i(Z)$. Combining Equations E.17, E.20, and E.21 gives a tractable expression for the divergence of the velocity field:

$$\nabla\cdot\boldsymbol{u} = \frac{1}{T}\left(\frac{DZ}{Dt}\frac{\partial T}{\partial Z}\bigg|_{h_T} + \frac{Dh_T}{Dt}\frac{\partial T}{\partial h_T}\bigg|_{Z}\right) - \frac{1}{\mathscr{M}}\frac{DZ}{Dt}\frac{d\mathscr{M}}{dZ} \tag{E.22}$$

Equation E.23 can be used in FDS by introducing the conservation equations for mixture fraction and total sensible enthalpy:

$$\frac{DZ}{Dt} = \frac{1}{\rho}\left[\nabla\cdot(\rho D\nabla Z) + S_Z\right] \tag{E.24}$$

$$\frac{Dh_T}{Dt} = \frac{1}{\rho}\left[\nabla\cdot(\rho D\nabla h_T) + S_{h_T}\right] \tag{E.25}$$

The mixture fraction source terms is equal in magnitude but opposite in sign to the soot formation/oxidation source term:

$$S_Z = -\dot{\omega}_s''' \tag{E.26}$$

The total enthalpy source term is the sum of radiant emission, radiant absorption, and the change in gas-phase enthalpy due to soot formation or oxidation:

$$S_{h_T} = \dot{q}_e''' + \dot{q}_a''' + \dot{\omega}_{sf}'''h_f^\circ + \dot{\omega}_{so}'''h_{CO}^\circ \tag{E.27}$$

APPENDIX F ADJUSTMENT OF TEMPERATURE PREDICTION

It was shown in Section A.4.1 that for the methane flame under consideration, the calculated temperature was too high on the fuel side and too cool on the oxidant side, even when using experimentally measured species composition to determine the enthalpy of the products. There are several possible explanations for this, including finite rate kinetics, preferential diffusion of heat and species, and nonequal diffusivities. In order to gain a better understanding of the controlling phenomena, a detailed enthalpy flux calculation was performed using the experimental measurements of Smyth[1] for methane burning on a Wolfhard-Parker slot burner. This calculation is given in Section F.1, and the enthalpy correction that was chosen is given in Section F.2.

F.1 Calculation of Enthalpy Flux on a Wolfhard-Parker Slot Burner

From Williams (pg 644, eqn E-46)[2], the complete expression for the heat flux vector $\boldsymbol{q}$ is:

$$\boldsymbol{q} = -k\nabla T + \rho\sum_{i=1}^{N} Y_i h_{T,i}\overline{\boldsymbol{V}_i} + R^0 T\sum_{i=1}^{N}\sum_{j=1}^{N}\left(\frac{X_j D_{T,i}}{M_i D_{ij}}\right)\left(\boldsymbol{V}_i - \boldsymbol{V}_j\right) + \boldsymbol{q_R} \qquad \text{(F.1)}$$

The last two terms on the RHS account for Dufour effects and radiation. The $\boldsymbol{V}_i$ term represents a diffusion velocity and can be approximated by introducing an effective diffusion coefficient D_i for each species, as suggested by Williams (pg 636, eqn E-25)[2]:

$$\boldsymbol{V}_i = -\frac{D_i \nabla Y_i}{Y_i} \qquad \text{(F.2)}$$

Williams goes on to caution (see his Section E.2.4) that the approximation in Equation F.2 can be applied consistently for only *N*-1 species to ensure that $\sum_{i=1}^{N} D_i \nabla Y_i = 0$. Also, he suggests that D_i can be estimated from the binary diffusion coefficient of species *i* diffusing into the background species, which is taken in this case to be nitrogen. After neglecting Dufour effects and radiation, introducing Equation F.2 with D_i approximated as the binary diffusion coefficient of species *i* diffusing into nitrogen, and writing total enthalpy as the sum of chemical and sensible enthalpy, Equation F.1 can be written as:

$$\boldsymbol{q} = -k\nabla T - \rho \sum_{i=1}^{N} \left(h_i^{\circ} + h_i(T)\right) D_{i-N_2} \nabla Y_i \tag{F.3}$$

Considering only the lateral direction, Equation F.3 can be written as:

$$q_x = -k \frac{\partial T}{\partial x} - \rho \sum_{i=1}^{N} \left(h_i^{\circ} + h_i(T)\right) D_{i-N_2} \frac{\partial Y_i}{\partial x} \tag{F.4}$$

Equation F.4 was evaluated using the experimental measurements made in the Smyth methane flame at a height of 9mm, for lateral positions greater than zero, *i.e.* the right-hand flame. The spatial derivatives $\partial T/\partial x$ and $\partial Y_i/\partial x$ were estimated with one-sided differences from the *actual temperature and species composition measurements* in the Wolfhard-Parker methane flame. These measurements include 16 chemical species.

Evaluation of Equation F.4 is particularly difficult because the thermodynamic and transport properties of each of the 16 species are temperature-dependent. The sensible enthalpy of each species was determined as a function of temperature using the polynomials fits from the NASA Chemical Equilibrium Code[3], as discussed in Section D.2. However, values for the

thermal conductivity k and the diffusion coefficient of species *i* diffusing into nitrogen D_{i-N_2} are also required. The thermal conductivity was estimated as

$$k \approx \sum_{i=1}^{N} Y_i k_i \tag{F.5}$$

Strehlow[4] was consulted for guidance in estimating k_i, the thermal conductivity of each species as a function of temperature. He gives an a correction factor that can be used to determine the thermal conductivity of a gas with arbitrary molecular structure from its "monatomic" thermal conductivity:

$$k_i = k_{i,mono}\left[0.115 + 0.354\frac{\gamma_i}{\gamma_i - 1}\right] \tag{F.6}$$

The monatomic thermal conductivity (in units of $\mathrm{J/m \cdot s \cdot K}$) can be estimated from Chapman-Enskog theory[4]:

$$k_{i,mono} = 2.6330\times10^{-5}\frac{\sqrt{T/M_i}}{\sigma_{0,i}^2\Omega_\mu} \tag{F.7}$$

In Equation F.8, $\sigma_{0,i}$ is a species-specific constant and Ω_μ is a function of kT/ε, where ε/k is also fuel-specific constant. Although Ω_μ is usually given in tabular format, the following curvefit was found to give an excellent approximation:

$$\Omega_\mu\left(\frac{T}{\varepsilon/k}\right) = \alpha_{\mu1}\left(\frac{T}{\varepsilon/k}\right)^{\alpha_{\mu2}} + \alpha_{\mu3}\exp\left(\alpha_{\mu4}\frac{T}{\varepsilon/k}\right) + \alpha_{\mu5}\exp\left(\alpha_{\mu6}\frac{T}{\varepsilon/k}\right) \tag{F.9}$$

The parameters in Equation F.9 are given below in Table F-1. In Equation F.6, γ is the ratio of the constant pressure specific heat to the constant volume specific heat:

$$\gamma = c_p / c_v \tag{F.10}$$

Note that by introducing Equation F.10, the quantity $\gamma/(\gamma-1)$ in Equation F.6 can be rewritten as $c_p/(c_p - c_v)$. Recall the definition of the universal gas constant *R*:

$$R = c_p - c_v \tag{F.11}$$

Equations F.10 and F.11 can be used to show that:

$$\frac{\gamma}{\gamma-1} = \frac{c_p}{R} \tag{F.12}$$

Using Equation F.12, the thermal conductivity expression in Equation F.6 was evaluated by replacing $\gamma/(\gamma-1)$ with c_p/R. The variation of c_p/R with temperature was determined from the polynomial fits in the NASA Chemical Equilibrium Code[3]. The binary diffusion coefficient in Equation F.4 was also evaluated from Chapman-Enskog theory. Strehlow[4] gives the following equation to estimate the binary diffusion coefficient for gas 1 diffusing into gas 2:

$$D_{12} = 5.9543\times10^{-6}\,\frac{\sqrt{T^3\left[(1/M_1)+(1/M_2)\right]}}{p(\sigma_0)_{12}^2\,\Omega_{D_{12}}} \tag{F.13}$$

$(\sigma_0)_{12}$ and $(\varepsilon/k)_{12}$ are average values for the two gases:

$$(\sigma_0)_{12} = \frac{1}{2}(\sigma_{0_1} + \sigma_{0_2}) \tag{F.14}$$

$$\left(\frac{\varepsilon}{k}\right)_{12} = \sqrt{\left(\frac{\varepsilon}{k}\right)_1 \left(\frac{\varepsilon}{k}\right)_2} \tag{F.15}$$

The value of $\Omega_{D_{12}}$ is determined from a curvefit similar to that for Ω_μ given above in Equation F.9:

$$\Omega_{D_{12}}\left(\frac{T}{(\varepsilon/k)_{12}}\right) = \alpha_{D1}\left(\frac{T}{(\varepsilon/k)_{12}}\right)^{\alpha_{D2}} + \alpha_{D3}\exp\left(\alpha_{D4}\frac{T}{(\varepsilon/k)_{12}}\right) + \alpha_{D5}\exp\left(\alpha_{D6}\frac{T}{(\varepsilon/k)_{12}}\right) \tag{F.16}$$

The parameters appearing in Equation F.16 are given in Table F-1.

Table F-1. Collision integral curvefit parameters.

Coefficient	μ	D
α_1	1.16145	1.080794
α_2	-0.14874	-0.16033
α_3	0.52487	0.605009
α_4	-0.7732	-0.88524
α_5	2.16178	2.115672
α_6	-2.43787	-2.98308

These transport properties were used to evaluate the lateral enthalpy flux from the expression given as Equation F.4. The result is shown below in Figure F-1. In this figure, the heat flux contribution from the $-k\frac{\partial T}{\partial x}$ term is labeled "Conduction" and the contribution from the $\rho\sum_{i=1}^{N}\left(h_i^\circ + h_i(T)\right)D_{i-N_2}\frac{\partial Y_i}{\partial x}$ term is labeled "Diffusion". Their sum is labeled "Net".

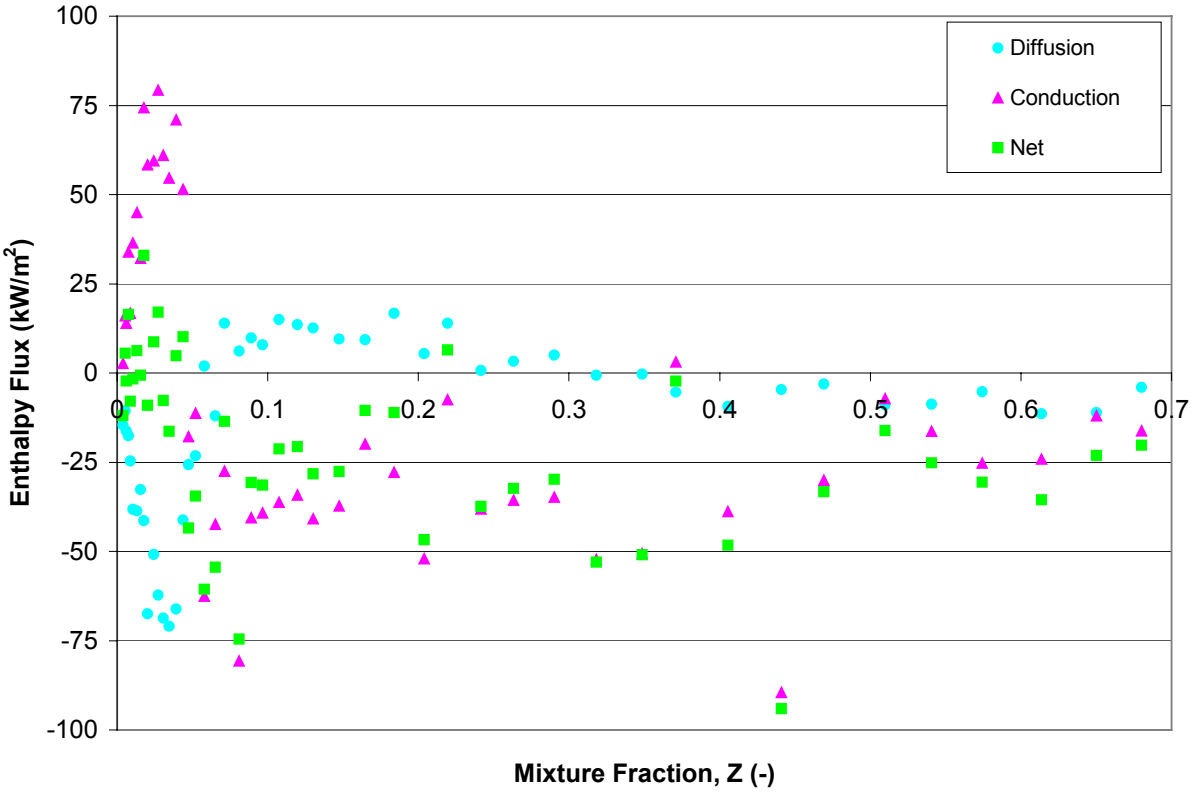

Figure F-1. Heat flux calculation in methane flame on Wolfhard-Parker burner.

The noisiness in Figure F-1 can be attributed to the fact that the diffusion and conduction heat fluxes have determined by spatial derivatives of experimentally-measured species and temperature profiles. However, very important subtle trends are apparent upon closer examination. Most noticeable is that the net heat flux term is negative on the fuel side, but becomes positive on the oxidant side. This implies that enthalpy is being moved from the fuel side to the oxidant side, most likely due to nonunity Lewis number effects and preferential diffusion of certain species. It also helps explains the observation that the temperatures calculated from simple thermodynamics relations using the experimental species composition measurements are too high on the fuel side and too low on the oxidant side.

In order to improve the temperature predictions, it is necessary to introduce a correction that decreases the temperature on the fuel side and increases it on the oxidant side. It was shown

in this section that enthalpy is moved from the fuel side to the oxidant side; therefore, it makes sense to apply a correction that mimics this behavior.

F.2 An "Enthalpy Correction" to Improve Temperature Predictions

In order to artificially remove enthalpy from the fuel side and add enthalpy to the oxidant side, an enthalpy correction is applied in mixture fraction space. It is shown for methane in Figure F-1.

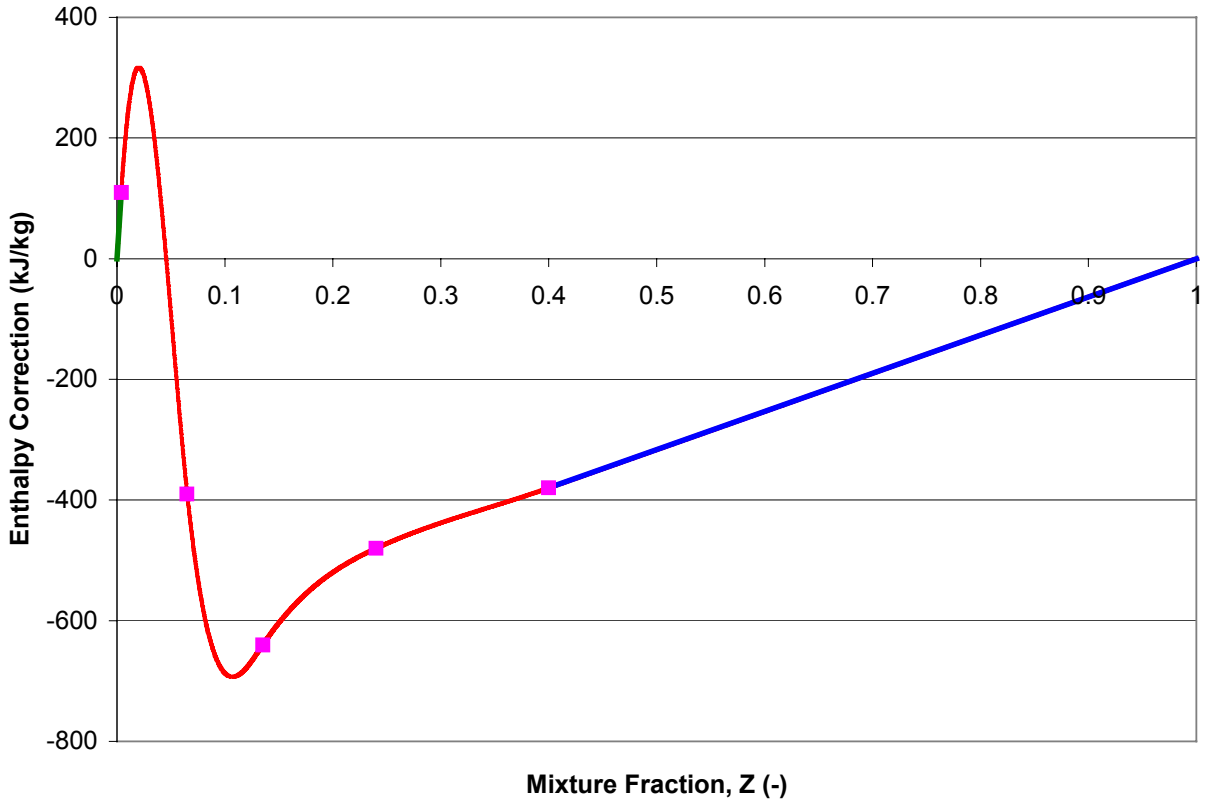

Figure F-2. Enthalpy correction applied in mixture fraction space.

The enthalpy correction has a value of 0 at Z=0 and Z=1. It consists of two straight-line segments connected by four "natural" cubic-spline segments, *i.e.* cubic splines having a zero second derivative at their end points. The points that were specified to generate Figure F-2 are listed below in Table F-2.

Table F-2. Enthalpy correction points specified for methane.

Z	Enthalpy Offset
0.000	0
0.004	110
0.065	-390
0.135	-640
0.240	-480
0.400	-380
1.000	0

The enthalpy correction shown in Figure F-3 is applied by adding it the chemical enthalpy of the products. In this way, the adiabatic sensible enthalpy is artificially altered, thereby modifying the $T(Z, h_T)$ table. Figure F-4 shows how this correction affects the enthalpy of the products, and Figure F-5 shows its effect on the adiabatic temperature. These plots were generated using state relations generated from complete combustion reactions with the smoothing parameter α (See Appendix C) set to 0.8.

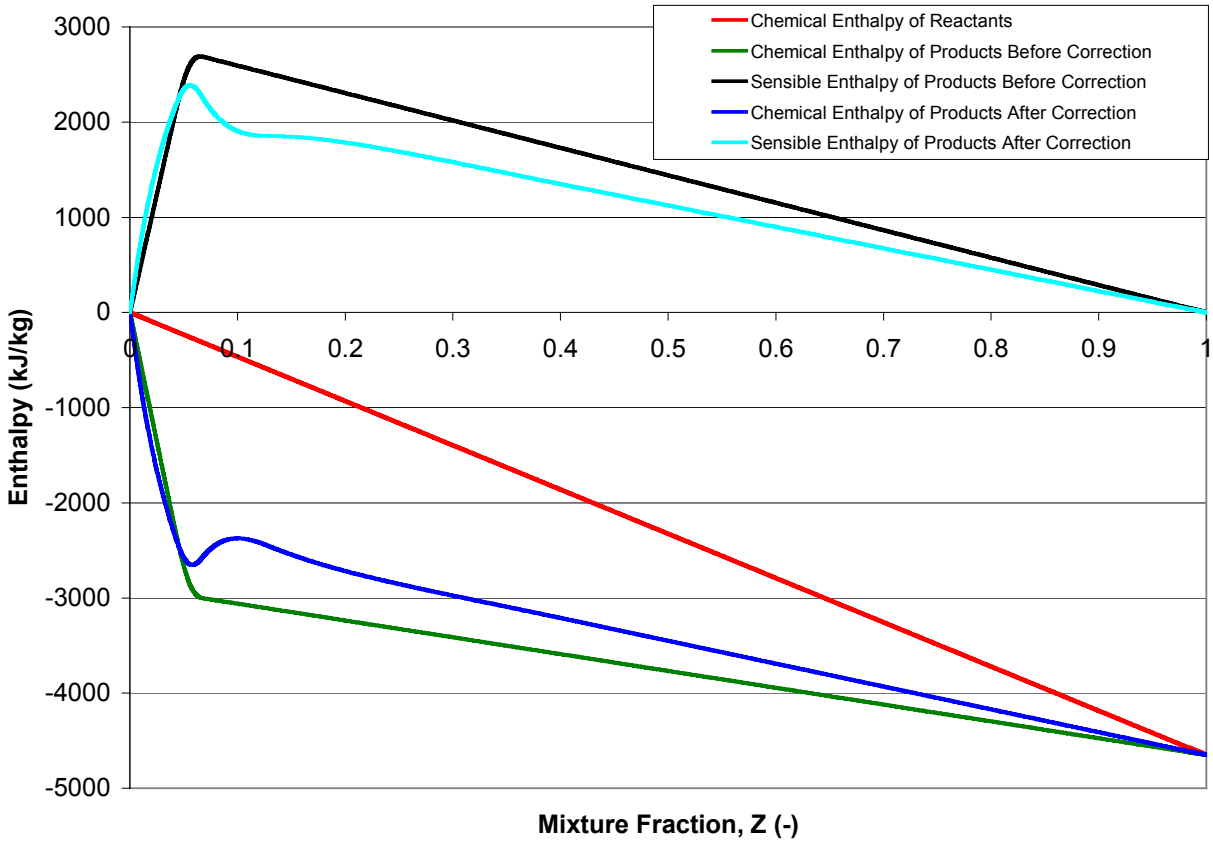

Figure F-4. Enthalpies before and after correction is applied.

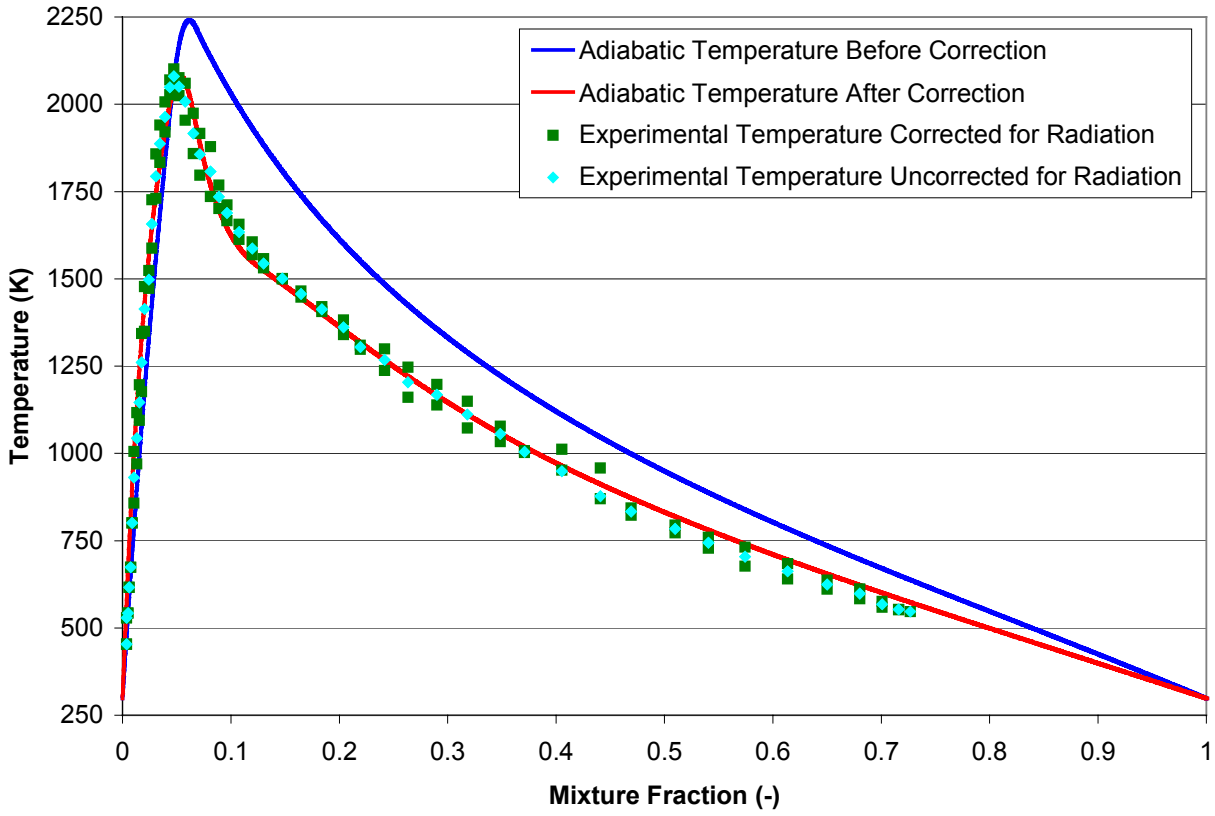

Figure F-5. Adiabatic temperature before and after correction is applied.

F.3 Appendix F References

1. Smyth, K.C. http://www.bfrl.nist.gov (1999).

2. Williams, F.A., *Combustion Theory: The Fundamental Theory of Chemically Reacting Flow Systems*, 2nd Edition, The Benjamin/Cummings Publishing Company, Menlo Park, CA, 1985.

3. Gordon, S. and McBride, B.J., "Computer Program for Calculation of Complex Chemical Equilibrium Compositions and Applications," NASA Reference Publication 1311, 1994.

4. Strehlow, R.A., *Combustion Fundamentals*, McGraw-Hill Book Company, New York, 1984.

APPENDIX G DETERMINING THE POLYNOMIAL COEFFICIENTS OF THE SOOT FORMATION/OXIDATION FUNCTIONS

Several functional forms of explicit expressions in Z and T were considered. In the end, standard polynomials were selected due to their ease of implementation and ability to assume almost any shape at higher orders. An N^{th} –order polynomial with x as the independent variable can be expressed succinctly as

$$f(x) = \sum_{n=0}^{N-1} a_n x^n \tag{G.1}$$

In Equation G.1, the a_n's are the coefficients of the polynomial. The shapes of the $f(Z)$ and $f(T)$ functions can be determined by specifying certain desired characteristics of the curve (*i.e.* by giving a series of point-value or point-slope pairs) and then finding the coefficients by solving the resulting set of linear equations. This process is illustrated here for a cubic polynomial (four coefficients). Extension of this procedure to higher order polynomials is straightforward. A general cubic polynomial $f(x)$ and its first derivative are given as Equations G.2 and G.3:

$$f(x) = a_0 + a_1 x + a_2 x^2 + a_3 x^3 \tag{G.2}$$

$$\frac{df(x)}{dx} = a_1 + 2a_2 x + 3a_3 x^2 \tag{G.3}$$

Assume that $f(x)$ that rises from a value of zero at x_L (x-low) to a peak value of f_P at x_P (x-peak), and then falls back to zero at x_H (x-high). The general shape of this polynomial is shown in Figure G-1 with arbitrarily chosen values of x_L, x_P, x_H, and f_P. $df/dx = 0$

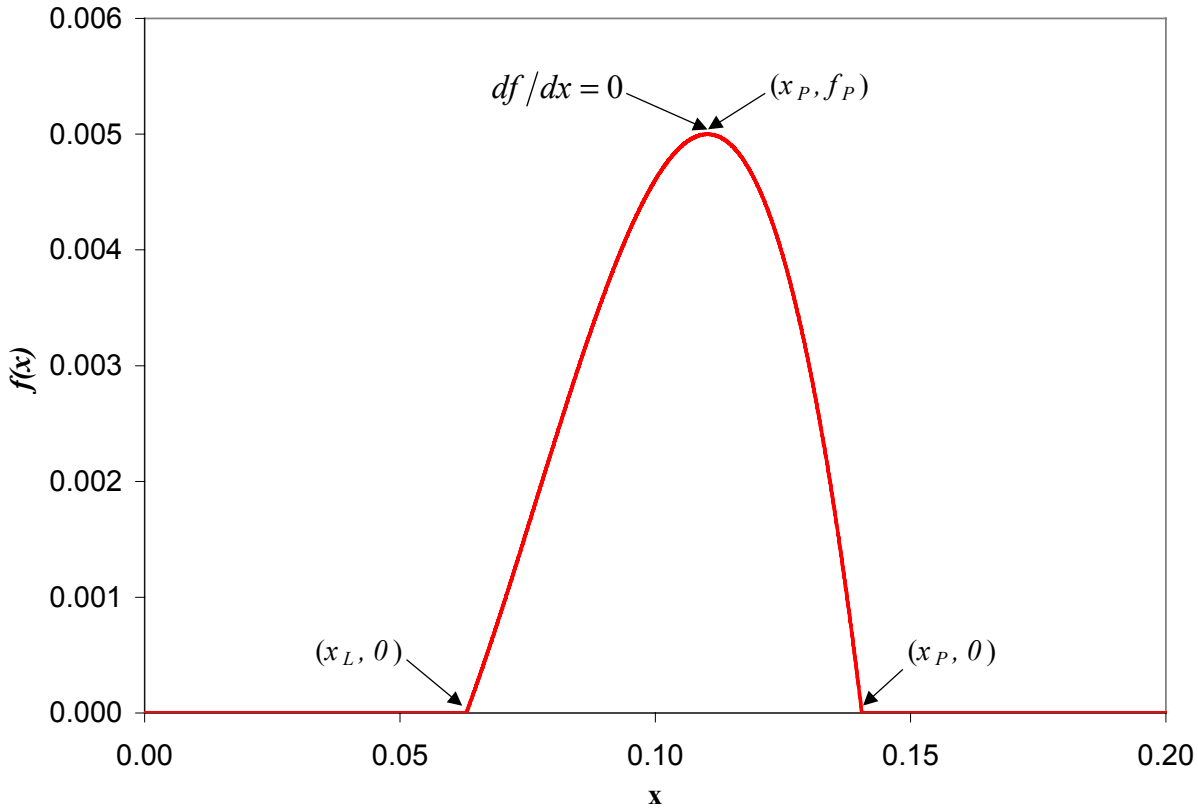

Figure G-1. General cubic polynomial.

The four coefficients of the polynomial can be determined since four conditions have been specified: $f(x_L)=0$, $f(x_P)=f_P$, $f(x_H)=0$, and $df(x_P)/dx=0$. The last condition is a result of the function having a local maximum at x_p. Combined with Equations G.2 and G.3, these four conditions yield a set of four linear equations with four unknowns that can be expressed in matrix notation as:

$$\begin{bmatrix} 1 & x_L & x_L^2 & x_L^3 \\ 1 & x_P & x_P^2 & x_P^3 \\ 1 & 2x_P & 3x_P^2 & 0 \\ 1 & x_H & x_H^2 & x_H^3 \end{bmatrix} \begin{bmatrix} a_0 \\ a_1 \\ a_2 \\ a_3 \end{bmatrix} = \begin{bmatrix} 0 \\ f_P \\ 0 \\ 0 \end{bmatrix} \tag{G.4}$$

The coefficients a_0 through a_3 in Equation G.4 can be determined by several techniques and Gauss-Jordan elimination is used. Using the general technique outlined here, the coefficients of

the soot formation and oxidation polynomials can be determined by specifying a series of point-value and point-slope pairs.

G.1 Appendix G References

1. Press, W.H., Teukolksy, S.A., Vetterling, W.T., and Flannery, B.P., *Numerical Recipes in Fortran 77 The Art of Scientific Computing* 2nd Edition, Cambridge University Press, Cambridge, 1992.

APPENDIX H SOOT ABSORPTION COEFFICIENT

This Appendix is a contribution of Dr. John L. de Ris. Both theory and experiment[1,2] indicate that the spectral absorption-emission coefficient $k_{s\lambda}$ of soot is proportional to the soot volume fraction f_v, while being approximately inversely proportional to wavelength λ:

$$k_{s\lambda} = \frac{B_s f_v}{\lambda} \tag{H.1}$$

Soot particles are typically much smaller than the wavelength, in which case the proportionality constant

$$B_s = \frac{36\pi n\kappa}{\left(n^2 - \kappa^2 + 2\right)^2 + 4n^2\kappa^2} \tag{H.2}$$

where $m = n - i\kappa$ is the soot complex index of refraction. Dalzell and Sarofim[3] suggested the index of refraction $n - i\kappa = 1.57 - 0.56i$. This value yields $B_s = 4.9$. It is common for experimentalists to employ this same index of refraction when inferring soot volume fractions from radiant absorption measurements in flames. To be consistent we must use this same index of refraction, together with $B_s = 4.9$, when calculating the radiant emission from the flames, whose reported f_v values are matched to measurements using this index of refraction.

Recent gravimetric measurements[6] of soot volume fractions suggest instead that $B_s = 8.6$. This means that the soot volume fractions reported in the literature are actually too large by a factor of $8.6/4.9 \approx 1.76$. Here we used Dalzell and Sarofim value and $B_s = 4.9$ to remain consistent with the reported values of f_v.

The emission from a homogeneous cloud of soot of depth, L,

$$\varepsilon_\lambda = 1 - \exp(-k_{s\lambda} L) \tag{H.3}$$

Multiplying by Planck's black body emission $e_{b\lambda}(T)$ at temperature T, and substituting for $k_{s\lambda}$ from Equation H.1 the overall emissivity of the soot cloud is

$$\begin{aligned} \varepsilon_s &= \left(1/\sigma T^4\right)\int_0^\infty \left[1 - \exp(-B_s f_v L/\lambda)\right] e_{b\lambda}(T)\, d\lambda \\ &= 1 - \frac{15}{\pi^4}\psi^{(3)}\left(1 + \frac{B_s f_v L T}{C_2}\right) \end{aligned} \tag{H.4}$$

where $\psi^{(3)}(x) = \int_0^\infty \frac{t^3 e^{-xt}}{1 - e^{-t}}\, dt$ is the classical Pentagamma function[4] and $C_2 = 0.0144(\text{mK})$ is Planck's second constant. The expression $1 - \frac{15}{\pi^4}\psi^{(3)}(1 + x)$ can be approximated by $1 - \exp(-3.6x)$ with little loss of accuracy[5] to yield:

$$\begin{aligned} \varepsilon_s &\cong 1 - \exp(-3.6 B_s f_v L T / C_2) \\ &= 1 - \exp(-\kappa_s L) \end{aligned} \tag{H.5}$$

Equation H.5 yields the soot absorption-emission coefficient

$$\kappa_s = 3.6 B_s f_v T / C_2 = 1225 f_v T \left(\text{m}^{-1}\right). \tag{H.6}$$

H.1 Appendix H References

1. de Ris, J., "Fire Radiation – A Review," *Proceedings of the Combustion Institute* **17**: 1003-1016 (1979).
2. Tien, C.L. and Lee, S.C., "Flame Radiation," *Progress in Energy Combustion Science,* **8:** 41-59 (1982).
3. Dalzell, W.H. and Sarofim, A.L., *J. Heat Transfer* **91**:100 (1969).

4. Abromowitz, M. and Stegun, I.A. *Handbook of Mathematical Functions*, Applied Mathematics Series, **55**, NBS (1964), reprinted by Dover Publications (1968).

5. Yuen, W. W. and Tien, C. L., "A Simple Calculation Scheme for the Luminous Flame Emissivity," *Proceedings of the Combustion Institute* **16**: 1481-1487 (1977).

6. Choi, M.Y., Mulholland, G.W., Hamins, A. and Kashiwagi, T., "Comparisons of the Soot Volume Fraction Using Gravimetric and Light Extinction Techniques," *Combustion and Flame* **102**: 161-169 (1995).

APPENDIX I A NEW QUALITATIVE THEORY FOR SOOT OXIDATION

In general, the present model underpredicts the rate of soot oxidation in the upper regions of the flame, except for the ethylene flames shown in Section A.7. One reason that oxidation is usually underpredicted is that the available soot surface area decreases as the soot volume fraction decreases. Since oxidation is assumed to be proportional to the available soot surface area, this decreases the soot oxidation rate in downstream regions. However, this negative feedback is not seen experimentally in the flames studied here[1]. Therefore, soot oxidation may not be a surface area-controlled process.

Puri, Santoro, and Smyth[2,3] experimentally studied the oxidation of soot and carbon monoxide in laminar axisymmetric methane, methane/butane and methate/1-butene diffusion flames. They measured OH* radical as well as the CO and soot concentration profiles at several axial positions and found that the OH* concentrations are far higher than their equilibrium values throughout much of the flame. In general, OH* reacts more readily with CO than with soot. This explains why CO tends to be consumed first. The presence of soot, however, significantly depresses OH* concentrations in soot-laden regions. In general, O_2 concentrations are very small in regions of active soot oxidation, but they remain larger than their equilibrium values. This is important from a modeling perspective. It means that the generation of OH* and therefore the consumption of CO and soot are controlled by the diffusion of O_2 into the soot oxidation zone rather than being controlled by the surface area of soot. When the radiant heat loss from the soot cools the flame below 1400K, the generation of OH* decreases and soot oxidation slows to the point of releasing soot. Once the soot leaves the active flaming region, its oxidation is likely to be surface area controlled.

One can gain further understanding of soot oxidation process by considering the following simplified soot oxidation reaction mechanism:

$$C_{soot} + OH^* \rightarrow CO + H^* \quad \text{(I.1a)}$$

$$CO + OH^* \rightarrow CO_2 + H^* \quad \text{(I.1b)}$$

$$O_2 + H^* \rightarrow OH^* + O^* \quad \text{(I.1c)}$$

$$O^* + H_2O \rightarrow OH^* + OH^* \quad \text{(I.1d)}$$

$$H^* + OH^* + (M) \rightarrow H_2O + (M) \quad \text{(I.1e)}$$

The above reactions collectively sum to

$$C_{soot} + O_2 \rightarrow CO_2 \quad \text{(I.2)}$$

The first four reactions (Equations 1a through 1d), being bimolecular, are relatively fast when temperatures are above 1400K. However, Equation 1e is a three-body recombination reaction that is quite slow because it requires the simultaneous collision of three molecules. Its slowness leads to a build-up of H* and OH* radicals far above their equilibrium values. The super-equilibrium concentration of radicals leads to the immediate consumption of any molecular oxygen that manages to diffuse to the reaction zone. When the temperature decreases below 1400K, the reaction 1c between O_2 and H* slows and becomes the rate controlling reaction for the entire mechanism. In such circumstances, the concentration of molecular oxygen builds up. Meanwhile, fewer radicals are generated and the soot and CO oxidation reactions, 1a and 1b, slow down leading to the possible release of any soot or CO that had not been previously oxidized.

The above mechanism of soot oxidation in diffusion flames can be modeled by the volumetric soot oxidation rate that depends principally on the mixture fraction with its maximum near the stoichiometric value. The temperature-dependence should be roughly proportional to the rate controlling reaction 1c, $O_2 + H^* \rightarrow OH^* + O^*$. This will allow for the release of soot

under conditions of strong radiant cooling. The experimentally observed[4,5,6] exact similarity of axisymmetric diffusion flames at their smoke points corroborates the claim here that soot oxidation is controlled by the diffusion of molecular oxygen rather than the surface area of soot. If the surface area were controlling, the observed similarity would never be achieved for the wide range of tested fuel smoke points. Future work is planned to investigate this hypothesis.

I.1 Appendix I References

1. Smyth, K.C. http://www.bfrl.nist.gov (1999).
2. Puri, R., Santoro, R.J., and Smyth, K.C., "The Oxidation of Soot and Carbon Monoxide in Hydrocarbon Diffusion Flames," *Combustion and Flame* **97**: 125-144 (1994).
3. Puri, R., Santoro, R.J., and Smyth, K.C., "Erratum - The Oxidation of Soot and Carbon Monoxide in Hydrocarbon Diffusion Flames," *Combustion and Flame* **102**: 226-228 (1995).
4. Markstein, G.H. and de Ris, J., "Radiant Emission and Absorption by Laminar Ethylene and Propylene Diffusion Flames," *Proceedings of the Combustion Institute* **20**:1637-1646 (1984).
5. Kent, J.H., "Turbulent Diffusion Flame Sooting---Relationship to Smoke-Point Test," *Combustion and Flame* **67**: 223 (1987).
6. Gülder, Ö.L., "Influence of Hydrocarbon Fuel Structural Constitution and Flame Temperature on Soot Formation in Laminar Diffusion Flames," *Combustion and Flame*, **78**: 179-194 (1989).

APPENDIX J EFFICIENT INTEGRATION TECHNIQUES IN TURBULENT FLAMES

This appendix presents numerical techniques that can be applied to PDF methods for turbulent nonpremixed combustion.

J.1 Recursive Algorithm for Integration of a Beta PDF and a Standard Polynomial

This appendix gives a method to efficiently integrate the product of a standard Nth order polynomial $f(Z)$ and an assumed beta probability distribution function $P(Z)$ on the interval [0,1]:

$$I = \int_0^1 f(Z)P(Z)dZ \tag{J.1}$$

Here $f(Z)$ is an Nth order polynomial:

$$f(Z) = \sum_{n=0}^{N-1} d_n Z^n \tag{J.2}$$

$P(Z)$ is an assumed beta distribution:

$$P(Z) = \frac{Z^{a-1}(1-Z)^{b-1}}{B(a,b)} \tag{J.3}$$

Where *a* and *b* are determined from the mean value of mixture fraction and its variance:

$$a = \overline{Z}\left(\frac{\overline{Z}(1-\overline{Z})}{\overline{Z''^2}} - 1\right) \tag{J.4}$$

$$b = \frac{a}{\overline{Z}} - a \tag{J.5}$$

In Equation J.3, $B(a,b)$ is the beta function:

$$B(a,b) = \int_0^1 Z^{a-1}(1-Z)^{b-1}dZ \tag{J.6}$$

The beta function can also be expressed as several gamma functions $\Gamma(x)$:

$$B(a,b) = \frac{\Gamma(a)\Gamma(b)}{\Gamma(a+b)} \tag{J.7}$$

The gamma function is related to the factorial as:

$$\Gamma(x) = (x-1)! \tag{J.8}$$

Now define C_n as follows:

$$C_n = \int_0^1 d_n Z^n P(Z) dZ \qquad \therefore I = \sum_{n=0}^{N} C_n \tag{J.9}$$

Substitute the definition of $P(Z)$ from Equation J.3 into Equation J.9 and move the constant d_n outside the integral:

$$C_n = d_n \int_0^1 Z^n \frac{Z^{a-1}(1-Z)^{b-1}}{B(a,b)} dZ \tag{J.10}$$

Noting that $Z^x Z^y = Z^{x+y}$

$$C_n = d_n \int_0^1 \frac{Z^{a+n-1}(1-Z)^{b-1}}{B(a,b)} dZ \tag{J.11}$$

Note that the numerator in Equation J.11 is equivalent to $B(a+n,b)$

$$C_n = d_n \frac{B(a+n,b)}{B(a,b)} \tag{J.12}$$

This crux of this method involves establishing a recursive relation between C_n and C_{n-1}, where C_{n-1} is simply:

$$C_{n-1} = d_{n-1} \frac{B(a+n-1,b)}{B(a,b)} \tag{J.13}$$

The ratio of C_n / C_{n-1} is:

$$\frac{C_n}{C_{n-1}} = \frac{d_n \dfrac{B(a+n,b)}{B(a,b)}}{d_{n-1} \dfrac{B(a+n-1,b)}{B(a,b)}} = \frac{d_n}{d_{n-1}} \frac{B(a+n,b)}{B(a+n-1,b)} \tag{J.14}$$

Replace the beta functions with a series of gamma functions:

$$\frac{C_n}{C_{n-1}} = \frac{d_n}{d_{n-1}} \frac{\Gamma(a+n)\Gamma(b)}{\Gamma(a+n+b)} \frac{\Gamma(a+n-1+b)}{\Gamma(a+n-1)\Gamma(b)} \tag{J.15}$$

Cancel like terms and replace $\Gamma(x)$ with $(x-1)!$ (*i.e.* using Equation J.8):

$$\frac{C_n}{C_{n-1}} = \frac{d_n}{d_{n-1}} \frac{\Gamma(a+n)}{\Gamma(a+n+b)} \frac{\Gamma(a+n-1+b)}{\Gamma(a+n-1)} = \frac{d_n}{d_{n-1}} \frac{(a+n-1)!}{(a+n+b-1)!} \frac{(a+n+b-2)!}{(a+n-2)!} \tag{J.16}$$

Group like terms and replace $x!/(x-1)!$ with x:

$$\frac{C_n}{C_{n-1}} = \frac{d_n}{d_{n-1}} \frac{(a+n-1)!}{(a+n-2)!} \frac{(a+n+b-2)!}{(a+n+b-1)!} = \frac{d_n}{d_{n-1}} \frac{a+n-1}{a+n+b-1} \tag{J.17}$$

Equation J.17 can be used to show that:

$$\frac{C_1}{C_0} = \frac{d_1}{d_0} \frac{a}{a+b}$$

$$\frac{C_2}{C_1} = \frac{d_2}{d_1} \frac{a+1}{a+b+1}$$

$$\frac{C_3}{C_2} = \frac{d_3}{d_2} \frac{a+2}{a+b+2}$$

$$\frac{C_4}{C_3} = \frac{d_4}{d_3} \frac{a+3}{a+b+3}$$

And Equation J.9 can be used to show that $C_0 = d_0$ because $Z^0 = 1$ and $\int_0^1 P(Z)dZ = 1$. Therefore, the sequence of C_n's can be determined as follows:

$$C_0 = d_0$$

$$C_1 = d_0 \frac{d_1}{d_0} \frac{a}{a+b} = d_1 \frac{a}{a+b}$$

$$C_2 = d_1 \frac{a}{a+b} \frac{d_2}{d_1} \frac{a+1}{a+b+1} = d_2 \frac{a}{a+b} \frac{a+1}{a+b+1}$$

$$C_3 = d_2 \frac{a}{a+b} \frac{a+1}{a+b+1} \frac{d_3}{d_2} \frac{a+2}{a+b+2} = d_3 \frac{a}{a+b} \frac{a+1}{a+b+1} \frac{a+2}{a+b+2}$$

$$C_4 = d_3 \frac{a}{a+b} \frac{a+1}{a+b+1} \frac{a+2}{a+b+2} \frac{d_4}{d_3} \frac{a+3}{a+b+3} = d_4 \frac{a}{a+b} \frac{a+1}{a+b+1} \frac{a+2}{a+b+2} \frac{a+3}{a+b+3}$$

This recursive algorithm can be used to evaluate the integral in Equation B-46 in approximately 3 adds, 2 divides, and 2 multiplies for each coefficient in the polynomial. Therefore, the integral of a 19th order polynomial and the PDF can be evaluated with approximately 140 operations. However, the polynomial must be defined on the interval 0 to 1. Therefore this technique cannot be directly used to integrate the soot formation and oxidation polynomials.

J.2 Integration of an Assumed Beta PDF Using Chebyshev Polynomials and Fast Fourier Transforms

This section is a contribution of Dr. John L. de Ris. It explains how the integral $I = \int_0^1 f(Z)P(Z)dZ$ can be evaluated by approximating both $f(Z)$ and $P(Z)$ in terms of Chebyshev polynomials. The Chebyshev coefficients are to be evaluated using Fast Fourier Transforms.

The integral $I = \int_0^1 f(Z)P(Z)dz$ describes the generation and oxidation of soot in turbulent flames. Here *Z* is the mixture fraction, *P(Z)* is the probability density function that the particular fluid element has mixture fraction between *Z* and $Z + \Delta Z$, while *f(Z)* is the net rate of soot formation of a fluid element having mixture fraction *Z*. Chebyshev polynomials are usually expressed the interval $-1 \le x \le +1$ with weighting function $1/\sqrt{1-x^2}$, yielding

$$I = \int_0^1 f(Z)P(Z)dZ = \int_{-1}^1 \left[f(\frac{x+1}{2}) \right] \left[P(\frac{x+1}{2}) \frac{\sqrt{1-x^2}}{2} \right] \frac{dx}{\sqrt{1-x^2}} \tag{J.18}$$

Continuous Approximation

Chebyshev polynomials are defined over the interval –1 to +1 such that

$$T_n(x) = \cos(n \cos^{-1} x) = \cos(n\theta) \tag{J.19}$$
$$(x = \cos\theta)$$

Any continuous function *f(x)*, defined over the interval $-1 \le x \le +1$, can be expressed in terms of these Chebyshev polynomials:

$$f(x) = \sum_1^\infty c_j T_{j-1}(x) - \frac{c_1}{2} \tag{J.20}$$

The Chebyshev coefficients, c_j, generally decrease rapidly once j becomes sufficiently large for the Chebyshev polynomials to approximate the behavior of *f(x)*. This allows one to truncate the expansion at some value *N*-1. One advantage of the Chebyshev approximation is that the approximation error is evenly distributed across the entire interval $-1 \le x \le +1$. The errors tend to be largest at the maxima of the next higher polynomial, $T_N(x)$, and close to zero near the roots of this same (next higher) polynomial.

The Chebyshev definition, Equation J.19, immediately yields the orthoganality property

$$\int_{-1}^1 \frac{T_j(x)T_k(x)}{\sqrt{1-x^2}} dx = \int_0^\pi \cos(j\theta)\cos(k\theta)d\theta = \frac{\pi}{2}\{\delta_{j\,k} + \delta_{j\,0}\delta_{k\,0}\} \tag{J.21}$$

We now define the following Chebyshev expansions.

$$f(\frac{x+1}{2}) = g(x) \cong \sum_{j=1}^N a_j T_{j-1}(x) - \frac{a_1}{2} \tag{J.22a}$$

$$P(\frac{x+1}{2})\frac{\sqrt{1-x^2}}{2} = q(x) \cong \sum_{j=1}^{N} b_j T_{j-1}(x) - \frac{b_1}{2} \tag{J.22b}$$

With coefficients a_k and b_j given by:

$$a_k = \frac{2}{\pi}\int_{-1}^{1} \frac{g(x)T_{k-1}(x)}{\sqrt{1-x^2}}dx \tag{J.23a}$$

$$b_k = \frac{2}{\pi}\int_{-1}^{1} \frac{q(x)T_{k-1}(x)}{\sqrt{1-x^2}}dx \tag{J.23b}$$

To validate the coefficients specified by Equations J.23a and J.23b, we substitute Equations J.22a and J.22b for $g(x)$ and $q(x)$ into Equations J.23a and J.23b and obtain the identities

$$a_k = \frac{2}{\pi}\int_{-1}^{1}\left[\frac{a_1}{2} + \sum_{j=2}^{N} a_j T_{j-1}(x)\right] T_{k-1}(x)\frac{dx}{\sqrt{1-x^2}} = a_k \tag{J.24a}$$

$$b_k = \frac{2}{\pi}\int_{-1}^{1}\left[\frac{b_1}{2} + \sum_{j=2}^{N} b_j T_{j-1}(x)\right] T_{k-1}(x)\frac{dx}{\sqrt{1-x^2}} = b_k \tag{J.24b}$$

after applying the orthoganality property, Equation J.21. Thus the expansions given by the above definitions immediately yield the solution for the integral.

$$\begin{aligned} I &= \int_{-1}^{1} g(x)q(x)\frac{dx}{\sqrt{1-x^2}} \\ &\cong \int_{-1}^{1}\left[\sum_{k=1}^{N} a_k T_{k-1}(x) - \frac{a_1}{2}\right]\left[\sum_{j=1}^{N} b_j T_{j-1}(x) - \frac{b_1}{2}\right]\frac{dx}{\sqrt{1-x^2}} = \frac{\pi}{2}\left\{\sum_{k=1}^{N} a_k b_k - \frac{a_1 b_1}{2}\right\} \end{aligned} \tag{J.25}$$

It remains now to evaluate the Chebyshev coefficients a_k and b_j. The integrals defined in Equation J.22 can be readily evaluated in terms the function values at discrete locations described below.

Discrete Approximation

The Chebyshev coefficients c_j for the function *f(x)* of Equation J.23 can be obtained from a set of *N* discrete values of the function, $f(x_k)$ as follows:

$$c_j = \frac{2}{N}\sum_{1}^{N} f(x_k)T_{j-1}(x_k) \qquad \text{for } j < N \tag{J.26}$$

where the discrete positions x_k are the *N* roots of the Chebyshev polynomial $T_N(x)$, given by

$$x_k = \cos\left[\frac{\pi(k-1/2)}{N}\right] \quad \text{for } k = 1,2,3,...N \tag{J.27}$$

To validate the above expression for the coefficients, we substitute Equation J.20 into Equation J.26 to obtain

$$c_j = \frac{2}{N}\sum_{j=1}^{N}\left[\sum_{m=1}^{N} c_m T_{m-1}(x_k) - \frac{c_1}{2}\right]T_{j-1}(x_k) = c_j \tag{J.28}$$

after using the discrete identity property of Chebyshev polynomials

$$\sum_{k=1}^{N} T_{m-1}(x_k)T_{j-1}(x_k) = \frac{N}{2}\left\{\delta_{mj} + \delta_{m0}\delta_{j0}\right\} \tag{J.29}$$

Evaluation using Fast Fourier Transforms

The definition (Equation J.19) of the Chebyshev polynomials allows one to express Equation J.29 as

$$c_j = \frac{2}{N}\sum_{j=1}^{\grave{N}} f(x_k)\cos\left[\frac{\pi(j-1)(k-1/2)}{N}\right] \tag{J.30}$$

with the x_k given by Equation J.27. Fast Fourier Transforms have a very similar appearance. The forward Fast Fourier Transform of a sequence $\{f_\ell \ for \ \ell = 0,1,2,..,N-1\}$ of N numbers is yields the transformed sequence

$$F_m = \sum_{\ell=0}^{N-1} f_\ell \cos\left[\frac{\pi m(\ell+1/2)}{N}\right] \quad \text{for } m = 1,\ 2 \ldots N \tag{J.31}$$

Using the Inverse Fast Fourier Transform one can recover the same sequence of numbers,

$$f_\ell = \frac{2}{N} \sum_{m=0}^{N-1}{}' F_m \cos\left[\frac{\pi m(\ell+1/2)}{N}\right] \quad for\ \ell = 1,\ 2 \ldots N \tag{J.32}$$

The prime on the latter summation means that the term for the lowest index is multiplied by ½. To evaluate the c_j one makes the following substitutions into Equation J.31

$$\begin{aligned} &\ell = k-1 \\ &m = j-1 \\ &f_\ell = f(x_k) \\ &c_j = \frac{2}{N} F_m = \frac{2}{N} \sum_{\ell=0}^{N-1} f_\ell \cos\left[\frac{\pi m(\ell+1/2)}{N}\right] \\ &\quad = \frac{2}{N} F_{j-1} = \frac{2}{N} \sum_{k=1}^{N} f(x_k) \cos\left[\frac{\pi(j-1)(k-1/2)}{N}\right] \end{aligned} \tag{J.33}$$

which has the same appearance as Equation J.30.

The algorithm "cosft2(y, n, isign)" in Press *et. al.*[1] calculates the forward and inverse Fast Fourier Transforms defined by Equations J.28 and J.29. Here *y(n)* serves as both the input and output vectors while n is its length. Finally, isign is +1 for the forward transform and –1 for the inverse transform. The evaluation of Fast Fourier Transforms is much faster when the length, *n* is some power of 2 -- say either 64 or 128.

J.3 Appendix J References

1. Press, W.H., Teukolksy, S.A., Vetterling, W.T., and Flannery, B.P., *Numerical Recipes in Fortran 77 The Art of Scientific Computing* 2nd Edition, Cambridge University Press, Cambridge, 1992.

APPENDIX K THERMODYNAMIC AND TRANSPORT PROPERTIES

This appendix gives the thermodynamic and transport property coefficients that have been used in this work. These are listed because they have either been incorporated into the code and/or used in calculations discussed throughout this thesis. The literature sources for the coefficients are given in Table K-1. In this table "LJ" denotes Lennard-Jones coefficients, and "NASA" denotes coefficients given in the NASA Chemical Equilibrium Code format. The numbers correspond to the references at the end of this appendix.

Table K-1. Sources of thermodynamic and transport property coefficients.

Species	c_p NASA	μ NASA	μ LJ	k NASA	k LJ	D LJ
Air	1		2		2	2
Ar	1	1	2	1	2	2
C_2H_2	1	1	2	1	2	2
C_2H_4	1	1	2	1	2	2
C_2H_6	1	1	3	1	3	3
C_3H_8	1		3		3	3
i-C_4H_{10}			3		3	3
n-C_5H_{12}			3		3	3
n-C_6H_{14}			3		3	3
n-C_8H_{18}			3		3	3
Cyclohexane			3		3	3
C_6H_6	1		3		3	3
CH	1		2		2	2
CH_2O	1					
CH_3	1					
CH_4	1	1	2	1	2	2
CN	1					
CO	1	1	2	1	2	2
CO_2	1	1	2	1	2	2
H	1	1	2	1	2	2
H_2	1	1	2	1	2	2
H_2O	1	1	2	1	2	2
HCN	1	1	2	1	2	2
He	1	1	2	1	2	2
N	1	1	2	1	2	2
N_2	1	1	2	1	2	2
N_2O	1	1	2	1	2	2
Ne	1	1	2	1	2	2
NH			2		2	2
NH_3	1	1	2	1	2	2
NO	1	1	2	1	2	2
NO_2	1	1		1		
O	1	1	2	1	2	2
O_2	1	1	2	1	2	2
OH	1	1	2	1	2	2

K.1 Thermodynamic and Transport Property Coefficients

Table K-2. Molecular weight and enthalpy of formation.

Species	Name	M g/mol	$h^\circ_{298.15}$ J/mol	$h^\circ_{298.15}$ kJ/kg
N_2	Nitrogen	28.01348	0.000	0.000
O_2	Oxygen	31.99880	0.000	0.000
CO_2	Carbon Dioxide	44.00950	-393510.000	-8941.479
H_2O	Water Vapor	18.01528	-241826.000	-13423.383
CO	Carbon Monoxide	28.01010	-110535.196	-3946.262
H_2	Hydrogen	2.01588	0.000	0.000
CH_4	Methane	16.04246	-74600.000	-4650.160
C_3H_8	Propane	44.09562	-104680.000	-2373.932
C_7H_{16}	Heptane	100.20194	-187780.000	-1874.016
C_2H_2	Acetylene	26.03728	+228200.000	+8764.356
C_2H_4	Ethylene	28.05316	+52500.000	+1871.447
C_6H_6	Benzene	78.11184	+82880.000	+1061.043
HCHO	Formaldehyde	30.02598	-108580.000	-3616.202
CH_3	Methyl	15.03452	+146900.000	+9770.847
CH	Methylidyne	13.01864	+587370.604	+45117.662
NO	Nitric Oxide	30.00614	+91271.310	+3041.754
H	H atom	1.00794	+217998.828	+216281.552
O	O atom	15.99940	+249175.003	+15574.022
OH	Hydroxyl Radical			

Table K-3. NASA specific heat polynomial coefficients for 200K < T < 1000K.

Spec.	a_1	a_2	a_3	a_4	a_5	a_6	a_7	a_8
N_2	2.210371497E+04	-3.818461820E+02	6.082738360E+00	-8.530914410E-03	1.384646189E-05	-9.625793620E-09	2.519705809E-12	7.108460860E+02
O_2	-3.425563420E+04	4.847000970E+02	1.119010961E+00	4.293889240E-03	-6.836300520E-07	-2.023372700E-09	1.039040018E-12	-3.391454870E+03
CO_2	4.943650540E+04	-6.264116010E+02	5.301725240E+00	2.503813816E-03	-2.127308728E-07	-7.689988780E-10	2.849677801E-13	-4.528198460E+04
H_2O	-3.947960830E+04	5.755731020E+02	9.317826530E-01	7.222712860E-03	-7.342557370E-06	4.955043490E-09	-1.336933246E-12	-3.303974310E+04
CO	1.489045326E+04	-2.922285939E+02	5.724527170E+00	-8.176235030E-03	1.456903469E-05	-1.087746302E-08	3.027941827E-12	-1.303131878E+04
H_2	4.078322810E+04	-8.009185450E+02	8.214701670E+00	-1.269714360E-02	1.753604930E-05	-1.202860160E-08	3.368093160E-12	2.682484380E+03
CH_4	-1.766850998E+05	2.786181020E+03	-1.202577850E+01	3.917619290E-02	-3.619054430E-05	2.026853043E-08	-4.976705490E-12	-2.331314360E+04
C_3H_8	-2.431722550E+05	4.653455400E+03	-2.937377870E+01	1.188288030E-01	-1.375333190E-04	8.807975650E-08	-2.341112880E-11	-3.539084140E+04
C_7H_{16}	-6.127432750E+05	1.184085400E+04	-7.487188410E+01	2.918466000E-01	-3.416795410E-04	2.159285210E-07	-5.655852550E-11	-8.013408770E+04
C_2H_2	1.598133250E+05	-2.216675050E+03	1.265725610E+01	-7.980170140E-03	8.055801510E-06	-2.433944610E-09	-7.509454610E-14	3.712633790E+04
C_2H_4	-1.163613270E+05	2.554860520E+03	-1.609750300E+01	6.625786370E-02	-7.885086390E-05	5.125223790E-08	-1.370338460E-11	-6.176236060E+03
Ar	0.000000000E+00	0.000000000E+00	2.500000000E+00	0.000000000E+00	0.000000000E+00	0.000000000E+00	0.000000000E+00	-7.453750000E+02
C_6H_6	-1.682826540E+05	4.412514520E+03	-3.722063930E+01	1.641918150E-01	-2.023219880E-04	1.309662940E-07	-3.448887830E-11	-1.039254320E+04
CH_2O	-1.173922110E+05	1.873636547E+03	-6.890327710E+00	2.641571472E-02	-2.186402425E-05	1.005702110E-08	-2.023502935E-12	-2.307355518E+04
CH_3	-2.876188806E+04	5.093268660E+02	2.002143949E-01	1.363605829E-02	-1.433989346E-05	1.013556725E-08	-3.027331936E-12	1.411181918E+04
CH	2.220590133E+04	-3.405411530E+02	5.531452290E+00	-5.794964260E-03	7.969554880E-06	-4.465911590E-09	9.596338320E-13	7.240783270E+04
H	0.000000000E+00	0.000000000E+00	2.500000000E+00	0.000000000E+00	0.000000000E+00	0.000000000E+00	0.000000000E+00	2.547370801E+04
NO	-1.143916503E+04	1.536467592E+02	3.431468730E+00	-2.668592368E-03	8.481399120E-06	-7.685111050E-09	2.386797655E-12	9.098214410E+03
O	-7.953611300E+03	1.607177787E+02	1.966226438E+00	1.013670310E-03	-1.110415423E-06	6.517507500E-10	-1.584779251E-13	2.840362437E+04
OH	-1.998858990E+03	9.300136160E+01	3.050854229E+00	1.529529288E-03	-3.157890998E-06	3.315446180E-09	-1.138762683E-12	3.239683480E+03

Table K-4. NASA specific heat polynomial coefficients for 1000K < T < 6000K.

Spec.	a_1	a_2	a_3	a_4	a_5	a_6	a_7	a_8
N_2	5.87712406E+05	-2.23924907E+03	6.06694922E+00	-6.13968550E-04	1.49180668E-07	-1.92310549E-11	1.06195439E-15	1.28321042E+04
O_2	-1.03793902E+06	2.34483028E+03	1.81973204E+00	1.26784758E-03	-2.18806799E-07	2.05371957E-11	-8.19346705E-16	-1.68901093E+04
CO_2	1.17696242E+05	-1.78879148E+03	8.29152319E+00	-9.22315678E-05	4.86367688E-09	-1.89105331E-12	6.33003659E-16	-3.90835059E+04
H_2O	1.03497210E+06	-2.41269856E+03	4.64611078E+00	2.29199831E-03	-6.83683048E-07	9.42646893E-11	-4.82238053E-15	-1.38428651E+04
CO	4.61919725E+05	-1.94470486E+03	5.91671418E+00	-5.66428283E-04	1.39881454E-07	-1.78768036E-11	9.62093557E-16	-2.46626108E+03
H_2	5.60812338E+05	-8.37149134E+02	2.97536304E+00	1.25224993E-03	-3.74071842E-07	5.93662825E-11	-3.60699573E-15	5.33981585E+03
CH_4	3.73004276E+06	-1.38350149E+04	2.04910709E+01	-1.96197476E-03	4.72731304E-07	-3.72881469E-11	1.62373721E-15	7.53206691E+04
C_3H_8	6.42142917E+06	-2.66001757E+04	4.53451297E+01	-5.02125648E-03	9.47247800E-07	-9.57680928E-11	4.01030806E-15	1.45572981E+05
C_7H_{16}	1.28153359E+07	-5.41256205E+04	9.80119459E+01	-1.38270652E-02	3.43267831E-06	-4.35995372E-10	2.20016728E-14	2.96664874E+05
C_2H_2	1.71379212E+06	-5.92897095E+03	1.23611564E+01	1.31470625E-04	-1.36286904E-07	2.71274606E-11	-1.30208685E-15	6.26648973E+04
C_2H_4	0.00000000E+00	0.00000000E+00	1.12896000E+01	0.00000000E+00	0.00000000E+00	0.00000000E+00	0.00000000E+00	1.11900000E+03
Ar	2.01053848E+01	-5.99266107E-02	2.50006940E+00	-3.99214116E-08	1.20527214E-11	-1.81901558E-15	1.07857664E-19	-7.44993961E+02
C_6H_6	4.54977027E+06	-2.26153394E+04	4.69220720E+01	-4.19680822E-03	7.87029727E-07	-7.91921643E-11	3.30343000E-15	1.39238840E+05
CH_2O	1.70079900E+06	-7.62078666E+03	1.47244099E+01	-1.64907993E-03	3.29206332E-07	-3.49494520E-11	1.52608199E-15	3.14676911E+04
CH_3	2.76080266E+06	-9.33653117E+03	1.48772961E+01	-1.43942977E-03	2.44447795E-07	-2.22455578E-11	8.39506576E-16	7.48471957E+04
CH	2.06076344E+06	-5.39620666E+03	7.85629385E+00	-7.96590745E-04	1.76430831E-07	-1.97638627E-11	5.03042951E-16	1.06223659E+05
H	6.07877425E+01	-1.81935442E-01	2.50021182E+00	-1.22651286E-07	3.73287633E-11	-5.68774456E-15	3.41021020E-19	2.54748640E+04
NO	2.23901872E+05	-1.28965162E+03	5.43393603E+00	-3.65603490E-04	9.88096645E-08	-1.41607686E-11	9.38018462E-16	1.75031766E+04
O	2.61902026E+05	-7.29872203E+02	3.31717727E+00	-4.28133436E-04	1.03610459E-07	-9.43830433E-12	2.72503830E-16	3.39242806E+04
OH	1.01739338E+06	-2.50995728E+03	5.11654786E+00	1.30529993E-04	-8.28432226E-08	2.00647594E-11	-1.55699366E-15	2.04448713E+04

Table K-5. Coefficients used in NASA viscosity calculation for 200K < T < 1000K.

Species	A	B	C	D
N_2	0.62526577	-31.779652	-1640.79830	1.74549920
O_2	0.60916180	-52.244847	-599.74009	2.04108010
CO_2	0.51137258	-229.513210	13710.67800	2.70755380
H_2O	0.50019557	-697.127960	88163.89200	3.08365080
CO	0.62526577	-31.779652	-1640.79830	1.74549920
H_2	0.74553182	43.555109	-3257.93400	0.13556243
CH_4	0.57643622	-93.704079	869.92395	1.73333470
C_2H_2	0.56299896	-153.048650	4601.97340	1.88545280
C_2H_4	0.59136053	-140.889380	3001.28000	1.70189320

Table K-6. Coefficients used in NASA viscosity calculation for 1000K < T < 5000K.

Species	A	B	C	D
N_2	0.87395209	561.5222200	-173948.0900	-0.39335958
O_2	0.72216486	175.5083900	-57974.8160	1.09010440
CO_2	0.63978285	-42.6370760	-15522.6050	1.66288430
H_2O	0.58988538	-537.6981400	54263.5130	2.33863750
CO	0.87395209	561.5222200	-173948.0900	-0.39335958
H_2	0.96730605	679.3189700	-210251.7900	-1.82516970
CH_4	0.66400044	10.8608430	-7630.7841	1.03239840
C_2H_2	0.64038318	-7.2360229	-29612.2770	1.23930320
C_2H_4	0.66000894	39.1149990	-52676.4890	1.10336010

Table K-7. Lennard-Jones parameters.

Species	σ_0	ε/k	M
Air	3.711	78.6	28.964
Ar	3.542	93.3	39.948
Br	3.672	236.6	79.916
Br_2	4.296	507.9	159.832
C_2H_2	4.033	231.8	26.038
C_2H_4	4.163	224.7	28.054
C_2H_6	4.418	230.0	30.07
C_3H_8	5.061	254.0	44.09
i-C_4H_{10}	5.341	313.0	58.12
n-C_5H_{12}	6.769	345.0	72.15
n-C_6H_{14}	5.909	413.0	86.17
n-C_8H_{18}	7.451	320.0	114.22
Cyclohexane	6.093	324.0	84.16
C_6H_6	5.270	440.0	78.11
CH	3.370	68.6	13.009
CH_4	3.758	148.6	16.043
Cl	3.613	130.8	35.453
Cl_2	4.217	316.0	70.906
CN	3.856	75.0	26.018
CO	3.690	91.7	28.011
CO_2	3.941	195.2	44.01
F	2.986	112.6	18.999
F_2	3.357	112.6	37.998
H	2.708	37.0	1.008
H_2	2.827	59.7	2.016
H_2O	2.641	809.1	18.016
HBr	3.353	449.0	80.924
HCl	3.339	344.7	36.465
HCN	3.630	569.1	27.026
He	2.551	10.22	4.003
HF	3.148	330.0	20.006
N	3.298	71.4	14.007
N_2	3.798	71.4	28.013
N_2O	3.828	232.4	44.016
Ne	2.820	32.8	20.179
NH	3.312	65.3	15.015
NH_3	2.900	558.3	17.031
NO	3.492	116.7	30.008
O	3.050	106.7	16.0
O_2	3.467	106.7	31.999
OH	3.147	79.8	17.008

Table K-8. Smoke point heights as measured by Tewarson.

Fuel	Smokepoint m
Ethanol	0.225
Acetone	0.205
Pentane	0.155
Isopropanol	0.148
Hexane	0.125
Nylon	0.12
Ethylene	0.106
Heptane	0.11
PMMA	0.105
Cyclohexane	0.085
Isooctane	0.08
PP	0.05
PE	0.045
Propylene	0.029
PS	0.015
Toluene	0.005

Table K-9. Smoke point heights as measured by Schug *et. al.*

Fuel	Smokepoint m
C_2H_2	0.019
C_2H_4	0.106
C_2H_6	0.243
C_3H_6	0.029
C_3H_8	0.162
$1,3\text{-}C_4H_6$	0.015
$i\text{-}C_4H_8$	0.019
$n\text{-}C_4H_{10}$	0.16

Table K-10. Smoke point heights as reported by Tewarson from the literature: (a) alkanes; (b) alkenes, polyolefins, dienes, alkynes, and aromatics

	Fuel Name	Formula	MW kg/kmol	h_c° molar	h_c° kJ/kg	ℓ_e m	Notes
Normal Alkanes	Methane	CH_4	16	-74.6	-4662.5	0.29	
	Ethane	C_2H_6	30	-83.851544	-2795.1	0.243	
	Propane	C_3H_8	44	-104.68	-2379.1	0.162	
	Butane	C_4H_{10}	58	-125.79	-2168.8	0.16	
	Pentane	C_5H_{12}	72	-146.76	-2038.3	0.139	
	Hexane	C_6H_{14}	86	-166.92	-1940.9	0.118	
	Heptane	C_7H_{16}	100	-187.78	-1877.8	0.123	
	Octane	C_8H_{18}	114	-208.75	-1831.1	0.118	
	Nonane	C_9H_{20}	128			0.11	
	Decane	$C_{10}H_{22}$	142	-249.7	-1758.5	0.11	
	Undecane	$C_{11}H_{24}$	156	-270.3	-1732.7	0.11	
	Dodecane	$C_{12}H_{26}$	170	-290.9	-1711.2	0.108	
	Tridecane	$C_{13}H_{28}$	184	-311.5	-1692.9	0.106	
	Tetradecane	$C_{14}H_{30}$	198	-332.1	-1677.3	0.109	
Substituted Alkanes	Hexadecane	$C_{16}H_{34}$	226			0.118	
	2-Methylbutane	C_5H_{12}	72	-153.7	-2134.7	0.113	
	Dimethylbutane	C_6H_{14}	86	-177.8	-2067.4	0.089	2,2-dimethyl-butane
	2-Methylpentane	C_6H_{14}	86	-174.3	-2026.7	0.094	
	Dimethylpentane	C_7H_{16}	100	-202.1	-2021.0	0.096	2,4-dimethyl-pentane
	Methylhexane	C_7H_{16}	100	-195	-1950.0	0.109	2-methyl-hexane
	Trimethylpentane	C_8H_{18}	114	-216.4	-1898.2	0.07	2,3,3-trimethyl-pentane
	Methyl-ethylpentane	C_8H_{18}	114	-215	-1886.0	0.082	3-ethyl-3-methyl-pentane
	Ethylhexane	C_8H_{18}	114	-210.9	-1850.0	0.093	
	Dimethylhexane	C_8H_{18}	114	-219.4	-1924.6	0.089	2,4-dimethyl-hexane
Cyclic Alkanes	Methylheptane (3-)	C_8H_{18}	114	-212.6	-1864.9	0.101	
	Cyclopentane	C_5H_{10}	70	-76.4	-1091.4	0.067	
	Methylcyclopentane	C_6H_{12}	84	-106.7	-1270.2	0.052	
	Cyclohexane	C_6H_{12}	84	-123.1	-1465.5	0.087	
	Methylcyclohexane	C_7H_{14}	98	-154.8	-1579.6	0.075	
	Ethylcyclohexane	C_8H_{16}	112	-171.8	-1533.9	0.082	
	Dimethylcyclohexane	C_8H_{16}	112			0.057	
	Cyclooctane	C_8H_{16}	112			0.085	
	Decalin	$C_{10}H_{18}$	138			0.032	

(a)

	Fuel Name	Formula	MW kg/kmol	h° molar	h° kJ/kg	ℓ_e m	Notes
Normal Alkenes and Polyolefins	Bicyclohexyl	$C_{12}H_{22}$	166	-218.4	-1315.7	0.058	
	Ethylene	C_2H_4	28	52.5	1875.0	0.106	
	Propylene	C_3H_6	42	20	476.2	0.029	
	Butylene	C_4H_8	56	-0.63	-11.3	0.019	1-butene
	Pentene	C_5H_{10}	70	-28	-400.0	0.053	2-pentene(Z)
	Hexene	C_6H_{12}	84	-42.09	-501.1	0.063	1-hexene
	Heptene	C_7H_{14}	98	-62.3	-635.7	0.073	1-heptene
	Octene	C_8H_{16}	112	-82.93	-740.4	0.08	1-octene
	Nonene	C_9H_{18}	126			0.084	
	Decene	$C_{10}H_{20}$	140	-124.6	-890.0	0.079	1-decene
	Dodecene	$C_{12}H_{24}$	168	-165.4	-984.5	0.08	1-dodecene
	Tridecene	$C_{13}H_{26}$	182			0.084	
	Tetradecene	$C_{14}H_{28}$	196			0.079	
	Hexadecene	$C_{16}H_{32}$	224	-248.4	-1108.9	0.08	1-hexadecene
	Octadecene	$C_{18}H_{36}$	252			0.075	
	Polyethylene	$(C_2H_4)_n$	601			0.045	
Cyclic Alkenes	Polypropylene	$(C_3H_6)_n$	720			0.05	
	Cyclohexene	C_6H_{10}	82	-4.32	-52.7	0.044	
	Methylcyclohexene	C_7H_{12}	96	-81.25	-846.4	0.043	1-methylcyclohexene
Dienes	Pinene	$C_{10}H_{16}$	136			0.024	
	1-3 Butadiene	C_4H_6	54	110	2037.0	0.015	
Normal Alkynes	Cyclooctadiene (1,5)	C_8H_{12}	108	57	527.8	0.037	
	Acetylene	C_2H_2	26	228.2	8776.9	0.019	
	Heptyne	C_7H_{12}	96	103.8	1081.3	0.035	
	Octyne	C_8H_{14}	110	80.7	733.6	0.03	
	Decyne	$C_{10}H_{18}$	138	41.9	303.6	0.043	
Aromatics	Dodecyne	$C_{12}H_{22}$	166			0.03	
	Benzene	C_6H_6	78	82.88	1062.6	0.007	
	Toluene	C_7H_8	92	50.17	545.3	0.006	
	Styrene	C_8H_8	104	148.3	1426.0	0.006	check
	Ethylbenzene	C_8H_{10}	106	29.92	282.3	0.005	check
	Xylene	C_8H_{10}	106	17.9	168.9	0.006	
	Phenylpropyne	C_9H_8	116	268.2	2312.1	0.006	
	Indene	C_9H_8	116			0.008	
	Propylbenzene	C_9H_{12}	120	7.82	65.2	0.009	
	Trimethylbenzene	C_9H_{12}	120	-13.9	-115.8	0.006	1,2,4-trimethylbenzene
	Cumene	C_9H_{12}	120	3.9	32.5	0.006	
	Napthalene	$C_{10}H_8$	128	150.6	1176.6	0.005	
	Tetralin	$C_{10}H_{12}$	132	26	197.0	0.006	
	Butylbenzene	$C_{10}H_{14}$	134	-13.8	-103.0	0.007	
	Diethylbenzene	$C_{10}H_{14}$	134			0.007	
	p-Cymene	$C_{10}H_{14}$	146			0.007	
	Methylnapthalene	$C_{11}H_{10}$	142	116.1	817.6	0.006	
	Pentylbenzene	$C_{11}H_{16}$	148			0.009	
	Dimethylnapthalene	$C_{12}H_{12}$	156			0.006	
	Cyclohexylbenzene	$C_{12}H_{16}$	160	-16.7	-104.4	0.007	
	Di-isopropylbenzene	$C_{12}H_{18}$	162			0.007	
	Triethylbenzene	$C_{12}H_{18}$	162			0.006	
	Triamylbenzene	$C_{21}H_{36}$	288			0.007	
	Polystyrene	$(C_8H_8)_n$	200			0.015	

(b)

K.2 Appendix K References

1. Gordon, S. and McBride, B.J., "Computer Program for Calculation of Complex Chemical Equilibrium Compositions and Applications," NASA Reference Publication 1311, 1994.

2. Strehlow, R.A., *Combustion Fundamentals*, McGraw-Hill Book Company, pg. 481, New York, 1984.

3. Bird, R.B., Stewart, W.E., and Lightfoot, E.N., *Transport Phenomena*, John Wiley & Sons, pp. 744-745, New York, 1960.

4. Tewarson, A., "Prediction of Fire Properties of Materials-Part I: Aliphatic and Aromatic Hydrocarbons and Related Polymers," Factory Mutual Research Corporation J.I. 0K3R3.RC, (NBS Grant #60NANB4D-0043), 1986.

5. Schug, K.P., Manheimer-Timnat, Y., Yaccarino, P., and Glassman, I., "Sooting Behavior of Gaseous Hydrocarbon Diffusion Flames and the Influence of Additives," *Combustion Science and Technology* **22**:235-250 (1980).

APPENDIX L USER'S GUIDE TO NEW FEATURES

It is assumed that the reader is familiar with FDS and has had some experience setting up and running calculations using the code. This appendix describes the modifications to the FDS code that that can be accessed from the standard ASCII input file by through the `&SOOT` namelist group. For example, the following line would be added to a FDS input file to tell the code to use the new soot model but to not calculate the thermophoresis source term:

```
&SOOT SOOTMODEL = .TRUE., THERMOPHORESIS = .FALSE. /
```

The available keywords are summarized below, grouped together by their functionality.

L.1 General Simulation Parameters

The user specifies which fuel to burn by setting the integer constant `IUSERFUEL` (index of user-specified fuel) to a value between 7 and 15. The fuel type and properties corresponding to each `IUSERFUEL` are listed in Table L-1. The default value is 11 (ethylene). The value of `IUSERFUEL` must be 7 or greater because the program assigns N_2, O_2, CO_2, H_2O, CO, and H_2 species numbers of 1 through 6. More fuels will be added in the future.

Table L-1. Fuel properties.

#	Fuel	Formula	MW	$h^{\circ}_{298.15}$	ℓ_s	ΔH_T	ΔH_c	ν_{O_2}	ν_{CO_2}	ν_{H_2O}
			kg/kmol	J/mole	m	MJ/kg	MJ/kg			
7	Methane	CH_4	16.04246	-74600	0.29	50.1	49.6	2.0	1.0	2.0
8	Propane	C_3H_8	44.09562	-104680.0	0.162	46.0	43.7	5.0	3.0	4.0
9	Heptane	C_7H_{16}	100.20194	-187780.0	0.123	44.6	41.2	11.0	7.0	8.0
10	Acetylene	C_2H_2	26.03728	228200.0	0.019	47.8	36.7	2.5	2.0	1.0
11	Ethylene	C_2H_4	28.05316	52500.0	0.106	48.0	41.5	3.0	2.0	2.0
12	Propylene	C_3H_6	42.07974	20000.0	0.029	46.4	40.5	4.5	3.0	3.0
13	Ethane	C_2H_6	30.06904	-83851.544	0.243	47.1	45.7	3.5	2.0	3.0
14	Isobutene	C_4H_8	56.10632	-17100.0	0.019	45.6	40.0	6.0	4.0	4.0
15	1,3-Butadiene	C_4H_6	54.09044	110000.0	0.015	44.6	33.6	5.5	4.0	3.0

The temperature-dependent specific heat, as taken from the NASA Chemical Equilibrium Code, is used to determine the sensible enthalpy as a function of temperature for each species. The temperature-dependency of the molecular viscosity is also evaluated using coefficients taken

from the NASA Chemical Equilibrium Code for N_2, O_2, CO_2, H_2O, CO, H_2, CH_4, C_2H_2, and C_2H_4. The viscosities of C_3H_8 and C_2H_6 are estimated from Chapman-Enskog theory. No viscosity coefficients were available for heptane, propylene, isobutene, or 1,3-butadiene so it was arbitrarily decided to use the viscosity of methane for these fuels.

Additional parameters are summarized below:

`ORIGINALFORM` The code will revert to its original form (i.e. with no modifications performed as part of this work) if the user specifies `ORIGINALFORM = .TRUE.`. By default `ORIGINALFORM = .FALSE.`.

`LAMINAR` In laminar calculations, soot concentration gradients do not cause a diffusion of soot due to the negligible diffusivity of soot particles. Therefore the soot conservation equation does not have a diffusive term. In turbulent calculations, diffusion of soot is due to turbulent mixing and a diffusive term is included in the soot conservation equation. Also, in laminar calculations the Smagorinsky eddy viscosity calculation is bypassed. The default value is `LAMINAR = .TRUE.`.

`NASAVISCOSITY` In laminar calculations, by default the molecular viscosity μ is determined as a function of mixture fraction and temperature using Equations A-24 and A-25. As mentioned above, the $\mu(T)$ curvefits for each individual species are taken from the NASA Chemical Equilibrium Code except for propane and ethane where $\mu(T)$ is calculated from Chapman-Enskog theory. However, if the user specifies `NASAVISCOSITY = .FALSE.`, then the viscosity of the background species (air) as calculated by FDS from Chapman-Enskog theory is used.

CLIPHT (Clip total enthalpy) By default, the total enthalpy in a cell is not allowed to exceed its adiabatic value or fall below the chemical enthalpy of the products. If such an overshoot or undershoot occurs, the value of the total enthalpy is "clipped". However, this clipping may be bypassed by specifying CLIPHT = .FALSE..

SIVATHANU The Sivathanu and Faeth state relations (See Section C.3) have been implemented into the code and can be used by specifying SIVATHANU = .TRUE.. By default SIVATHANU = .FALSE. and the complete combustion state relations are used.

SMOOTHING_FACTOR This is the value of α that appears in Equations C.24 through C.27. It is used to "smooth" the complete combustion state relations. The piecewise-linear state relations are retained when SMOOTHING_FACTOR = 1.0, and the level of smoothing increases as SMOOTHING_FACTOR decreases. By default, SMOOTHING_FACTOR = 0.8.

DIVGCHEAT (divergence cheat). The expression derived from the continuity equation for the divergence of the velocity field as given in Section E.2 was found to be problematic in turbulent calculations. More research is intended to determine the cause of this. For the time being, the original velocity divergence expression can be used by specifying DIVGCHEAT = .TRUE.. It is recommended that in laminar calculations DIVGCHEAT = .FALSE. and in turbulent calculations DIVGCHEAT = .TRUE.. By default DIVGCHEAT = .FALSE. because the code defaults to a laminar calculation.

ZMIN This is the minimum allowed value of mixture fraction. This overrides the value specified in the &CLIP namelist group.

`TAD` (Adiabatic temperature) This is the highest expected temperature. It is only used to dynamically allocate memory for the arrays storing $c_{p,i}(T)$, $h_i(T)$, and $h_{T,i}(T)$. It does not affect the calculation in any way as long as a high enough value is specified. It is by default 2600K, but may need to be increased for simulations in enriched oxygen.

L.2 General Soot Formation / Oxidation Model Options

`SOOTMODEL` Unless the user specifies `SOOTMODEL = .FALSE.`, the new soot model will be used and a separate conservation equation will be solved for the soot mass fraction.

`SOOT_FORMATION_TYPE` This parameter is an integer between 1 and 3 that tells the model which soot growth mechanism(s) to use. If `SOOT_FORMATION_TYPE = 1` then *only surface area-dependent* growth will be used. If `SOOT_FORMATION_TYPE = 2` then *only surface area-independent* growth will be used. If `SOOT_FORMATION_TYPE = 3` then *both* growth mechanisms will be used. The default is 3 (both).

`THERMOPHORESIS` The thermophoresis term $\nabla\cdot(\mu Y_s/Y)\nabla T$ can be calculated by setting `THERMOPHORESIS = .TRUE.`. By default its value is `.TRUE.`. Note that whether or not this term is actually used in the soot conservation equation is determined by the value of `THERMPSOURCE` (see below).

`THERMPSOURCE` (Thermophoresis source) This is a remnant of the debugging process. If the user wishes to calculate the magnitude of the thermophoresis source term but not actually use it in the soot conservation equation (*e.g.* just to view the thermophoresis source term using

Smokeview) then THERMPSOURCE can be set to .FALSE.. By default, THERMPSOURCE = .TRUE. if THERMOPHORESIS = .TRUE., and is irrelevant otherwise.

SOOTINCEPTIONAREA By default, the soot inception area A_0 $\left(\mathrm{m}^2\ \mathrm{soot}/\mathrm{m}^3\ \mathrm{mixture}\right)$ is calculated as $A_0 \approx 1.0 + 1.6\dot{\omega}''_{sf,P}\left(h^\circ - h^\circ_{CH_4}\right)$. However, the user may specify a different inception area that overrides this value by setting the value of SOOTINCEPTIONAREA.

FVTOSOOTAREASLOPE The soot surface area is related to the soot inception area and the soot volume fraction as $A_s = A_0 + \beta f_v$. The parameter β is 8.0×10^7 by default, but the user may specify an alternate value by setting the parameter FVTOSOOTAREASLOPE.

TWOPHASE (two-phase density) The two-phase density ρ_2 is related to the gas-phase density ρ_g and the soot mass fraction Y_s as $\rho_2 = \rho_g/\left(1 - Y_s\right)$. By default, the density term used in the soot conservation equation is the two-phase density. Note that ρ_g is always used in the mixture fraction conservation equation. However, the gas-phase density may be used in the soot conservation equation by setting TWOPHASE = .FALSE..

ZSOURCETERM (Mixture fraction source term) The mixture fraction is classically defined as a perfectly conserved scalar with no source or sink. However, 30% or more of the fuel mass may locally be converted to soot in heavily sooting fuels. For this reason, a mechanism has been added to the code that will add a source term to the mixture fraction conservation equation of equal magnitude but opposite sign to the soot formation term. This accounts for the conversion of fuel to soot and the mixture fraction is therefore a gas-phase quantity. By default, ZSOURCETERM = .TRUE..

HTSFOSOURCETERM (h_T soot formation/oxidation source term) The effect of soot formation and oxidation on the gas-phase enthalpy are unclear. As a first approximation, a source term equal to $\dot{\omega}_s'''h_f^\circ$ for $\dot{\omega}_s''' > 0$ and $\dot{\omega}_s'''h_{CO}^\circ$ for $\dot{\omega}_s''' < 0$ S_{h_T} can be included in the conservation equation for total enthalpy. Using this approximation, soot formation constitutes a *source* of gas-phase enthalpy for fuels with a *positive* standard enthalpy of formation, but a *sink* of gas-phase enthalpy for fuels with a *negative* standard enthalpy of formation. Soot oxidation is always a source of gas-phase enthalpy. By default, HTSFOSOURCETERM = .TRUE..

SOOT_DENSITY The soot density ρ_s affects the radiation calculation because the soot volume fraction is determined from the soot mass fraction as $f_v = \rho_2 Y_s / \rho_s$, and then the soot contribution to the total absorption coefficient is calculated as $\kappa_s = C_{\kappa_s} f_v T$.

YSMIN This is the minimum allowed value of the soot mass fraction. In any cell where Y_s falls below YSMIN, it will be increased to YSMIN. The default value is –0.001.

YSMAX, This is the maximum allowed value of the soot mass fraction. In any cell where Y_s goes above YSMAX, it will be decreased to YSMAX. The default value is 0.5.

L.3 Specifying the Soot Formation / Oxidation Polynomials

The specific forms of the soot formation and oxidation polynomials are determined by assigning values to the parameters listed in Tables L-2 and L-3. Unless the user specifies otherwise, the default value in the rightmost column will be used. A user-specified value takes precedence over the default value.

The polynomials are all 5th order (6 coefficients) by default, except for the linear soot oxidation temperature function. Future work will be performed to recalibrate the global model constants using 3rd order polynomials (4 coefficients). To expedite this process and eliminate the need for additional FORTRAN coding, a mechanism has been added to force the polynomials to be 3rd order by setting any or all of the logical constants `ZSFPUAIS3RDORDER`, `ZSFPUVIS3RDORDER`, `ZSOPUAIS3RDORDER`, `TSFPUAIS3RDORDER`, or `TSFPUVIS3RDORDER` to be `.TRUE.`. It is not necessary to specify the slope (*e.g.* `SLOPE_L_SF_PUA` OR `SLOPE_H_SF_PUA`) for 3rd order polynomials. Rather, only the three ψ values and the peak value of the function must be specified.

Table L-2. Soot formation and oxidation mixture fraction polynomial keywords.

Keyword	Symbol	Description	Default Value
PSI_L_SF_PUA	ψ_{sf,Z_L}^{PUA}	Sets Z_L for $f''_{Zsf}(Z)$	1.03
PSI_P_SF_PUA	ψ_{sf,Z_P}^{PUA}	Sets Z_P for $f''_{Zsf}(Z)$	1.7
PSI_H_SF_PUA	ψ_{sf,Z_H}^{PUA}	Sets Z_H for $f''_{Zsf}(Z)$	2.1
SLOPE_L_SF_PUA	ϕ_{sf,Z_L}^{PUA}	Sets $df''_{Zsf}(Z)/dZ$ at Z_L	1.7
SLOPE_H_SF_PUA	ϕ_{sf,Z_H}^{PUA}	Sets $df''_{Zsf}(Z)/dZ$ at Z_H	1.2
PSI_L_SF_PUV	ψ_{sf,Z_L}^{PUV}	Sets Z_L for $f'''_{Zsf}(Z)$	1.02
PSI_P_SF_PUV	ψ_{sf,Z_P}^{PUV}	Sets Z_P for $f'''_{Zsf}(Z)$	1.65
PSI_H_SF_PUV	ψ_{sf,Z_H}^{PUV}	Sets Z_H for $f'''_{Zsf}(Z)$	2.2
SLOPE_L_SF_PUV	ϕ_{sf,Z_L}^{PUV}	Sets $df'''_{Zsf}(Z)/dZ$ at Z_L	1.9
SLOPE_H_SF_PUV	ϕ_{sf,Z_H}^{PUV}	Sets $df'''_{Zsf}(Z)/dZ$ at Z_H	0.5
PSI_L_SO_PUA	ψ_{so,Z_L}^{PUA}	Sets Z_L for $f''_{Zso}(Z)$	0.55
PSI_P_SO_PUA	ψ_{so,Z_P}^{PUA}	Sets Z_P for $f''_{Zso}(Z)$	0.85
PSI_H_SO_PUA	ψ_{so,Z_H}^{PUA}	Sets Z_H for $f''_{Zso}(Z)$	1.07
SLOPE_L_SO_PUA	ϕ_{so,Z_L}^{PUA}	Sets $df''_{Zso}(Z)/dZ$ at Z_L	1.0
SLOPE_H_SO_PUA	ϕ_{so,Z_H}^{PUA}	Sets $df'''_{Zso}(Z)/dZ$ at Z_H	1.0
PEAKSFRATE_PUA	$\dot{\omega}''_{sf,P}$	Peak PUA soot formation rate $(\mathrm{kg/m^2 \cdot s})$	$0.0015/\ell_s^{0.6}$
PEAKSFRATE_PUV	$\dot{\omega}'''_{sf,P}$	Peak PUV soot formation rate $(\mathrm{kg/m^3 \cdot s})$	$0.15/\ell_s^{0.6}$
PEAKSORATE_PUA	$\dot{\omega}''_{so,P}$	Peak soot oxidation rate $(\mathrm{kg/m^2 \cdot s})$	-0.007

Table L-3. Soot formation and oxidation temperature polynomial keywords.

Keyword	Constant	Description	Default Value
TMIN_SF_PUA	$T_{L,sf}^{PUA}$	Minimum T for PUA soot formation	1400K
TPEAK_SF_PUA	$T_{P,sf}^{PUA}$	T for peak PUA soot formation	1600K
TMAX_SF_PUA	$T_{H,sf}^{PUA}$	Maximum T for PUA soot formation	1925K
TSLOPE_L_SF_PUA	$df_{Tsf}^{PUA}(T_L)/dT$	$df_{Tsf}^{PUA}(T)/dT$ at $T_{L,sf}^{PUA}$	0.0045
TSLOPE_H_SF_PUA	$df_{Tsf}^{PUA}(T_H)/dT$	$df_{Tsf}^{PUA}(T)/dT$ at $T_{H,sf}^{PUA}$	-0.004
TMIN_SF_PUV	$T_{L,sf}^{PUV}$	Minimum T for PUV soot formation	1375K
TPEAK_SF_PUV	$T_{P,sf}^{PUV}$	T for peak PUV soot formation	1475K
TMAX_SF_PUV	$T_{H,sf}^{PUV}$	Maximum T for PUV soot formation	1575K
TSLOPE_L_SF_PUV	$df_{Tsf}^{PUV}(T_L)/dT$	$df_{Tsf}^{PUV}(T)/dT$ at $T_{L,sf}^{PUV}$	0.0002
TSLOPE_H_SF_PUV	$df_{Tsf}^{PUV}(T_H)/dT$	$df_{Tsf}^{PUV}(T)/dT$ at $T_{H,sf}^{PUV}$	-0.0005
TMIN_SO_PUA	$T_{L,so}^{PUA}$	Minimum T for soot oxidation	1400K
TSLOPE_SO_PUA	$df_{Tso}^{PUA}(T_L)/dT$	Slope of $f_{Tso}(T)$ at $T_{L,so}^{PUA}$	0.006

L.4 Probability Density Function Parameters

In turbulent calculations, the grid-scale soot formation/oxidation rate may be calculated by integration over a probability density function (PDF). This takes into account subgrid-scale fluctuations in mixture fraction and temperature rather than evaluating the soot formation rate from the mean value of temperature and mixture fraction in each cell.

`PDF` The user may instruct the code to use the PDF by specifying the logical constant `PDF = .TRUE.`. By default, `PDF = .FALSE.`.

`IDELTAZPDF` (index of ΔZ_{PDF}) Using the PDF option is computationally expensive because an inefficient approximation by rectangles integration technique is used. By

default, the value of ΔZ used in this integration is 0.0001. However, the size of ΔZ can be increased by setting the value of the integer `IDELTAZPDF` to be greater than 1, thereby reducing the computational cost. More specifically, $\Delta Z = 0.0001/\texttt{IDELTAZPDF}$. Future work is planned to implement more efficient integration techniques.

`CSCALE` The subgrid-scale variance of the mixture fraction is estimated using the principle of scale-similarity. The parameter C_{scale} in Equation B-31 is used to determine the subgrid-scale variance. The numerical value of C_{scale} can be changed from its default value of 1.3 by setting the value of `CSCALE`.

L.5 Radiation Parameters

`CKAPPAS` The contribution of the soot volume fraction to the mean absorption coefficient is calculated as $\kappa_s = C_{\kappa_s} f_v T$. The default value of C_{κ_s} is 1186 $(\text{mK})^{-1}$, but a different value may be used by setting the parameter `CKAPPAS`.

`MEAN_BEAM_LENGTH` The gas-phase contribution κ_g to the mean absorption coefficient is calculated using RADCAL by evaluating the integral $\kappa_g(Z,T) = \int_{\lambda_1}^{\lambda_2} \kappa\left(T, L, P_{H_2O}, P_{CO_2}, P_F, \lambda\right) d\lambda$. The parameter L in this integral is the radiation pathlength. Unless the user specifies otherwise, L is set to the mean beam length of the *computational domain* as evaluated using the standard $L = 3.6V/A$ formula. However, a mean beam length characteristic of the flame envelope is more appropriate for near-field radiation calculations, and the user may specify an alternate mean beam length with the keyword `MEAN_BEAM_LENGTH`.

DT_RC and DZ_RC (ΔT RADCAL and ΔZ RADCAL). At the start of a calculation, the value of κ_g is stored as a function of mixture fraction and temperature using RADCAL. κ_g is stored at a discrete number of *Z*-*T* combinations to save storage overhead and CPU time at the start of a calculation. During runtime, the value of κ_g in a cell is determined by finding the *Z*-*T* combination in the lookup table that most closely matches the local values in a cell. The user can specify the size of the mixture fraction and temperature "buckets" by setting the values of DT_RC and DZ_RC . By default DZ_RC is 0.005 and DT_RC is 50K. This means that the value of mixture fraction in a cell will be rounded by a maximum of 0.0025 and the value of temperature in a cell will be rounded by a maximum of 25K when determining the value of κ_g in that cell. The user may use smaller buckets by specifying smaller values of DT_RC and DZ_RC. This results in greater storage cost but little or no computational cost beyond the time required to generate the tables at the start of the calculation.

SOOTEMISSION By default, the soot contribution to the total absorption coefficient is calculated as $\kappa_s = C_{\kappa_s} f_v T$. However, the user may wish to prevent soot from contributing to the absorption coefficient in which case κ_s can be set to 0 by specifying SOOTEMISSION = .FALSE..

GASEMISSION By default, the gas-phase contribution to the total absorption coefficient is calculated using RADCAL to evaluate the integral $\kappa_g(Z,T) = \int_{\lambda_1}^{\lambda_2} \kappa(T, L, P_{H_2O}, P_{CO_2}, P_F, \lambda) d\lambda$. However, κ_g can be set to 0 by specifying GASEMISSION = .FALSE..

USERHRR (user-specified heat release rate) This parameter does not affect the calculation, but rather is used to determine the global radiant fraction by evaluating $\chi_r = \int \left(\dot{q}_e''' - \dot{q}_a'''\right) dV \Big/ \text{USERHRR}$. It must be specified in kW, and its default value is 1.0 although this is arbitrary.

L.6 Enthalpy/Temperature Correction

The enthalpy (or temperature) correction is applied as described in Section F.2 by specifying up five pairs of ZCORR_,HCORR_ where the underscore is an integer between 1 and 5. In other words, ZCORR1 is the *Z* value of the first temperature correction point, and HCORR1 is the corresponding value of the enthalpy correction (in kJ/kg) at ZCORR1. *Positive* values correspond to an *increase* of the adiabatic stoichiometric temperature, and *negative* values correspond to a *decrease* of the adiabatic stoichiometric temperature.

Each of the user-specified correction points is connected by a cubic spline with its second derivative equal to zero at its endpoints. The first correction point (ZCORR1,HCORR1) is connected to (0,0) by a straight line, and the last correction point is connected to the point (1,0) by a straight line. The user must specify the number of correction points by setting integer NCORR (number of correction points). For example, if NCORR = 4 then a straight line will be drawn from (ZCORR4,HCORR4) to (1,0). By default, NCORR = 5, and the ZCORR_/HCORR_ values are given below in Table L-4. Future work is planned to generalize this correction by scaling the values by the stoichiometric value of mixture fraction.

Table L-4. Default values of ZCORR and HCORR for temperature correction.

Parameter	Value	Parameter	Value
ZCORR1	0.004	HCORR1	110
ZCORR2	0.065	HCORR2	-390
ZCORR3	0.135	HCORR3	-640
ZCORR4	0.240	HCORR4	-480
ZCORR5	0.400	HCORR5	-380

L.7 New Smokeview Quantities

Several quantities that can be visualized in Smokeview were added to the code. They are summarized below in Table L-5:

Table L-5. New Smokeview quantities.

Quantity	Description	Units
MDOTSOOTMEAN	Mean soot formation rate	$\mathrm{kg}/(\mathrm{m}^3 \cdot \mathrm{s})$
MDOTSOOTACT	Actual soot formation rate used in conservation equation	$\mathrm{kg}/(\mathrm{m}^3 \cdot \mathrm{s})$
MDOTSOOTPDF	Soot formation rate using PDF	$\mathrm{kg}/(\mathrm{m}^3 \cdot \mathrm{s})$
MDOTSOOTDIFF	MDOTSOOTPDF minus MDOTSOOTMEAN	$\mathrm{kg}/(\mathrm{m}^3 \cdot \mathrm{s})$
SFRATE_PUA_MEAN	$\dot{\omega}''_{sf}$	$\mathrm{kg}/(\mathrm{m}^2 \cdot \mathrm{s})$
SFRATE_PUV_MEAN	$\dot{\omega}'''_{sf}$	$\mathrm{kg}/(\mathrm{m}^3 \cdot \mathrm{s})$
SORATE_PUA_MEAN	$\dot{\omega}''_{so}$	$\mathrm{kg}/(\mathrm{m}^2 \cdot \mathrm{s})$
PUA_SF_ON_PUV_BASIS	$A_s \dot{\omega}''_{sf}$	$\mathrm{kg}/(\mathrm{m}^3 \cdot \mathrm{s})$
THERMOPHORESIS_SOURCE	$0.55\nabla \cdot (Y_s \mu / T)\nabla T$	$\mathrm{kg}/(\mathrm{m}^3 \cdot \mathrm{s})$
YS_TOTAL_SOURCE	Thermophoresis plus soot formation	$\mathrm{kg}/(\mathrm{m}^3 \cdot \mathrm{s})$
SOOT_MASS_FRACTION	Y_s	kg soot/kg mixture
SOOT_VOLUME_FRACTION	f_v	m^3 soot/m^3 mixture
TOTAL_ENTHALPY	h_T	kJ/kg
LOCAL_CHI_RAD	local nonadiabaticity (χ)	[-]
RADIANT_EMISSION	$\dot{q}'''_e = 4\sigma\kappa T^4$	kW/m^3
TEMP_LOSS	$T_{ad}(Z) - T$	K
DZDT	$\frac{DZ}{Dt} = \frac{1}{\rho}[\nabla \cdot (\rho D \nabla Z) + S_Z]$	s^{-1}
DHTDT	$\frac{Dh_T}{Dt} = \frac{1}{\rho}[\nabla \cdot (\rho D \nabla h_T) + S_{h_T}]$	$\mathrm{kJ}/(\mathrm{kg} \cdot \mathrm{s})$
DZDTDTDZ	$\frac{DZ}{Dt}\frac{\partial T}{\partial Z}\Big\|_{h_T}$	K/s
DHTDTDTDHT	$\frac{Dh_T}{Dt}\frac{\partial T}{\partial h_T}\Big\|_{Z}$	K/s
HTSOURCE	Total source term for gas-phase enthalpy	kW/m^3
QSFO	Source of gas-phase enthalpy due to soot formation/oxidation	kW/m^3
SGSZVARIANCE	Subgrid-scale mixture fraction variance	[-]
PDFOMEANEMISSION	PDF emission over mean emission (not currently used)	[-]

APPENDIX M USER'S GUIDE TO SLICETOCSV COMPANION PROGRAM

It is possible to gain a broad understanding of a particular quantity's space-time evolution by using Smokeview to visualize slice files generated by the FDS solver. However, visualization techniques cannot provide the user with detailed quantitative data. If the user is interested in a specific quantity at a particular location in the computational domain, it is possible to insert "thermocouples" using the `THCP` keyword. This can become quite cumbersome if the user is interested in tens, or even hundreds of points throughout the flowfield.

A simple program called `slicetocsv.exe` was written to extract quantitative data from FDS-generated slice files and convert it to a `.CSV` (comma separated variable) file that is easily imported into commercial spreadsheet packages such as Microsoft Excel. It dumps the value in every cell of the particular quantity stored in a slice file to a simple ASCII `.CSV` file. The information can then be examined in detail, without resorting to specification of hundreds of thermocouples. This program was primarily used in this research to extract a particular flowfield variable (*e.g.* T or f_v) and import the data into a spreadsheet for comparison of model prediction and experiment. This was done primarily with laminar 2D steady-state flame simulations so a single snapshot fully portrays the computation.

However, in simulations of turbulent fire plumes, a single snapshot does not completely characterize the plume. Although turbulence is inherently unsteady, the statistical properties of a turbulent flow are reproducible if the boundary conditions don't change. For this reason, it is often desirable to examine time-averaged output from simulations. The program slicetocsv can also be used to time-average data from transient slice file.

Using `slicetocsv`

Copy the file `slicetocsv.exe` to the directory containing the slice files generated by FDS from which data are to be extracted. The program is executed from the command line by typing

```
slicetocsv < sliceread.txt
```

where `sliceread.txt` is the full name (including extension) of a text file containing information on the slice files to process. The input file should be organized as follows:

Line 1: `CHID` of simulation (from FDS input file)
Line 2: Simulation time at which to begin time-averaging
Line 3: Simulation time at which to end time-averaging
Line 4: Number of slice files to process (integer)
Line 5: Suffix (after `CHID`) of slice file #1 to process
Line 6: Suffix (after `CHID`) of slice file #2 to process
Line 7: etc., up to the total number of slice files to process

As an example, the data contained in the slice files `plume_01.sf` and `plume_02.sf` would be extracted and time-averaged from 5 seconds to 20 seconds by creating a text file called `plume.read` that contains the following lines

```
PLUME
5.0
20.0
2
_01.sf
_02.sf
```

and then typing from the command prompt:

```
slicetocsv < plume.read
```

Files called `PLUME_01.sf.CSV` and `PLUME_02.sf.CSV` would be created in the current directory. They are simply ASCII text files with each entry separated by a comma. They can be imported by double-clicking from within Windows Explorer if your system recognizes the `.CSV` extension. If not, you must manually import them into your spreadsheet program, e.g.

by using File...Open. Once opened, the file will have the form shown in Tables M-1 through M-3 (where T_{ij} is a quantity such as temperature in the i^{th}, j^{th} cell) depending on whether the slice file is an xz (zx), xy (yx), or yz (zy) plane.

Table M-1. Spreadsheet format of slicetocsv output for *xz* slicefile.

	A	B	C	D	E
1		x_1	x_2	x_3	x_4
2	z_1	T_{11}	T_{12}	T_{13}	T_{14}
3	z_2	T_{21}	T_{22}	T_{23}	T_{24}
4	z_3	T_{31}	T_{32}	T_{33}	T_{34}
5	z_4	T_{41}	T_{42}	T_{43}	T_{44}

Table M-2. Spreadsheet format of slicetocsv output for *xy* slicefile.

	A	B	C	D	E
1		x_1	x_2	x_3	x_4
2	y_1	T_{11}	T_{12}	T_{13}	T_{14}
3	y_2	T_{21}	T_{22}	T_{23}	T_{24}
4	y_3	T_{31}	T_{32}	T_{33}	T_{34}
5	y_4	T_{41}	T_{42}	T_{43}	T_{44}

Table M-3. Spreadsheet format of slicetocsv output for *yz* slicefile.

	A	B	C	D	E
1		y_1	y_2	y_3	y_4
2	z_1	T_{11}	T_{12}	T_{13}	T_{14}
3	z_2	T_{21}	T_{22}	T_{23}	T_{24}
4	z_3	T_{31}	T_{32}	T_{33}	T_{34}
5	z_4	T_{41}	T_{42}	T_{43}	T_{44}